

# A First Search for coincident Gravitational Waves and High Energy Neutrinos

Von der Fakultät für Mathematik und Physik  
der Gottfried Wilhelm Leibniz Universität Hannover  
zur Erlangung des Grades

**Doktorin der Naturwissenschaften**  
**Dr. rer. nat.**

genehmigte Dissertation  
von

**Dottoressa Irene Di Palma**  
geboren am 07 März 1985 in Rom/Italien



MAX-PLANCK-GESELLSCHAFT

2012

Referent: Herr Prof. Dr. Bruce Allen, Frau Dr. Maria Alessandra Papa  
Korreferent: Herr Prof. Dr. Szabolcs Marka  
Tag der Promotion: 14 August 2012

*Alla mia famiglia...*

*.. l'amor che move il sole e l'altre stelle.*



# Contents

<b>Abstract</b>	<b>9</b>
<b>Kurzfassung</b>	<b>11</b>
<b>Summary</b>	<b>13</b>
<b>1 Gravitational Waves</b>	<b>21</b>
1.1 Introduction . . . . .	21
1.2 Gravitational Waves in General Relativity . . . . .	23
1.3 Theory of Gravitational Waves . . . . .	25
1.4 A perturbation of the Minkowski spacetime . . . . .	27
1.5 Solution in vacuum . . . . .	30
1.6 The $TT$ -gauge . . . . .	31
1.6.1 A single particle effected by a gravitational wave . . . . .	33
1.7 Interaction of gravitational waves with test masses . . . . .	33
<b>2 Sources of Gravitational Waves</b>	<b>41</b>
2.1 Introduction . . . . .	41
2.2 Supernovae and gravitational collapse . . . . .	42
2.3 Coalescing binaries . . . . .	42
2.4 Gravitational radiation from individual neutron stars . . . . .	44
2.5 Stochastic background . . . . .	45
<b>3 Common sources of Gravitational Waves and High Energy Neutrinos</b>	<b>47</b>
3.1 Introduction . . . . .	47
3.2 Galactic Sources . . . . .	49
3.2.1 Microquasars . . . . .	49

3.2.2	Soft gamma-ray repeaters . . . . .	50
3.3	An exotic class of source: cosmic strings . . . . .	51
3.4	Extragalactic sources: Gamma Ray Bursts . . . . .	51
3.4.1	GRB Progenitors: double neutron stars (NS/NS) and black Hole Neutron Star, BH/NS . . . . .	53
3.5	Fireball Model . . . . .	57
3.6	The GRB puzzle . . . . .	58
3.7	Search time window . . . . .	60
<b>4</b>	<b>LIGO: the Laser Interferometer Gravitational Wave Observ- atory</b>	<b>63</b>
4.1	Introduction . . . . .	63
4.2	Worldwide detector network . . . . .	64
4.3	Principle of detection . . . . .	65
4.3.1	Optic configuration: power recycled Fabry Perot Michel- son . . . . .	65
4.3.2	Mirrors . . . . .	67
4.3.3	Laser . . . . .	67
4.3.4	Sensing and Control . . . . .	68
4.4	Instrumental performance . . . . .	69
<b>5</b>	<b>Neutrino interactions and detection principles</b>	<b>73</b>
5.1	Introduction . . . . .	73
5.2	Neutrino interaction . . . . .	74
5.3	Discovery of the Cherenkov emission . . . . .	75
5.4	Description of the Cherenkov effect . . . . .	76
5.5	Muon propagation . . . . .	80
<b>6</b>	<b>ANTARES Neutrino Telescope</b>	<b>83</b>
6.1	Introduction . . . . .	83
6.2	The ANTARES project . . . . .	83
6.3	Layout of the ANTARES detector . . . . .	85
6.4	Detector status . . . . .	87
6.5	Sources of background for ANTARES telescope . . . . .	90
6.5.1	Atmospheric neutrinos and muons . . . . .	90
6.5.2	$^{40}K$ decay and bioluminescence light . . . . .	91
6.6	Position calibration . . . . .	92
6.7	High Energy Neutrino selection strategy . . . . .	93

6.7.1	Assumptions and hits selection . . . . .	94
6.7.2	Monte Carlo sample . . . . .	96
6.7.3	Angular error . . . . .	97
<b>7</b>	<b>A coherent search method for unmodelled GW burst</b>	<b>101</b>
7.1	Introduction . . . . .	101
7.2	GW Search Method . . . . .	102
7.2.1	Use of the search window . . . . .	102
7.2.2	GW Event Generation . . . . .	103
7.2.3	GW Search . . . . .	105
7.3	Formalism . . . . .	109
7.3.1	Standard Likelihood . . . . .	111
7.3.2	Projection Operators and the Null Energy . . . . .	112
7.3.3	Dominant Polarization Frame and Other Likelihoods . . . . .	113
7.3.4	Statistical Properties . . . . .	115
7.3.5	Incoherent Energies and Background Rejection . . . . .	115
7.3.6	Glitch rejection . . . . .	117
7.3.7	Detection and upper limits . . . . .	120
<b>8</b>	<b>The 2007 data search</b>	<b>127</b>
8.1	Introduction . . . . .	127
8.1.1	ANTARES trigger list . . . . .	127
8.2	Handling 2-line ANTARES triggers . . . . .	128
8.2.1	Probability distribution . . . . .	132
8.3	Check performed: coincidences with the GWG Catalogue . . . . .	133
8.4	Injected waveforms . . . . .	134
8.5	Search procedure: low and high frequency analysis . . . . .	140
8.6	Coincident Search Results . . . . .	141
8.6.1	Per-HEN GW Candidates . . . . .	144
8.7	Follow up . . . . .	145
8.7.1	Gaussianity check . . . . .	145
8.7.2	Figures of merit from Hanford and Livingston and data quality near trigger . . . . .	148
8.7.3	Omega scan . . . . .	152
8.8	Search for a cumulative excess: Binomial Test . . . . .	154
8.9	Upper limits and exclusion distances . . . . .	157
8.10	Astrophysical implications . . . . .	160

8.10.1	Upper limits on GW-HEN populations . . . . .	161
8.10.2	Comparison of limits with existing estimates . . . . .	161
8.11	Conclusions . . . . .	162
<b>9</b>	<b>Tables</b>	<b>163</b>
<b>10</b>	<b>Appendix A</b>	<b>I</b>
10.1	Dominant Polarization Frame . . . . .	I
10.2	Standard likelihood . . . . .	III
10.3	Meaning of DPF . . . . .	V
<b>11</b>	<b>Appendix B</b>	<b>IX</b>
11.1	Introduction . . . . .	IX
11.2	Generalities . . . . .	X
11.3	The z-component of the point of closest approach $z_c$ and its distance $d_c$ . . . . .	XII
11.4	Photon inclination with respect to the detector line, $\cos\theta_\gamma$ . .	XIV
11.5	Travel path of the photon $d_\gamma$ . . . . .	XV
11.6	The arrival time $t_\gamma$ of a Cherenkov photon at the detector line	XVI
11.7	Reconstruction of the muon track with only two detector lines	XVII
	References . . . . .	XXXIV
	<b>Acknowledgements</b>	<b>LV</b>
	<b>List of Publications</b>	<b>LVII</b>

# Abstract

We present the results of the first search for gravitational wave (GW) bursts associated with high energy neutrinos (HEN), detected by the underwater neutrino telescope ANTARES in its 5 lines configuration, during the fifth LIGO science run and first Virgo science run. The data used in this analysis were collected from February 9 to September 30 2007.

Cataclysmic cosmic events with burst activity can be plausible sources of concomitant GW and HEN. Such messengers could reveal new, hidden sources that are not observed by conventional photon astronomy, in particular at high energy.

In a first stage of the analysis, HEN candidates, detected during the operation of the ANTARES Telescope were selected. In a second stage, GW candidates in time and space correlation with the HEN events were searched for in LIGO and Virgo data.

During this first joint GW+HEN search, no coincident event was observed. We set limits on the population density of different types of concurrent GW-HEN sources. For short GRB-like sources, related to the merger of two compact objects, the density upper limit is  $\rho_{\text{GW-HEN}}^{\text{SGRB}} \lesssim 10^{-2} \text{Mpc}^{-3} \text{yr}^{-1}$ . This limit is several orders of magnitude higher than theoretical predictions. For long GRB-like sources, related to the collapse of massive stars, the limit is  $\rho_{\text{GW-HEN}}^{\text{LGRB}} \lesssim 10^{-3} \text{Mpc}^{-3} \text{yr}^{-1}$ . This limit is within a factor of ten of the optimistic predictions and shows that future searches at improved sensitivities may yield detections or constraining upper limits. We also place a lower limit on the distance to GW sources associated with every HEN trigger. We are able to rule out the existence of coalescing binary neutron star systems of  $(1.35 - 1.35)M_{\odot}$  and black hole - neutron star systems of  $(5 - 1.35)M_{\odot}$  up to distances that are typically of 5 Mpc and 10 Mpc respectively. For generic waveform limits in the low frequency band typical distance limits can be as high as 17 Mpc.

**Keywords:** Burst gravitational waves, high energy neutrinos, data analysis.

# Kurzfassung

Wir legen die Ergebnisse der ersten kombinierten Suche von Gravitationswellen (GW) und Hochenergie-Neutrinos (HEN) vor. Das Unterwasser ANTARES Teleskop detektierte Neutrinos während LIGO und Virgo zeitgleich ihre fünfte bzw. erste wissenschaftlichen Datenaufnahmen durchführten (für diese Veröffentlichung wurden die Daten vom 9. Februar bis zum 30. September 2007 verwendet).

Gewaltige kosmische Ereignisse sind wahrscheinliche Quellen für kausal zusammenhängende Emission von GW und HEN. Die Detektion solcher Quellen könnten neu, bisher verborgene Quellen zeigen, die bislang durch optische 'Photonen-Astronomie', insbesondere im Hochenergiebereich, nicht entdeckt wurden.

In einem ersten Schritt werden HEN Kandidaten vom ANTARES Teleskop ausgewählt, die dann in einem zweiten Schritt sowohl zeitlich als auch räumlich mit den LIGO und Virgo Daten korreliert werden. In dieser ersten kombinierten Suche wurden keine korrelierten Ereignisse gefunden.

Wir definieren Grenzen für die Dichte unterschiedlicher Typen von GW-HEN-Quellen.

Für kurze GRB-artige Quellen, die mit der Kollision zweier kompakter Objekte in Zusammenhang gebracht werden können, beträgt die obere Grenze  $\rho_{\text{GW-HEN}}^{\text{SGRB}} \lesssim 10^{-2} \text{Mpc}^{-3} \text{ yr}^{-1}$ .

Diese Grenze überschreitet theoretische Voraussagen um mehrere Größenordnungen.

Für lange GRB-artige Quellen, die mit dem Kollaps massiver Sterne zusammenhängen, beträgt die Grenze  $\rho_{\text{GW-HEN}}^{\text{LGRB}} \lesssim 10^{-3} \text{Mpc}^{-3} \text{ yr}^{-1}$ . Diese Grenze liegt innerhalb der 10fachen optimistischen Voraussagen. Daraus ist zu erkennen, das zukünftige Suchen mit verbesserter Empfindlichkeit zu Detektionen führen können oder die oberen Grenzen beschränken.

Für alle HEN-Messungen können wir auch untere Grenzen für die Entfer-

nung zu GW-Quellen angeben. Wir können somit die Existenz von Neutronenstern Doppelsystemen im Verschmelzungsprozess mit Massen von  $(1.35 - 1.35)M_{\odot}$  und Binärsysteme mit schwarzen Löchern und Neutronensternen mit Massen von  $(5 - 1.35)M_{\odot}$  bis zu typischen Entfernungen von 5 Mpc, bzw. bis 10 Mpc ausschließen. Für allgemeine Wellenformen im Niederfrequenzband können Schranken für typische Entfernungen bis zu 17 Mpc sein.

**Stichworte:** Gravitationswellen, Hochenergie-Neutrinos, Datenanalyse.

# Summary

Many of the cataclysmic phenomena observed in our Universe are potential emitters of gravitational waves and high energy neutrinos. As cosmic messengers, both gravitational waves and neutrinos are complementary to photons in that they can escape very dense media and travel unabsorbed over cosmological distances, carrying information from the innermost regions of their astrophysical sources. Hence, these messengers could also reveal new, hidden engines that have not yet been observed by conventional astronomy.

Gravitational waves, predicted by Albert Einstein in 1916, are ripples in the space-time metric which are believed to propagate as a wave at the speed of light. These waves warp spacetime, changing the distance between nearby points in a characteristic pattern. Scientists attempt to detect gravitational waves using instruments called Michelson interferometers, that bounce laser beams along two perpendicular arms. Measuring the interference between the beams allows to sense tiny variations in the arm lengths that may be caused by gravitational waves. LIGO is a network of three such instruments in the USA; one in Livingston, LA (4 km arm length) and two in Hanford, WA (4 km and 2 km arm lengths in 2007). Virgo is a 3 km detector located at the European Gravitational Observatory in Cascina, Italy.

Neutrinos, on the other hand, are common yet enigmatic particles. They are stable, almost massless, and carry no electric charge, interacting with other particles through the weak force. The ANTARES collaboration has built an underwater neutrino telescope at a depth of 2475 m in the Mediterranean Sea to detect high-energy cosmic neutrinos using a three-dimensional array of roughly 900 light detectors (photomultipliers) distributed along 12 lines. Unlike conventional telescopes, ANTARES looks downward, using the Earth to act as a shield, or filter, against all particles except neutrinos (which can easily pass through the Earth). A small fraction of the neutrinos passing upwards through the Earth will interact with the rock in the seabed to



Figure 1: These pictures show the Virgo interferometer (on the left), the 4 km in Livingston (in the center) and an artists' impression of the ANTARES neutrino telescope, which is at a depth of about 2500m in the Mediterranean Sea (on the right).

produce charged particles called muons, moving at near the speed of light. As these muons move through the water, they produce a flash of light called Cherenkov radiation. The photomultipliers detect this radiation, and from its arrival times the flight direction of the original neutrino can be estimated.

Several known astrophysical sources are expected to produce both gravitational waves and high-energy neutrinos. Soft Gamma Repeaters are X-ray pulsars in our galaxy that exhibit bursts of soft gamma rays ("flares"), which may be associated with star-quakes. The deformation of the star during the outburst could produce gravitational waves, while neutrinos could emerge from the flares. On the extragalactic scale, the most promising sources are gamma-ray bursts (GRBs), which are known to be very energetic. The most popular models for GRBs involve either the collapse of a rapidly rotating massive star or the merger of a binary system of compact objects (neutron star/neutron star or black hole/neutron star). In both scenarios, jets moving close to the speed of light are produced that give rise to the observed gamma-ray burst. The presence of protons or other hadrons in the jets would ensure the production of high-energy neutrinos, while gravitational waves would be produced by the binary merger or by any of several plausible mechanisms in the collapsing star scenario.

The present analysis combines data from ANTARES, LIGO, and Virgo from 2007 to search for gravitational waves coincident with neutrinos. ANTARES data were used to determine the arrival time and direction of candidate high-energy neutrino events. The LIGO-Virgo data were then scanned for a gravitational wave around the time of each putative neutrino. The ANTARES

Collaboration has selected 216 potential neutrino events (this number being compatible with the expected background induced by cosmic ray interactions with the atmosphere): 18 reconstructed with 3 lines of the detector and 198 with only 2 lines (in 2007 only 5 of the 12 lines of ANTARES photomultipliers had been installed). The neutrino track is reconstructed by using the time and charge of the hits on the photomultipliers. The subsequent LIGO-Virgo analysis exploits our knowledge of the time and possible directions of the neutrino event to improve the search sensitivity, allowing the detection of weaker gravitational-wave signals than would be possible without the neutrino information. We split the gravitational wave band into two regions: 60-500 Hz, and 500-2000 Hz. The low-frequency band is analyzed for all HEN triggers, while the high-frequency one is analysed only for the 3-line events that are a small subset of the total trigger list and the most reliable. We found no coincidences between a gravitational signal and a neutrino candidate. In addition, a statistical analysis of the gravitational-wave data for all neutrino candidates together showed no evidence for a weak collective signal (figure 2). We set limits on the population density of different types of concurrent GW-HEN sources. For short GRB-like sources, related to the merger of two compact objects, the density upper limit is  $\rho_{\text{GW-HEN}}^{\text{SGRB}} \lesssim 10^{-2} \text{Mpc}^{-3} \text{ yr}^{-1}$ . This limit is several orders of magnitude higher than theoretical predictions. For long GRB-like sources, related to the collapse of massive stars, the limit is  $\rho_{\text{GW-HEN}}^{\text{LGRB}} \lesssim 10^{-3} \text{Mpc}^{-3} \text{ yr}^{-1}$ . This limit is within a factor of ten of the optimistic predictions and shows that future searches at improved sensitivities may yield detections or constraining upper limits. We also place a lower limit on the distance to GW sources associated with every HEN trigger. We are able to rule out the existence of coalescing binary neutron star systems of  $(1.35 - 1.35)M_{\odot}$  and black hole - neutron star systems of  $(5 - 1.35)M_{\odot}$  up to distances that are typically of 5 Mpc and 10 Mpc respectively, see plots 3. For generic waveform limits in the low frequency band typical distance limits can be as high as 17 Mpc, see plot 3, while for those in the high-frequency band the typical limits are of order 1 Mpc, see plot 4.

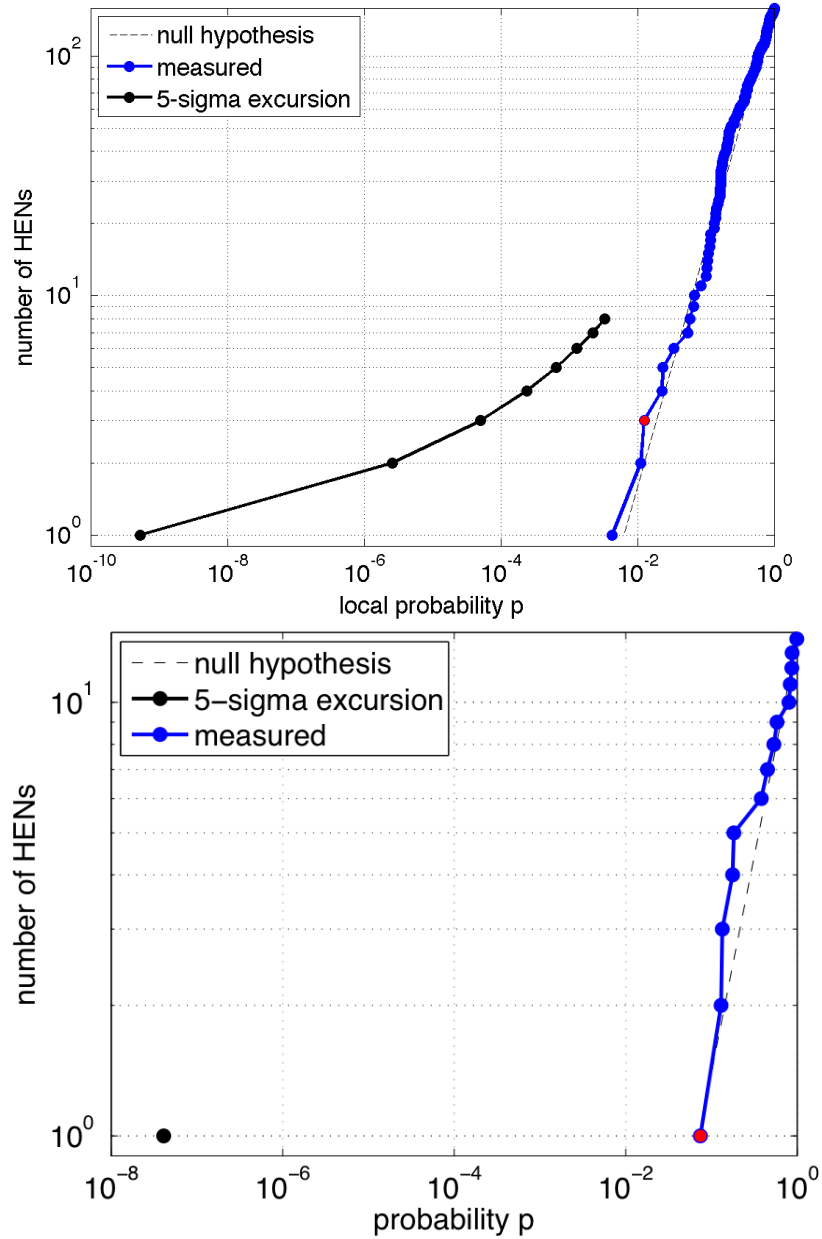


Figure 2: The plots show the binomial test for the low-frequency analysis (top) and for the high-frequency one (bottom). The distribution of measured probability values (denoted by the blue dots) is consistent with the hypothesis that the potential neutrino events originated from the background expected from cosmic ray interactions with the atmosphere. The most significant deviation from this background hypothesis is indicated by the red dot. However, to imply a detection, one of the blue dots would have to lie to the left of the line composed of black dots.

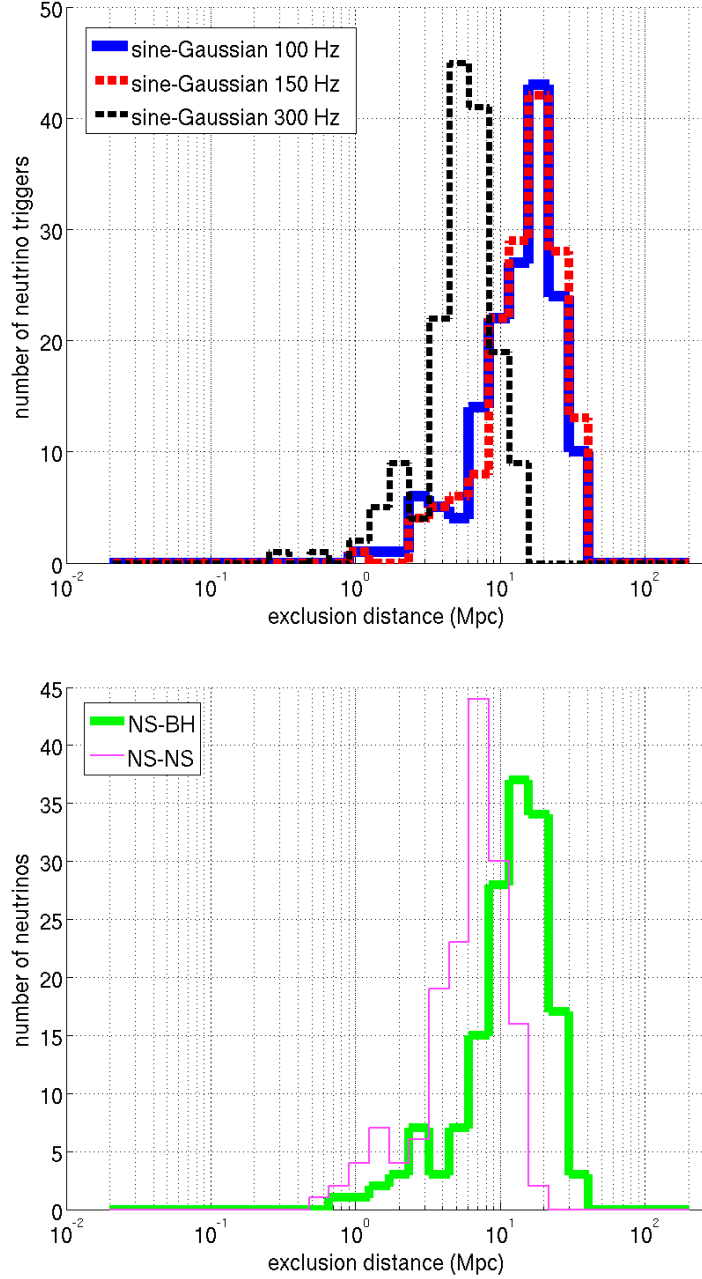


Figure 3: These histograms show the distances to which the analysis would be sensitive to different classes of signal. Low-frequency analysis: the top plot is the histogram for the sample of analysed neutrinos of the distance exclusions at the 90% confidence level for the 3 types of circular sine-Gaussian models considered: 100 Hz, 150 Hz and 300 Hz. A standard siren gravitational wave emission of  $E_{GW} = 10^{-2} M_{\odot} c^2$  is assumed. The bottom plot shows histogram across the sample of analysed neutrinos of the distance exclusions at the 90% confidence level for the 2 families of binary inspiral models considered: NS-NS and BH-NS.

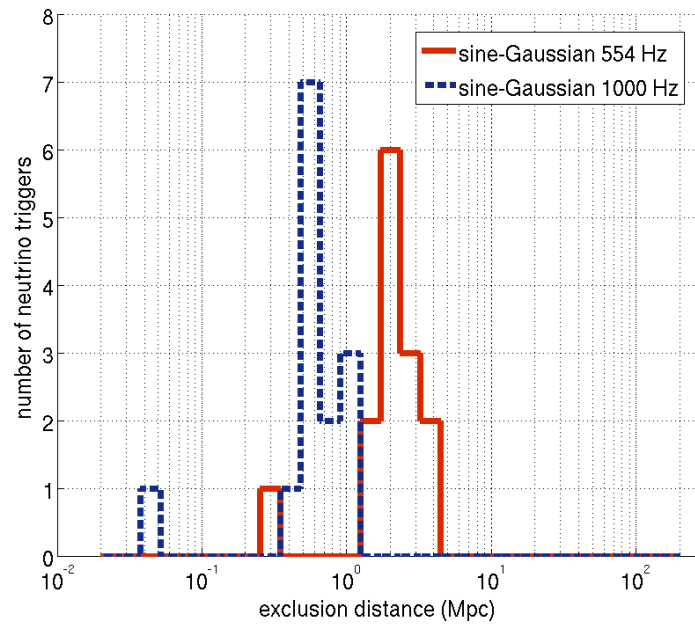


Figure 4: These histograms show the distances to which the analysis would be sensitive to different classes of signal. High-frequency analysis: the histogram for the sample of analysed neutrinos of the distance exclusions at the 90% confidence level for the 2 frequencies of circular sine-Gaussian models considered: 554 Hz and 1000 Hz.

## List of publications connected to this thesis

- Publications:
  - *A First Search for coincident Gravitational Waves and High Energy Neutrinos using LIGO, Virgo and ANTARES data from 2007*, Adrián-Martínez et al., arXiv:1205.3018 (I. Di Palma corresponding author)
  - *Multi-messenger astronomy with gravitational waves and high-energy neutrinos*, V. Van Elewyck et al. arXiv:1203.5192.
  - *Multi-messenger Science Reach and Analysis Method for Common Sources of Gravitational Waves and High-energy Neutrinos* B. Baret et al, 2012 PRD 85, 103004, arXiv:1112.1140v1.
  - *Bounding the Time Delay between High-energy Neutrinos and Gravitational wave Transients from Gamma-ray Bursts*, B. Baret et al. (2011), arXiv:1101.4669.
- Technical paper:
  - *Derivation of the ANTARES 2-line muon trajectory reconstruction cases in the context of GW-HEN analysis*, I. Di Palma, Document Number LIGO-T1100197.
  - *Description of the X Pipeline output web page*, I. Di Palma et al. Document Number LIGO-T1100287.
- Proceeding:
  - *First joint analysis between Gravitational Waves and High Energy Neutrinos using LIGO, Virgo and ANTARES data*, I. Di Palma, TAUP 2011, Journal of Physics: Conference Series Volume 375 062002, 2012.
  - *Joint search between Gravitational Wave Interferometers and High Energy Neutrino Telescopes: science reach and analysis strategies* V. Van Elewyck et al. arXiv:0906.4957.

- Public Science Summary

- *New Cosmic Messengers: first joint search for gravitational waves and high energy neutrinos*

- [http://www.ligo.org/science/Publication-S5LV\\_ANTARES/index.php](http://www.ligo.org/science/Publication-S5LV_ANTARES/index.php).

# Chapter 1

## Gravitational Waves

Note: this chapter is adapted from written notes that Prof. V. Ferrari used during her lectures in 2011 at the University 'La Sapienza' in Rome (<http://www.roma1.infn.it/teongrav/teaching2011-12.html>).

### 1.1 Introduction

Energy and mass produce a curvature of four dimensional space time and matter moves in response to this curvature. This is the fundamental notion in general relativity. While Maxwell's equations describe the relationship between electric charge and electromagnetic fields, the Einstein field equations describe the interaction between mass and space time curvature. Gravitational waves (GWs) are time dependent vacuum solutions to the Einstein field equations, as the electromagnetic waves are time dependent vacuum solutions to Maxwell's equations. As with electromagnetic waves, GWs travel at the speed of light and are transverse in character, i.e. the strain oscillations occur in directions orthogonal to the direction in which the wave is propagating. While electromagnetic waves are dipolar in nature, GWs are quadrupolar: the strain pattern contracts space along one transverse dimension, whereas expanding it along the orthogonal direction in the transverse plane (see figure 1.1).

Gravitational radiation is produced by oscillating multipole moments of the mass distribution of a system. The principle of mass conservation rules out monopole radiation, and the principles of linear and angular momentum conservation rule out gravitational dipole radiation. Quadrupole radiation

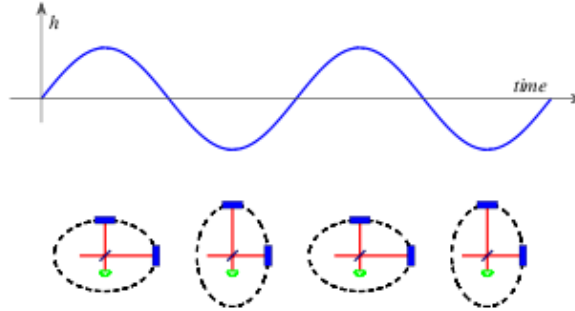


Figure 1.1: A gravitational waves traveling perpendicular to the plane of the diagram is characterized by a strain amplitude  $h$ . The wave distorts a ring of test particles into an ellipse, elongated in one direction in one half cycle of the wave, and elongated in the orthogonal direction in the next half cycle.

is the lowest allowed multiple order. In this case, the GW field strength is proportional to the second time derivative of the quadrupole moment of the source, and it falls off in amplitude inversely with distance from the source. The tensor character of gravity makes the hypothetical graviton a spin 2 particle: the transverse strain field comes in two orthogonal polarizations. These are commonly expressed in a linear polarization basis as the '+' polarization (depicted in figure 1.1) and the  $\times$  polarization, reflecting the fact that they are rotated  $45^\circ$  relative to one another. An astrophysical GW will, in general, be a mixture of both polarizations. GWs differ from electromagnetic waves in that they propagate essentially unperturbed through space, as they interact only very weakly with matter. Furthermore, GWs are intrinsically non linear, because the wave energy density itself generates additional curvature of space-time. This phenomenon is only significant, however, very close to strong sources of waves, where the wave amplitude is relatively large. In this chapter we discuss how gravitational waves emerge from general relativity and what their properties are.

## 1.2 Gravitational Waves in General Relativity

The theory of general relativity shows how the structure of the space is connected with its content. The gravity is not any more described as a force, but as a geometrical property of the space-time, as well the space-time is not the Euclidean space-time, but provided of a certain structure by the its metric tensor  $g_{\mu\nu}$ . The measure of an infinitesimal interval of the space-time is  $ds^2 = g_{\mu\nu}dx^\mu dx^\nu$ , where  $g_{\mu\nu} = \eta_{\mu\nu} + h_{\mu\nu}$  with

$$\eta_{\mu\nu} = \begin{pmatrix} 1 & 0 & 0 & 0 \\ 0 & -1 & 0 & 0 \\ 0 & 0 & -1 & 0 \\ 0 & 0 & 0 & -1 \end{pmatrix} \quad (1.1)$$

and  $|h_{\mu\nu}| \ll 1$ , hence under the condition of small perturbations.

The theoretical efforts of Einstein produced the *Einstein field equations* in general relativity:

$$R_{\mu\nu} - \frac{1}{2}g_{\mu\nu}R = \frac{8\pi G}{c^4}T_{\mu\nu} \quad (1.2)$$

where  $R_{\mu\nu}$  is the Ricci curvature tensor,  $R$  the scalar curvature,  $g_{\mu\nu}$  the metric tensor,  $G$  is Newton's gravitational constant,  $c$  the speed of light in vacuum, and  $T_{\mu\nu}$  the stress-energy tensor. The Einstein's equations define a system of second order differential equations in the unknown quantities  $g_{\mu\nu}$ . The Riemann curvature tensor in the four-dimensional space is defined as:

$$R_{\mu\gamma}^{\alpha} = \frac{\partial\Gamma_{\mu\nu}^{\alpha}}{\partial x^{\gamma}} - \frac{\partial\Gamma_{\mu\nu}^{\alpha}}{\partial x^{\nu}} + \Gamma_{\rho\gamma}^{\alpha}\Gamma_{\mu\nu}^{\rho} - \Gamma_{\rho\nu}^{\alpha}\Gamma_{\mu\gamma}^{\rho} \quad (1.3)$$

where the Christoffel symbols are

$$\Gamma_{\mu\gamma}^{\alpha} = \frac{1}{2}g^{\alpha\beta} \left( \frac{\partial g_{\beta\nu}}{\partial x^{\mu}} + \frac{\partial g_{\beta\mu}}{\partial x^{\nu}} - \frac{\partial g_{\mu\nu}}{\partial x^{\beta}} \right) \quad (1.4)$$

and the Ricci tensor is

$$R_{\mu\nu} = R_{\mu\gamma\nu}^{\gamma} \quad (1.5)$$

obtained from the contraction of the index in the Riemann tensor.  $R$  is the scalar curvature obtained from the contraction of the Ricci tensor.

The Einstein equations and the geodesic equation, that describes how freely-falling matter moves through space-time, form the mathematical core formulation of general relativity. It is possible to linearize eqs 1.2 under the

hypothesis of weak gravitational field ( $|T_{\mu\nu}| \rightarrow 0$ ),  $g_{\mu\nu} \approx \eta_{\mu\nu} + h_{\mu\nu}$  where  $h_{\mu\nu}$  is a small perturbation ( $|h_{\mu\nu}| \ll 1$ ). In the flat Minkowski space eqs 1.2 assume the shape of wave equation for  $h_{\mu\nu}$

$$\square h_{\mu\nu} = 0. \quad (1.6)$$

The solution of this differential equation is a plane wave that travels at the speed of light

$$\bar{h}_{\mu\nu} = \Re \{ A_{\mu\nu} e^{ik_\alpha x^\alpha} \}. \quad (1.7)$$

It's convenient to make a transformation of coordinates to simplify the expression of the matrix  $h$  by using the Lorentz conditions on the plane-wave solution

$$A_{\mu\alpha} k^\alpha = 0 \quad (1.8)$$

and with a suitable transformation for  $A_{\mu\nu}$  in the transverse traceless gauge (TT-gauge) we obtain a new traceless tensor  $h_{kk} = 0$ , and  $h_{\mu 0} = 0$ , in which only the spatial components are different from zero. Last equation implies the condition  $h_{00} = 0$  that means that we have only three independent Lorentz conditions. The name TT-gauge comes from the fact that the metric perturbation is traceless and perpendicular to the wave vector. In the simple case of a monochromatic wave that travels along the x direction we have

$$h_{\mu\nu}^{TT} = \begin{pmatrix} 0 & 0 & 0 & 0 \\ 0 & 0 & 0 & 0 \\ 0 & 0 & h_{yy} & h_{yz} \\ 0 & 0 & h_{yz} & -h_{yy} \end{pmatrix}. \quad (1.9)$$

The wave plane is described from the combination of two terms:

$$h_{\oplus} = \Re A_{\oplus} e^{-j(\omega t - \frac{x}{c})} \quad (1.10)$$

$$h_{\otimes} = \Re A_{\otimes} e^{-j(\omega t - \frac{x}{c})} \quad (1.11)$$

that correspond to the two independent states of polarization, where  $h_{yy} = h_{\oplus}$  and  $h_{yz} = h_{\otimes}$ . Usually the polarization states are represented through the two tensors  $e_{\oplus}$  and  $e_{\otimes}$  and two scalar quantities  $a_{\oplus}$  and  $a_{\otimes}$ ,

$$A_{\oplus} = a_{\oplus} e_{\oplus} \quad (1.12)$$

$$A_{\otimes} = a_{\otimes} e_{\otimes}. \quad (1.13)$$

In the rest of this chapter there is the mathematical derivation of what we explain briefly in this section.

### 1.3 Theory of Gravitational Waves

GWs are oscillating perturbations to the Minkowski flat space time metric, and can be thought of equivalently as an oscillating strain in space time or as an oscillating tidal force between free test masses. When gravitational waves propagate the geometry and the distance between particles change in time. One can study gravitational waves by following several approaches: one based on perturbative methods, the second on the solution of the non linear Einstein equations.

*The perturbative approach*

Be  $g_{\mu\nu}^0$  a known exact solution of Einstein's equations, and now let us consider a small perturbation of  $g_{\mu\nu}^0$  caused by some source described by a stress-energy tensor  $T^{\mu\nu}$ . We write the metric tensor of the perturbed spacetime,  $g_{\mu\nu}$ , as follows

$$g_{\mu\nu} = g_{\mu\nu}^0 + h_{\mu\nu} \quad (1.14)$$

where  $h_{\mu\nu}$  is the small perturbation

$$|h_{\mu\nu}| \ll |g_{\mu\nu}^0| \quad (1.15)$$

The inverse metric is

$$g^{\mu\nu} = g^{0\mu\nu} - h^{\mu\nu} + O(h^2) \quad (1.16)$$

where the indices of  $h_{\mu\nu}$  have been raised with the unperturbed metric

$$h^{\mu\nu} \equiv g^{0\mu\alpha} g^{0\nu\beta} h_{\alpha\beta} \quad (1.17)$$

Indeed, with this definition,

$$(g^{0\mu\nu} - h^{\mu\nu}) (g_{\nu\alpha}^0 + h_{\nu\alpha}) = \delta_{\alpha}^{\mu} + O(h^2). \quad (1.18)$$

We write Einstein's equations for the metric (1.14) in the following form, in order to find the equations that describe  $h_{\mu\nu}$ ,

$$R_{\mu\nu} = \frac{8\pi G}{c^4} \left( T_{\mu\nu} - \frac{1}{2} g_{\mu\nu} T_{\lambda}^{\lambda} \right) \quad (1.19)$$

where  $T_{\mu\nu}$  is the sum of two terms, one associated to the source that generates the background geometry  $g_{\mu\nu}^0$ , say  $T_{\mu\nu}^0$ , and one associated to the sources of the perturbation  $T_{\mu\nu}$ . We remind that the Ricci tensor  $R_{\mu\nu}$  is

$$R_{\mu\nu} = \frac{\partial}{\partial x^{\alpha}} \Gamma_{\mu\nu}^{\alpha} - \frac{\partial}{\partial x^{\nu}} \Gamma_{\mu\alpha}^{\alpha} + \Gamma_{\sigma\alpha}^{\alpha} \Gamma_{\mu\nu}^{\sigma} - \Gamma_{\sigma\nu}^{\alpha} \Gamma_{\mu\alpha}^{\sigma} \quad (1.20)$$

and that the similar connections  $\Gamma_{\beta\mu}^\gamma$  are

$$\Gamma_{\beta\mu}^\gamma = \frac{1}{2}g^{\alpha\gamma} \left[ \frac{\partial}{\partial x^\mu} g_{\alpha\beta} + \frac{\partial}{\partial x^\beta} g_{\alpha\mu} - \frac{\partial}{\partial x^\alpha} g_{\beta\mu} \right] \quad (1.21)$$

The  $\Gamma_{\beta\mu}^\gamma$  computed for the perturbed metric (1.14) are

$$\begin{aligned} \Gamma_{\beta\mu}^\gamma(g_{\mu\nu}) &= \frac{1}{2} [g^{0\alpha\gamma} - h^{\alpha\gamma}] \cdot \\ &\cdot \left[ \left( \frac{\partial}{\partial x^\mu} g_{\alpha\beta}^0 + \frac{\partial}{\partial x^\beta} g_{\alpha\mu}^0 - \frac{\partial}{\partial x^\alpha} g_{\beta\mu}^0 \right) + \left( \frac{\partial}{\partial x^\mu} h_{\alpha\beta} + \frac{\partial}{\partial x^\beta} h_{\alpha\mu} - \frac{\partial}{\partial x^\alpha} h_{\beta\mu} \right) \right] \\ &= \frac{1}{2}g^{0\alpha\gamma} \left[ \frac{\partial}{\partial x^\mu} g_{\alpha\beta}^0 + \frac{\partial}{\partial x^\beta} g_{\alpha\mu}^0 - \frac{\partial}{\partial x^\alpha} g_{\beta\mu}^0 \right] + \frac{1}{2}g^{0\alpha\gamma} \left[ \frac{\partial}{\partial x^\mu} h_{\alpha\beta} + \frac{\partial}{\partial x^\beta} h_{\alpha\mu} - \frac{\partial}{\partial x^\alpha} h_{\beta\mu} \right] + \\ &\quad - \frac{1}{2}h^{\alpha\gamma} \left[ \frac{\partial}{\partial x^\mu} g_{\alpha\beta}^0 + \frac{\partial}{\partial x^\beta} g_{\alpha\mu}^0 - \frac{\partial}{\partial x^\alpha} g_{\beta\mu}^0 \right] + O(h^2) \\ &= \Gamma_{\beta\mu}^\gamma(g^0) + \Gamma_{\beta\mu}^\gamma(h) + O(h^2) \end{aligned} \quad (1.23)$$

where  $\Gamma_{\beta\mu}^\gamma(h)$  are terms that are first order in  $h_{\mu\nu}$

$$\Gamma_{\beta\mu}^\gamma(h) = \frac{1}{2}g^{0\alpha\gamma} \left[ \frac{\partial}{\partial x^\mu} h_{\alpha\beta} + \frac{\partial}{\partial x^\beta} h_{\alpha\mu} - \frac{\partial}{\partial x^\alpha} h_{\beta\mu} \right] - \frac{1}{2}h^{\alpha\gamma} \left[ \frac{\partial}{\partial x^\mu} g_{\alpha\beta}^0 + \frac{\partial}{\partial x^\beta} g_{\alpha\mu}^0 - \frac{\partial}{\partial x^\alpha} g_{\beta\mu}^0 \right] \quad (1.24)$$

When we substitute these expressions of the  $\Gamma_{\beta\mu}^\gamma(g_{\mu\nu})$  in the Ricci tensor we get

$$\begin{aligned} R_{\mu\nu}(g_{\mu\nu}) &= R_{\mu\nu}(g^0) + \\ &\quad + \frac{\partial}{\partial x^\alpha} \Gamma_{\mu\nu}^\alpha(h) - \frac{\partial}{\partial x^\nu} \Gamma_{\mu\alpha}^\alpha(h) + \\ &\quad + \Gamma_{\sigma\alpha}^\alpha(g^0) \Gamma_{\mu\nu}^\sigma(h) + \Gamma_{\sigma\alpha}^\alpha(h) \Gamma_{\mu\nu}^\sigma(g^0) + \\ &\quad - \Gamma_{\sigma\nu}^\alpha(g^0) \Gamma_{\mu\alpha}^\sigma(h) - \Gamma_{\sigma\nu}^\alpha(h) \Gamma_{\mu\alpha}^\sigma(g^0) + O(h^2) = \\ &= \frac{8\pi G}{c^4} \left( T_{\mu\nu} - \frac{1}{2}g_{\mu\nu} T_\lambda^\lambda \right) \end{aligned} \quad (1.25)$$

Since  $g_{\mu\nu}^0$  is by assumption an exact solution of Einstein's equations in vacuum  $R_{\mu\nu}(g^0) = \frac{8\pi G}{c^4} (T_{\mu\nu}^0 - \frac{1}{2}g_{\mu\nu}^0 T_\lambda^{0\lambda})$ ; if we retain only first order terms, the equations for the perturbations  $h_{\mu\nu}$  reduce to

$$\frac{\partial}{\partial x^\alpha} \Gamma_{\mu\nu}^\alpha(h) - \frac{\partial}{\partial x^\nu} \Gamma_{\mu\alpha}^\alpha(h) + \quad (1.26)$$

$$\Gamma_{\sigma\alpha}^{\alpha}(g^0)\Gamma_{\mu\nu}^{\sigma}(h) + \Gamma_{\sigma\alpha}^{\alpha}(h)\Gamma_{\mu\nu}^{\sigma}(g^0) + \\ - \Gamma_{\sigma\nu}^{\alpha}(g^0)\Gamma_{\mu\alpha}^{\sigma}(h) - \Gamma_{\sigma\nu}^{\alpha}(h)\Gamma_{\mu\alpha}^{\sigma}(g^0) = \frac{8\pi G}{c^4} \left( T_{\mu\nu} - \frac{1}{2}g_{\mu\nu}T_{\lambda}^{\lambda} \right)$$

that are linear in  $h_{\mu\nu}$ . Their solution will describe the propagation of gravitational waves in the background. This approximation works well because gravitational waves are very weak. *The exact approach* The different approach to study gravitational waves is based on exact solutions of Einstein's equations which describe both the source and the emitted wave, but no solution has been found so far. Exact solutions of Einstein's equations, describing gravitational waves, can be found only in particular case: when one imposes some particular symmetry, as for example plane, spherical, or cylindrical symmetry.

## 1.4 A perturbation of the Minkowski spacetime

Let consider the flat spacetime described by the metric tensor  $\eta_{\mu\nu}$  and a small perturbation  $h_{\mu\nu}$ , such that the resulting metric can be written as

$$g_{\mu\nu} = \eta_{\mu\nu} + h_{\mu\nu}, |h_{\mu\nu}| \ll 1 \quad (1.27)$$

The similar connections computed for this metric are

$$\Gamma_{\mu\nu}^{\lambda} = \frac{1}{2}\eta^{\lambda\rho} \left[ \frac{\partial}{\partial x^{\mu}}h_{\rho\nu} + \frac{\partial}{\partial x^{\nu}}h_{\rho\mu} - \frac{\partial}{\partial x^{\rho}}h_{\mu\nu} \right] + O(h^2) \quad (1.28)$$

Since the metric  $g_{\mu\nu}^0 \equiv \eta_{\mu\nu}$  is constant,  $\Gamma_{\mu\nu}^{\lambda}(g^0) = 0$  and the right-hand side of the eq. (1.23) reduces to

$$\frac{\partial\Gamma_{\mu\nu}^{\alpha}}{\partial x^{\alpha}} - \frac{\partial\Gamma_{\mu\alpha}^{\alpha}}{\partial x^{\nu}} + O(h^2) \quad (1.29) \\ = \frac{1}{2} \left\{ -\square h_{\mu\nu} + \left[ \frac{\partial^2}{\partial x^{\lambda}\partial x^{\mu}}h_{\nu}^{\lambda} + \frac{\partial^2}{\partial x^{\lambda}\partial x^{\nu}}h_{\mu}^{\lambda} - \frac{\partial^2}{\partial x^{\mu}\partial x^{\nu}}h_{\lambda}^{\lambda} \right] \right\} + O(h^2)$$

The operator  $\square$  is the D'Alembertian in flat space

$$\square = \eta^{\alpha\beta} \frac{\partial}{\partial x^{\alpha}} \frac{\partial}{\partial x^{\beta}} = -\frac{\partial^2}{c^2\partial t^2} + \nabla^2 \quad (1.30)$$

Einstein's equations (1.19) for  $h_{\mu\nu}$  finally become

$$\left\{ \square h_{\mu\nu} - \left[ \frac{\partial^2}{\partial x^\lambda \partial x^\mu} h_\nu^\lambda + \frac{\partial^2}{\partial x^\lambda \partial x^\nu} h_\mu^\lambda - \frac{\partial^2}{\partial x^\mu \partial x^\nu} h_\lambda^\lambda \right] \right\} = -\frac{16\pi G}{c^4} \left( T_{\mu\nu} - \frac{1}{2} \eta_{\mu\nu} T_\lambda^\lambda \right) \quad (1.31)$$

To simplify eq. (1.31) it's convenient to choose a coordinate system in which is satisfied,

$$g^{\mu\nu} \Gamma_{\mu\nu}^\lambda = 0. \quad (1.32)$$

This condition is the harmonic gauge condition. Using this condition the term in square brackets in eq. 1.31 vanishes, and Einstein's equations reduce to a wave equation

$$\left\{ \begin{aligned} \square h_{\mu\nu} &= -\frac{16\pi G}{c^4} \left( T_{\mu\nu} - \frac{1}{2} \eta_{\mu\nu} T_\lambda^\lambda \right) \\ \frac{\partial}{\partial x^\mu} h_\nu^\mu &= \frac{1}{2} \frac{\partial}{\partial x^\nu} h_\mu^\mu \end{aligned} \right. \quad (1.33)$$

If we introduce the tensor

$$\bar{h}_{\mu\nu} \equiv h_{\mu\nu} - \frac{1}{2} \eta_{\mu\nu} h_\lambda^\lambda \quad (1.34)$$

eqs. (1.33) become

$$\left\{ \begin{aligned} \square \bar{h}_{\mu\nu} &= -\frac{16\pi G}{c^4} T_{\mu\nu} \\ \frac{\partial}{\partial x^\mu} \bar{h}_\nu^\mu &= 0 \end{aligned} \right. \quad (1.35)$$

and outside the source where  $T_{\mu\nu} = 0$

$$\left\{ \begin{aligned} \square \bar{h}_{\mu\nu} &= 0 \\ \frac{\partial}{\partial x^\mu} \bar{h}_\nu^\mu &= 0. \end{aligned} \right. \quad (1.36)$$

These equations show that a perturbation of a flat, or Minkowski, spacetime propagates as a wave travelling at the speed of light, and that Einstein's theory of gravity predicts the existence of gravitational waves. As in electrodynamics, the solution of eqs. (1.35) can be written in terms of retarded potentials

$$\bar{h}_{\mu\nu}(t, \vec{x}) = \frac{4G}{c^4} \int \frac{T_{\mu\nu}(t - \frac{|\vec{x} - \vec{x}'|}{c}, \vec{x}')}{|\vec{x} - \vec{x}'|} d^3 x' \quad (1.37)$$

and the integral extends over the past light-cone of the event  $(t, x)$ . This equation represents the gravitational waves generated by the source  $T_{\mu\nu}$ . When the harmonic-gauge condition is not satisfied in a reference frame, we

can always find a new frame where it is, by making an infinitesimal coordinate transformation

$$x^{\lambda'} = x^\lambda + \epsilon^\lambda \quad (1.38)$$

provided

$$\square\epsilon_\rho = \frac{\partial h_\rho^\beta}{\partial x^\beta} - \frac{1}{2} \frac{\partial h_\beta^\beta}{\partial x^\rho} \quad (1.39)$$

We shall now demonstrate eq. 1.39, when we change the coordinate system  $\Gamma^\lambda = g^{\mu\nu}\Gamma_{\mu\nu}^\lambda$  transforms according to equation

$$\Gamma^{\lambda'} = \frac{\partial x^{\lambda'}}{\partial x^\rho} \Gamma^\rho - g^{\rho\sigma} \frac{\partial^2 x^{\lambda'}}{\partial x^\rho \partial x^\sigma} \quad (1.40)$$

where, from eq (1.38)

$$\frac{\partial x^{\lambda'}}{\partial x^\rho} = \delta_\rho^\lambda + \frac{\partial \epsilon^\lambda}{\partial x^\rho} \quad (1.41)$$

If  $g_{\mu\nu} = \eta_{\mu\nu} + h_{\mu\nu}$

$$\Gamma^\rho = \eta^{\rho k} \left\{ h_{k,\mu}^\mu - \frac{1}{2} h_{\nu,k}^\nu \right\} \quad (1.42)$$

moreover

$$\begin{aligned} g^{\rho\sigma} \frac{\partial^2 x^{\lambda'}}{\partial x^\rho \partial x^\sigma} &= g^{\rho\sigma} \left[ \frac{\partial}{\partial x^\rho} \left( \frac{\partial x^{\lambda'}}{\partial x^\sigma} + \frac{\partial \epsilon^{\lambda'}}{\partial x^\sigma} \right) \right] = \\ g^{\rho\sigma} \left[ \frac{\partial}{\partial x^\rho} \left( \delta_\sigma^\lambda + \frac{\partial \epsilon^\lambda}{\partial x^\sigma} \right) \right] &\approx \eta^{\rho\sigma} \left[ \frac{\partial^2 \epsilon^\lambda}{\partial x^\rho \partial x^\sigma} \right] = \square\epsilon^\lambda \end{aligned} \quad (1.43)$$

therefore in the new gauge the condition  $\Gamma^{\lambda'} = 0$  becomes

$$\Gamma^{\lambda'} = \eta^{\rho k} \left[ \delta_\rho^\lambda + \frac{\partial \epsilon^\lambda}{\partial x^\rho} \right] \left[ \frac{\partial h_k^\mu}{\partial x^\mu} - \frac{1}{2} \frac{\partial h_\nu^\nu}{\partial x^k} \right] - \square\epsilon^\lambda \quad (1.44)$$

If we neglect second order terms in  $h$  last eq 1.44 becomes

$$\Gamma^{\lambda'} = \eta^{\lambda k} \left[ \frac{\partial h_k^\mu}{\partial x^\mu} - \frac{1}{2} \frac{\partial h_\nu^\nu}{\partial x^k} \right] - \square\epsilon^\lambda = 0 \quad (1.45)$$

Contracting with  $\eta_{\lambda\alpha}$  and remembering that  $\eta_{\lambda\alpha}\eta^{\lambda k} = \delta_\alpha^k$  we find

$$\square\epsilon_\alpha = \frac{\partial h_\alpha^\mu}{\partial x^\mu} - \frac{1}{2} \frac{\partial h_\nu^\nu}{\partial x^\alpha} \quad (1.46)$$

This equation can in principle be solved to find the components of  $\epsilon_\alpha$  which identify the coordinate system in which the harmonic gauge condition is satisfied.

## 1.5 Solution in vacuum

The simplest solution of the wave equation in vacuum (1.36) is a monochromatic plane wave

$$\bar{h}_{\mu\nu} = \Re \{ A_{\mu\nu} e^{ik_\alpha x^\alpha} \} \quad (1.47)$$

where  $A_{\mu\nu}$  is the polarization tensor, the wave amplitude and  $\vec{k}$  is the wave vector. Making the substitution of (1.47) into the first equation we have

$$\begin{aligned} \square \bar{h}_{\mu\nu} &= \eta^{\alpha\beta} \frac{\partial}{\partial x^\alpha} \frac{\partial}{\partial x^\beta} (e^{ik_\gamma x^\gamma}) = \eta^{\alpha\beta} \frac{\partial}{\partial x^\alpha} \left[ ik_\gamma \frac{\partial x^\gamma}{\partial x^\beta} (e^{ik_\gamma x^\gamma}) \right] = \\ &= \eta^{\alpha\beta} \frac{\partial}{\partial x^\alpha} [ik_\gamma \delta_\beta^\gamma e^{ik_\gamma x^\gamma}] = \eta^{\alpha\beta} \frac{\partial}{\partial x^\alpha} [ik_\beta e^{ik_\gamma x^\gamma}] = \\ &= -\eta^{\alpha\beta} k_\alpha k_\beta e^{ik_\gamma x^\gamma} = 0 \quad \rightarrow \quad \eta^{\alpha\beta} k_\alpha k_\beta = 0 \end{aligned} \quad (1.48)$$

thus, (1.47) is a solution of (1.36) if  $\vec{k}$  is a null vector. In addition the harmonic gauge condition requires that

$$\frac{\partial}{\partial x^\mu} \bar{h}_\nu^\mu = 0 \quad (1.49)$$

which can be written as

$$\eta^{\mu\alpha} \frac{\partial}{\partial x^\mu} \bar{h}_{\alpha\nu} + 0 \quad (1.50)$$

Using eq (1.47) it gives

$$\eta^{\mu\alpha} \frac{\partial}{\partial x^\mu} A_{\alpha\nu} e^{ik_\gamma x^\gamma} = 0 \quad \rightarrow \quad \eta^{\mu\alpha} A_{\alpha\nu} k_\mu = 0 \quad \rightarrow \quad k_\mu A_\nu^\mu = 0 \quad (1.51)$$

This further condition expresses the orthogonality of the wave vector and of the polarization tensor.

Since  $\bar{h}_{\mu\nu}$  is constant on those surfaces where

$$k_\alpha x^\alpha = \text{const} \quad (1.52)$$

these are the equations of the wavefront. It is conventional to refer to  $k^0$  as  $\frac{\omega}{c}$  where  $\omega$  is the frequency of the waves. Consequently

$$\vec{k} = \left( \frac{\omega}{c}, \mathbf{k} \right) \quad (1.53)$$

Since  $\vec{k}$  is a null vector

$$-(k_0)^2 + (k_x)^2 + (k_y)^2 + (k_z)^2 = 0 \quad (1.54)$$

$$\omega = ck_0 = c\sqrt{(k_x)^2 + (k_y)^2 + (k_z)^2} \quad (1.55)$$

where  $(k_x, k_y, k_z)$  are the component of the unit 3-vector  $\mathbf{k}$ .

## 1.6 The $TT$ -gauge

To understand how many of the ten components of  $h_{\mu\nu}$  have a real physical meaning and what the degrees of freedom of a gravitational plane wave are, we consider a wave propagating in flat spacetime along the  $x^1 = x$ -direction. Since  $h_{\mu\nu}$  is independent of  $y$  and  $z$ , eqs. (1.36) become (as before we raise and lower indices with  $\eta_{\mu\nu}$ )

$$\left(-\frac{\partial^2}{c^2\partial t^2} + \frac{\partial^2}{\partial x^2}\right)\bar{h}_\nu^\mu = 0 \quad (1.56)$$

$\bar{h}_\nu^\mu$  is an arbitrary function of  $t \pm \frac{x}{c}$ , and

$$\frac{\partial}{\partial x^\mu}\bar{h}_\nu^\mu = 0 \quad (1.57)$$

Let us consider, for example, a progressive wave  $\bar{h}_\nu^\mu = \bar{h}_\nu^\mu[\chi(t, x)]$ , where  $\chi(t, x) = t - \frac{x}{c}$ . Being

$$\begin{cases} \frac{\partial}{\partial t}\bar{h}_\nu^\mu = \frac{\partial\bar{h}_\nu^\mu}{\partial\chi}\frac{\partial\chi}{\partial t} = \frac{\partial\bar{h}_\nu^\mu}{\partial\chi} \\ \frac{\partial}{\partial x}\bar{h}_\nu^\mu = \frac{\partial\bar{h}_\nu^\mu}{\partial\chi}\frac{\partial\chi}{\partial x} = -\frac{1}{c}\frac{\partial\bar{h}_\nu^\mu}{\partial\chi} \end{cases} \quad (1.58)$$

eq (1.57) gives

$$\frac{\partial}{\partial x^\mu}\bar{h}_\nu^\mu = \frac{1}{c}\frac{\partial\bar{h}_\nu^t}{\partial t} + \frac{\partial\bar{h}_\nu^x}{\partial x} = \frac{1}{c}\frac{\partial}{\partial\chi}[\bar{h}_\nu^t - \bar{h}_\nu^x] = 0 \quad (1.59)$$

This equation can be integrated, and the constants of integration can be set equal to zero because we want only the part of solution dependent on time. The result is

$$\bar{h}_t^t = \bar{h}_t^x, \quad \bar{h}_y^t = \bar{h}_y^x \quad (1.60)$$

$$\bar{h}_x^t = \bar{h}_x^x, \quad \bar{h}_z^t = \bar{h}_z^x \quad (1.61)$$

The harmonic gauge condition does not determine the gauge uniquely. Indeed, if we make an infinitesimal coordinate transformation

$$x^{\mu'} = x^\mu + \xi^\mu \quad (1.62)$$

from eq (1.40) we find that, if in the old frame  $\Gamma^\rho = 0$ , in the new frame  $\Gamma^{\lambda'} = 0$ , provided

$$\eta^{\rho\sigma} \frac{\partial^2 x^{\lambda'}}{\partial x^\rho \partial x^\sigma} = 0 \quad (1.63)$$

namely, if  $\xi^\mu$  satisfies the wave equation

$$\square \xi^\mu = 0. \quad (1.64)$$

Thus, we can use the four functions  $\xi^\mu$  to set to zero the following four quantities

$$\bar{h}_x^t = \bar{h}_y^t = \bar{h}_z^t = \bar{h}_y^x = \bar{h}_z^x = 0 \quad (1.65)$$

From eqs (1.60, 1.61) it then follows that

$$\bar{h}_x^x = \bar{h}_y^x = \bar{h}_z^x = \bar{h}_t^x = 0 \quad (1.66)$$

the remaining non-vanishing components are  $\bar{h}_y^z$  and  $\bar{h}_y^y - \bar{h}_z^z$ . We have exhausted our gauge freedom so we cannot set equal to zero these components. From eq. (1.65) and (1.66) it follows that

$$\bar{h}_\mu^\mu = \bar{h}_t^t + \bar{h}_x^x + \bar{h}_y^y + \bar{h}_z^z = 0 \quad (1.67)$$

and since

$$\bar{h}_\mu^\mu = h_\mu^\mu - 2h_\mu^\mu = -h_\mu^\mu \quad (1.68)$$

it follows that

$$h_\mu^\mu = 0 \quad \rightarrow \quad \bar{h}_\nu^\nu \equiv h_\nu^\nu. \quad (1.69)$$

Eq. 1.69 shows that in this gauge  $h_{\mu\nu}$  and  $\bar{h}_{\mu\nu}$  coincide and are traceless. A plane gravitational wave propagating along the x-axis is characterized by two functions  $h_{xy}$  and  $h_{yy} = -h_{zz}$ , while the remaining components can be set to zero by choosing the gauge as we have seen

$$\begin{pmatrix} 0 & 0 & 0 & 0 \\ 0 & 0 & 0 & 0 \\ 0 & 0 & h_{yy} & h_{yz} \\ 0 & 0 & h_{yz} & -h_{yy} \end{pmatrix} \quad (1.70)$$

Hence, a gravitational wave has only two physical degrees of freedom which correspond to the two possible polarization states. The gauge in which this is manifested is called the  $TT$ -gauge, where  $TT$  (Transverse Traceless) indicates that the components of the metric tensor  $h_{\mu\nu}$  are different from zero only in the plane orthogonal to the direction of propagation (transverse), and that  $h_{\mu\nu}$  is traceless.

### 1.6.1 A single particle effected by a gravitational wave

Consider a particle at rest in flat spacetime before the passage of the wave, set an inertial frame attached to this particle, and take the x-axis coincident with the direction of propagation of an incoming TT-gravitational wave. The particle will follow a geodesic of the curved spacetime generated by the wave

$$\frac{\partial^2 x^\alpha}{\partial \tau^2} + \Gamma_{\mu\nu}^\alpha \frac{\partial x^\mu}{\partial \tau} \frac{\partial x^\nu}{\partial \tau} \equiv \frac{dU^\alpha}{d\tau} + \Gamma_{\mu\nu}^\alpha U^\mu U^\nu = 0 \quad (1.71)$$

where  $x^\alpha$  is the trajectory of the particle and  $U$  its speed. At  $t = 0$  the particle is at rest  $U^\alpha = (1, 0, 0, 0)$  and the acceleration impressed by the wave will be

$$\left( \frac{dU^\alpha}{d\tau} \right)_{(t=0)} = -\Gamma_{00}^\alpha = -\frac{1}{2} \eta^{\alpha\beta} [h_{\beta 0,0} + h_{0\beta,0} - h_{00,\beta}] \quad (1.72)$$

but we are in the  $TT$ -gauge, that means

$$\left( \frac{dU^\alpha}{d\tau} \right)_{(t=0)} = 0 \quad (1.73)$$

Thus,  $U^\alpha$  remains constant also at later times, which means that the particle is not accelerated neither at  $t = 0$  nor later. It remains at a constant coordinate position, regardless of the wave. Hence, we cannot detect a gravitational wave by studying the motion of a single particle.

## 1.7 Interaction of gravitational waves with test masses

To study the relative motion of particles in the gravitational field produced by a gravitational wave we need to consider two neighbouring particles A

and B, and choose a reference frame with origin coincident with the position of the particle A

$$x_A^\lambda = (1, 0, 0, 0) . \quad (1.74)$$

The two particles are initially at rest with respect to this frame, and a plane-fronted gravitational wave reaches them at some time  $t = 0$ , propagating along the x-axis. We also assume that we are in the  $TT$ -gauge, so that the only non-vanishing components of the wave are those on the  $(y, z)$  plane. We use the equation of geodesic deviation to study the effect of the passage of the wave. Be  $\delta x^\mu$  the vector which separates the two particles, initially

$$\delta x^\mu = (0, x_B, y_B, z_B) \quad (1.75)$$

The equation of geodesic deviation is

$$\frac{d^2 \delta x^\lambda}{d\tau^2} = R_{\nu\beta\mu}^\lambda \frac{dx^\beta}{d\tau} \frac{dx^\nu}{d\tau} \delta x^\mu \quad (1.76)$$

and written in the gauge we have 6, it becomes

$$\frac{d^2}{d\tau^2} \delta x^\lambda = R_{00\mu}^\lambda \delta x^\mu \quad (1.77)$$

If the gravitational wave is due to a perturbation  $h_{\mu\nu}$  of the flat metric  $\eta_{\mu\nu}$  the Riemann tensor can be written as

$$R_{iklm} = \frac{1}{2} \left( \frac{\partial^2 g_{im}}{\partial x^k \partial x^l} + \frac{\partial^2 g_{kl}}{\partial x^i \partial x^m} - \frac{\partial^2 g_{il}}{\partial x^k \partial x^m} - \frac{\partial^2 g_{km}}{\partial x^i \partial x^l} \right) + g_{np} (\Gamma_{kl}^n \Gamma_{im}^p - \Gamma_{km}^n \Gamma_{il}^p) \quad (1.78)$$

with  $g_{\mu\nu} = \eta_{\mu\nu} + h_{\mu\nu}$ . After neglecting terms which are second order in  $h_{\mu\nu}$ , eq 1.78 becomes

$$R_{iklm} = \frac{1}{2} \left( \frac{\partial^2 h_{im}}{\partial x^k \partial x^l} + \frac{\partial^2 h_{kl}}{\partial x^i \partial x^m} - \frac{\partial^2 h_{il}}{\partial x^k \partial x^m} - \frac{\partial^2 h_{km}}{\partial x^i \partial x^l} \right) + O(h^2) \quad (1.79)$$

consequently

$$R_{i00m} = \frac{1}{2} \left( \frac{\partial^2 h_{im}}{\partial x^0 \partial x^0} + \frac{\partial^2 h_{00}}{\partial x^i \partial x^m} - \frac{\partial^2 h_{i0}}{\partial x^0 \partial x^m} - \frac{\partial^2 h_{0m}}{\partial x^i \partial x^0} \right) = \frac{1}{2} h_{im,00}^{TT} \quad (1.80)$$

because in the  $TT$ -gauge  $h_{i0} = h_{00} = 0$ .  $i$  and  $m$  are different from zero only for the values 2 and 3, they refer to the  $y$  and  $z$  components. It follows that

$$R_{00m}^\lambda = \eta^{\lambda i} R_{i00m} = \frac{1}{2} \eta^{\lambda i} \frac{\partial^2 h_{im}^{TT}}{c^2 \partial t^2} \quad (1.81)$$

and the equation of geodesic deviation (1.77) becomes

$$\frac{d^2}{dt^2}\delta x^\lambda = \frac{1}{2}\eta^{\lambda i}\frac{\partial^2 h_{im}^{TT}}{\partial t^2}\delta x^m \quad (1.82)$$

For  $t \leq 0$  the two particles are at rest relative to each other, and consequently

$$\delta x^j = \delta x_0^j, \quad \text{with } \delta_0^j = \text{const}, \quad t \leq 0 \quad (1.83)$$

Since  $h_{\mu\nu}$  is a small perturbation, when the wave arrives the relative position of the particles will change only by infinitesimal quantities, and therefore we set

$$\delta x^\lambda(t) = \delta x_0^\lambda + \delta x_1^\lambda(t), \quad t > 0 \quad (1.84)$$

where  $\delta x_1^\lambda(t)$  has to be considered as a small perturbation with respect to the initial position  $\delta x_0^\lambda$ . Substituting (1.84) in (1.82), remembering that  $\delta x_0^\lambda$  is a constant and retaining only terms of order  $O(h)$  eq (1.82) becomes

$$\frac{d^2}{dt^2}\delta x_1^\lambda = \frac{1}{2}\eta^{\lambda i}\frac{\partial^2 h_{ik}^{TT}}{\partial t^2}\delta x_0^k \quad (1.85)$$

This equation can be integrated and the solution is

$$\delta x^\lambda = \delta x_0^\lambda + \frac{1}{2}\eta^{\lambda i}h_{ik}^{TT}\delta x_0^k \quad (1.86)$$

which shows the transverse nature of the gravitational wave; indeed, using the fact that if the wave propagates along  $x$  only the components  $h_{22} = -h_{33}$ ,  $h_{23} = h_{32}$  are different from zero, from eqs. (1.86) we have

$$\delta x^0 = \delta x_0^0 + \frac{1}{2}\eta^{00}h_{0k}^{TT}\delta x_0^k = 0 \quad (1.87)$$

$$\delta x^1 = \delta x_0^1 + \frac{1}{2}\eta^{11}h_{1k}^{TT}\delta x_0^k = \delta x_0^1 \quad (1.88)$$

$$\delta x^2 = \delta x_0^2 + \frac{1}{2}\eta^{22}h_{2k}^{TT}\delta x_0^k = \delta x_0^2 + \frac{1}{2}(h_{22}^{TT}\delta x_0^2 + h_{23}^{TT}\delta x_0^3) \quad (1.89)$$

$$\delta x^3 = \delta x_0^3 + \frac{1}{2}\eta^{33}h_{3k}^{TT}\delta x_0^k = \delta x_0^3 + \frac{1}{2}(h_{32}^{TT}\delta x_0^2 + h_{33}^{TT}\delta x_0^3) \quad (1.90)$$

In this way, the particles will be accelerated only in the plane orthogonal to the direction of propagation. To study the effect of the polarization of the

wave we need to consider a plane wave whose nonvanishing components are (omitting the superscript  $TT$ )

$$h_{yy} = -h_{zz} = 2\Re \{A_+ e^{i\omega(t - \frac{x}{c})}\} \quad (1.91)$$

$$h_{yz} = h_{zy} = 2\Re \{A_\times e^{i\omega(t - \frac{x}{c})}\} \quad (1.92)$$

Having two particles located, as indicated in figure (1.2) at  $(0, y_0, 0)$  and  $(0, 0, z_0)$ . Considering the polarization  $+$  first, we assume

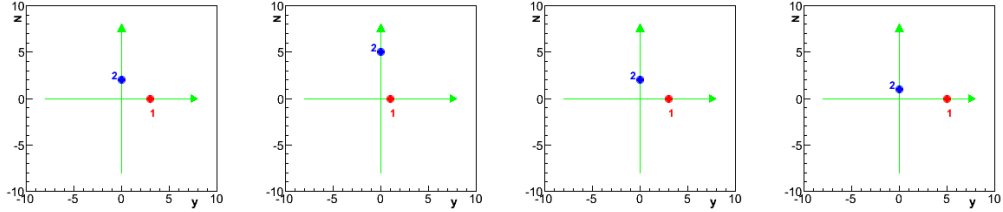


Figure 1.2: The effect of the '+' polarization of a gravitational wave changes the distances between two particles.

$$A_+ \neq 0 \quad \text{and} \quad A_\times = 0 \quad (1.93)$$

Assuming  $A_+$  real, eqs (1.91-1.92) give

$$h_{yy} = -h_{zz} = 2A_+ \cos \omega \left( t - \frac{x}{c} \right) \quad (1.94)$$

$$h_{yz} = h_{zy} = 0 \quad (1.95)$$

If at  $t = 0$   $\omega(t - \frac{x}{c}) = \frac{\pi}{2}$ , eqs (1.87-1.90) written for the two particles for  $t > 0$  give

$$1) z = 0, \quad y = y_0 + \frac{1}{2} h_{yy} y_0 = y_0 [1 + A_+ \cos \omega(t - \frac{x}{c})] \quad (1.96)$$

$$2) y = 0, \quad z = z_0 + \frac{1}{2} h_{zz} z_0 = z_0 [1 - A_+ \cos \omega(t - \frac{x}{c})] \quad (1.97)$$

After a quarter of a period ( $\cos \omega(t - \frac{x}{c}) = -1$ )

$$1) z = 0, \quad y = y_0 [1 - A_+] \quad (1.98)$$

$$2)y = 0, \quad z = z_0[1 + A_+] \quad (1.99)$$

After half a period ( $\cos\omega(t - \frac{x}{c}) = 0$ )

$$1)z = 0, \quad y = y_0 \quad (1.100)$$

$$2)y = 0, \quad z = z_0 \quad (1.101)$$

After three quarters of a period ( $\cos\omega(t - \frac{x}{c}) = 1$ )

$$1)z = 0, \quad y = y_0[1 + A_+] \quad (1.102)$$

$$2)y = 0, \quad z = z_0[1 - A_+] \quad (1.103)$$

Similarly, if we consider a ring of particles centered at the origin, the effect produced by a gravitational wave with polarization '+' can be seen in figure (1.3). Now, we consider  $A_\times \neq 0$  and  $A_+ = 0$ :

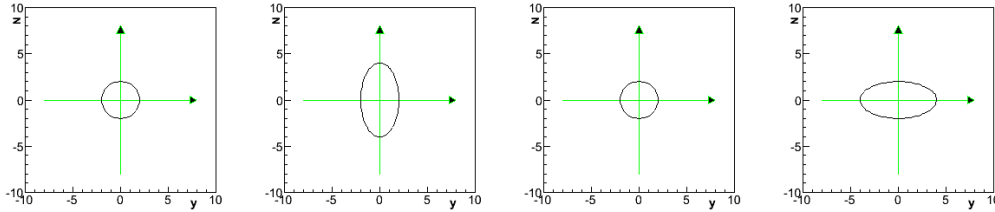


Figure 1.3: The effect produced by a gravitational waves with '+' polarization on a ring of test particles.

$$h_{yy} = h_{zz} = 0 \quad (1.104)$$

$$h_{yz} = h_{zy} = 2A_\times \cos\omega(t - \frac{x}{c}) \quad (1.105)$$

Comparing with eqs (1.87-1.90) we see that a generic particles initially at  $P = (y_0, z_0)$ , when  $t > 0$  will move according to the equations

$$y = y_0 + \frac{1}{2}h_{yz}z_0 = y_0 + z_0A_\times \cos\omega(t - \frac{x}{c}) \quad (1.106)$$

$$z = z_0 + \frac{1}{2}h_{zy}y_0 = z_0 + y_0A_\times \cos\omega(t - \frac{x}{c}) \quad (1.107)$$

Taking four particles disposed as indicated in figure (1.4)

$$1)y = r, \quad z = r \quad (1.108)$$

$$2)y = -r, \quad z = r \quad (1.109)$$

$$3)y = -r, \quad z = -r \quad (1.110)$$

$$4)y = r, \quad z = -r \quad (1.111)$$

As before, we shall assume that the initial time  $t = 0$  corresponds to  $\omega(t -$

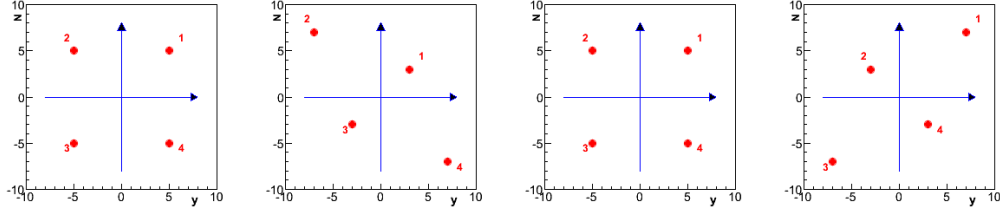


Figure 1.4: The effect produced by a gravitational waves with 'x' polarization changes the distances between four particles.

$\frac{x}{c} = \frac{\pi}{2}$ . After a quarter of a period ( $\cos\omega(t - \frac{x}{c}) = -1$ ), the particles will have the following positions

$$1)y = r[1 - A_x], \quad z = r[1 - A_x] \quad (1.112)$$

$$2)y = r[-1 - A_x], \quad z = r[1 + A_x] \quad (1.113)$$

$$3)y = r[-1 + A_x], \quad z = r[-1 + A_x] \quad (1.114)$$

$$4)y = r[1 + A_x], \quad z = r[-1 - A_x] \quad (1.115)$$

After half a period ( $\cos\omega(t - \frac{x}{c}) = 0$ ), and the particles go back to the initial positions. After three quarters of a period, when ( $\cos\omega(t - \frac{x}{c}) = 1$ )

$$1)y = r[1 + A_x], \quad z = r[1 + A_x] \quad (1.116)$$

$$2)y = r[-1 + A_x], \quad z = r[1 - A_x] \quad (1.117)$$

$$3)y = r[-1 - A_x], \quad z = r[-1 - A_x] \quad (1.118)$$

$$4)y = r[1 - A_x], \quad z = r[-1 + A_x] \quad (1.119)$$

The motion of the particles is indicated in figure (1.4). It follows that a small ring of particles centered at the origin, will again become an ellipse, but rotated at  $45^\circ$  (see figure (1.5)) with respect to the other polarization. In conclusion, we can define  $A_+$  and  $A_\times$  as the polarization amplitudes of the wave. The wave will be linearly polarized when only one of the two amplitudes is different from zero.

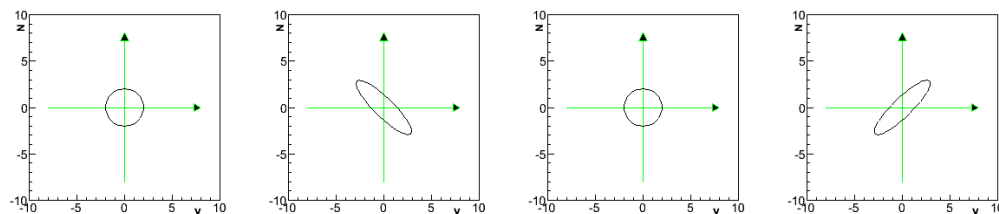


Figure 1.5: The effect produced by a gravitational waves with 'x' polarization on a ring of test particles.



# Chapter 2

## Sources of Gravitational Waves

### 2.1 Introduction

For more than 50 years, until the analysis of timing residuals of the orbital period of the binary pulsar PSR 1913 + 16, by Russell Hulse and Joseph Taylor, gravitational waves, have been only a theoretical prediction. PSR 1913 + 16 is a system composed of two neutron stars with an orbital period of 7.75 h. By monitoring the precise timing of radio pulses emitted by one of the neutron stars over several decades, Hulse and Taylor showed that the orbital period of the system is slowly decreasing at the rate foreseen for the general relativistic emission of gravitational waves [117]. These two scientists were awarded the Nobel Prize in Physics for this work in 1993. In about 300 million years, the orbit of PSR 1913 + 16 will collapse and the two neutron stars will coalesce into a single compact object. At 6kpc, that process will generate detectable gravitational waves. Waiting this time, the first direct detection of gravitational waves requires powerful sources with large masses moving in strong gravitational fields.

In this chapter we focus our attention on the sources of gravitational radiation that seem to be most likely to be detected from ground based detectors.

## 2.2 Supernovae and gravitational collapse

Supernovae are among the most violent events known to astronomy and they were the primary target for GW bar detectors<sup>1</sup>. They are also an important potential source for ground based interferometers which should be able to detect such bursts with an amplitude of  $10^{-21}$ .

Supernovae (of type II) are the result of the gravitational collapse of an evolved star. The collapse emanates a significant amount of energy, about  $0.15 M_{\odot} c^2$ . The majority of this energy should be carried away by neutrinos. This hypothesis is supported by the neutrino observations of supernova SN1987A.

To calibrate the sensitivity of detectors one can calculate the amplitude of the gravitational wave produced when a certain fraction of the emitted energy is converted into gravitational waves. The expression for the energy flux carried by the gravitational wave, with amplitude  $h$ , is [11]

$$F = \frac{c^3}{16\pi G} |\dot{h}|^2 \quad (2.1)$$

If we consider the emission of a burst of gravitational waves by a source at distance  $r$  from the detector and a total energy  $E$  emitted predominately at a frequency  $f_{gw}$  in a timescale  $\tau$ , from the flux formula we can calculate the strain amplitude  $h$  of a gravitational wave

$$\begin{aligned} h &= 5 \times 10^{-22} \left[ \frac{E}{10^{-3} M_{\odot} c^2} \right]^{1/2} \left[ \frac{\tau}{1 \text{ms}} \right]^{-1/2} \left[ \frac{f_{gw}}{1 \text{kHz}} \right]^{-1} \left[ \frac{r}{15 \text{Mpc}} \right]^{-1} \\ &= 3 \times 10^{-18} \left[ \frac{E}{10^3 M_{\odot} c^2} \right]^{1/2} \left[ \frac{\tau}{1000 \text{s}} \right]^{-1/2} \left[ \frac{f_{gw}}{1 \text{MHz}} \right]^{-1} \left[ \frac{r}{3 \text{Gpc}} \right]^{-1} \end{aligned} \quad (2.2)$$

This amplitude may be detected by ground based interferometers that can reveal a burst that emits  $10^{-3} M_{\odot} c^2$  in gravitational wave energy at the distance of the Virgo Cluster (18 Mpc).

## 2.3 Coalescing binaries

Coalescences of compact binaries, composed of either neutron stars (NSs) or black holes (BHs), are thought to be among the most promising sources for

<sup>1</sup>Weber introduced the bar detector as the first type of instrument to reveal GW.

ground based interferometers. Due to their mutual gravitational attraction the two bodies in the system rotate around each other. This not Newtonian system loses energy radiating gravitational wave and then coalesces to become a unique compact object.

We can identify three phases to describe the dynamic of compact binaries system: the inspiral, merger and ringdown phase. In the inspiral phase the binaries are far from each other. To conserve the angular momentum they come closer, rotate faster and emit gravitational waves. The inspiral phase ends at the last stable orbit, known as the innermost stable circular orbit (ISCO). At this point the binaries are very close and plunge into each other to form a black hole, this is the merger phase. After the coalescence, in the ringdown phase, the produced black hole radiates quasi-normal mode gravitational waves.

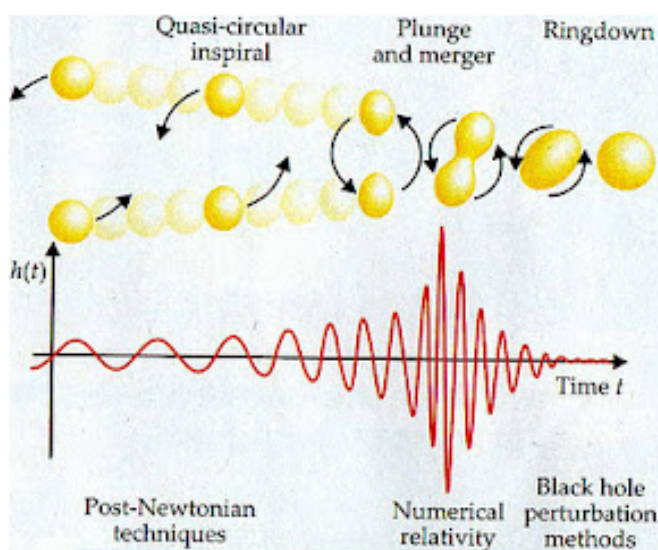


Figure 2.1: The top sketch displays the progressive phases of coalescence: the inspiral, the plunge and merger, and the ringdown phase. The bottom part shows the corresponding amplitude of the emitted gravitational waves. Image credit: Baumgarte and Shapiro 2011.

The inspiral stage of coalescence can be well modelled through Post-

Newtonian (PN) expansions [216]. They provide an analytic characterization of the gravitational flux and describe the two bodies motion. In addition they can supply initial dynamical data at the beginning of the plunge, like their positions and momenta, to be used as initial conditions in numerical relativity to model the merger phase. Significant gravitational wave emission is expected from the plunge phase after the stars reach the last stable orbit and fall rapidly towards one another, and from the merger event. No analytic waveforms exist for the merger phase; calculating these waveforms is one of the primary goals of numerical relativity [217]. The ringdown phase is described by an exponentially damped sinusoid, determined by the quasi-normal mode frequency and damping time, see picture 2.1.

Detection of gravitational waves from binary systems will establish evidence for the existence of BHs besides important tests of their characteristics as predicted by general relativity [214]. Multiple observations will provide information about the population of binary systems up to distances of hundreds of Megaparsecs (Mpc <sup>2</sup>) in the universe.

The event rate of coalescing binaries is highly uncertain. Estimates are based on studies of pulsar detections in binary systems [21] [22], and on theoretical studies of binary evolution [19] [20]. In the first case, observations of pulsars in binary systems suggest a formation rate of about  $10^{-6}yr^{-1}$  in the Galaxy. On the other hand, studies of evolution prospect a larger population of systems, with a rate that may be  $10^{-4}yr^{-1}$  in the Galaxy. The rate obtained from pulsars is a lower limit and if converted we have about one event per year out to a distance of 200 Mpc.

## 2.4 Gravitational radiation from individual neutron stars

If individual neutron stars, isolated or in binary systems, spin or are significantly asymmetric, they can also radiate gravitational waves. Their asymmetry may come from irregularities associated with their formation, or from unevenness in the crust.

Rotating neutron stars can emit continuous gravitational wave signals. In fact if in these systems a quadrupole mass asymmetry or ellipticity,  $\epsilon$ , is

---

<sup>2</sup>1 parsec = 3.3 light years

present then there will be gravitational wave emission at twice the NS rotation frequency. The NSs internal structure and the equation of state regulate the maximum sustainable ellipticity and hence the maximum GW emission. To put an upper limit on  $h$  we can use the spindown. The most interesting examples are provided by the Crab and Vela pulsar. In both cases, knowing the observed spindown ( $\dot{f}$ ) from radio measurements and imposing that the whole kinetic energy loss is due to gravitational radiation, it's possible to derive an indirect upper limit (spindown upper limit) on  $h$  for these two pulsars. Recent GW analyzes beat such indirect limits in both cases: for the Crab the spindown (sd) limit on detectable strain is  $h^{sd} \leq 1.4 \times 10^{-24}$  at about 59.6 Hz while the direct upper limit from GW search is  $h \leq 3.4 \times 10^{-25}$  [220]. In the same way for the Vela pulsar the spindown indirect upper limit is  $h^{sd} \leq 3.3 \times 10^{-24}$ , that is above the frequentist direct upper limit using GW analysis  $h \leq 2.1 \times 10^{-24}$  [219].

## 2.5 Stochastic background

A stochastic background of GWs could result from the superposition of an extremely large number of unresolved and independent GW emission events [221]. Similarly to the cosmic microwave background radiation, it's possible that the Big Bang has left also a background of gravitational radiation. This radiation is unchanged since it was produced due to the weak interaction with matter. On the contrary the microwave background was thermalized and coupled to matter until the epoch of recombination. For these reasons, while the gravitational wave background was produced probably about  $10^{-35}$  s after the Big Bang, the microwave background comes from about  $10^5$  years after the Big Bang.

The stochastic radiation consists of a huge quantity of undetermined sources since the beginning of stellar activity. One can characterize its energy density as a function of frequency. The spectrum is usually described by the dimensionless quantity  $\Omega_{GW}(f)$ , which is the GW energy density per unit logarithmic frequency, divided by the critical energy density  $\rho_c$ :

$$\Omega_{gw} = \frac{f}{\rho_c} \frac{d\rho_{gw}}{df} \quad (2.3)$$

where  $\rho_{gw}(f)$  is the energy density per unit frequency and  $\rho_c = 2 \times 10^{-43} Jm^{-3}$  for a Hubble constant of  $100 Km s^{-1} Mpc^{-1}$ .



# Chapter 3

## Common sources of Gravitational Waves and High Energy Neutrinos

### 3.1 Introduction

Many astrophysical sources and cataclysmic phenomena are expected to produce gravitational waves and high-energy cosmic radiation in our Universe, in the form of photons, hadrons, and presumably also neutrinos. Both gravitational waves (GW) and high-energy neutrinos (HEN) are cosmic probes that can escape very dense media and travel unabsorbed over cosmological distances, carrying information from the innermost regions of the astrophysical sources. While GWs originate from the dynamics of the bulk motion of the progenitor, HENs trace the interactions of accelerated protons and heavier nuclei with ambient matter and radiation in and around the source. Such complementary messengers could also reveal new, hidden engines that have not been observed by conventional photon astronomy, and play a crucial role in multimessenger astronomy.

Sources of joint emission include two groups of galactic sources which could be accessible to the current generation of GW interferometers and HEN telescopes [150, 151]: Microquasars and Soft Gamma Repeaters.

*Microquasars* are believed to be X-ray binaries involving a compact object that accretes matter from a companion star and re-emits it in relativistic jets associated with intense radio (and IR) flares [152]. Such objects could emit

GWs during both in the accretion and ejection phases; and if the jet has an hadronic component [153] the ejection phase could also present a HEN signal.

*Soft Gamma Repeaters* (SGRs) are X-ray pulsars with a soft  $\gamma$ -ray bursting activity which, according to the magnetar model, can be associated with star-quakes [152]. The deformation of the star during the outburst could produce GWs, while HENs could emerge from hadron-loaded flares.

On the extragalactic scale the most promising sources are Gamma Ray Bursts (GRBs). The commonly accepted explanation of GRBs is the so-called "fireball model" which involves a relativistic jet of plasma produced by a central source (probably compact but yet to be determined) or a binary system. In this scenario, collisions of a neutron star and a black hole or two neutron stars are likely to generate gravitational waves that are strong enough to be detected on Earth. At the same time, observed  $\gamma$ -rays result from the dissipation (through synchrotron or inverse Compton emission) of the jet kinetic energy. A particular kind of GRB is called choked GRB [154, 33], in which the jet does not break out of the central source, hence failing to produced a flash of  $\gamma$ -rays. On the contrary, high energy neutrinos can escape from very dense matter due to their weak interaction. Gravitational waves are expected from the coalescence of compact binaries, that are considered the GRB progenitors. Such GW signals from  $\sim 15$  Mpc distance are detectable with the first generation of interferometers. Choked GRBs are thought to be relevant sources of HENs and they are expected to produce gravitational waves, as also expected in the case of successful GRBs.

A more exotic class of source is cosmic strings, topological defects formed during phase transitions in the early Universe. Emission of gravitational waves is considered the main channel for cosmic string loops to decay. In particular, cosmic string cusps appear to be potential sources of gravitational waves due to the very large Lorentz factor achieved when they contract. Cosmic strings in general are also of interest to high energy neutrino astronomy as they can produce particles, including neutrinos, up to the Planck scale ( $\approx 10^{19}$  GeV) [39, 42, 40, 41].

In this chapter we describe these sources and their characteristics. Then, we will focus our attention on the most plausible astrophysical common emitters: Gamma Ray Bursts, known to be very energetic and to have a burst activity, and their progenitors.

## 3.2 Galactic Sources

### 3.2.1 Microquasars

Microquasars (MQs) or radio emitting X-ray binary systems are galactic strong e variable radio emitters. The radio jets are produced by matter falling from a normal star, called donor, to a black hole (of few solar masses) or a neutron star. Gravitational potential energy is released from the in-falling matter that creates an accretion disk, very luminous in the optical and X-ray, surrounding a central object. During active states, the X-ray flux and spectrum can vary substantially, with a total luminosity that often exceeds the Eddington limit. Their activity involves ejection within jets with kinetic power that appears to constitute a considerable fraction of the liberated accretion energy, giving rise to intense radio and IR flares [72].

The duration of major ejection events is typically of the order of days, while that of less powerful flares is correspondingly shorter (minutes to hours). The correlation between the X-ray and synchrotron emissions indicates a connection between the accretion process and the jet activity.

Whether radio and IR outbursts represent actual ejection of blobs of plasma or, alternatively, formation of internal shocks in a quasi-steady jet is unclear. In any case, since the overall time scale of outbursts is much longer than the dynamical time of the compact object (milliseconds), it is likely that shocks will continuously form during the ejection event. If a fraction of at least a few percent of the jet power is used to accelerate electrons to very high energies then emission of high-energy gamma rays is anticipated, in addition to the observed radio and IR emission.

In the case of windy microquasars in particular, hadronic interactions seem to be unavoidable [77]. The detected  $\gamma$ -rays should then be accompanied by a flux of high energy neutrinos emerging from the decays of  $\pi^\pm$  mesons produced in pp and/or p $\gamma$  interactions [82]. The flux of TeV neutrinos, which can be estimated on the basis of the detected TeV  $\gamma$ -ray flux, taking into account the internal  $\gamma\gamma \rightarrow e^+e^-$  absorption, depends significantly on the location of  $\gamma$ -ray production region. HESS/EGRET data agree well with a production of  $\gamma$  (and neutrinos) at the base of the jet, very close to the source of the acceleration phase (and its corresponding GW signal). The effect of strong magnetic fields, however, can attenuate the neutrino signal through the cooling of charged pions and muons.

The detectability by IceCube, ANTARES and other future  $km^3$ -scale tele-

scopes strongly depends on the high energy cutoff in the spectrum of parent protons. Romero and Vila in [102] also remarked that internal absorption in the inner jets of MQs can suppress high energy gamma-ray emission leading to 'dark' neutrino sources.

Two kinds of processes could lead to detectable GW signals from MQs. Firstly, the matter accreted around the central object could fall into it, and, provided that the process is fast enough, trigger the resonance of normal modes in the central object [159]. This would typically result in a damped sine signal, which could continue into the ejection phase. For these signals, the amplitude will depend critically on the mass of the central object. The time-lag between the two processes is unknown, and could range from ms up to several days.

### 3.2.2 Soft gamma-ray repeaters

Soft gamma-ray repeaters (SGRs) are X-ray pulsars which have quiescent soft (2-10 keV) periodic X-ray emissions with periods ranging from 5 to 10 s. They exhibit repetitive bursting episodes lasting few hours each and composed of numerous very short ( $\sim$  ms) pulses. Every once in a while they emit a giant flare in which a short ( $< 0.5$ ) s spike of harder radiation is observed. Such flares can reach peak luminosity of  $\sim 10^{40}$  J/s, in X-rays and  $\gamma$ -rays.

Few SGR sources are known, most of which in the Milky Way and one in the Large Magellanic Cloud. Their population has been increasing in the last years, thanks to more sensitive instruments and better monitoring; see for example [112], [99], [113].

The principal magnetar model for these objects is a neutron star with a huge magnetic field  $B > 10^{15}$  G [31], [32], which is subject to star-quakes that are thought e.g. to fracture the rigid crust, causing outbursts. The giant flares result from the formation and dissipation of strong localized currents coming from magnetic field rearrangements associated with the quakes, liberating a high flux of X- and  $\gamma$ -rays. Sudden changes in the large magnetic fields would accelerate protons or nuclei that produce neutral and charged pions in interactions with thermal radiation. These subsequently decay into TeV or even PeV energies  $\gamma$ -rays and neutrinos [45], making flares from SGRs potential sources of HENs.

During the crustal disruption, a fraction of the initial magnetic energy is annihilated and released as photons, and the stored elastic energy is also converted into shear vibrations. These vibrations are able to excite non-

radial  $f$ -modes of the neutron star core with frequencies in the kHz range. Those modes are efficiently damped by GW emission [29], with damping time of  $\sim 200$  ms. While detailed predictions about the GW amplitude are difficult to get, the maximum GW energy has been estimated to be of the order-of-magnitude of  $10^{48}$  erg -  $10^{49}$  erg.

### 3.3 An exotic class of source: cosmic strings

Cosmic strings are topological defects produced in the early universe. In particle physics models they can produce a wide assortment of observational effects such as: gravitational lensing, and gravitational radiation, both in the form of a stochastic background and localized bursts [34, 35].

Cosmic strings act as thin superconducting wires to external electromagnetic fields. Moving through cosmic magnetic fields they develop electric currents. When such loops of current-carrying string oscillate, they emit highly boosted charged particles from cusps (short segments where the string velocity momentarily gets very close to the speed of light). These released particles and their decay products can be detected as high-energy cosmic rays, neutrinos and gamma ray bursts [36, 37, 38].

The remarkable importance of cosmic strings is based on tremendous energies of neutrinos achievable by these sources. In fact, topological defects can generate particles, including neutrinos, up to the Planck scale ( $\approx 10^{28}$  eV) and above [39, 40, 41, 42], while astrophysical sources can accelerate particles to energies  $10^{21} - 10^{22}$  eV at most.

The production of enormously high energy particles is an interesting property of cosmic strings, that, at the same time, are considered emitters of gravitational waves. In fact, it seems that emission of gravitational waves is expected from the main channel of cosmic string loops decay. They are potential sources of GW due to the very large Lorentz factor achieved when they contract.

### 3.4 Extragalactic sources: Gamma Ray Bursts

Gamma-Ray bursts (GRBs) are detected as an intense and short lived flash of gamma rays with energies ranging from tens of keVs to tens of GeVs.

The morphology of their light curves is highly variable and typically exhibits millisecond variability, suggesting very compact sources and relativistic expansion.

GRBs are divided into two classes depending on the duration of their prompt gamma-ray emission, which appears to be correlated with the hardness of their spectra and are believed to arise from different progenitors: the short hard bursts last less than 2 seconds, while the emission of long-soft bursts can last up to tens of minutes. Short GRBs are believed to originate from the merger of binary neutron stars or neutron star-black hole systems. Long GRBs are thought to be related to the collapse of massive stars to form a neutron star or black hole.

In the standard picture, the mechanism responsible for the enormous energy release ( $\sim 10^{50} - 10^{52}$  ergs) and super-Eddington luminosity of GRBs, is the dissipation (via internal shocks, magnetic dissipation and/or external shocks) of bulk kinetic or magnetic energy into highly relativistic particles, which are accelerated to a non-thermal energy distribution via Fermi mechanism in a relativistically expanding fireball ejected by the GRB central engine [73], [75]. The accelerated electrons (and positrons) in the intense magnetic field emit non-thermal photons via synchrotron radiation and inverse Compton scattering.

Provided that the outflowing jet has a baryonic component, protons will also be shock-accelerated and will undergo interactions with the gamma-rays and/or other protons inside the fireball, producing charged pions and kaons that will subsequently decay into HENs ( $\pi^\pm, K^\pm \rightarrow \mu^\pm + \nu_\mu/\bar{\nu}_\mu \rightarrow e^\pm + \nu_e/\bar{\nu}_e + \nu_\mu/\bar{\nu}_\mu$ ). Such neutrinos are emitted in spatial and temporal coincidence with the GRB prompt electromagnetic signal; their energy is typically in the range  $\sim$  TeV to PeV. Neutrinos with higher (up to  $\sim 10^{10}$  GeV) energy can also be emitted at the beginning of the afterglow phase, when the outflow is decelerated by external shocks with ambient material and the accelerated protons undergo interactions with the matter outside of the jet [51].

While gamma-ray and HEN emission from GRBs are related to the mechanisms driving the relativistic outflow, GW emission is closely connected to the central engine and hence to the progenitor of the GRB. Short-hard GRBs, ( $\Delta t \lesssim 2s$ ), are thought to be driven by neutron star-neutron star or neutron star-black hole mergers. Coalescing binaries are expected to emit GWs that are detectable from large distances [63],  $\sim 15$  Mpc with the first generation of GW detectors and  $\sim O(100)$  Mpc with the advanced LIGO and Virgo

expected to first come online in 2014-2015. These distances coincide with the range where the HEN flux is thought to be large enough for detection with current HEN detectors.

Long-soft GRBs, ( $\Delta t > 2s$ ) are most probably induced by 'collapsars', i.e. collapses of a massive star into a black hole, with the formation of an accretion disk and a jet that emerges from the stellar envelope [107]. The high rotation rate required to form the accretion disk that powers the GRB allows the production of GWs via bar or fragmentation instabilities. Asymmetrically infalling matter produces the GW burst signals not only at the moment of core bounce when the central density exceeds the nuclear density [135], but also at the moment of black hole formation, followed by the subsequent ring-down phases [136]. In addition, general relativistic effects predict the precession of the inner hyperdense accretion disk with the consequent production of GWs [137]

A particular kind of GRBs is called failed GRBs. Failed GRBs are described as '*choked jets, which are completely shock heated and do not break out of the star*' [207], due to the opacity of the stellar matter to the  $\gamma$  rays. In fact, it's only possible to detect a gamma ray flux from a core collapse supernovae when the emission is able to break out of the star. Since jets reach relativistic velocities as they leave the He core, if the jet duration is less than the time taken to leave the star, the jet will be unable to break out of the star, so we have a choked jet that is dark in gamma rays. On the contrary, high energy neutrinos can escape from very dense matter due to their weak interaction. Choked GRBs are thought to be relevant sources of HENs and they are expected to produce gravitational waves, as well as successful GRBs, for these reason they are the most plausible common sources for the GW+HEN analysis.

### 3.4.1 GRB Progenitors: double neutron stars (NS/NS) and black Hole Neutron Star, BH/NS

GRBs are likely produced from binary mergers and collapsars: double neutron stars (NS/NS), black hole and neutron star (BH/NS), black hole and white dwarf (BH/WD), black hole and helium star (BH/He), and fast rotating massive stellar collapses, as seen before. NS/NS and BH/NS mergers can produce short GRBs with durations under a second, but they are unlikely to emit long GRBs with durations of tens or hundred of seconds. On the

contrary, long GRBs might be generated from BH/WD and BH/He mergers and collapsars.

The theoretical rates of these progenitors have been estimated for ground based detectors. Astrophysical estimates for compact coalescence rates are between  $0.01$  and  $50 \text{ Mpc}^{-3} \text{ Myr}^{-1}$  for NS-NS systems and between  $6 \times 10^{-4}$  and  $1 \text{ Mpc}^{-3} \text{ Myr}^{-1}$  for NS-BH systems, see [139].

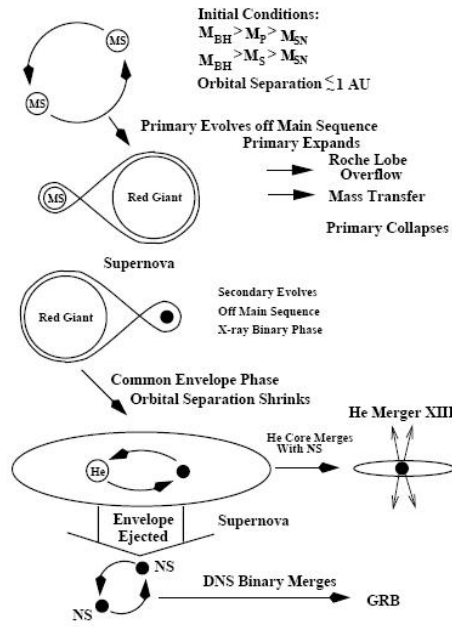


Figure 3.1: Evolution of two main sequence's stars to form a NS/NS binary system. (MS denotes a main sequence star and NS and He are a neutron star and an Helium star, respectively.) The primary star evolves off the main sequence, overfills its Roche lobe and transfers mass to its companion. The primary explodes as a supernovae and forms a neutron star. The system of a neutron star and massive companion is created. They pass through an X ray phase and then the secondary expands and generates a common envelope. NS/He system is formed after the ejection of the secondary's hydrogen mantle. When the helium star explodes as a supernova, the system is composed of two neutron stars. Their coalescence occurs as a consequence of gravitational radiation. Source of picture: Fryer C., Woosley E. and Hartmann D. H. 1999 *Astrophys. J.* 526.

According to the stellar evolution the birth of a close orbit NS/NS sys-

tem begins with two massive stars in the Main Sequence (MS) with masses between  $\sim 8M_{\odot}$  and  $\sim 20M_{\odot}$ . In the standard scenario, the primary star overfills its Roche lobe, hence transfers mass to the secondary star (its companion), see fig. 3.1. In fact, the Roche lobe overflow causes the fall of the excess material into the other object's Roche lobe. The transfer of mass lead to the disintegration of the star, since a reduction of the object's mass causes its Roche lobe to shrink. Such evolution guides the primary star at the end of its life, in fact it explodes as a supernova with the formation of a neutron star. If the explosion doesn't destroy the binary, at this point, the configuration consists of a neutron star and a massive companion. The massive star (the secondary star) expands, overfills its Roche lobe and transfers mass to the neutron star. The matter falling from the secondary star to the compact object (neutron star) forms an accretion disk around the compact object, heats up because of friction and produces X-rays. Hence, the system has an X ray binary phase and the generation of a common envelope. The neutron star spirals into the massive secondary and loses orbital kinetic energy. This process causes the ejection of the secondary's hydrogen mantle, to form a binary system with a neutron star and an helium star. The transfer of angular momentum to the neutron star, due to the mass accretion on the primary star, allows to spin up or 'recycle' it as a pulsar. The explosion of the helium star generates the second neutron star in the system. The resulting close NS/NS binary will merge and emit gravitational wave radiation.

An alternative scenario to form close NS/NS systems is suggested by Brown [110], when the two massive stars in the initial binary system have similar masses, see fig. 3.2. The primary star expands, overfills its Roche lobe and transfers mass to the companion. The primary expels its hydrogen mantle and becomes an helium star<sup>1</sup>. During the common envelope phase also the secondary star evolves and ejects its hydrogen mantle to become the second helium star of the system. In such combined hydrogen envelope the two helium cores orbit. This envelope is ejected when the two stars explode one after the other. If the explosions don't destroy the binary, a system of double neutron stars is formed.

Initial stars with masses larger than  $\sim 8M_{\odot}$  are thought to collapse to form a neutron star remnant and a core collapse supernovae. More massive initial

---

<sup>1</sup>When a low mass star exhausts the supply of hydrogen in its core, cannot balance the gravity anymore. The core collapses until it reaches a high enough density to start converting helium to carbon.

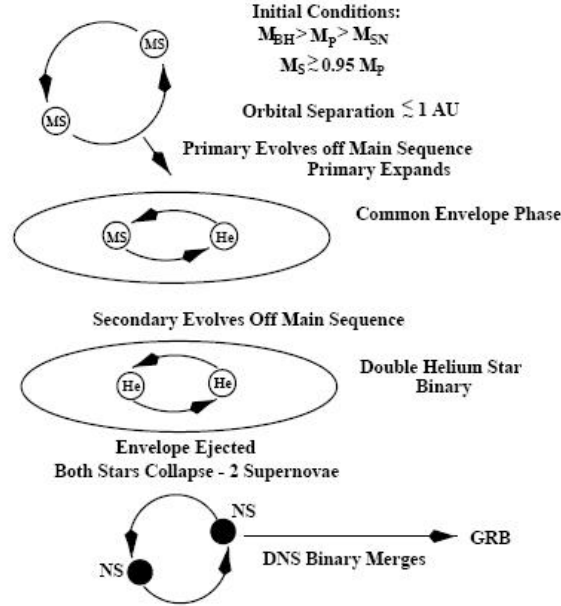


Figure 3.2: The mechanism supported by Brown for the formation of a double NS/NS system [110]. (MS denotes a main sequence star and NS and He are a neutron stars and an Helium star, respectively.) In this case the stars have almost equal mass and the secondary star evolves off the main sequence before the primary collapses, forming a double helium star binary. The subsequent collapse of these helium stars creates the NS/NS system. Source of picture: Fryer C., Woosley E. and Hartmann D. H. 1999 *Astrophys. J.* 526.

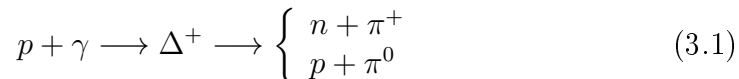
star,  $> 20M_{\odot}$  are thought to result in a black hole remnant. Also, when a star explodes (dies) the decisive quantity is the mass.

From neutron star binaries also a BH/NS system can be formed. If the primary neutron star reaches a mass bigger than few solar masses, through the Roche lobe overflow of the companion during the common envelope phase, it collapses in a black hole. This scenario forms a binary consisting of a neutron star and black hole [107], both in the standard scenario and in the Brown model.

### 3.5 Fireball Model

The progenitor scenarios, we describe above, are thought to be the central engines for the production of GRBs. In fact, the formation of GRB could originate either with the merger of a binary system or with the collapse of a massive star. Both these events produce a black hole with a disk of material around it. This engine pumps out a jet of material at close to the speed of light and shock waves in this matter give off radiation. The leading theory for GRBs' formation is the fireball model. The characteristic of this schema is the huge amount of released energy, between  $10^{51}$  erg and  $10^{54}$  erg, in a short time, between 0.1 and 100 seconds, from the very compact central object, order of  $10^6$  cm in diameter.

As discussed before the merger of a binary system is likely to generate gravitational waves that are strong enough to be detected on Earth, while the emission of high energy neutrinos comes from protons accelerated in the fireball internal shocks, where GRB  $\gamma$ -rays are expected to be produced. Protons lose energy via photo-production of pions by interacting with fireball photons. Their interactions should produce a huge amount of neutrinos almost simultaneously with the GRB through the decay



Charged pions decay and produce as results high energy neutrinos,



The fireball model is divided in three phases: pre-burst, burst emission and afterglow phase. The dissipation of kinetic or magnetic energy into high relativistic particles, accelerated through the Fermi mechanism, causes the emission of a giant quantity of energy in a relativistic fireball ejected by the GRB engine [73], [75]. This process constitutes the pre-burst phase. The accelerated electrons and positrons, generated from internal shocks between shells of matter ejected by the GRB central engine, emit photons through Synchrotron radiation and inverse Compton process. This burst emission is the direct probe of the jet, isolated from the medium. Shock-accelerated protons will interact with the gamma rays and/or other protons inside the

fireball, producing charged pions and kaons that will decay into high energy neutrinos. Then, the collision of the shells with the interstellar medium creates external shock that lead the afterglow emission. The reverse shock produces a bright optical flash which decays very rapidly [43]. This optical radiation carries fundamental information on the composition of the jet and the nature of the environment such as density of the circum-burst and interstellar medium.

### 3.6 The GRB puzzle

The evolution of the GRB is modelled in the fireball scheme, but we don't have any precise information about the astrophysical process that produces the energetic ultrarelativistic jets. In the following we put the information from the fireball model in a temporal scenario and we try to interpret what the detection shows. Our aim is to construct a reasonable time window in which we can look for a common signal between GW and HEN. From detection we know that:

- the enormous amount of released energy, between  $10^{51}$  erg and  $10^{54}$  erg, is a predominant fraction of the binding energy of a stellar compact object. The inner engine must be able to produce this energy.
- According to the overall duration, the burst emissions are divided in two groups. Short bursts with  $T < 2sec$  and long ones with  $T > 2sec$ . Due to the different duration time scales, this may imply the existence of dissimilar inner engines.
- The majority of GRBs are collimated with typical opening angles  $10^\circ < \theta < 20^\circ$ . The central object must be able to collimate the relativistic outflow.
- The uncertainty time scale can vary between 0.1 s and hundreds of seconds. According to the model, these time scales are determined by the activity of the inner object.

The specialists interpret these clues as the presence of an accretion disk around a compact object, probably a newborn black hole. Due to the short time scales is required a compact engine, while the accretion disk is needed to generate the two different time scales, and in particular the prolonged

activity and the energetics. The disk can form at the same time of the black hole creation. This drives to the conclusion that GRBs come along with the formation of black holes. Such model is supported by observations of relativistic jets from active galactic nuclei (AGNs)<sup>2</sup>

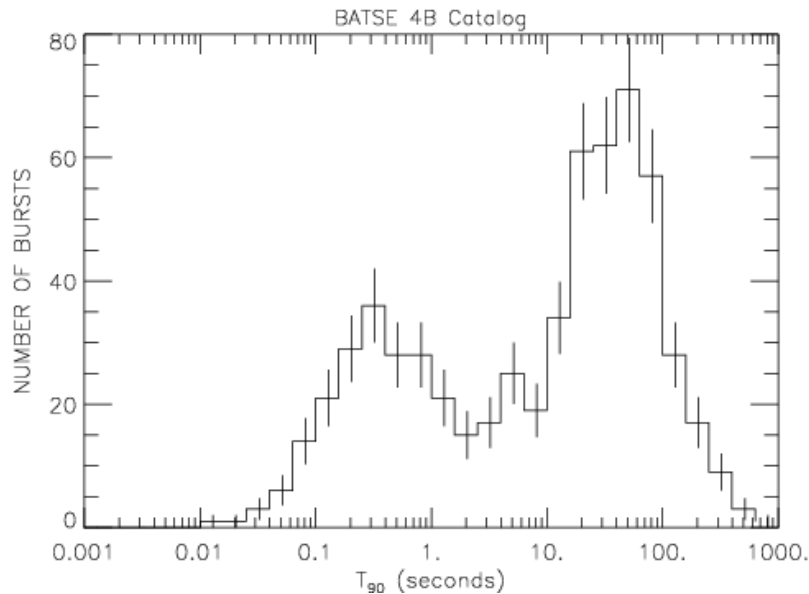


Figure 3.3: This plot shows the durations of the 4B Catalog Gamma-Ray Bursts recorded with the Burst and Transient Source Experiment on board NASA's Compton Gamma-Ray Observatory. The duration parameter used is T<sub>90</sub>, which is the time over which a burst emits from 5% of its total measured counts to 95%. Source: NASA's webpage <http://www.batse.msfc.nasa.gov/batse/grb/duration>.

---

<sup>2</sup>An active galactic nucleus constitutes the center of some galaxy in which the the nucleus (or central core) produces more radiation than the entire rest of the galaxy.

### 3.7 Search time window

By knowing the information from detection, we can decide which temporal scale to use in our analysis. In fact, the first requirement imposed for our triggered search for GWs in association with HENs is that the candidate signal has to be coincident in time, within an astrophysically motivated window with neutrino. To achieve and fix our search window, we can start from a simple calculation to show what time gap we obtain in theory with some approximations between a gravitational wave that travels at the speed of light and a high energy neutrino with speed  $v_\nu$ . Let's consider a neutrino particle of mass  $m_\nu$ , and speed  $v_\nu$ , its energy  $E_\nu$  is

$$E_\nu = \frac{m_\nu}{\sqrt{1 - v_\nu^2}} \quad (3.3)$$

If we consider the velocity of neutrino similar to the speed of light  $v_\nu = (1 - \varepsilon)c$  where  $\varepsilon$  is very small, and we set  $c = 1$ ,

$$v_\nu^2 \simeq (1 - 2\varepsilon) \quad (3.4)$$

using the approximation 3.4 in the eq. 3.3 we obtain the equation for the energy

$$E_\nu = \frac{m_\nu}{\sqrt{2\varepsilon}} \quad (3.5)$$

Now, we insert reasonable number for the energy of our high energy neutrino  $E_\nu = 1\text{TeV}$  and its mass  $m_\nu = 1\text{eV}$  in eq 3.5: to obtain  $E_\nu/m_\nu = 10^{12}$ , and hence  $2\varepsilon = 10^{-24}$ . The travel time for the neutrino from the source to the detector can be written as:

$$T_\nu = \frac{L}{v_\nu} = \frac{L}{(1 - \varepsilon)c} = \frac{L}{c}(1 + \varepsilon) \quad (3.6)$$

where  $L$  is the source distance for which we take  $L = 1\text{Gpc} = 10^9 \times 3 \times 10^{16}\text{m} = 3 \times 10^{25}\text{m}$ . Finally, we can calculate the difference in the arrival time  $\Delta T$  between the high energy neutrino  $T_\nu$  and the gravitational wave that travels at the speed of light  $T_{GW} = \frac{L}{c}$

$$\Delta T = T_\nu - T_{GW} = \frac{L}{c}(1 + \varepsilon) - \frac{L}{c} = \frac{1}{2} \frac{L}{c} 10^{-24} \quad (3.7)$$

$$\Delta T = \frac{1}{2} \frac{3 \times 10^{25} \times 10^{-24}\text{m}}{c} = \frac{15\text{m}}{c} \sim 10^{-9}\text{s} \quad (3.8)$$

---

The very small quantity  $\Delta T \sim 10^{-9}$  s accounts only for the difference in speed between gravitational waves and high energy neutrinos under the assumption of a simultaneous emission.  $\Delta T \sim 10^{-9}$  is negligible because it is well under the time resolution of our search. Hence, the most significant source of delay between the GW and HEN trigger arrival times stems from a delay between the respective emissions. In order to estimate the maximum reasonable delay we recall here the most interesting astrophysical sources and their emission mechanisms [249], see plot 3.3.

- As seen in paragraph 3.4, internal shocks can be produced before the visible outflow emerged from the stellar envelope, so the production of high energy neutrinos can happen before the observed  $\gamma$ -ray emission. The inner object, responsible for a precursor phase, can be already in activity up to  $\sim 100$  s before the gamma prompt emission [103, 104].
- According to the model, during the precursor phase we expect prompt neutrino emission to overlap with prompt  $\gamma$ -ray emission of GRBs. The BATSE (Burst Alert and Transient Source Experiment) Collaboration studied more than 2000 GRBs and determined the precursor time for this data set to be  $\sim 250$  s, [92].
- In most of observed GRB cases (95%), the duration of the emission due to inner compact object's activities is order of  $\sim 150$  s [93] and both GW and HEN can be emitted.
- We cannot exclude a potential joint emission of GW and HEN from the afterglow phase, but it's not possible at the moment to define a unique time scale for this emission part.

Since HEN and GW could be present during the precursor time, the main emission or the afterglow we decided to consider a much wider search window than the sum of the times listed before to include possible unknown mechanisms. For our analysis we consider a search window of  $\pm 500$  s around the neutrino trigger time, see chapter 7.



# Chapter 4

## LIGO: the Laser Interferometer Gravitational Wave Observatory

### 4.1 Introduction

The objective of LIGO, the Laser Interferometer Gravitational Wave Observatory [115], is to study and detect GWs of astrophysical origin. This goal will open a new window on the universe, with the promise of new physics and astrophysics. LIGO could detect a variety of GW signals such as those emitted during a: stellar core collapse which triggers a type II supernova; the inspiral, merger and ringdown phase of a binary system of compact objects; rapidly rotating, non-axisymmetric NSs; and also processes in the early universe that produce a stochastic background of GWs [116], as seen chapter 2. By design, the initial LIGO detectors were sensitive to GWs in a frequency band 40 – 7000 Hz, and capable of detecting a GW strain amplitude as small as  $10^{-21}$  [115]. The construction for the LIGO sites started in the late 1990s, and the commissioning periods took the first 5 years of this decade. They operated and took data during several science run. The data analyzed for the present work are from the fifth science run (S5). In this science run the detectors operated at their design sensitivity in a continuous data taking mode from November 2005 to September 2007 [114]. This chapter focuses on LIGO which operates the most sensitive detectors yet built.

## 4.2 Worldwide detector network

LIGO is a network of three Michelson interferometers. These detectors are all kilometer-scale power recycled Michelson laser interferometers with orthogonal Fabry-Perot arms [181] able to detect the quadrupolar strain in space produced by GWs. Multiple reflections between mirrors located at the end points of each arm extend the effective optical length of each arm, and enhance the sensitivity of the instrument.

There are two LIGO observatories: one located at Hanford, WA and the other at Livingston, LA. The Hanford site houses two interferometers: one with 4 km arms, denoted H1, and a second with 2 km arms, denoted H2. The Livingston observatory has a 4 km interferometer, L1. The observatories are separated by a distance of 3000 km, corresponding to a time-of-flight separation of 10 ms. Multiple detectors at separated sites are crucial for rejecting instrumental and environmental artifacts in the data, by requiring coincident detections in all data streams. Source localization requires triangulation of three detectors.

A network of detectors is necessary to extract the direction of travel and



Figure 4.1: LIGO observatories at Hanford, Washington (left) and Livingston, Louisiana (right).

complete polarization of the impinging GWs. The German-British GEO project operates a 600 m interferometer near Hanover, Germany [120]; the European Gravitational Observatory built the 3 Km-long interferometer Virgo near Pisa, Italy [121] and the Japanese TAMA project built a 300 m interferometer outside Tokyo, Japan [119]. Probably, during the next decade a new GW detector will develop in India [122] and KAGRA [123].

Since the beginning LIGO and GEO600 have operated as a network of detec-

tors and performed jointly the analysis of their data. The GEO600 project is a member of the LIGO Scientific Collaboration (LSC). Virgo and the LSC negotiated an agreement to collect, analyze data and publish results jointly.

### 4.3 Principle of detection

The scale of these detectors is their key feature: the orthogonal arms are build as long as practically possible to increase the signal due to a GW strain. The effect of a GW is to warp spacetime and during their crossing they produce a relative variation among two free masses. For this reason at the end of each arm of the detector there is a mirror as a free mass. The distance of the free masses will alternately decrease and increase during the passage of a gravitational wave. The dimensionless amplitude of gravitational waves  $h$  is the measure of relative variation  $\Delta L$  among the two free masses. With a  $h \sim 10^{-21}$  from the equation

$$\frac{\Delta L}{L} \sim h \quad (4.1)$$

where  $L \sim 4 \times 10^3$  m is the distance between the two masses, we obtain  $\Delta L \sim 10^{-18}$  m, a thousand times smaller than the diameter of a proton. In fact, this challenge involves the use of special interferometry techniques,

- state of the art optics,
- highly stable lasers,
- multiple layers of vibration isolation,

which are described in the sections that follow.

#### 4.3.1 Optic configuration: power recycled Fabry Perot Michelson

The LIGO detectors are Michelson interferometers where mirrors act as gravitational test masses. An interference pattern is generated by splitting a beam into two pathways of light on the beamsplitter, bouncing the beams back and recombining them, see figure 4.2. This set up was invented by Albert Abraham Michelson to detect a passing GW that will impress a phase modulation on the light in each arm of the Michelson, with a relative phase shift of  $180^\circ$

between the arms. If the light from the two arms doesn't recombine in the photodetector, the distortion in length for one arm caused by a passing GW, we will observe a modified interference pattern.

Each arm includes a resonant optical cavity, known as Fabry Perot, made up of a partially transmitting input mirror and a high reflecting end mirror, see picture 4.2. In these cavities the light bounces back and forth multiple times in the arms, and increases the carrier power and phase shift for a given strain amplitude. The Fabry-Perot cavities, in the LIGO detectors, multiply the signal by a factor of 100 for a 100 Hz GW.

In addition, a partially reflecting mirror is placed between the laser and beamsplitter to implement power recycling [118]. This allows the formation of an optical cavity between the power recycling mirror and the beamsplitter. The laser power stored in the interferometer can be increased by matching the transmission of the recycling mirror to the optical losses in the Michelson, and resonating the recycling cavity. With this configuration, called power recycled Fabry Perot Michelson, the LIGO interferometers increase the power in the arms with respect to a simple Michelson by a factor of  $\sim 8000$ .

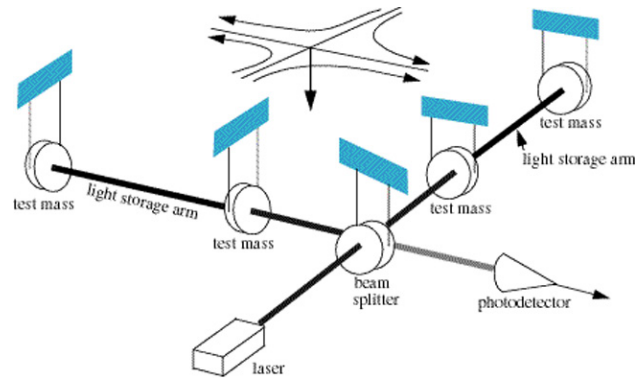


Figure 4.2: A diagram of the LIGO detector. The laser interferometer measures how long the laser light bounces back and forth between the mirrors on the arms before returning to a light detector at the corner. They should theoretically return to the light detector at the same time because the mirror arms are identical distances, unless a passing gravitational wave distorts the local space-time fabric and changes the distance. Source of picture: LIGO's website, <http://www.ligo.org/>.

### 4.3.2 Mirrors

Test masses compose the interferometer optics, they are fused silica substrates with multilayer dielectric coatings, manufactured to have extremely low scatter and low absorption. A technique, known for producing ultralow-loss mirrors [124], [125] using ion-beam sputtering, creates the mirror coatings. For these mirrors only a tiny fraction of the light is absorbed by the atoms in a mirror, this is the thermal motion of the mirror surfaces that produces mechanical losses in the optical coatings.

Scattered light, in addition to being a source of optical loss, is also a complicated noise source. When light, reflected or scattered from a vibrating surface, recombines with the main beam [127], where its phase modulation mimics a gravitational-wave signal. To trap scattered light, various baffles are employed within the vacuum system [127], [128]. About 200 baffles are contained in each 4 Km long beam tube to catch light scattered at small angles from the test masses.

### 4.3.3 Laser

The laser source is a diode that emits 10 W with  $\lambda = 1064nm$  wavelength. Fluctuations in the laser intensity limit the sensitivity of interferometers through: radiation pressure on the mirrors and the presence of a large amount of junk light that isn't of interest to the experiment at the photodiode. The radiation pressure is caused by the impact of photons on the suspended masses and the transfer of a small amount of momentum to the masses that is proportional to the light power. In the second case intensity noise masks the signal at the detector.

The power stabilization of the laser fluctuations is done by directing a sample of the beam to a photodetector, filtering its signal and feeding it back to the power amplifier.

The laser frequency stabilization is done in several steps:

- pre-stabilization
- phase modulation
- Faraday isolator.

The pre-stabilization phase uses the technique called Pound Drever Hall (PDH) technique [129]. The pre-mode cleaner transmits the pre-stabilized beam, filtering out both any light not in the fundamental Gaussian spatial mode and laser noise at frequencies above a few megahertz [131], in this way the beam in output is weakly phase-modulated.

The beam passes into the LIGO vacuum system<sup>1</sup>, after the phase modulation. First, the in-vacuum beam passes into the mode cleaner (MC), that is a vibrationally isolated cavity 12 m long. The mode cleaner stabilizes the beam with additional filtering of laser noise above several kilohertz [193]. The Faraday isolator after the mode cleaner is a reflective 3-mirror telescope that expands the beam and matches it to the arm cavity mode.

### 4.3.4 Sensing and Control

In order to maintain the interferometer at the proper operating point [196], it's essential for the two Fabry Perot arms and power recycling to achieve the LIGO sensitivity design.

In each cavity the round trip length must be maintained to an integer multiple of the laser wavelength so that newly introduced carrier light interferes constructively with light from previous round trips. The light inside the cavities, under these conditions, builds up and the cavities are said to be on resonance.

Besides the monitoring of these three cavity lengths, the Michelson phase must be controlled to remain in operation mode. To stabilize the differential arm length feedback controls to the two end mirrors, to the beamsplitter to control the Michelson phase and to the recycling mirror to monitor the recycling cavity length are used. The coil-magnet actuators applied directly to the mirrors their feedback signals.

To acquire lock is the other function of the control system. That means to

---

<sup>1</sup>All the main interferometer optical components and beam paths are enclosed in the ultra-high vacuum system ( $10^{-8} - 10^{-9}$  Torr) for acoustical isolation and to reduce phase fluctuations from light scattering off residual gas [133]. The long beam tubes are particularly noteworthy components of the LIGO vacuum system. These 1.2 m diameter, 4 km long stainless steel tubes were designed to have low-outgassing so that the required vacuum could be attained by pumping only from the ends of the tubes. This was achieved by special processing of the steel to remove hydrogen, followed by an in situ bakeout of the spiral-welded tubes, for approximately 20 days at 160° C. Description taken from B. P. Abbott et al., Phys. Rev. D 80, 102001 (2009), 0905.0020.

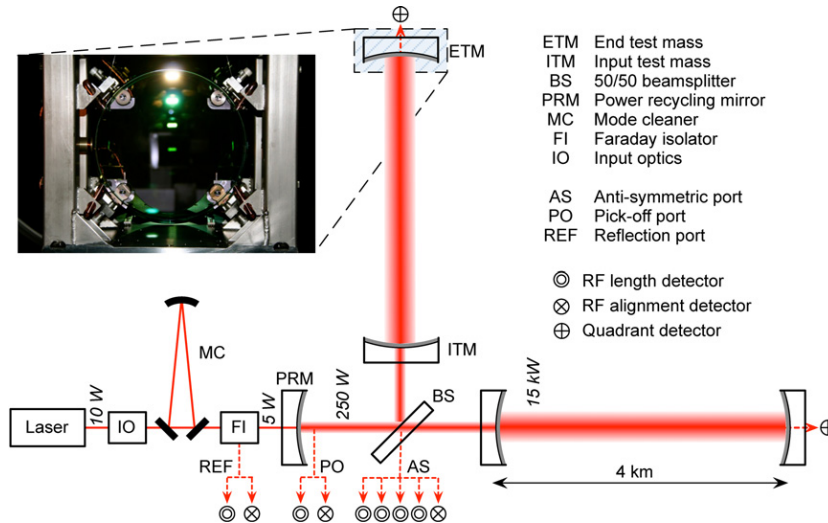


Figure 4.3: Optical and sensing configuration of the LIGO 4 km interferometers. Source of picture: LIGO's website, <http://www.ligo.org/>.

initially stabilize the relative optical positions and to establish the resonance conditions. The basic procedure of the lock acquisition system is to monitor in sequence: the power recycled Michelson, a resonance of one arm cavity and at the end a resonance of the other arm cavity to achieve full power buildup. The key element of this process is the real time, an aspect that we will consider in the last chapter of this work. The interferometers can stay locked for many hours. Usually lock is lost due to instrument malfunction or environmental disturbances.

## 4.4 Instrumental performance

The performance of each interferometer is characterized by an amplitude spectral density of detector noise (the square root of the power spectrum). Typical sensitivity strain noise spectra are shown in figure 4.4.

During the S5 science run, the strain sensitivity of the interferometers improved by up to 40% compared with the beginning of the run.

At the same time, the main obstacle to the detection of gravitational

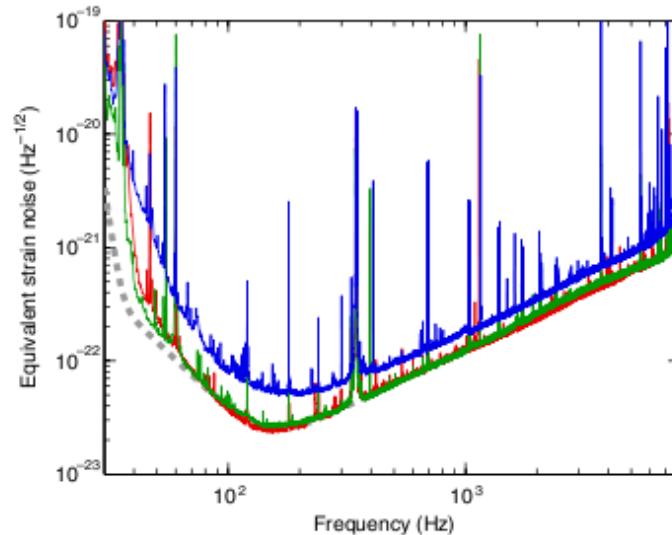


Figure 4.4: Strain sensitivities, expressed as amplitude spectral densities of detector noise converted to equivalent GW strain. The vertical axis denotes the rms strain noise in 1 Hz of bandwidth. Shown are typical high sensitivity spectra for each of the three interferometers (red: H1; blue: H2; green: L1), along with the design goal for the 4 km detectors (dashed gray). The strain noises shown in this figure consist of spectral lines superimposed on a continuous broadband noise spectrum. The majority of the lines are due to power lines (60, 120, 180 Hz, etc), *violin mode* mechanical resonances (350, 700 Hz, etc) and calibration lines (55, 400 and 1100 Hz). Source: B. P. Abbott et al., Phys. Rev. D 80, 102001 (2009), 0905.0020.

waves is the noise that is the sum of several different noise sources:

- the *seismic noise* motions of the earth's surface driven by wind, ocean waves, low level earthquakes and human activity limit the sensitivity at the lowest frequencies. The seismic noise contribution is measured through accelerometers that estimate vibrations and propagations of motion to the test masses. It dominates below approximately 45 Hz.
- Mechanical *thermal noise* accounts for sources of energy dissipation

and limit the detector at intermediate frequencies (between 60 Hz and a few hundred hertz). Thermal noise driven by thermal excitations is the sum of at least two components: one due to the Brownian motion of the mirrors, associated with the dissipations in the mirrors' material; and the other due to the suspension of the mirrors, due to the losses in the wires' material. Mirrors have very low mechanical dissipations and it is difficult to accurately establish the level of broadband thermal noise in situ. The mechanical dissipation for the wires takes place near the ends of the suspension wire, where the wire flexes. It helps to make the wire as thin as possible to limit thermal noise because the elastic energy in the flexing regions depends on the wire radius to the fourth power. For this reason, the pendulums are made with steel wire for its strength; with a diameter of  $300\ \mu\text{m}$ .

- The *shot noise* is the Poisson statistical fluctuation in the number of photons arriving at the photodetector and produces uncertainty about the exact position of the test masses. The shot noise is the dominant noise source above 100 Hz. An increase in power for the laser will decrease the fractional uncertainty, but will introduce another source of noise: the radiation pressure on the mirrors.



# Chapter 5

## Neutrino interactions and detection principles

### 5.1 Introduction

Our knowledge of the Universe mostly comes from the observation of photons. Photons are stable and electrically neutral, easy to detect over a wide energy range and copiously produced. Despite that we cannot directly observe photons coming from dense and hot regions, which form the central engines of stars, active galactic nuclei and other astrophysical energy sources. In order to reach the engines of physical objects and obtain, over a large range of energy, a description of the Universe, we need a probe which is stable, so that it will reach us from distant sources; electrically neutral, so that its trajectory will not be affected by magnetic fields; and weakly interacting so that it will penetrate regions which are opaque to photons. This is the exact description of the neutrino. There exist three flavors of neutrinos: electron neutrinos, muon neutrinos and tau neutrinos and each type has also a corresponding antiparticle, called antineutrino.

Neutrinos are created

- in nuclear reactions<sup>1</sup>;
- in radioactive decay<sup>2</sup>;

---

<sup>1</sup>such as those that take place in the Sun

<sup>2</sup>The beta decay produces the emission of an electron (or positron) from an atom. In the same process is also emitted an electron antineutrino (or an electron neutrino).

- when cosmic rays<sup>3</sup> hit atoms.

Wolfgang Pauli postulated the existence of neutrino in 1930 to explain the conservation of energy, momentum and angular momentum (spin) in the beta decay. In 1933 Enrico Fermi coined the term neutrino developing the theory of beta decay. The journal *Nature* rejected his paper, saying that the theory was '*too remote from reality*'. An Italian journal accepted it, but he decided to switch to experimental physics due to a lack of interest in his theory. More than twenty years later Clyde Cowan and Frederick Reines published confirmation of the neutrino detection and this result was rewarded the Nobel Prize in 1995.

In this chapter we discuss the neutrino interaction processes and the typical event signatures. Emphasis is put on the charged-current interaction channel of the muon neutrino, which is most important for neutrino telescope. The neutrino detection technique based on the optical Cherenkov effect is also explained.

## 5.2 Neutrino interaction

In the Standard Model of elementary particle physics, neutrinos are the most elusive particles interacting only via the weak force. They can escape dense regions and reach the Earth unabsorbed and undeflected. This characteristic offers an excellent chance to use neutrinos as unique cosmic messengers from regions inaccessible to other messengers.

On the other hand, the detection of neutrinos is a huge challenge and requires large volumes detectors. Due to the lack of direct detection techniques based on the weak interaction, neutrinos can only be detected indirectly by measuring their interaction products.

The neutrino interaction cross section, for cosmic neutrino fluxes, is dominated by deep inelastic scattering off the target nucleons. The main channels are thus the charged current deep inelastic scattering

$$\nu_l + N \rightarrow l^- + X \quad (5.1)$$

$$\bar{\nu}_l + N \rightarrow l^+ + X \quad (5.2)$$

---

<sup>3</sup>They are composed of energetic charged subatomic particles, originating in outer space. Cosmic rays produce secondary particles that arrive in the Earth's surface and atmosphere.

where  $l = e, \mu, \tau$  and an (anti-)neutrino (of arbitrary flavour) interacts via the exchange of a  $W^\pm$  boson with a nucleon  $N$  to produce a hadronic cascade  $X$  and an (anti-)lepton (of corresponding flavour). The neutral current reaction is

$$\nu + N \rightarrow \nu + X \quad (5.3)$$

where a neutrino exchanges a  $Z$  boson with the target nucleon <sup>4</sup>.

As shown through the Feynman diagrams, figure 5.1, the topologies of

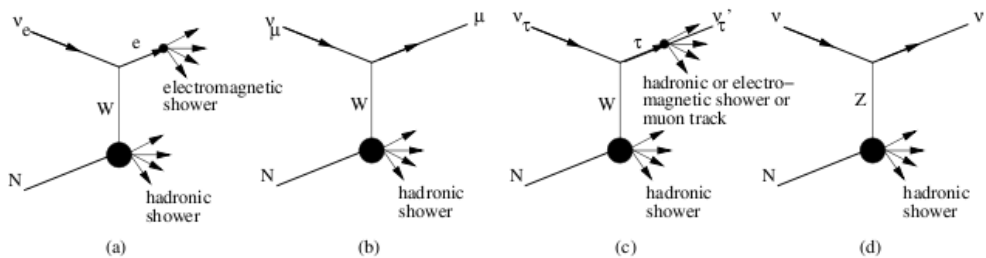


Figure 5.1: This cartoon shows the Feynman diagrams for the charged current reactions for the three different flavours (a) (b) (c) and the neutral current process (d). Source of image: 'Quarks and Leptons: An Introductory Course in Modern Particle Physics', F. Halzen and A. D. Martin

charged current channels for the different flavours are not the same. An electromagnetic shower is produced from the electron neutrino  $\nu_e$  interaction, while a long range muon track is obtained from the muon neutrino  $\nu_\mu$  channel. The tau neutrino  $\nu_\tau$  interactions can produce two distinct showers.

### 5.3 Discovery of the Cherenkov emission

Cherenkov photons are emitted when charged particles travel in a transparent medium with the phase velocity greater than the speed of light in that medium [141]. The early observations of Cherenkov light were made in the same period of optics and luminescence studies. In 1926 Mallet was the first to study the phenomenon. He saw the bluish-white light emitted from a wide

<sup>4</sup>In this case only the hadronic cascade originating from the interaction vertex can be observed.

variety of transparent bodies placed close to a radioactive source. He noticed also the absence of line and band structure in the spectrum. However, he didn't pursue his work, and the subject was considered again from Cherenkov only in 1934. Cherenkov started a huge series of experiments and he was the first to characterize rigorously the process. For this reason he was rewarded the Nobel Prize in 1958.

## 5.4 Description of the Cherenkov effect

It is appropriate at this point to explain the basic principle of the Cherenkov effect. We like to report the clear exposition of the Cherenkov effect from the book, 'Cherenkov radiation and its application', J. V. Jelley 1998.

*"Suppose an electron to be moving relatively slowly through a piece of glass*

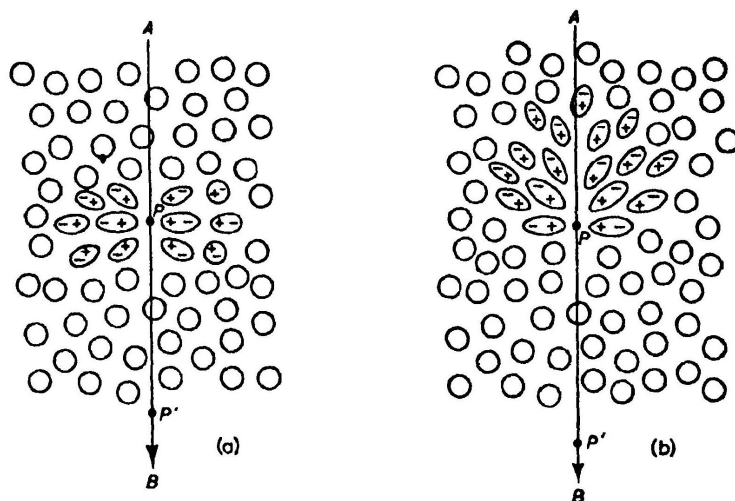


Figure 5.2: The polarization set up in a dielectric by the passage of a charged particle. (a) At low velocity. (b) At high velocity

*or other transparent medium. Fig. 5.2 (a) shows a section of the glass in the vicinity of the track  $\overline{AB}$  of this electron, the circles representing the individual atoms composing the glass. Normally these will be roughly spherical in shape, and undistorted. However, in the region close to the passing electron, which at a particular instant in time is for instance at the point  $P$ , the electric field*

of the particle distorts the atoms so that the negative charges of the electrons are displaced to one side of the heavier positive charges of the nuclei of these atoms. The medium thus becomes polarized about the point  $P$ . When now the electron moves on to another point, say  $P'$ , the elongated atoms around  $P$  return to their normal shape.

While the atoms are distorted they behave like elementary dipoles, with the negative poles pointing away from the track if the passing particle is a negative electron, or vice versa for a positron or proton. Thus, as the particle passes through the medium, each elemental region of the glass along the track will in turn receive a very brief electromagnetic pulse. Owing to the complete symmetry of the polarization field surrounding the electron, there will be no resultant field at large distances and therefore no radiation. There is symmetry both in azimuth and along the axis, in this case. If however the electron is moving fast, that is at a speed comparable to that of light in the medium, the picture is quite different (see Fig. 5.2 b). In this case the polarization field is no longer completely symmetrical. In the azimuthal plane, symmetry is preserved, but along the axis there is a resultant dipole field which will be apparent even at large distances from the track of the electron. Such a field will be momentarily set up by the electron at each element along the track in turn, each element then radiating a brief electromagnetic pulse. The radiation will be spread over a band of frequencies corresponding to the various Fourier components of this pulse.

In the general case, the radiated wavelets from all parts of the track interfere destructively so that, at a distant point, the resultant field intensity is still zero. However, if the velocity of the particle is higher than the phase velocity of the light in the medium, it is possible for the wavelets from all portions of the track to be in phase with one another so that, at a distant point of observation, there is now a resultant field.

It will be understood from the Huygens construction shown in Fig. 5.3 only observed at a particular angle  $\vartheta$  with respect to the track of the particle, namely that angle at which the wavelets from arbitrary points such as  $P_1$ ,  $P_2$  and  $P_3$  on the track  $\overline{AB}$  are coherent and combine to form a plane wave front  $\overline{BC}$ . This coherence takes place when the particle traverses  $\overline{AB}$  in the same time that the light travels from  $A$  to  $C$ . If the velocity of the particle is  $\beta c$  where  $c$  is the velocity of light in vacuo and  $n$  the refractive index of the medium, in a time  $\Delta T$  the particle will travel a distance  $\overline{AB} = \beta c \Delta T$ , and

the light a distance  $\overline{AC} = \Delta T \frac{c}{n}$ . From this we obtain:

$$\cos \vartheta = \frac{1}{\beta n} \tag{5.4}$$

which is known as the *Cherenkov relation*. It is seen that:

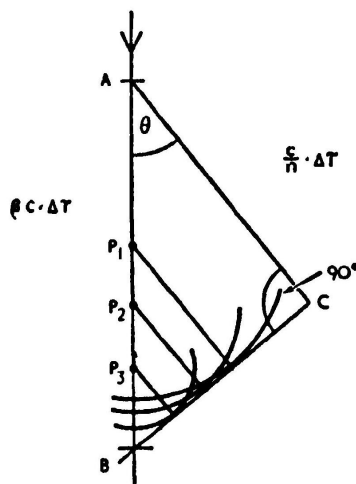


Figure 5.3: Huygens construction to illustrate coherence

1. for a medium of given refractive index  $n$ , there is a threshold velocity  $\beta_{min} = \frac{1}{n}$ , below which no radiation takes place. At this critical velocity the direction of radiation coincides with that of the particle;
2. for an ultra relativistic particle, for which  $\beta = 1$ , there is a maximum angle of emission, given by  $\vartheta_{max} = \frac{1}{\cos(\frac{1}{n})}$ ;
3. the radiation occurs mainly in the visible and near-visible regions of the spectrum: for which  $n > 1$ .

The figure 5.3 has been drawn in one plane only. There is complete symmetry about the axis of the particle. The light originating from each element of track is propagated along the surface of a cone whose apex is at this element, whose axis coincides with the track, and whose semi vertical angle is the angle  $\vartheta$ . There are two further conditions to be fulfilled to achieve coherence:

- *the length  $l$  of the track of the particle in the medium shall be large compared with the wavelength  $\lambda$  of the radiation in question, otherwise diffraction effects will become dominant and light distributed over an angle  $\delta\vartheta \sim \frac{\lambda}{l \sin \vartheta}$ , instead of appearing at only one angle  $\vartheta$  as in eq 5.4;*
- *the velocity of the particle must be constant during its passage through the medium, or, to be more specific, the differences in the times for the particle to traverse successive distances  $\lambda$  shall be small compared with the period  $\frac{\lambda}{c}$  of the emitted wave.”*

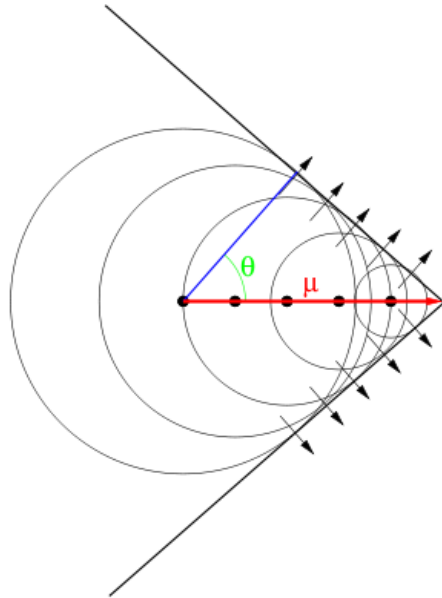


Figure 5.4: Illustration of the Cherenkov effect. Local distortions of the charge configuration in the medium lead to the emission of electromagnetic waves. The individual contributions along the track (red line) interfere constructively on their envelope which forms a cone. Cherenkov photons (blue line) are emitted under a characteristic angle  $\theta$ .

Equation 5.4 for sea water with refractive index  $n \approx 1.35$  and for highly relativistic particles ( $\beta \sim 1$ ) yields a Cherenkov angle approaches  $\theta = 42^\circ$ .

The Cherenkov radiation intensity is proportional to the frequency of the emitted photon, when the refractive index is almost constant. The number of photons emitted from a charged particle per path length can be determined as

$$\frac{d^2N}{dx d\lambda} = \frac{2\pi\alpha}{\lambda^2} \left( 1 - \frac{1}{n^2\beta^2} \right) \quad (5.5)$$

where  $\lambda$  is the Cherenkov photon wavelength and  $\alpha$  is the fine structure constant. Considering the wavelength range relevant for water based neutrino telescopes of about 300nm to 600 nm, the number of photons per track length is approximately

$$\frac{dN}{dx} = 34000 /m \quad (5.6)$$

## 5.5 Muon propagation

The detection principle of a neutrino telescope relies on the observation of the Cherenkov light produced by muons which are created in the charged-current interactions of muon-neutrinos, see relations 5.1-5.2, in the medium surrounding the apparatus. Such muons preserve the information on the direction of the incident neutrino and can traverse several kilometers of sea water. By measuring the arrival time of the Cherenkov light, we can reconstruct the direction of the muon and track back the neutrino arrival direction. In the charged current channel the initial neutrino and the outgoing muon are almost collinear. Hence, the angle between the muon track and the parent neutrino is very small. A parameterization of this angle can be written as

$$\langle \theta_{\mu\nu} \rangle = \frac{0.7^\circ}{\sqrt{E_\mu [TeV]}} \quad (5.7)$$

The original direction and also the sky position of the source that emitted the neutrino can be obtained with a good precision by measuring the direction of the muon.

In order to correlate the measured muon spectrum with the original neutrino spectrum, we need to determine the energy losses from the muons and the resolution of the detector. A muon can interact with matter through several processes [234].

- A muon can radiate a photon in the nuclear electric field of an atom (Bremsstrahlung process).

- 
- It can create an electron-positron pair, the process is known as pair production.
  - Through radiative processes, a muon can interact with atoms.
  - By the exchange of a (virtual) photon a muon can interact with an atomic nucleus.
  - A muon can transfer a small amount of energy passing through matter, ionizing or exciting the surrounding atoms.

The energy of the muons sets the relative importance of these processes, see figure 5.5.

Below approximately  $1TeV$ , the energy loss is dominated by the ionization process. Above  $1TeV$ , radiative processes dominate the total energy loss. The radiative processes have an approximately linear dependence on the energy of the muon and the energy loss through ionization is approximately constant, as shown in the plot 5.5. Due to the stochastic nature of the radiative processes, the actual energy loss shows large fluctuations.

Hard energy losses are more likely to happen with Bremsstrahlung showers. In fact, if one expresses the cross sections of the radiative processes as function of the fractional energy loss  $\nu$ . While the cross section for Bremsstrahlung scales with  $1/\nu$ , for pair-production the section scaling between  $\nu^{-2}$  and  $\nu^{-3}$ .

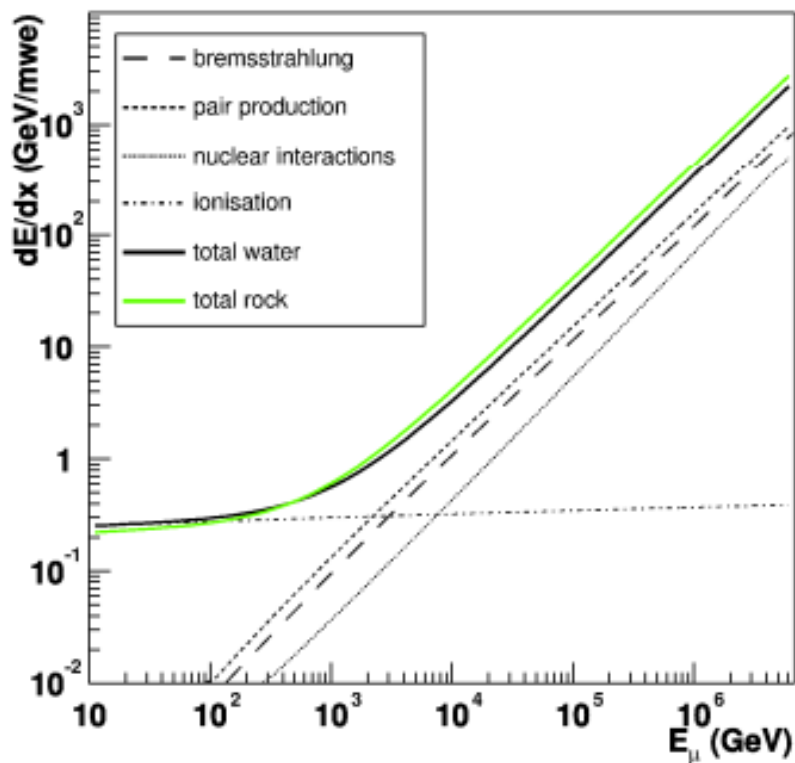


Figure 5.5: Muon energy loss in GeV per meter of water (solid black line) and rock (solid green line). The separate contributions to the energy loss in water are indicated by the other line types. The short dashed line indicates pair production, the long dashed line Bremsstrahlung, the dotted line nuclear interactions and the dash dotted line ionization losses. Courtesy of the ANTARES Collaboration.

# Chapter 6

## ANTARES Neutrino Telescope

### 6.1 Introduction

In 1960 Markov proposed for the first time to use large volumes of sea/lake water or antartic ice to build neutrino telescopes [232]. The revolutionary idea is to set in a transparent and deep medium like a natural basing ice or water, a matrix of light detectors. Such medium

- shields the detector from cosmic rays and sunlight;
- doesn't interfere with the propagation of Cherenkov light produced by relativistic particles in neutrino interaction;
- constitutes a huge volume of free target for neutrino interactions.

This chapter introduces the ANTARES neutrino telescope, one of such detectors.

### 6.2 The ANTARES project

The ANTARES detector (Astronomy with a Neutrino Telescope and Abyss environmental RESearch) is currently the unique deep sea high energy neutrino telescope, and is operating in the Northern hemisphere. As a European effort, the ANTARES collaboration was formed in 1996 with the objective of designing and building a large underwater Cherenkov neutrino telescope in the Mediterranean sea. The first detection line was installed and connected in early 2006. Since then data has been taken continuously with a

growing detector configuration. The completion of the works occurred at the end of May 2008 with the connection of the last two strings (detection units). ANTARES is the largest instrument in the Northern hemisphere, and it represents the first step for the next generation KM3NeT detector [231], imagined for construction in the Mediterranean sea.

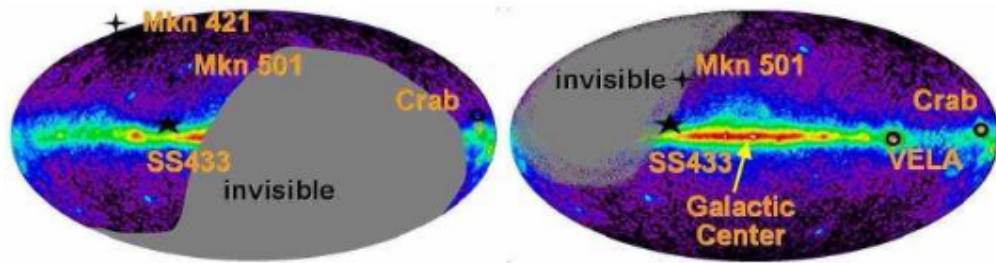


Figure 6.1: The pictures indicate the comparison between the field of view of the neutrino telescope at the South Pole, IceCube (left), and ANTARES (right), superimposed to the gamma-ray sky seen from H.E.S.S. . The gray regions are invisible portions of the sky for the detectors. The position of ANTARES in the Northern hemisphere allows a direct view on the galactic center for 67% of the observation time. A few neutrino source candidates are shown as well. Source: U. Katz, 'KM3NeT: Towards a  $km^3$  Mediterranean Neutrino Telescope' 2006.

Unlike conventional telescopes, ANTARES looks downward, using the Earth to act as a shield, or filter, against all particles except neutrinos. A small fraction of the neutrinos passing upwards through the Earth will interact with the rock in the seabed to produce charged particles called muons, moving at nearly the speed of light. As these muons move through the water, they produce a flash of light called Cherenkov radiation. Its detection allows the determination of the muon trajectory. This detection technique requires discriminating upward travelling muons against the much higher flux of downward atmospheric muons (see figure 6.9). To simplify the discrimination, the detector is installed in a deep site where a layer of water would shield it.

The telescope covers an area of about  $0.1 \text{ km}^2$  in the Mediterranean sea bed,

at a depth of 2475 m, 40 km off the coast of Toulon, France, at  $42^{\circ}50'N$ ,  $6^{\circ}10'E$ , as indicated in Figure 6.2. The installation of ANTARES in the North hemisphere enables an annual sky coverage of  $3.5\pi$  sr. It shares a common field of view of  $1.5\pi$  sr with IceCube, the neutrino telescope at the South Pole.

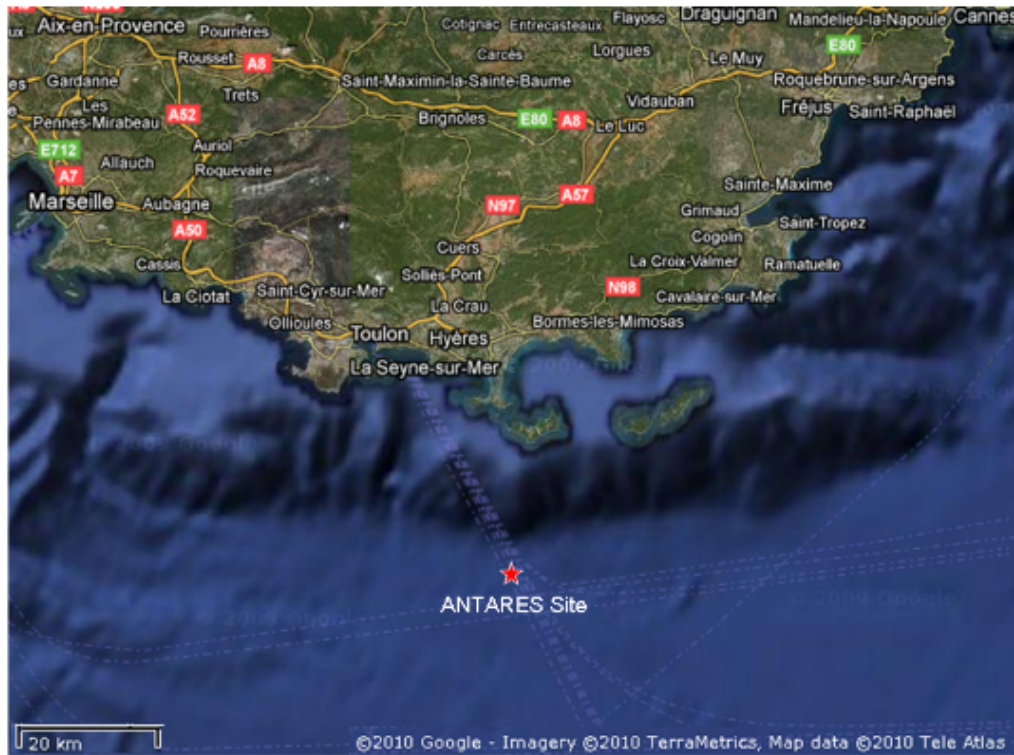


Figure 6.2: The geographical position of ANTARES detector in the Mediterranean sea is  $42^{\circ}50'N$  and  $6^{\circ}10'E$  at a depth of 2475 meters, approximately 40 km off Toulon at the French coast. The detector has an effective area of  $0.1 \text{ km}^2$ . Satellite picture taken from Google Maps.

### 6.3 Layout of the ANTARES detector

The detector is conceived as a three-dimensional array of about 900 photomultiplier tubes (PMTs), hosted in pressure resistant glass spheres, called

optical modules (OMs). In its full configuration, it is composed of 12 detection lines or stings, each line is an electro-optical mechanical cable (EMC) which measures 450 m. Each string comprises up to 25 triplets of PMTs, storeys, regularly distributed with a spacing of 14.5 m on the EMC, see picture 6.5. At a height of 100 m above the sea floor is located the first storey of each line. The storey holds the sensors and the electronics which are connected to the bottom string socket (BSS) for readout and power supply. On each of the storeys there are three optical modules, they are mounted radially looking downwards at an angle of  $45^\circ$  with respect to the horizontal, see figures 6.6, 6.7. The 12 lines formed an octagonal structure, see Figure 6.4, and the interline spacing is of order of 50 m. The detector layout is shown in Figure 6.3.

The three-dimensional grid of photomultiplier tubes is used to measure the arrival time and position of Cherenkov photons induced by the passage of relativistic charged particles through the sea water. This information, together with the characteristic emission angle of the light (about 42 degrees), is used to determine the direction of the muon and hence infer that of the incident neutrino.

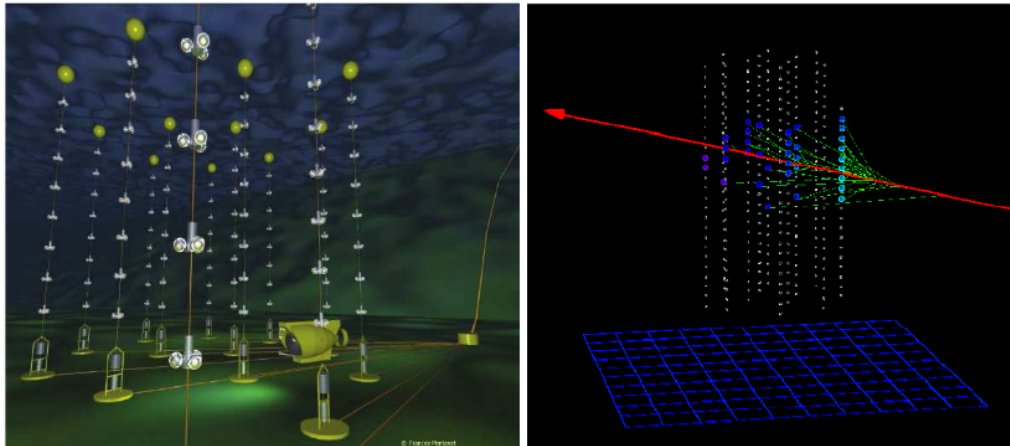


Figure 6.3: (Left) Artistic view of the detector in which only 8 out of 25 storeys per line are shown. (Right) Graphic reconstruction of a real event of neutrino, in which the muon track is shown in red and the Cherenkov photon trajectories are in green. Courtesy of the ANTARES Collaboration.

## 6.4 Detector status

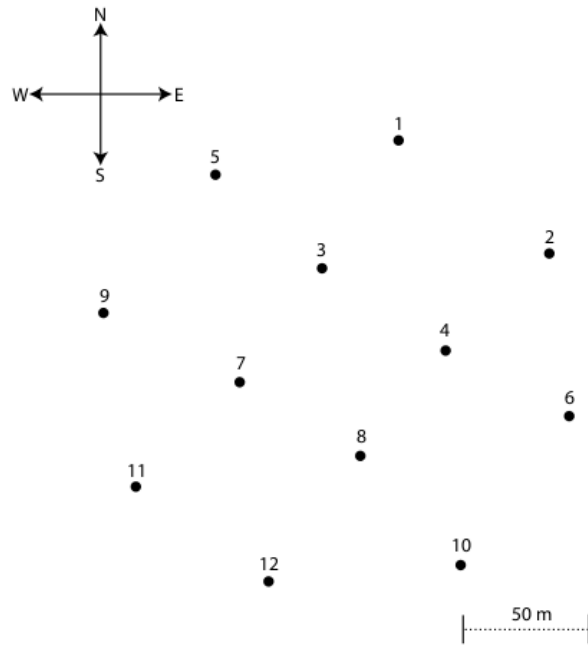


Figure 6.4: Floor layout of lines in the ANTARES configuration. Each detection unit is identified by its number. Courtesy of the ANTARES Collaboration.

The installation and deployment of the three dimensional array of photon detectors took two years. The first detection line was installed and connected on March 2<sup>nd</sup> 2006; the second line was put in operation on September 21<sup>st</sup> September 2006, and three more lines (strings 3-5) were connected by the end of 2007, so that a total of 5 lines were taking data in 2007. At this point the ANTARES had exceeded the Baikal<sup>1</sup> telescope in volume to become the largest neutrino telescope on the Northern Hemisphere. Five addi-

---

<sup>1</sup>Baikal is an underwater neutrino telescope located in the Siberian lake Baikal at a depth of approximately 1 km.

tional lines, together with an instrumentation line (containing an ensemble of oceanographic sensors dedicated to the measurement of environmental parameters), were connected on December 7<sup>th</sup> 2007. The telescope reached its nominal configuration, with 12 lines immersed and taking data, on May 28<sup>th</sup> 2008. Detector units that displayed problems during operation have been removed, repaired and replaced. Between June 25<sup>th</sup> and September 5<sup>th</sup> 2008, the detector was out of operation for a fault in the main electro-optical cable.

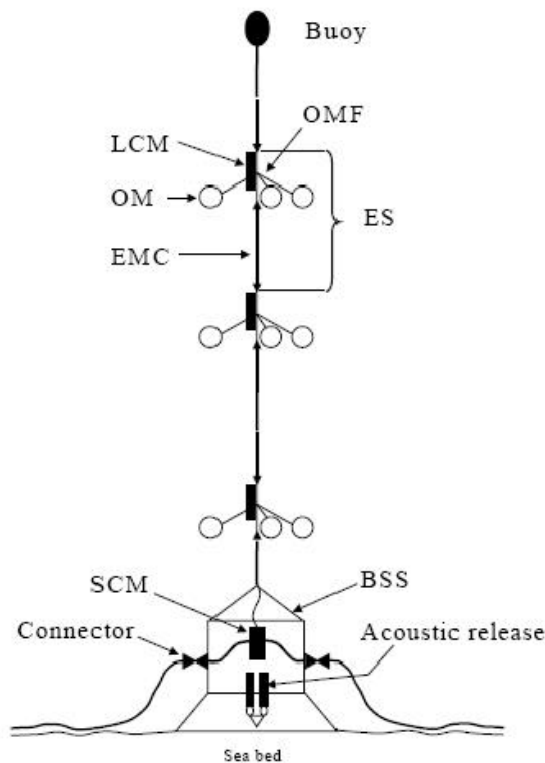


Figure 6.5: Profile of a single ANTARES string. From the top to the bottom we can see: the optical module frame (OMF); local control module (LCM); optical module (OM); electro-optical mechanical cable (EMC). The string control module (SCM); bottom string socket (BSS). Courtesy of the ANTARES Collaboration. Courtesy of the ANTARES Collaboration.

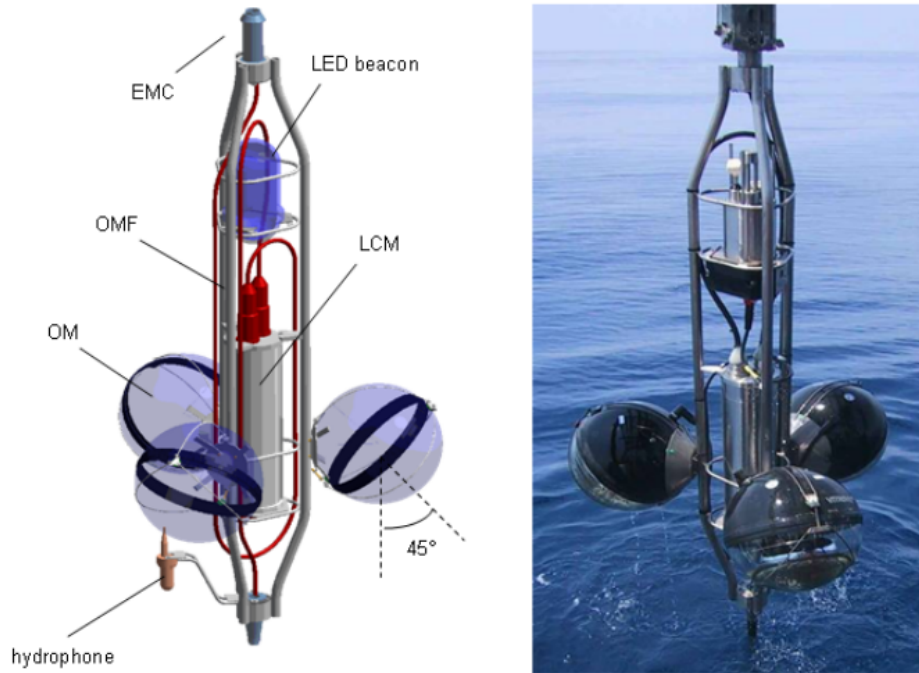


Figure 6.6: Storey with three Optical Modules

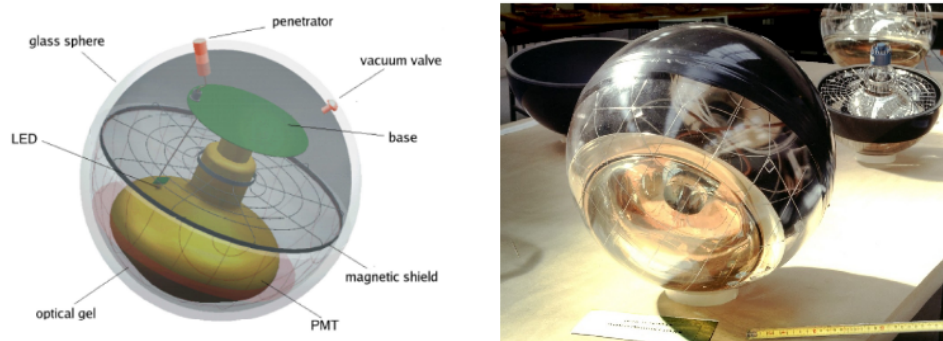


Figure 6.7: Schematical representation of an optical module (left), the main component are indicated. Picture of an optical module (right).

## 6.5 Sources of background for ANTARES telescope

### 6.5.1 Atmospheric neutrinos and muons

The search of cosmic neutrinos is affected by spurious background events. The noise level is composed of atmospheric muons and neutrinos. These atmospheric particles show the same signature of cosmic neutrinos, see picture 6.8, and they are produced in the interactions of charged cosmic rays in the Earth atmosphere.

The interactions in the atmosphere between cosmic rays and air molecules and air showers produce charged mesons<sup>2</sup> that are likely to decay and produce atmospheric muons and neutrinos. Such neutrinos can traverse the Earth and interact close to the detector via charged currents to produce muons. Despite the detector is located deep underwater, the exposure to the flux of atmospheric muons isn't completely negligible. Atmospheric muons

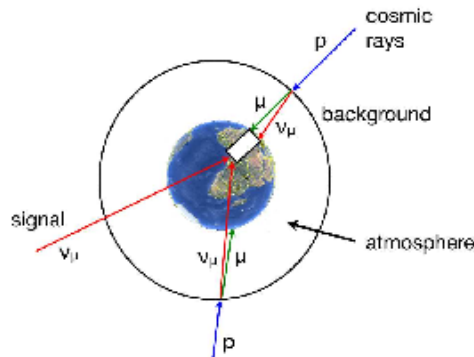


Figure 6.8: Schematic view of different sources of muons that can be detected in a deep sea neutrino telescope: atmospheric muons as well as cosmic and atmospheric neutrino induced muons. These events have the same experimental signature in the detector. Courtesy of the ANTARES Collaboration.

<sup>2</sup>hadronic subatomic particles, in which one quark and one antiquark are bounded together by strong interaction.

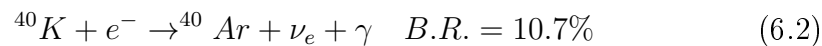
can reach the detector only from above and they can therefore be differentiated from up-going neutrino events, even though a down-going muon can be wrongly reconstructed as up-going.

To differentiate between atmospheric and cosmic neutrinos is a much harder task. In fact, atmospheric neutrinos are considered, to some extent, an irreducible background. The atmospheric neutrino data can be also used to optimize the track reconstruction for astrophysical neutrino events. In general, atmospheric neutrinos and muons are a valuable tool for calibration and reconstruction fine tuning.

The flux of muons produced by atmospheric muons and atmospheric neutrinos is shown in figure 6.9. One can see that atmospheric muons reaching the detector are only propagating as down-going through the medium surrounding the telescope. On the contrary, atmospheric neutrinos have nearly isotropic arrival directions, for this reason they are considered as an irreducible background. The flux of atmospheric neutrinos is enhanced due to the increased path length in the upper atmosphere, corresponding to the horizontal direction  $\cos\theta = 0$ , which favors mesons decays and neutrino production.

### 6.5.2 $^{40}K$ decay and bioluminescence light

Further background light is produced by the decay of radioactive potassium ( $^{40}K$ ) and by bioluminescence, see figure 6.11. The background light from radioactive decays is constant in time.



These are the two channels in which the  $^{40}K$  can decay, where the branching rate (B.R.) denotes which channel is predominant. The electron, produced in the main channel of the potassium-40 decay, emits about 43 Cherenkov-photons [235] on average.

The rate of bioluminescence light produced by micro organisms is not constant in time. It depends on weather and environmental conditions on the sea surface and deep. Fortunately, these single processes produce uncorrelated photon signals in individual photomultiplier, hence they can be removed. Larger multicellular organisms like fluorescent squids, crustaceans or fish are more annoying, because they generate localized and aperiodic optical bursts.

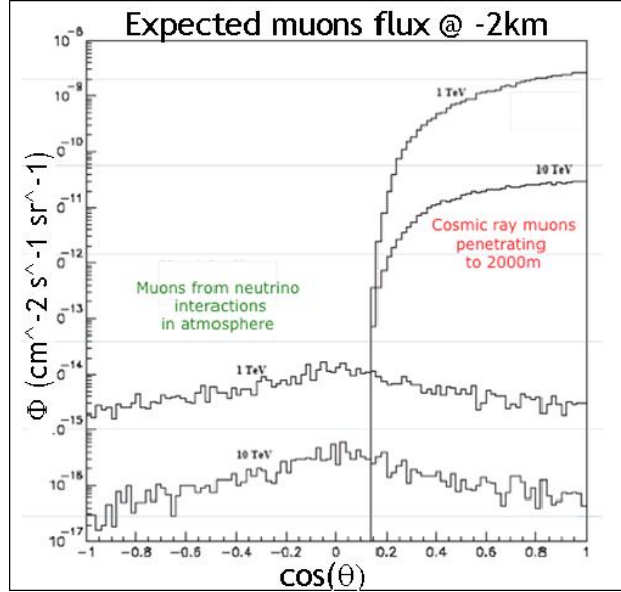


Figure 6.9: The plots shows the flux of atmospheric muons and of atmospheric neutrino induced muons as a function of the cosine of the zenith angle.  $\cos\theta = 1$  indicates that the muon is propagating downward through the detector, while  $\cos\theta = -1$  indicates that the neutrino induced muon is seen as upward-going through the telescope.  $\cos\theta = 0$  is the horizontal direction.

## 6.6 Position calibration

The ANTARES lines are not rigid in the deep sea environmental conditions. In fact, the strings are subject to sea currents that make them sway and torque.

It is fundamental for the reconstruction to determine the relative position of the photomultipliers, therefore two independent systems are in place. One is the acoustic positioning system to measure the travel times of acoustic pulses. It's also possible to make a three-dimensional reconstruction of the elements in the detector. The telescope is equipped with sound velocity meters and with independent pressure, temperature and salinity measuring devices because the speed of sound is dependent on pressure, temperature and salinity. The second system consists of biaxial tilt meters and compasses to

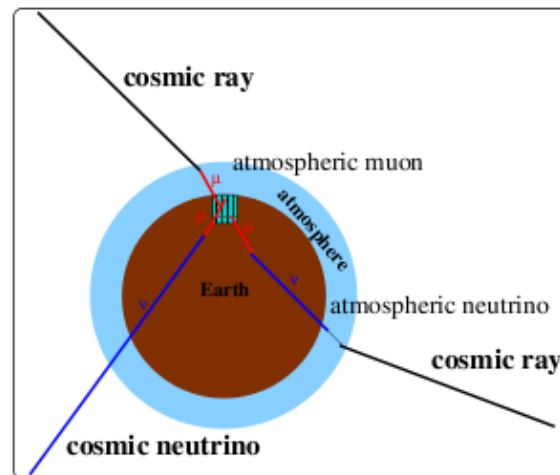


Figure 6.10: Physics signals in ANTARES.

determine pitch, roll and position of each OM within 10-20 cm for each local control module. Autonomous transponders, which have a known position, measure the absolute orientation of the detector. All these measurements are fundamental for the correct calibration of the detector.

## 6.7 High Energy Neutrino selection strategy

The observation of high energy neutrinos from non terrestrial sources is the main goal of the ANTARES neutrino telescope. This detector observes Cherenkov photons produced by the passage of relativistic charged particles produced in the detector or in its surrounding material. By measuring the arrival times and positions of these photons, the flight direction of these particles, that is nearly collinear with the incident neutrino direction, can be reconstructed. It's necessary to distinguish between neutrinos from astrophysical sources and background which originate in the Earth's atmosphere. In the following, we will explain the selection strategy to identify a set of astrophysical neutrino trigger candidates used in the present analysis.

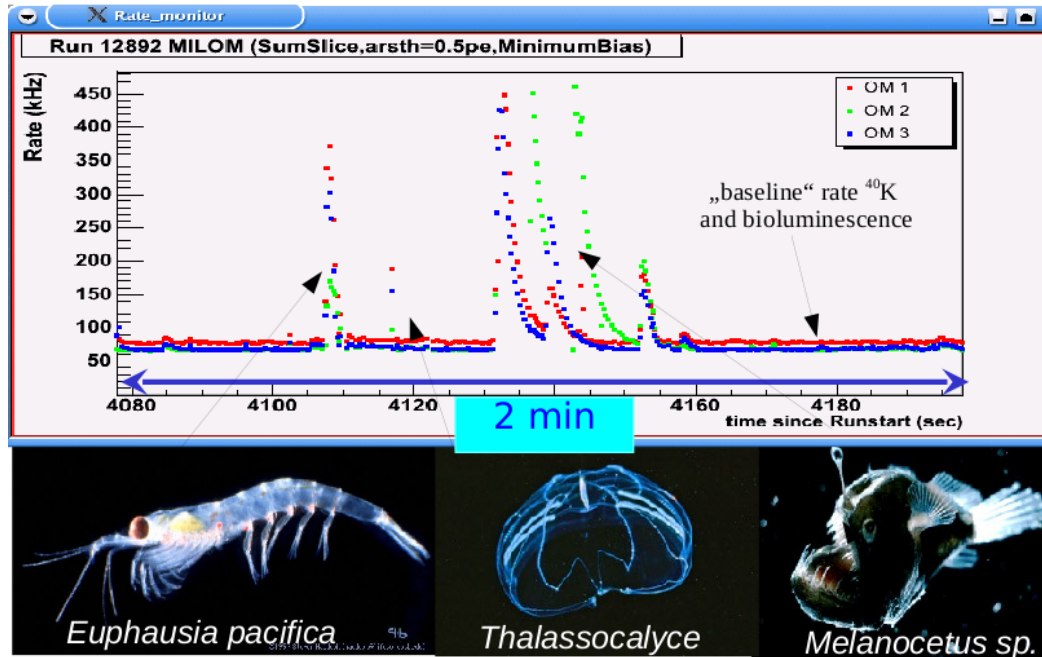


Figure 6.11: Optical background rate measured by three PMTs on the same storey of the ANTARES detector, (May 2007). Courtesy of the ANTARES Collaboration.

### 6.7.1 Assumptions and hits selection

The method considers only information of time and geometry, with the following approximations:

- the actual geometry of each storey is ignored, in fact only a single optical module, instead of three, is considered;
- each string is associated to a vertical line, without any considerations for the distortions due to sea currents;
- the muon track is a straight line, hence multiple scattering are ignored.

Except for the case in which the muon track is parallel to the detector lines, the selection strategy determines the point of closest approach of the muon track to the detector string which is where most of the Cherenkov photons

are expected.

The ANTARES trigger generation is composed of multiple steps in order to consider hits due to Cherenkov light and avoid random hits from the optical background or scattered late hits.

- The first level, so called *L0* hit, is an energy threshold of 0.5 pe (photoelectron) applied on each photomultiplier;
- the second step, *L1* hit, takes into account time coincidences hits, they have to occur in the same storey within 20 ns, and/or hits with energy bigger than 3 pe or 10 pe;
- the last stage, *L2* or *3N* hit, estimates features of L1 hits and seeks relations in time and space between each couple of 5 L1 hits in 2.2  $\mu s$ , that corresponds to the muon transit across the detector, using equations [250] [251]:

$$\Delta T_{ij} \leq \frac{d_{ij}}{c/n} + 20ns \quad (6.3)$$

where  $\Delta T_{ij}$  is the time gap between  $i^{th}$  and  $j^{th}$  hits coming from adjacent or next-to-adjacent storeys,  $d_{ij}$  is the space distance between them,  $n$  is the water refraction index and  $c$  is the speed of light.

More than 5 hits are needed for the reconstruction. Every space-time point of the track  $\vec{p}(t)$ , can be described as

$$\vec{p}(t) = \vec{q} + c(t - t_0)\hat{u} \quad (6.4)$$

The muon moves in the direction  $\hat{u}$  passing through the point  $\vec{q}$  at time  $t_0$  ( $\vec{q} = \vec{p}(t_0)$ ). A total number of 5 parameters defines completely the track: three values to fix  $\vec{q}$  for a given time and two angles to define  $\hat{u}$ :

$$\vec{u} = [\cos \theta \cos \phi, \cos \theta \sin \phi, \sin \theta] \quad (6.5)$$

where  $\theta$  is the elevation angle and  $\phi$  the azimuth angle. For an extensive description of the method and the derivation of these parameters see APPENDIX B.

The muon track reconstruction algorithm used for our period of interest is the BBFit package [236] based on a  $\chi^2$  minimization approach. The software

considers a set of photomultiplier hits for each line and estimates the best set of track parameters at a given time,  $t_0$ , position  $(x, y, z)$  and direction  $(\theta, \phi)$ . First of all, the algorithm takes L1 hits as a selection criteria, then it requires coincidence of 2 L1 hits in two adjacent storeys within 80 ns or 160 ns in two next to adjacent storeys. The obtained hits, called *T3* hits [260], are used for the fit procedure. The quality of the reconstruction is calculated through  $\chi^2$

$$\chi^2 = \frac{Q}{DOF} \quad (6.6)$$

where

$$Q = \sum_{i=1}^{N_{hit}} \left[ \frac{\Delta t^2}{\sigma_i^2} + \frac{q(q_i, q_0)d(d_\gamma)}{\langle q \rangle d_0} \right] \quad (6.7)$$

where  $d_\gamma$  is the photon travel path ( $d_0 = 50$  m),  $q_i$  is the hit amplitude ( $q_0 = 10$  pe),  $\sigma_i$  the timing error that is set to 10 ns for  $q_i > 2.5$  pe and to 20 ns otherwise. In eq 6.7, the first term is a time residual, it exploits the difference time  $\Delta t = (t_\gamma - t_i)$  between the hit time  $t_i$  and the expected arrival time of the photons  $t_\gamma$  from the muon track. The second term takes into account the loss of energy of muons by ionization.

The reconstruction package also calculates the so called mirror solutions for events reconstructed with 2 lines: a muon that impinges the geometrical plane passing through the two lines with an angle of incidence ( $\alpha$ , angle between the normal to the plane and the muon track) is indistinguishable from a muon that impinges with the mirror angle  $\phi - \alpha$  because the two cases generate the same hits at the same time. The mirror track constitutes an equiprobable muon track, and as such it is accounted for in the analysis, for more details see APPENDIX B, or [251].

### 6.7.2 Monte Carlo sample

Different samples of Monte Carlo (MC) neutrinos and atmospheric muons were generated and used for comparisons with data. Such simulations are useful to reproduce the behavior of background events for neutrino telescopes, in this way it's possible to discard noise events from the data. These fake events were simulated through the ANTARES detector simulation software called CORSIKA (COsmic Ray SIMulation for KAscade) [253]. A set of optimized parameters is selected to be used as input for the MC software. They

mimic the geometrical characteristics of the detector and a realistic description of the marine environment. In the simulation the interaction processes, energy loss through water and Cherenkov light generation are also included. Cosmic rays interact with the Earth's atmosphere and produce energetic muons, called atmospheric muons. Even though part of these muons is stopped by the Earth, an important part remains in the selected sample and they can be misreconstructed as up-going event. To study these misreconstructed muons a MC signal from down going atmospheric muons is simulated with CORSIKA <sup>3</sup>.

This simulation program allows the interaction and propagation of high energy cosmic rays in the Earth atmosphere and transport of high energy muons in underwater environments. In addition, one can choose among different models, the description of extensive air shower formation and the composition of primary cosmic ray. In the present case, more than  $10^{10}$  showers induced by Proton, Helium, Carbon, Magnesium and Fe nuclei were simulated in an energy range  $1 - 10^5$  TeV/nucleon and a polar angle  $\theta$  between  $0 - 85$  degree.

The other source of background in the detector is the presence of atmospheric neutrinos. For this reason, a sample of up-going and down-going neutrinos is simulated using GENHEN program [258]. This software generates simulation of neutrino interaction and the propagation of the induced muons to the simulated detector<sup>4</sup>. Upward going atmospheric neutrinos are an unavoidable background for cosmic neutrinos and can be discarded using only their respective energy.

### 6.7.3 Angular error

The distribution of the space angle  $x$  between the true neutrino arrival direction and the reconstructed muon track can be described accurately by a

---

<sup>3</sup>and weighted with the Battistoni parameterization [255] of the primary cosmic ray flux

<sup>4</sup>these neutrinos are generated in an energy range of  $10 - 10^7$  GeV and weighted according to the Bartol flux, see equation 2 [259], for the atmospheric neutrinos.

$$\phi(E_k) = K \left( E_k + b \exp[-c\sqrt{E_k}] \right)^{-\gamma} \quad (6.8)$$

where  $E_k$  is the kinetic energy per nucleon, the values of the parameters  $K$ ,  $b$ ,  $c$  and  $\gamma$  are given here [259].

log-normal distribution:

$$f(x) = \frac{1}{\sqrt{2}} \frac{e^{((\ln((x-\theta)/m))^2/2\sigma^2)}}{(x-\theta)\sigma} \quad (6.9)$$

where  $x \geq \theta$  and  $\sigma \geq 0$ .  $\theta$  is the location parameter,  $\sigma$  the shape parameter and  $m$  the scale parameter.

This distribution depends on the energy associated to the track (estimated through the number of photons detected) and its declination. This parameterization is used during the GW search to compute the significance of a hypothetical signal for the scanned directions inside the angular search window centered around the reconstructed neutrino arrival direction, see next chapter. Figure 6.12 shows the distribution of the space angle for a sample of MC neutrinos with an  $E^{-2}$  spectrum, together with the best-fit parameterization and the 50<sup>th</sup> and 90<sup>th</sup> percentiles of the distribution.

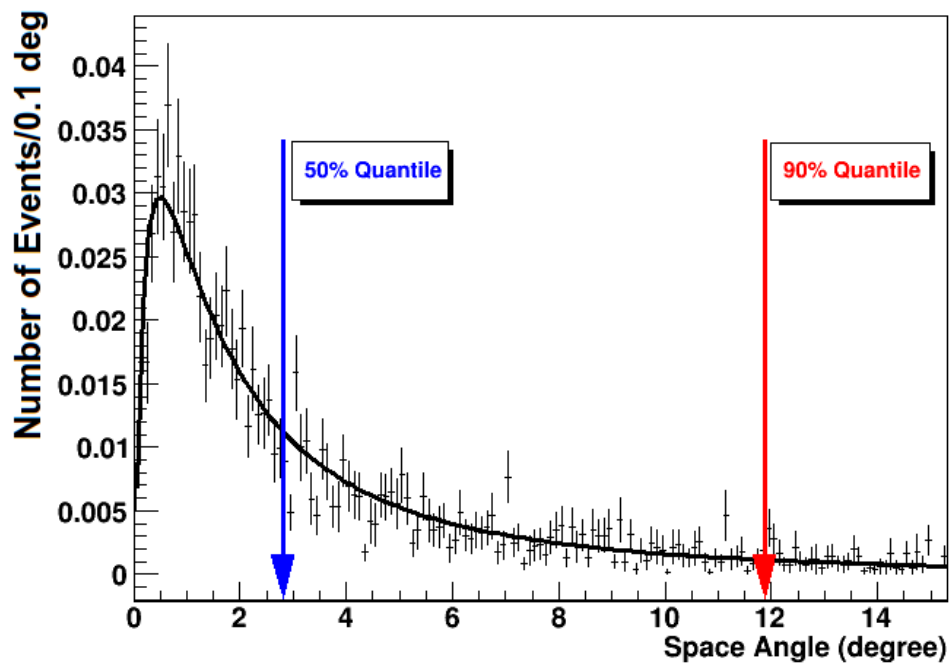


Figure 6.12: Space angle distribution with the associated fit to equation (6.9) obtained with a sample of Monte-Carlo HEN events, for a given declination and number of hits interval. The arrows indicate the 50<sup>th</sup> (median) and the 90<sup>th</sup> percentiles of the distribution. The distribution is normalized to unity.



# Chapter 7

## A coherent search method for unmodelled GW burst

### 7.1 Introduction

The simplest search that may be performed combining GW and HEN data is a GW search around the neutrino arrival time and aimed at the location in the sky that the neutrino candidate is estimated to come from. We use a coherent search technique, called X-Pipeline [247], that has been utilized to perform searches for GWs in association with GRBs [248]. We adapt the method and the software to the specific GW-HEN problem and characterize its performance. X-Pipeline is a software package designed to target Gravitational-Wave Bursts (GWB) associated with external astrophysical triggers such as gamma-ray bursts or neutrinos. It performs a coherent analysis of the data from arbitrary networks of gravitational wave detectors, and it is robust against noise-induced glitches. This robustness is achieved by optimizing the search sensitivity based on the noise characteristics and the detector performance at the time of the trigger.

The first requirement imposed in a triggered search is that the GW candidate signal be coincident in time, within an astrophysically motivated window with the external trigger, the neutrino one in this case (see Chapter 3). By using a subset of the available GW data, a triggered search can be performed with a lower detection threshold than an un-triggered search, giving a higher detection probability at a fixed false alarm probability and better limits in the absence of detection. The number of accidental coincidences between GW

detectors decreases with the size of the searched parameter space. Knowledge of the source direction allows us to search only a small part of the sky and veto candidate events seen in multiple detectors at times not consistent with the expected GW arrival time difference. Knowing the arrival time of the neutrino, we can restrict the time of the analysis to the specific search window and look for GW signals in coincidence with neutrino ones.

In this chapter we explain in details the search method and give an overview of the tools used for the GW-HEN analysis.

## 7.2 GW Search Method

### 7.2.1 Use of the search window

We introduced already the concept of search window in paragraph 3.7, now we consider its use in the actual analysis. For the purposes of our search for unmodelled gravitational-wave emission, a neutrino source is characterized by its sky position, the time of onset of neutrino emission, the trigger time  $t_0$ , and by the range of possible time delays, positive and negative, between the neutrino emission and the associated gravitational-wave emission. This search window, also called *on-source*, is the time interval which is searched for GW candidate signals, it is conservative enough to encompass most theoretical models of putative coincident GW-HEN emission<sup>1</sup>, see chapter 3. We consider a symmetric search window of  $t_0 \pm 500$  s [249] but the effective time in which we look for coincidences is  $[t_0 - 496s, t_0 + 496s]$ , because 4 sec of data are thrown away from the beginning and end of each block due to filter transients, see sketch 7.1.

Once the search is carried out, in order to evaluate the significance of the results one needs to estimate the background distributions. We set the *off-source* data to be all data within  $\pm 1.5$  hours of the neutrino time, excluding the on-source interval, see picture 7.2. This assures that the background does not contain any signal associated with the neutrino event but has similar statistical features as the data searched in association with the neutrino. This time range is limited enough so that the detectors should be in a similar state of operation as during the neutrino on-source interval, but long enough to provide off-source segments for estimating the background.

---

<sup>1</sup>It is now clear why the search window is also referred to as the on-source window.

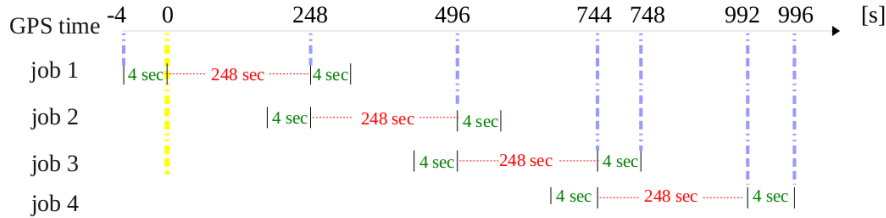


Figure 7.1: The search window is covered by blocks with fixed overlap, starting at the beginning of the on-source time. 4 sec of data are thrown away from the beginning and end of each block to filter transients, so consecutive blocks overlap by 8 sec. In our case the on-source window starts at GPS = 0 and ends at GPS = 992, and we use 256 sec blocks, the division into jobs looks like the following picture. Triggers are generated up to GPS 992. Also, note that for the analysis to work, we actually need science-mode data covering the interval  $[-4, +996]$  sec.

## 7.2.2 GW Event Generation

The basic search procedure consists in looking for excess power in time-frequency maps following the procedure used in [198]. Data from all detectors operating at the time of the trigger and which pass data-quality requirements are used for the GW search. The data from each detector are first whitened and time-shifted according to the sky location being analyzed so that a GW signal from that direction would appear simultaneous in each data stream. The data are then Fourier transformed to produce time-frequency maps. The maps are summed coherently (using amplitude and phase) with weighting determined by each detector's frequency-dependent sensitivity response to the sky location in question; the weights are chosen to maximize the signal-to-noise ratio expected for a circularly polarized GW signal, with a marginalization over possible signal amplitudes. This will be derived in section 7.3.1. Finally, the squared amplitude of these weighted Fourier transforms is computed and a threshold is placed on this quantity to retain the most significant 1% of pixels. Surviving pixels are grouped using next-nearest-neighbors clustering; each cluster of pixels is considered as a candidate GW event. Events are characterized by their duration, central occurrence time, bandwidth, and central frequency. Fig. 7.3 to 7.7 explain this process in schematic form.

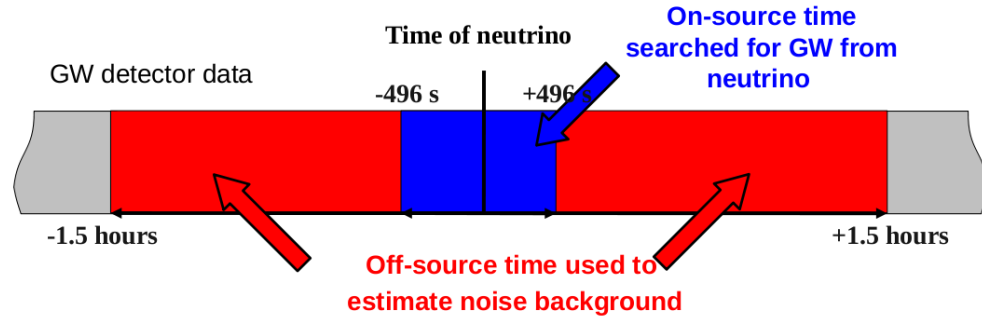


Figure 7.2: This sketch shows the difference between the on-source region and the off-source one. In the on-source region, that is the effective search window, we look for GW signals in coincidence with each neutrino trigger. The symmetric search window consists of  $\pm 496$  s around the neutrino time. The off-source window is defined as all data within  $\pm 1.5$  h of the neutrino time, excluding the on-source interval. This off-source data provides a sample of background that doesn't contain any signal associated with the neutrino event, but with statistical features similar to the data searched in association with the neutrino.

In addition to the marginalized circular polarization sum, other combinations of the data are constructed. Of particular importance are “null” combinations designed to cancel out the GW signal from the given sky location. Furthermore, comparison to corresponding “incoherent” combinations provides powerful tests for identifying events due to background noise fluctuations (“glitches”) [201], paragraph 7.3.5 and 7.3.6.

In order to maximize the sensitivity to GW signals of different durations the time-frequency analysis is repeated for different time baseline Fourier transforms: 1/128 s, 1/64 s, 1/32 s, 1/16 s, 1/8 s, 1/4 s. It is also repeated for every point in the 90% confidence neutrino source sky location, see paragraph 8.1.1 and 8.2. When GW events from different Fourier transforms or sky positions overlap in time-frequency, only the highest-ranking event is kept and the others are discarded.

This time-frequency analysis is performed on all of the data in the search window. To estimate the significance of the resulting GW candidates, the

same analysis is repeated on all data in the off-source window. The same set of detectors and data-quality requirements as in the on-source analysis are used for the off-source analysis. This off-source data does not contain any signal associated with the neutrino event, but has similar statistical features as the data searched in association with the neutrino. To increase the background sample, we also repeat the off-source analysis after having applied time shifts of multiples of 6 s to the data of the detectors relative to one another; with time slides we are able to produce  $O(10^3)$  background trials for each HEN.

Finally, the analysis is also repeated after “injecting” (adding) simulated GW signals to the on-source data. The amplitudes and morphologies tested are discussed in Section 8.4. We use these simulations to optimize and assess the sensitivity of the search, as discussed below.

### 7.2.3 GW Search

The sensitivity of searches for gravitational-wave bursts tends to be limited by the presence of non-Gaussian fluctuations of the background noise, known as glitches. To reduce this background, events that overlap in time within known instrumental and/or environmental disturbances are discarded. In addition GW consistency tests comparing the coherent and incoherent energies are applied to each event [201]. For all these tests acceptance/rejection thresholds have to be set.

There is a danger that any veto might falsly dismiss a real signal. In order to assess the probability of this happening, the detection efficiency of the pipeline for different sets of values of the thresholds is measured on data containing fake signal injections. The threshold value set for which the detection efficiency is highest, is chosen.

Once the thresholds have been fixed, these consistency tests are applied to the on-source events and to the off-source and injection events (not used for tuning). The surviving on-source event with the largest significance is taken to be the best candidate for a gravitational wave signal, and is referred to as the loudest event [202].

All surviving on-source events are assigned a false alarm probability by comparison to the distribution of loudest events from the off-source trials. Any on-source event with probability  $p < 0.01$  is subject to additional manual checks to try and determine the origin of the event, and additional background time slide trials are performed to improve the accuracy of the false

alarm probability estimate.

After the  $p$  values have been determined for the loudest events associated with each trigger, the collective set of  $p$  values is tested for consistency with the null hypothesis (no GW signal) using the binomial test, discussed in Section 8.8. In the absence of a detection, we set a frequentist upper limit on the strength of gravitational waves associated with each neutrino trigger, as discussed in Section 8.9.

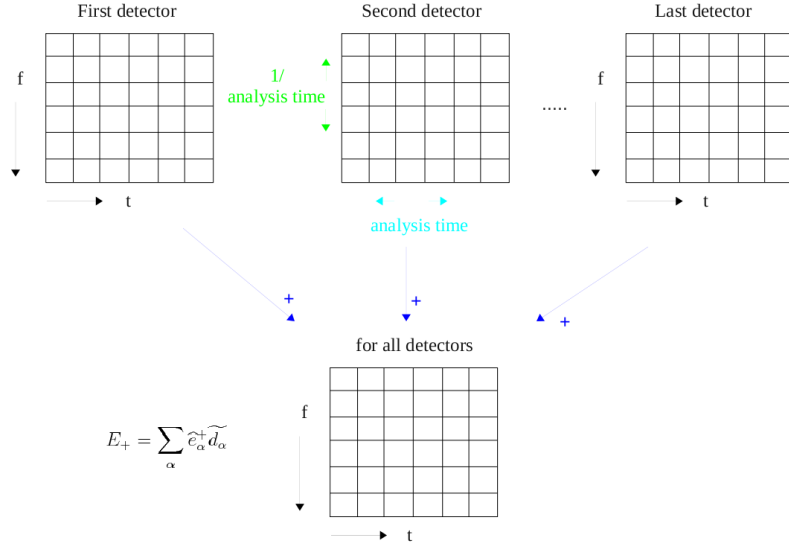


Figure 7.3: Our search data in 256 sec blocks and the data  $d_\alpha(t)$  where  $\alpha$  goes from 1 to 4 detectors.  $\widetilde{d}_\alpha$  is the FFT whitened data from each detector  $\alpha$  in the frequency domain. The calculation of a simple likelihood  $E_+$  (the same procedure is generated for all likelihoods):  $E_+$ :  $E_+ = \sum_k |\sum_\alpha \widehat{e}_\alpha^+ \widetilde{d}_\alpha|^2$  where  $\widehat{e}_\alpha^+ = \frac{f^+}{|f^+|}$  is the unit vector that is function of  $F_\alpha^{+, \times}$  antenna responses and noise level of different interferometer,  $S_\alpha[k]$ , and  $\widetilde{d}_\alpha$  are the whitened data in frequency domain. For each detector we have time-frequency map of FFT whitened data  $\widetilde{d}_\alpha$  in which the unit of the Y axis is  $resolution = \frac{1}{analysisTime}$ , and the X axis is analysis time in second (length of FFT in seconds). In this step we add maps together with weight  $\widehat{e}_\alpha^+$  to calculate  $E_+ = \sum_\alpha \widehat{e}_\alpha^+ \widetilde{d}_\alpha$ .

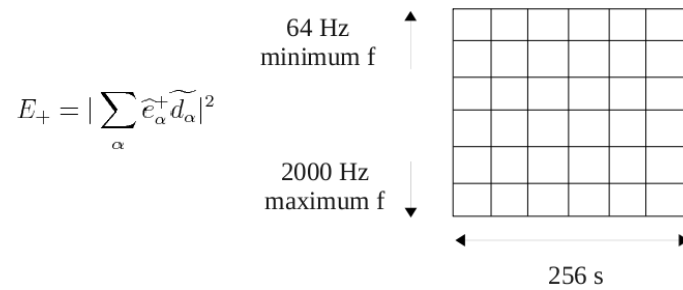


Figure 7.4: Square the map, so compute  $\left| \sum_{\alpha} \widehat{e}_{\alpha}^+ \widetilde{d}_{\alpha} \right|^2$ , all values are  $\geq 0$

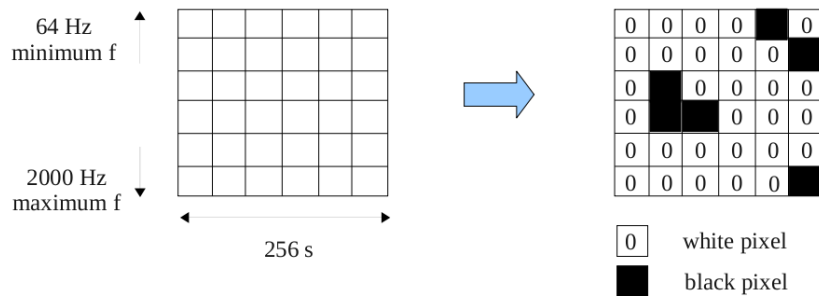


Figure 7.5: (The following is done for each likelihood). Threshold: Find the map value  $E_{threshold}$  such that only 1% of map value are  $\geq E_{threshold}$ . Zero out all other pixels, they are called white pixels. The ones we keep are black pixels.

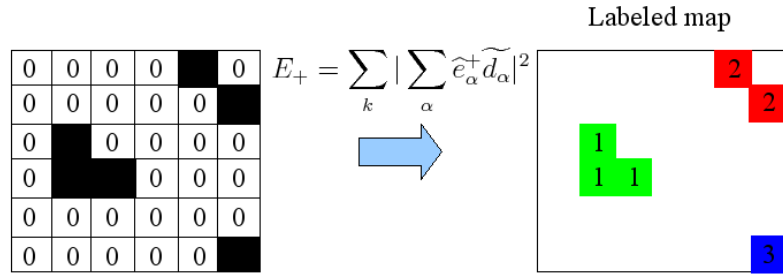


Figure 7.6: Identify clusters of connected black pixels (nearest and near-nearest, neighbors), they touch each other are neighbours. In this figure same-color pixels belong to the same cluster.

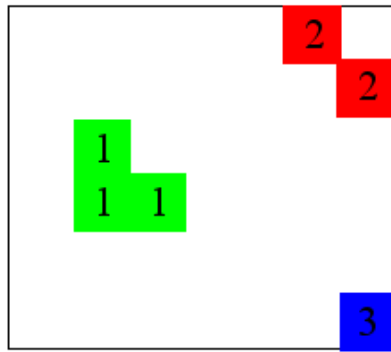


Figure 7.7: Do  $\sum_k$  (sum over cluster pixels): e.g. for cluster 2 we have  $E_+ = |\text{map}(1, 5)|^2 + |\text{map}(2, 6)|^2$

### 7.3 Formalism

Note: this section is adapted from the technical paper 'X-Pipeline: an analysis package for autonomous gravitational-wave burst searches', Sutton P. et al., New J. Phys. 12, 053034, 2010.

We introduce in this section the fundamental characteristics to understand the method strategy. When we consider a gravitational wave  $h_+(t, \vec{x})$ ,  $h_\times(t, \vec{x})$  from a direction  $\hat{\Omega}$ , the output  $d_\alpha$  of interferometer  $\alpha \in [1, \dots, D]$  is a linear combination of noise  $n_\alpha$  and signal:

$$d_\alpha(t + \Delta t_\alpha(\hat{\Omega})) = F_\alpha^+(\hat{\Omega})h_+(t) + F_\alpha^\times(\hat{\Omega})h_\times(t) + n_\alpha(t + \Delta t_\alpha(\hat{\Omega})), \quad (7.1)$$

where  $F_\alpha^+(\hat{\Omega})$ ,  $F_\alpha^\times(\hat{\Omega})$ , called *antenna response functions*, show the sensitivity of detector  $\alpha$  to the plus and cross polarizations (note that the choice of polarization basis is arbitrary; we use the  $\psi = 0$ , choice of Appendix B of [142]).  $\Delta t_\alpha(\hat{\Omega})$  is the time delay between the GW arrival time at position  $\vec{r}_\alpha$  of detector  $\alpha$  and at an arbitrary reference position  $\vec{r}_0$ :

$$\Delta t_\alpha(\hat{\Omega}) = \frac{1}{c}(\vec{r}_0 - \vec{r}_\alpha) \cdot \hat{\Omega}. \quad (7.2)$$

In the following we suppress the explicit mention of the time delay. We also write  $h_{+, \times}(t) \equiv h_{+, \times}(t, \vec{r}_0)$ .

The data from the detectors is sampled discretely, hence we adopt discrete notation. In the case of the discrete Fourier-transform  $\tilde{x}[k]$  of a time-series  $x[j]$  we have

$$\begin{aligned} \tilde{x}[k] &= \sum_{j=0}^{N-1} x[j] e^{-i2\pi jk/N}, \\ x[j] &= \frac{1}{N} \sum_{k=0}^{N-1} \tilde{x}[k] e^{i2\pi jk/N}, \end{aligned} \quad (7.3)$$

where  $N$  is the number of data points in the time domain. We change from continuous to discrete notation using  $x(t) \rightarrow x[j]$ ,  $\tilde{x}(f) \rightarrow f_s^{-1}\tilde{x}[k]$ ,  $\int dt \rightarrow f_s^{-1} \sum_j$ ,  $\int df \rightarrow f_s N^{-1} \sum_k$ ,  $\delta(t - t') \rightarrow f_s \delta_{jj'}$ , and  $\delta(f - f') \rightarrow N f_s^{-1} \delta_{kk'}$ , considering  $f_s$  the sampling rate. For example, the one-sided noise power spectral density  $S_\alpha[k]$  of the noise  $\tilde{n}_\alpha$  is

$$\langle \tilde{n}_\alpha^*[k] \tilde{n}_\beta[k'] \rangle = \frac{N}{2} \delta_{\alpha\beta} \delta_{kk'} S_\alpha[k], \quad (7.4)$$

where the angle brackets indicate an average over noise instantiations.

We define the noise-spectrum-weighted quantities as follow:

$$\tilde{d}_{w\alpha}[k] = \frac{\tilde{d}_\alpha[k]}{\sqrt{\frac{N}{2}S_\alpha[k]}}, \quad (7.5)$$

$$\tilde{n}_{w\alpha}[k] = \frac{\tilde{n}_\alpha[k]}{\sqrt{\frac{N}{2}S_\alpha[k]}}, \quad (7.6)$$

$$F_{w\alpha}^{+,\times}(\hat{\Omega}, k) = \frac{F_\alpha^{+,\times}(\hat{\Omega})}{\sqrt{\frac{N}{2}S_\alpha[k]}}. \quad (7.7)$$

The normalized whitened noise is

$$\langle \tilde{n}_{w\alpha}^*[k] \tilde{n}_{w\beta}[k'] \rangle = \delta_{\alpha\beta} \delta_{kk'}. \quad (7.8)$$

Using this notation, we can write in a matrix form the equation (7.1) for the data measured from a set of  $D$

$$\tilde{\mathbf{d}} = \mathbf{F}\tilde{\mathbf{h}} + \tilde{\mathbf{n}}, \quad (7.9)$$

where we don't write the explicit indices for frequency and sky position. The boldface symbols  $\tilde{\mathbf{d}}$ ,  $\mathbf{F}$ ,  $\tilde{\mathbf{n}}$  refer noise-weighted quantities that are vectors or matrices on the space of detectors;  $\tilde{\mathbf{h}}$  is not noise-weighted and is not in the space of the detectors, see section 10.3 and APPENDIX A for an extensive explanation:

$$\tilde{\mathbf{d}} \equiv \begin{bmatrix} \tilde{d}_{w1} \\ \tilde{d}_{w2} \\ \vdots \\ \tilde{d}_{wD} \end{bmatrix}, \quad \tilde{\mathbf{h}} \equiv \begin{bmatrix} \tilde{h}_+ \\ \tilde{h}_\times \end{bmatrix}, \quad \tilde{\mathbf{n}} \equiv \begin{bmatrix} \tilde{n}_{w1} \\ \tilde{n}_{w1} \\ \vdots \\ \tilde{n}_{wD} \end{bmatrix}, \quad (7.10)$$

and

$$\mathbf{F} \equiv [\mathbf{F}^+ \quad \mathbf{F}^\times] \equiv \begin{bmatrix} F_{w1}^+ & F_{w1}^\times \\ F_{w2}^+ & F_{w2}^\times \\ \vdots & \vdots \\ F_{wD}^+ & F_{wD}^\times \end{bmatrix}. \quad (7.11)$$

These quantities are function of frequency and sky position, through the antenna response. For this reason, coherent combinations typically have to be re-computed for every frequency bin as well as for every sky position. The matrix  $\mathbf{F}$ , defined by equation (7.11), contains all information on the sensitivity of the network as a function of frequency and sky position.

### 7.3.1 Standard Likelihood

In this section we describe the detection statistics likelihoods used for signal detection in our search, as anticipate in section 7.2.3. We begin with the simplest of all: the *standard* or *maximum likelihood*, first derived in [161, 142].

We write the probability of obtaining the whitened data  $\tilde{\mathbf{d}}$  in a time-frequency pixel in the presence of a known gravitational wave  $\tilde{\mathbf{h}}$  from a given direction,  $P(\tilde{\mathbf{d}}|\tilde{\mathbf{h}})$ , and we assume Gaussian noise,

$$P(\tilde{\mathbf{d}}|\tilde{\mathbf{h}}) = \frac{1}{(2\pi)^{D/2}} \exp \left[ -\frac{1}{2} \left| \tilde{\mathbf{d}} - \mathbf{F}\tilde{\mathbf{h}} \right|^2 \right]. \quad (7.12)$$

For a set  $\{\tilde{\mathbf{d}}\}$  of  $N_p$  time-frequency pixels,

$$P(\{\tilde{\mathbf{d}}\}|\{\tilde{\mathbf{h}}\}) = \frac{1}{(2\pi)^{N_p D/2}} \exp \left[ -\frac{1}{2} \sum_k^{N_p} \left| \tilde{\mathbf{d}}[k] - \mathbf{F}[k]\tilde{\mathbf{h}}[k] \right|^2 \right], \quad (7.13)$$

where  $k$  is the pixel index.  $L$  is the likelihood ratio defined by the log-ratio of the probability to have a signal under the null hypothesis:

$$L \equiv \ln \frac{P(\{\tilde{\mathbf{d}}\}|\{\tilde{\mathbf{h}}\})}{P(\{\tilde{\mathbf{d}}\}|\{0\})} = \frac{1}{2} \sum_k^{N_p} \left[ \left| \tilde{\mathbf{d}} \right|^2 - \left| \tilde{\mathbf{d}} - \mathbf{F}\tilde{\mathbf{h}} \right|^2 \right], \quad (7.14)$$

where  $P(\{\tilde{\mathbf{d}}\}|\{0\})$  is the probability of measuring the data  $\{\tilde{\mathbf{d}}\}$  when no GWB is present ( $\tilde{\mathbf{h}} = 0$ ).

In reality, we don't know the signal waveform *a priori*, so it isn't possible to compute the likelihood ratio (7.14). One solution is to treat the waveform values  $\tilde{\mathbf{h}} = (\tilde{h}_+, \tilde{h}_\times)$  in each time-frequency pixel as free parameters to be fit to the data. To maximize the likelihood ratio the best-fit values  $\tilde{\mathbf{h}}_{\max}$  are:

$$0 = \left. \frac{\partial L}{\partial \tilde{\mathbf{h}}} \right|_{\tilde{\mathbf{h}}=\tilde{\mathbf{h}}_{\max}}. \quad (7.15)$$

The linear equation (7.15) for  $\tilde{\mathbf{h}}_{\max}$  is due to the quadratic relation of the likelihood ratio  $L$  in  $\tilde{\mathbf{h}}$

$$\tilde{\mathbf{h}}_{\max} = (\mathbf{F}^\dagger \mathbf{F})^{-1} \mathbf{F}^\dagger \tilde{\mathbf{d}}, \quad (7.16)$$

where  $^\dagger$  is used to express the conjugate transpose. ( $\mathbf{F}$  is real, and the data vector  $\tilde{\mathbf{d}}$  are complex.) If we substitute the solution for  $\tilde{\mathbf{h}}_{\max}$  in (7.14), we obtain the *maximum or standard likelihood*,

$$E_{\text{SL}} \equiv 2L(\tilde{\mathbf{h}}_{\max}) = \sum_k \tilde{\mathbf{d}}^\dagger \mathbf{P}^{\text{GW}} \tilde{\mathbf{d}}, \quad (7.17)$$

where we indicate

$$\mathbf{P}^{\text{GW}} \equiv \mathbf{F} (\mathbf{F}^\dagger \mathbf{F})^{-1} \mathbf{F}^\dagger \quad (7.18)$$

and we have used the fact that  $\mathbf{P}^{\text{GW}}$  is Hermitian.

### 7.3.2 Projection Operators and the Null Energy

The operator  $\mathbf{P}^{\text{GW}}$ , seen in eq. 7.17, projects the data into the subspace spanned by  $\mathbf{F}^+$  and  $\mathbf{F}^\times$ . The contribution of any gravitational wave to data  $\tilde{\mathbf{d}}$  from a fixed sky position is restricted from the equations (7.1) or (7.9)-(7.11). The maximum amount of energy<sup>2</sup>, that is consistent in the whitened data with the hypothesis of a gravitational wave from a given sky position, is the standard likelihood.

On the contrary, the *total energy* in the data is

$$E_{\text{tot}} = \sum_k |\tilde{\mathbf{d}}|^2, \quad (7.19)$$

where  $k$  is the pixel index. The total energy contains only autocorrelation terms and no cross-correlation terms, for this reason is considered an incoherent statistic. In the case of a single detector network, such quantity can be computed for each time-frequency pixel in an excess-power search [142].

To cancel the maximum likelihood gravitational-wave signal, we use the projection operator  $\mathbf{P}^{\text{null}} \equiv (\mathbf{I} - \mathbf{P}^{\text{GW}})$ , that is orthogonal to  $\mathbf{P}^{\text{GW}}$

$$E_{\text{null}} \equiv E_{\text{tot}} - E_{\text{SL}} = \sum_k \tilde{\mathbf{d}}^\dagger \mathbf{P}^{\text{null}} \tilde{\mathbf{d}}. \quad (7.20)$$

---

<sup>2</sup>More precisely, since it is defined in terms of the noise-weighted data, the standard likelihood is the maximum possible squared signal-to-noise ratio  $\rho^2$  that is consistent with the hypothesis of a gravitational wave from a given sky position. See Section 7.3.4.

From this equation 7.20, we can deduce that the null energy is the smallest amount of energy in the whitened data that cannot be associated with a GW signal.

### 7.3.3 Dominant Polarization Frame and Other Likelihoods

We have seen in section 7.3 that the data from a set of  $D$  detectors is a vector in a  $D$ -dimensional complex space for a single time-frequency pixel. The set of single detector strains constitutes one basis of this space. This is the basis in which all the equations are written so far, but not the most convenient for writing statistics. One can consider the 2-dimensional subspace defined by  $\mathbf{F}^+$ ,  $\mathbf{F}^\times$  to start the construction of a better basis. In fact, when we take into account the properties of this bidimensional space, we find that there is a direction (a choice of polarization angle) in which the detector network has the maximum antenna response, and an orthogonal direction in which the network has minimum antenna response. Considering those two directions and completing this basis with an orthonormal vector for the null space, produces the convenient basis that we use to construct detection statistics. In addition, we define the  $+$ ,  $\times$  polarizations so that  $\mathbf{F}^+$  lies along the first basis vector, and  $\mathbf{F}^\times$  along the second. This choice of polarization definition is known as *dominant polarization frame* or DPF [165, 166].

To yield the DPF, the antenna response vectors are related to each other through a polarization angle  $\psi$

$$\mathbf{F}^+(\psi) = \cos 2\psi \mathbf{F}^+(0) + \sin 2\psi \mathbf{F}^\times(0), \quad (7.21)$$

$$\mathbf{F}^\times(\psi) = -\sin 2\psi \mathbf{F}^+(0) + \cos 2\psi \mathbf{F}^\times(0) \quad (7.22)$$

(see APPENDIX A section 10.1 for a complete demonstration). In this construction, for any direction on the sky, one can always chose a polarization frame in which  $\mathbf{F}^+(\psi)$  and  $\mathbf{F}^\times(\psi)$  are orthogonal and  $|\mathbf{F}^+(\psi)| > |\mathbf{F}^\times(\psi)|$ . In fact, given  $\mathbf{F}^+(0)$ ,  $\mathbf{F}^\times(0)$  in the original polarization frame, the rotation angle  $\psi_{DP}$  to the dominant polarization frame is:

$$\psi_{DP}(\hat{\Omega}, k) = \frac{1}{4} \text{atan2} \left( 2\mathbf{F}^+(0) \cdot \mathbf{F}^\times(0), |\mathbf{F}^+(0)|^2 - |\mathbf{F}^\times(0)|^2 \right). \quad (7.23)$$

where  $\text{atan2}(y, x)$  is the arctangent function with range  $(-\pi, \pi]$ .

We write the antenna response vectors in the DPF with the lower-case symbols  $\mathbf{f}^+$ ,  $\mathbf{f}^\times$ . Their properties are:

$$|\mathbf{f}^+|^2 \geq |\mathbf{f}^\times|^2, \quad (7.24)$$

$$\mathbf{f}^+ \cdot \mathbf{f}^\times = 0. \quad (7.25)$$

The unit vectors  $\mathbf{e}^+ \equiv \mathbf{f}^+ / |\mathbf{f}^+|$ ,  $\mathbf{e}^\times \equiv \mathbf{f}^\times / |\mathbf{f}^\times|$ , in the dominant polarization frame, constitute an orthonormal coordinate system; see Figure 7.8.

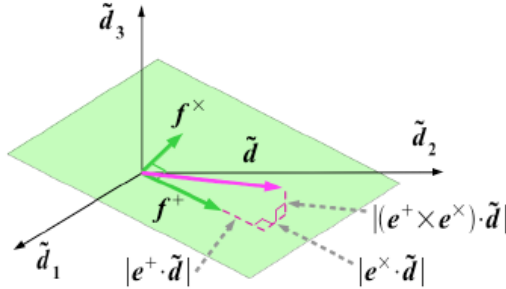


Figure 7.8: Space of detector strains for the 3-detector case for a data sample. The green plane is the plane defined by the antenna response vectors  $\mathbf{f}^+$ ,  $\mathbf{f}^\times$ . The thick magenta line is the vector of detector strains  $\tilde{\mathbf{d}}$  for one realization of noise and signal. The dashed lines show the projection of the data vector into the detector response plane and into the null space. Source: Sutton P. et al., New J. Phys. 12, 053034, 2010.

The projection operator  $\mathbf{P}^{\text{GW}}$  in the dominant polarization frame becomes

$$\mathbf{P}^{\text{GW}} = \mathbf{e}^+ \mathbf{e}^{+\dagger} + \mathbf{e}^\times \mathbf{e}^{\times\dagger}. \quad (7.26)$$

The standard likelihood (7.17) takes the form

$$E_{\text{SL}} = \sum_k \left[ \left| \mathbf{e}^+ \cdot \tilde{\mathbf{d}} \right|^2 + \left| \mathbf{e}^\times \cdot \tilde{\mathbf{d}} \right|^2 \right], \quad (7.27)$$

where  $\mathbf{a} \cdot \mathbf{b}$  denotes the dot product between  $D$  dimensional vectors  $\mathbf{a}$  and  $\mathbf{b}$ . The *plus energy* [165, 166] is the energy in the  $h_+$  polarization in the DPF:

$$E_+ \equiv \sum_k \left| \mathbf{e}^+ \cdot \tilde{\mathbf{d}} \right|^2. \quad (7.28)$$

The *cross energy* is defined analogously:

$$E_{\times} \equiv \sum_k \left| \mathbf{e}^{\times} \cdot \tilde{\mathbf{d}} \right|^2. \quad (7.29)$$

### 7.3.4 Statistical Properties

The important property of the projection likelihoods  $E_+$ ,  $E_{\times}$ ,  $E_{\text{SL}}$ ,  $E_{\text{null}}$ ,  $E_{\text{tot}}$  is that for a set of time-frequency pixels and a sky position chosen *a priori*, each of these energies follows a  $\chi^2$  distribution with  $2N_p D_{\text{proj}}$  degrees of freedom in Gaussian background noise:

$$2E \sim \chi_{2N_p D_{\text{proj}}}^2(\lambda). \quad (7.30)$$

Here  $N_p$  is the number of pixels of the event cluster and  $D_{\text{proj}}$  is the number of dimensions of the projection, which by construction is 1 for  $E_+$ ,  $E_{\times}$ , 2 for  $E_{\text{SL}}$ , and  $D$ , number of detectors, for  $E_{\text{tot}}$ . The factor of 2 in the degrees of freedom,  $2N_p D_{\text{proj}}$ , occurs because the data are complex. In general  $D_{\text{proj}} = D - 2$  for  $E_{\text{null}}$ , except for the particular case in which the null stream is built as the difference of the data streams from the two co-aligned LIGO-Hanford detectors, H1 and H2. In this case  $D_{\text{proj}} = D - 1$ , because the network H1-H2 is only sensitive to the same gravitational-wave polarization, hence only one dimension is removed in forming the null stream.

### 7.3.5 Incoherent Energies and Background Rejection

We calculate the different likelihoods  $E_{\text{SL}}$ ,  $E_+$ , *etc.* under the assumption of Gaussian background noise. On the contrary, real noise sources in detectors are not Gaussian. Real detectors contain short transients of excess strain, known as *glitches*, that can mimic the gravitational wave burst signals. The ability to distinguish true GW signals from noise glitches is a key point for burst searches. Since even a glitch in a single detector will create large values for combined likelihoods, coherent analyses can be extremely sensitive to such false alarms. In this section we introduce a technique to suppress such false alarms in coherent analyses.

Chatterji *et al.* [171] have shown how one can use the autocorrelation component of coherent energies to construct tests that are effective at rejecting glitches. Their proposed strategy to reject glitches is based on the null space, that is the subspace orthogonal to that used to define the standard

likelihood. By design the projection of the data  $\mathbf{d}$  on the null space includes only noise, and the presence or absence of GWs should not affect this projection in any way. On the contrary, noise doesn't have any relation with  $\mathbf{F}^+$ ,  $\mathbf{F}^\times$ , so glitches don't couple into the data streams and they will generally be present in the null space projection. This ensures the possibility to distinguish true GWs from glitches, by imposing the null energy to be small for a transient to be considered a GW [164].

To construct such coherent veto test we can rewrite equation (7.20) for the null energy as

$$E_{\text{null}} = \sum_k \sum_{\alpha, \beta} \tilde{d}_\alpha^\dagger P_{\alpha\beta}^{\text{null}} \tilde{d}_\beta. \quad (7.31)$$

where  $\alpha, \beta$  are detector indices. As shown in Chatterji *et al.* [171], both cross-correlation terms  $\tilde{d}_\alpha^\dagger \tilde{d}_\beta$  and auto-correlation terms  $\tilde{d}_\alpha^\dagger \tilde{d}_\alpha$  compose the null energy. In the case of a glitch, that is a transient signal not correlated between detectors, in the null energy the cross-correlation terms will be small compared to the auto-correlation terms. Hence, we expect for a glitch that the null energy is dominated by the auto-correlation terms:

$$E_{\text{null}} \simeq I_{\text{null}} \equiv \sum_k \sum_{\alpha} P_{\alpha\alpha}^{\text{null}} |\tilde{d}_\alpha|^2. \quad (\text{glitches}) \quad (7.32)$$

The auto-correlation part of the null energy is called the *incoherent energy*.

On the other hand, a true GW signal is correlated between the detectors according to equations (7.1) or (7.9)–(7.11). By design of the null projection operator, these correlation terms cancel in the null stream, in which there is only Gaussian noise. However, these correlations cannot cancel in  $I_{\text{null}}$ , because it is a purely incoherent statistic. Hence, for a strong GW we consider

$$E_{\text{null}} \ll I_{\text{null}}. \quad (\text{GW}) \quad (7.33)$$

Considering these aspects, the coherent veto test is designed to keep only transients with

$$I_{\text{null}}/E_{\text{null}} > C, \quad (7.34)$$

where  $C$  is some constant greater than 1. This test is efficient for eliminating large-amplitude glitches. In order to eliminate also small-amplitude glitches, in which  $E_{\text{null}}$  can be small compared to  $I_{\text{null}}$  due to statistical fluctuations we use in our search a modified test where the effective threshold  $C$  varies with the event energy, as discussed in Section 7.3.6.

Similar conditions can be requested on the other coherent energies,  $E_+$ ,  $E_\times$ , *etc.*. We indicate the corresponding incoherent energies by

$$I_+ \equiv \sum_k \sum_\alpha \left| e_\alpha^+ \tilde{d}_\alpha \right|^2, \quad (7.35)$$

$$I_\times \equiv \sum_k \sum_\alpha \left| e_\alpha^\times \tilde{d}_\alpha \right|^2, \quad (7.36)$$

$$I_{\text{SL}} \equiv \sum_k \sum_\alpha \left[ \left| e_\alpha^+ \tilde{d}_\alpha \right|^2 + \left| e_\alpha^\times \tilde{d}_\alpha \right|^2 \right] = I_+ + I_\times. \quad (7.37)$$

For each case, there is a comparison between the coherent energy  $E$  and its incoherent counterpart  $I$ , considering the expectation that for a glitch,  $E \simeq I$ . In the case of a strong GW, the signal summed over both polarizations should build coherently, so we have

$$E_{\text{SL}} > I_{\text{SL}}. \quad (\text{GW}) \quad (7.38)$$

Depending on the predominant polarization of the GW signal, we can find

$$\begin{aligned} E_+ &> I_+ \\ E_\times &< I_\times \end{aligned} \quad (\text{signal predominantly } h_+). \quad (7.39)$$

when the  $+$  polarization in the DPF is predominant, and

$$\begin{aligned} E_+ &< I_+ \\ E_\times &> I_\times \end{aligned} \quad (\text{signal predominantly } h_\times). \quad (7.40)$$

when the  $\times$  polarization in the DPF is predominant. A gravitational wave, in general, will be characterized by at least one of  $E_+ > I_+$  or  $E_\times > I_\times$ ; at least one of the two polarizations will show a coherent buildup of signal-to-noise across detectors.

### 7.3.6 Glitch rejection

Glitches tend to show a correlation between each coherent energy  $E_{\text{null}}$ ,  $E_+$ ,  $E_\times$ , and its corresponding incoherent energy  $I_{\text{null}}$ ,  $I_+$ ,  $I_\times$ . In our search we compare these energies to discard noise events that could mimic a real signal.

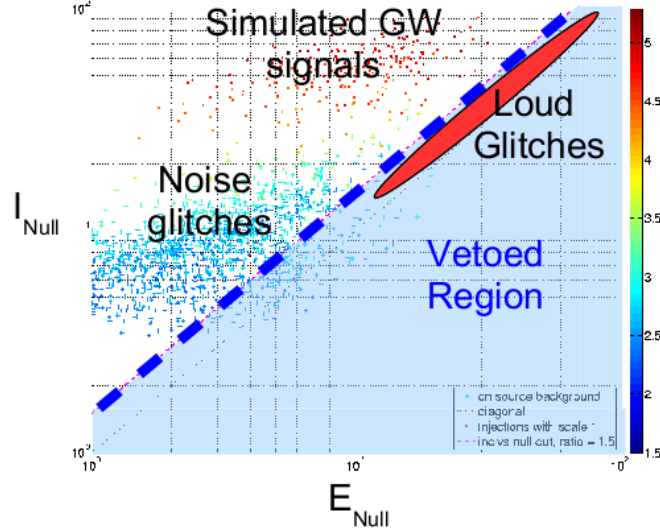


Figure 7.9: Coherent methods typically measure several properties of a GW candidate including energies of both GW polarizations (+,  $\times$ ) and a null stream. Null stream type tests for noise transient, glitch, rejection. For loud glitches  $E_{null} \sim I_{null}$  and for gravitational wave signals  $E_{null} < I_{null}$ . The plot shows an analysis of simulated LIGO H1-H2 data in which the blue line is the linear cut with  $\alpha = 1$  that is the dominant one, and the other linear cut  $\alpha = 0.8$  is not drawn. This plot shows that the linear cuts used are safe vetoes because they don't discard real signals.

In this direction, we use two types of coherent vetoes. Both are pass/fail tests. Following the discussion in Section 7.3.5, a cluster passes the coherent test if

$$|E_{null} - I_{null}| / (E_{null} + I_{null})^\alpha \geq r_{null}, \quad (7.41)$$

$$|E_+ - I_+| / (E_+ + I_+)^\alpha \geq r_+, \quad (7.42)$$

$$|E_\times - I_\times| / (E_\times + I_\times)^\alpha \geq r_\times, \quad (7.43)$$

where the thresholds  $r_{null}$ ,  $r_+$ , and  $r_\times$  are chosen by the adaptive automated procedure described in section 7.2.3.

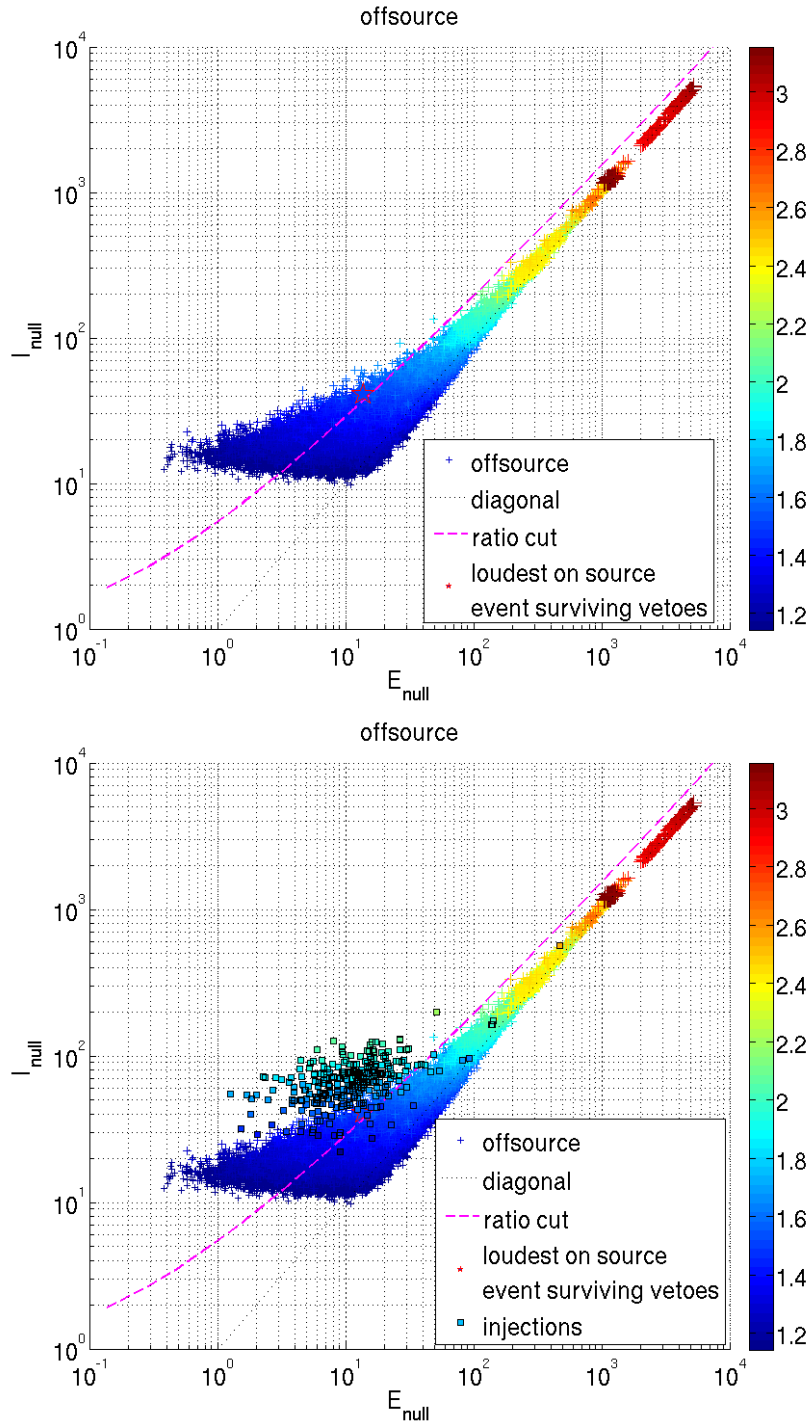


Figure 7.10:  $I_{\text{null}}$  vs.  $E_{\text{null}}$  for clusters produced by background noise (+) and by simulated gravitational-wave signals ( $\square$ ). The color axis is the base-10 logarithm of the cluster significance  $\mathcal{S}$ . Loud glitches are vetoed by discarding all clusters that fall below the dashed line.

The parameter  $\alpha$  characterizes the shape of the line cut, and  $r$  the strength of the cut of that shape, see figure 7.10. The tuning of the separation line is performed in two steps:

- first of all, a linear cut with  $\alpha = 1$ , is applied. This cut rejects all loud glitches that in general appear at the top right of the plot 7.10.
- In second step for tuning we use  $\alpha = 0.8$ . The purpose of this step is to reject the remaining glitches, on the edge between background and signal, while keeping the best detection sensitivity.

Plots 7.10 show  $I_{\text{null}}$  vs.  $E_{\text{null}}$  for clusters produced by background noise and by simulated gravitational-wave signals. Loud glitches are vetoed by discarding all clusters that fall below the dashed line.

Plot 7.11 shows how effective is the background rejection by using the glitch rejection test. The two curves draw the distribution of the loudest event significance seen in each of the off-source segments used for upper limit estimation, before and after the coherent glitch rejection test.

### 7.3.7 Detection and upper limits

#### Detection Procedure

In order to claim a detection of a gravitational wave, we need to be able to establish with high confidence that a candidate event is statistically inconsistent with the noise background. In our search, we use the *loudest event* statistic [187, 188] to characterise the outcome of the experiment. For each HEN the loudest event is the cluster in the on-source interval that has the largest significance using the standard likelihood (after application of all the vetoes); let us denote its significance by  $\mathcal{S}_{\text{max}}^{\text{on}}$ . We compare  $\mathcal{S}_{\text{max}}^{\text{on}}$  with the cumulative distribution  $C(\mathcal{S}_{\text{max}})$  of loudest significances of background noise (discussed below). We set a threshold on  $C(\mathcal{S}_{\text{max}})$  such that the probability of background noise producing a cluster in the on-source interval with significance above this threshold is a specific small value (for example, a 1% chance). The on-source data is then analyzed. If the significance  $C(\mathcal{S}_{\text{max}}^{\text{on}})$  of the loudest cluster is greater than our threshold, we consider the cluster as an event that warrants further investigations, see section 8.7.

If it is less significant it cannot be defined as a possible GW candidate and hence one can immediately set an upper limit on the strength of gravitational-wave emission associated with its neutrino trigger, see paragraph 7.3.7.

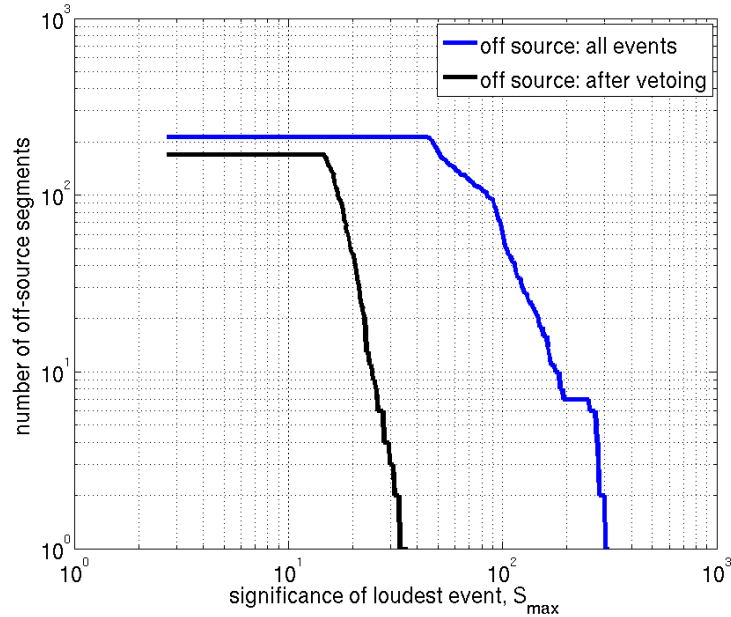


Figure 7.11: Distribution of the loudest event significance  $S_{max}$  seen in each of the off-source segments used for upper limit estimation, before and after the coherent glitch rejection. In this example 178 out of the 227 off-source segments have events that survive the test.

## Upper Limits

To define if there is a statistical excess associated with each HEN trigger we compare the surviving largest significance measured on the search window data,  $\mathcal{S}_{max}^{on}$ , to the cumulative distribution  $C(\mathcal{S}_{max})$  estimated from the off-source data. In absence of a statistically significant signal, we set a frequentist upper limit on the strength of gravitational waves associated with the HEN. In particular we will set a 90% confidence level upper limit on the signal amplitude, for a given gravitational wave signal model. This amplitude is the minimum amplitude for which there is a 90% or greater chance that a signal with such amplitude could produce a more significance cluster than the largest value  $\mathcal{S}_{max}^{on}$  measured.

We use the standard criterion for LIGO burst search to measure the signal

amplitude, the root-sum-squared amplitude  $h_{\text{rss}}$ , described by

$$\begin{aligned} h_{\text{rss}} &= \sqrt{\int_{-\infty}^{\infty} dt [h_+^2(t) + h_\times^2(t)],} \\ &= \sqrt{2 \int_0^{\infty} df [\tilde{h}_+^2(f) + \tilde{h}_\times^2(f)]}. \end{aligned} \quad (7.44)$$

$h_{\text{rss}}$  is expressed in  $\text{Hz}^{-1/2}$ , the same units used for the amplitude spectra of the detector noise, which is convenient to compare the two quantities. Under the assumption of isotropic emission, for narrow-band signals, the  $h_{\text{rss}}$  can be used in the calculation of the energy emitted in gravitational waves [190]

$$E_{\text{GW}}^{\text{iso}} \simeq \frac{\pi^2 c^3}{G} D^2 f_0^2 h_{\text{rss}}^2, \quad (7.45)$$

by a source distance  $D$  and emitting predominantly at a frequency  $f_0$ .  $h_{\text{rss}}$  doesn't involve the detector sensitivity (either antenna response or noise spectrum), hence, upper limits expressed in terms of  $h_{\text{rss}}$  will depend on the type and frequency of the putative signal as well as on the sky position of the source.

To calculate the upper limit, we need to know how strong a real gravitational wave signal needs to be in order to appear in the data with a given significance. In order to do this, we inject repeatedly simulated gravitational wave signals in the data from each interferometer and analyze the segments with the injections in the same way of the real search. After the application of vetoes and in association with a given injection, we determine the largest significance of all clusters.

In particular, the method to set upper limit is the following:

1. Select one or more families of waveforms for which the upper limit will be set. For example, a common choice in the GW searches is linearly or circularly polarized, Gaussian-modulated sinusoids (sine-Gaussians) with fixed central frequency and quality factor, and random peak time and polarization angle.
2. Find the significance  $\mathcal{S}_{\text{max}}^{\text{on}}$  of the loudest event in the original search (Section 7.3.6).
3. For each waveform family:

- 
- (a) Generate random parameter values for a large number  $N_{inj}$  ( $\approx 10^3$ ) of waveforms from the family (*e.g.*, specific peak times and polarization angles for the sine-Gaussian case), and with fixed  $h_{\text{rss}}$  amplitude.
  - (b) Add the waveforms one-by-one to the on-source data, perform the search and determine the largest significance of the surviving cluster associated,  $S_{max}^{inj}$  with each injection.
  - (c) Compare  $S_{max}^{inj}$  with  $S_{max}^{on}$  and if  $S_{max}^{inj} \geq S_{max}^{on}$  then update the numbers count  $N_{pass}$  of the detected injections. Compute the confidence  $C = \frac{N_{pass}}{N_{inj}}$
  - (d) Repeat 3a–3c using the same waveform family but with different  $h_{\text{rss}}$  amplitudes. The 90% confidence-level upper limit on the amplitude is  $h_{\text{rss}}^{90\%}$  for which  $C = 90\%$ .

Examples of detection efficiency curves for injections done at 100 Hz and 150 Hz are shown in the plots 7.12. The figures display the efficiency injection amplitude as black dots and the amplitude is scaled in terms of  $h_{\text{rss}}$ . The blue line is the linear interpolation of the efficiency curve, and in red there is the 90% efficiency amplitude while in yellow the 50% efficiency.

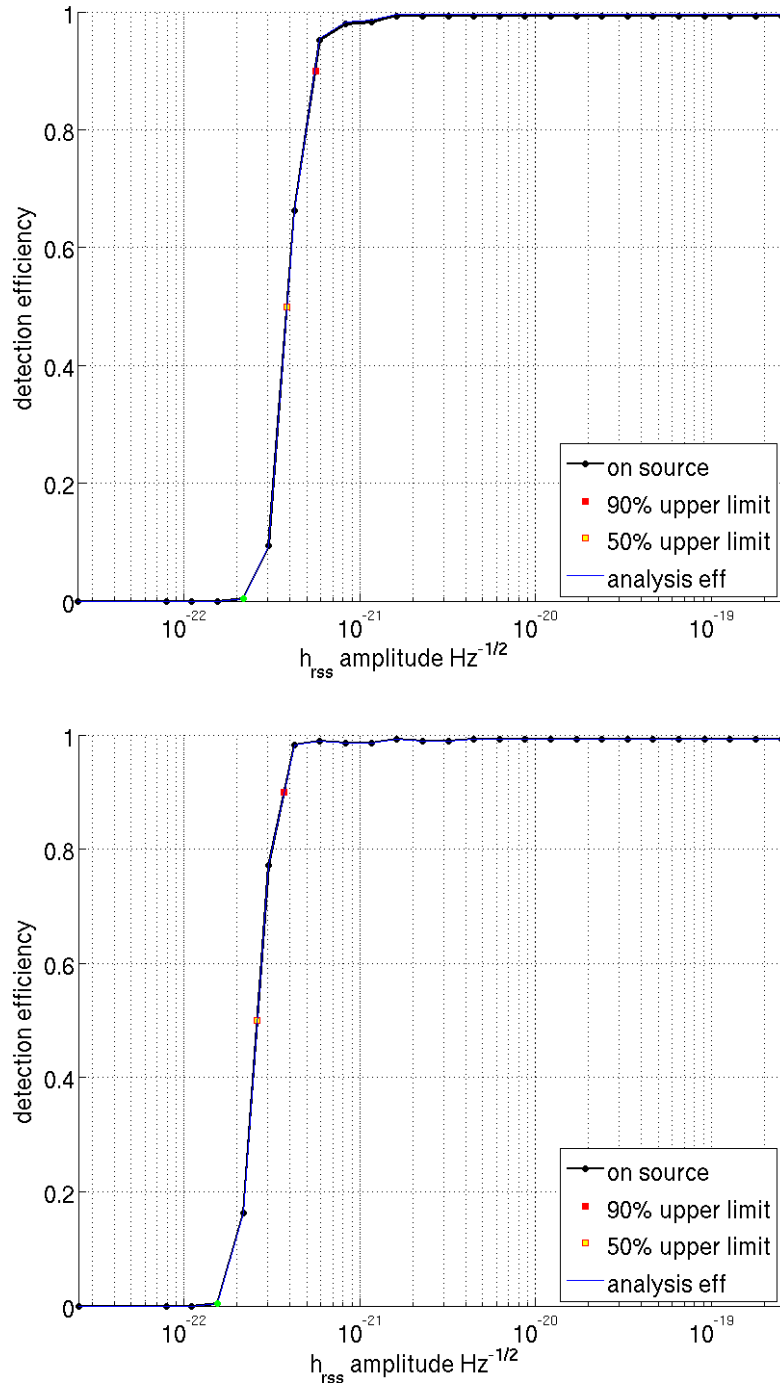


Figure 7.12: Efficiency plots from injections done at 100 Hz (top) and 150 Hz (bottom). Fraction of injections recovered with the significance greater than loudest event in (dummy) onsource. Black dots are sampled values, red and yellow dot is respectively the 90% and 50% efficiency obtained from interpolation. Green dot marks sampled valued with  $0 < \text{efficiency} < 5\%$ .

## Tuning and Closed-Box Analyses

The sensitivity of our analysis is identified by the relative significance of the clusters produced by real gravitational-wave signals to those produced by background noise. This is connected to the thresholds used for rejecting glitches. Low threshold allows background noise glitches to survive, but high threshold might reject the gravitational-wave signals.

To optimize the trade-off between signal acceptance and noise rejection, we maximize the search sensitivity on sets of fake signal injections. The data used is real data but it is not the data being searched in order to avoid biases in the upper limit.

For every set of veto thresholds the search computes an upper limit. The threshold, as will be described in more detail in 8.2, that gives the most constraining upper limit, is the one selected.

The details of this tuning are reported in a web page, one for each neutrino trigger, that is generated automatically at the time of the tuning analysis. When we run the actual search looking for the search window, to look for GW signals in coincidence with neutrino, we use the optimized thresholds. As a result of the actual search a second web page is produced listing detection candidates and upper limits.

## Statistical and Systematic Errors

There are several sources of error that can affect our analysis. The principal ones are calibration uncertainties (amplitude and phase response of the detectors, and relative timing errors)<sup>3</sup>, and uncertainty in the sky position of the HEN trigger<sup>4</sup>.

The search is able to account for these effects automatically in tuning and upper limit estimation. Specifically, X-PIPELINE's built-in simulation engine for injecting GWB signals perturbs the amplitude, phase, and time delays for each injection in each detector to simulate the presence of these

---

<sup>3</sup> We model the amplitude, phase, and time-delay errors as Gaussian distributions. We assume they are independent for each detector. The systematic errors in amplitude are order of 10% for each detector and in phase  $\sim 4^\circ$  below 1.9kHz. During S5/VSR1 it's considered systematic time delay of +120  $\mu$ s (L1) or 200  $\mu$ s (H1,H2) for the LIGO interferometers and 6  $\mu$ s for Virgo. This is taken as a approximate worst-case scenario for the problems in modelling the time delay.

<sup>4</sup>The uncertainties in sky position are connected to the lognormal distribution, see eq 6.9.

uncertainties. The perturbations are drawn from Gaussian distributions with mean and variance matching the calibration uncertainties for each detector. Furthermore, the HEN sky position can be perturbed in a random direction.

The effect of calibration and sky-position uncertainties is in the GW-HEN analysis in this manner, removing the need to do any additional error analysis.

# Chapter 8

## The 2007 data search

### 8.1 Introduction

In this chapter we present the results of the search for gravitational waves associated with 216 neutrino candidates that were identified by the underwater neutrino telescope ANTARES during the fifth LIGO science run and the first Virgo science run. The HEN data used in this analysis were collected from 2007 January 27 to 2007 September 30, they are shown in the table 9.1. The search uses the network analysis method described in chapter 7. We first describe before the peculiarity of the ANTARES trigger list, then how we address the issue related to the presence of a mirror image in the identification of the neutrino candidate and we conclude by presenting the results of our search.

#### 8.1.1 ANTARES trigger list

Of the sample 216 of neutrino candidates of table 9.1, 198 were reconstructed with two lines and 18 were reconstructed with 3 lines. The columns in the table correspond to:

- the neutrino arrival time in Julian Day specified for epoch J2000;
- the equatorial coordinates: right ascension and declination ( $\alpha, \delta$ ) of each trigger;
- number of lines and number of hits used in the fit of the track;

- angular search window (ASW) for both median and 90% quantile;
- the weight is equal to 0.5 for event reconstructed with 2 lines and equal to 1 for events reconstructed with 3 lines;
- Log-normal fit parameters ( $\theta$ ,  $m$  and  $\sigma$ ) for the distribution for the position error (see eq. 6.9);

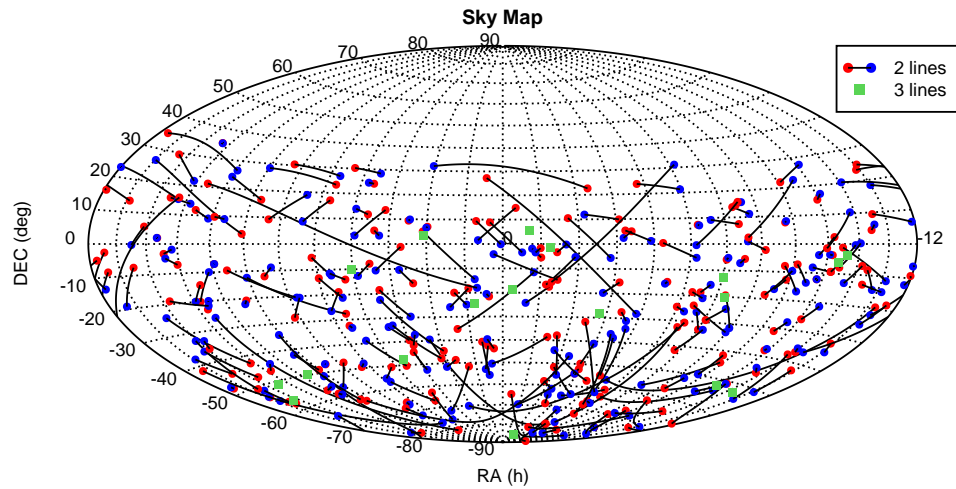


Figure 8.1: Skymap of the full set of selected 216 HEN events in equatorial coordinates. A line connects the associated mirror solutions for events reconstructed with two lines as described in Section 8.2 in which the red dot is the first realization and the blue one its image. Green squares indicate neutrinos reconstructed with three lines.

## 8.2 Handling 2-line ANTARES triggers

For a particle trajectory reconstructed from a Cherenkov cone (see paragraph 5.4) giving hits on only two straight detector lines, there always exists an alternative trajectory having an identical  $\chi^2$  value, but a different direction. The degenerate trajectory is the mirror image of the original track in the plane formed by the two lines, see APPENDIX B for a complete derivation. As a consequence, each event reconstructed with only two lines will have two

equiprobable arrival directions, which must be taken into account during the GW analysis. Figure 8.1 is a sky map of the full set of candidate HEN events showing the degenerate solutions connected with a black line and triggers reconstructed with 3 lines are in green.

In our search we set up a grid that covers the error circle regions associated with each neutrino location.. Two different examples of a neutrino candidate with its mirror solution and error box are shown in figure 8.2 and 8.3. Picture 8.2 displays one case in which the error boxes of the two neutrino locations overlap, on the contrary the plots in 8.3 show two error circles far from each other.

The GW search covers the sky position error box(es) with a set of points. Each point is assigned a prior probability of how likely it is to be the true position of the source (HEN). The most likely point is assigned a probability of one. The other points are assigned probabilities accordingly scaled. We perform the GW analysis as described in the chapter 7 (adding data streams, making time-frequency maps, finding clusters of loud pixels) separately for each grid point. Finally, clusters from different grid points are compared and then take the loudest from the entire set of points.

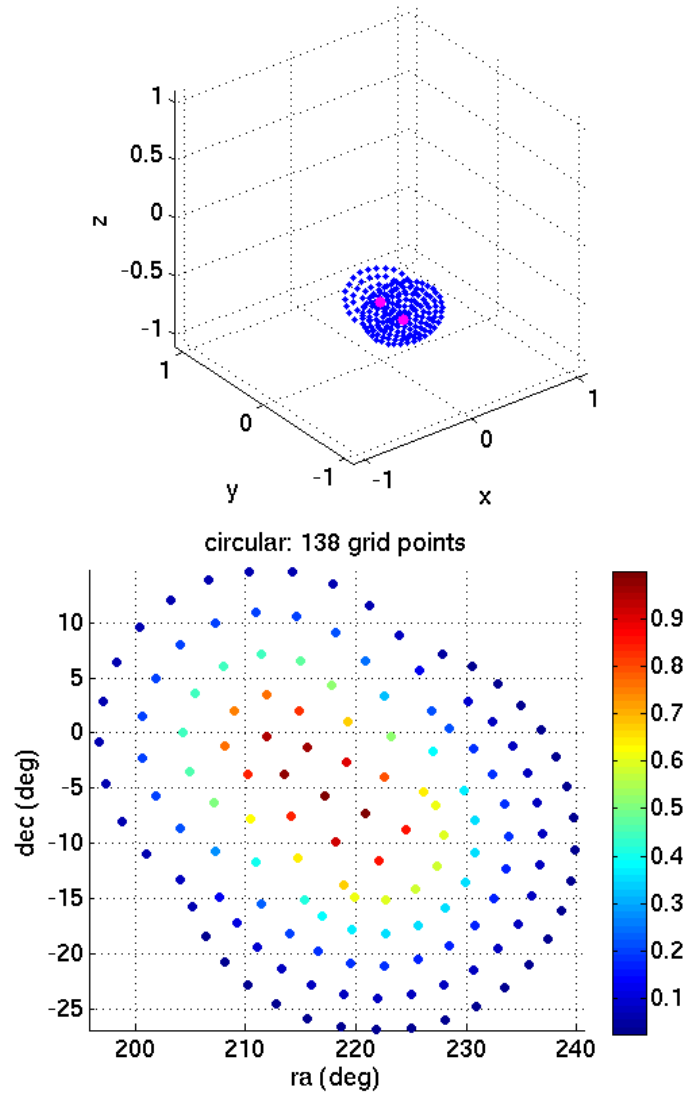


Figure 8.2: Searching for one point and its mirror image at once (example 1) the equatorial coordinates for the first trigger are  $\alpha_1 = 221.99$  [deg],  $\delta_1 = -9.38$  [deg]; for the second one  $\alpha_2 = 211.85$  [deg],  $\delta_2 = -0.36$  [deg], at the same GPS time 864109778.

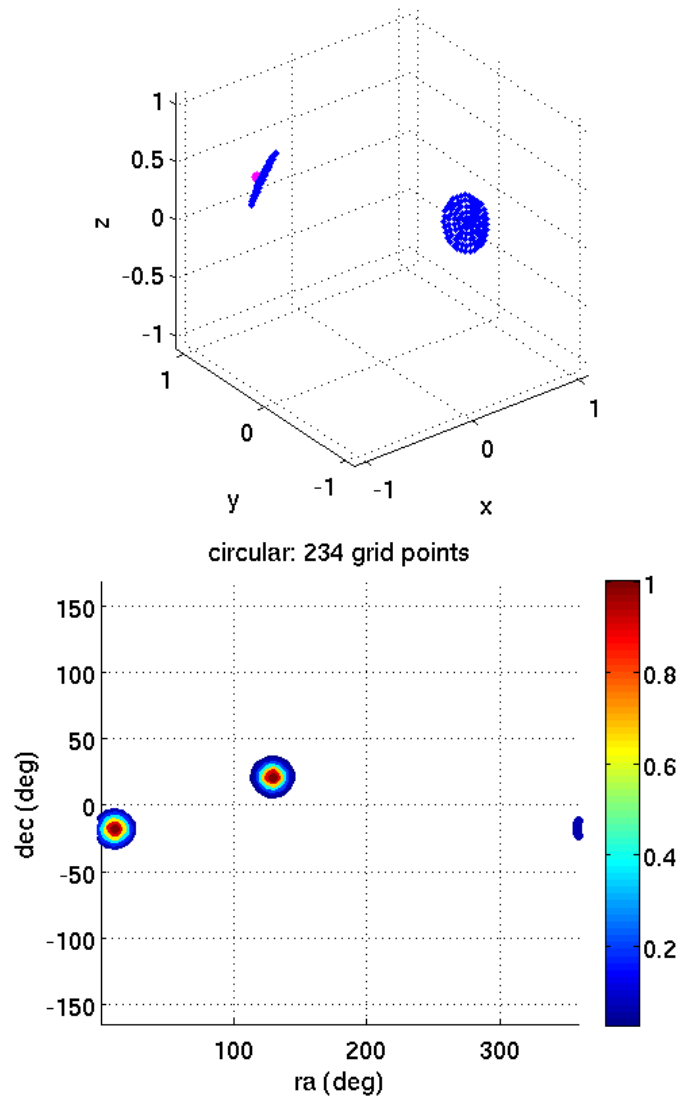


Figure 8.3: Searching for one point and its mirror image at once (example 2) the equatorial coordinates for the first trigger are  $\alpha_1 = 129.103$  [deg],  $\delta_1 = 21.156$  [deg] for the second one  $\alpha_2 = 10.426$  [deg],  $\delta_2 = -17.959$  [deg], at the same GPS time 868055770.

### 8.2.1 Probability distribution

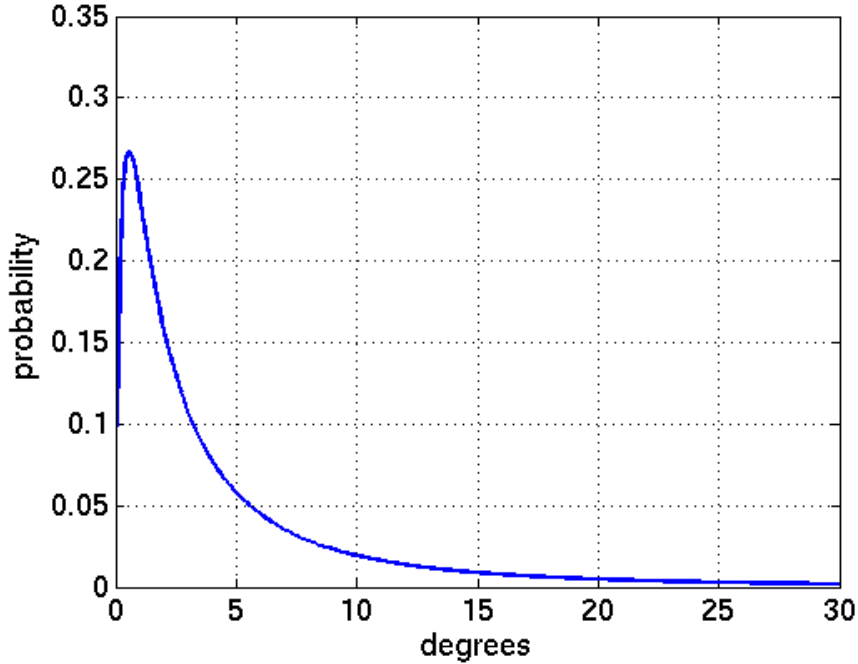


Figure 8.4: Example of LogNormal distribution  $f(x) = \frac{1}{\sqrt{2}} \frac{e^{-(\ln((x-\theta)/m))^2/2\sigma^2}}{(x-\theta)\sigma}$  where the parameters are  $\theta = 0.05033$ ,  $m = 2.59$  and  $\sigma = 1.186$ .

Fake signals are injected and then searched for at various stages of the analysis, for example for veto tuning and for the determination of the upper limits. The injections are performed assuming that the injected GW signal may come from any point in the error circle regions around the most likely neutrino location, each point with a probability which is described by eq. 6.9 where  $x$  is the angular distance to the most likely location, and displayed in the plot 8.4. Figure 8.5 shows a normalized histogram for  $x$  for a set of injections. The distribution agrees well (91% confidence in a Kolmogorov-Smirnov test) with that of 6.9, which demonstrates that this important part of the software works correctly.

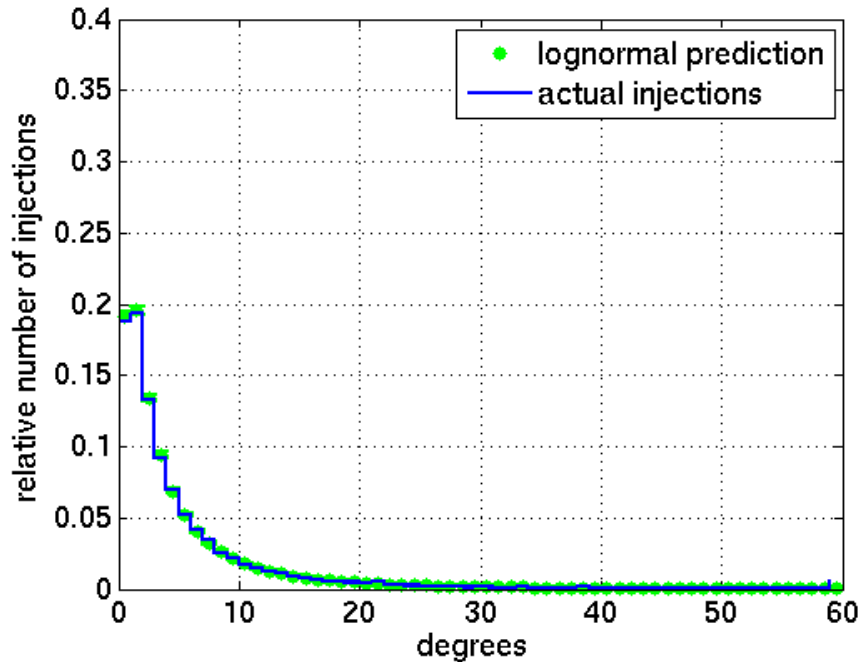


Figure 8.5: Plot shows the agreement between the sample of injections used (blue) and the Lognormal distribution (green).

### 8.3 Check performed: coincidences with the GWG Catalogue

In order to try and associate a neutrino candidate with its putative host galaxy we looked for spatial coincidence between our neutrino trigger list and the so called Gravitational Wave Galaxy Catalogue (GWGC) [244]. This catalogue is composed of all galaxies within 100 Mpc and it is currently being used to look for electromagnetic counterparts in gravitational wave searches. The GWG catalogue has been produced from the union of four existing catalogues: the Catalog of Neighboring Galaxies, an updated version of the Tully Nearby Galaxy Catalog, the V8k catalogue and HyperLEDA. The result is a catalogue of 53,255 galaxies with information on sky position, distance, blue magnitude, major and minor diameters, position angle, and galaxy type. The errors for these quantities are taken from the literature and

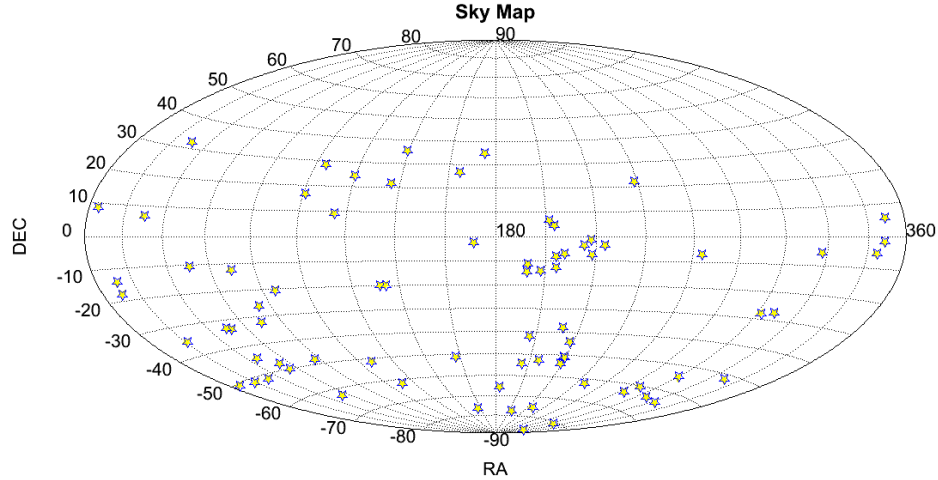


Figure 8.6: This picture displays 77 coincidences found between the neutrino list and the GWG catalogue. The yellow stars stand for the neutrino positions and the empty blue stars mark the galaxies.

measurement methods.

Considering the nominal error box for the ANTARES Telescope in the full 12-line configuration,  $0.3^\circ$ , we found 77 coincidences between the positions of our neutrino triggers and the galaxies contained in the GWG catalogue, as shown in the picture 8.6. Unfortunately, none of those galaxies is in a radius of 10 Mpc from the Earth which can be visible by the existing detectors of gravitational waves and neutrinos. However, this search may still find coincident GW-HENs from an isolated source.

## 8.4 Injected waveforms

In order to produce samples of data with gravitational wave signal, waveforms with different parameters are added in software to the data and the same trigger production and processing is applied to these samples. The waveforms used are chosen to be representative of our expectations for astrophysical models (compact binary coalescence and stellar collapse, see chapter 3). We inject the same waveform 582 times, in different noise. Half of these injections are used for tuning and half for sensitivity estimation, as described

in paragraph 7.3.7.

We use a mix of generic and few specific GW waveforms. The generic waveforms are Gaussian-modulated sinusoids, see plot 8.7:

$$h_+ = \frac{(1 + \cos^2 \iota)}{2} \frac{h_{\text{rss}}}{(2\pi\tau^2)^{\frac{1}{4}}} e^{-\frac{(t-t_0)^2}{4\tau^2}} \cos 2\pi f_0(t - t_0), \quad (8.1)$$

$$h_\times = \cos \iota \frac{h_{\text{rss}}}{(2\pi\tau^2)^{\frac{1}{4}}} e^{-\frac{(t-t_0)^2}{4\tau^2}} \sin 2\pi f_0(t - t_0). \quad (8.2)$$

Here  $f_0$  the central frequency,  $t_0$  is the central time, and we chose  $\tau = 1/f_0$  as the duration. We use central frequencies of 100 Hz, 150 Hz, and 300 Hz for the low-frequency analysis and 554 Hz and 1000 Hz for the high-frequency search. The quantity  $h_{\text{rss}}$  is the root-sum-square signal amplitude:

$$h_{\text{rss}} \equiv \sqrt{\int h_+^2(t) + h_\times^2(t) dt}. \quad (8.3)$$

This amplitude is related to the total energy  $E_{\text{GW}}$  in the gravitational-wave burst by

$$E_{\text{GW}} = \frac{2}{5} \frac{\pi^2 c^3}{G} h_{\text{rss}}^2 f_0^2 D^2 \quad (8.4)$$

as shown in section 7.3.7. This waveform is consistent with the GW emission from a rotating system viewed from an inclination angle  $\iota$  to the rotational axis. We select the inclination uniformly in  $\cos \iota$  with  $\iota \in [0^\circ, 5^\circ]$ . This corresponds to a nearly on-axis system, such as would be expected for association with an observed long GRB.

For astrophysical injections we use the gravitational-wave emission of inspiraling neutron star and black hole binaries, which are widely thought to be the progenitor of short GRBs. Specifically, we use the post-Newtonian model for the inspiral of a double neutron star system with component masses  $m_1 = m_2 = 1.35M_\odot$  see plot 8.8, that for a black-hole/neutron-star system with  $m_1 = 5M_\odot$ ,  $m_2 = 1.35M_\odot$  see plot 8.9, [198]. We set the component spins to zero in each case. Motivated by estimates of the jet opening angle for short GRBs, we select the inclination uniformly in  $\cos \iota$  with  $\iota \in [0^\circ, 30^\circ]$ .

For each HEN trigger, the injections are distributed uniformly in time over the search window. The injection sky positions are selected randomly following the estimated probability distribution (6.9) for the HEN trigger, to account for the uncertainty in the true HEN position. The polarization

angle (orientation of the rotational axis on the sky) is distributed uniformly. Each injection is characterized by the following parameters: GPS time; sky positions of the source; the polarization angle  $\psi$  that defines what is the axis of the oscillation for the  $h_+$  strain; the  $h_{\text{rss}}$ ; the central frequency  $f_0$  which defines the nominal duration  $\tau = \frac{1}{f_0}$ . By choice, all injections are circularly polarized, the only thing that changes is the starting point of the circular rotation, or in other words the instantaneous polarization at the waveform peak. The angle is drawn randomly from a uniform distribution in  $[0, \pi]$ . Finally, the amplitude and arrival time at each detector is perturbed randomly to simulate the effect of calibration errors in the LIGO and Virgo detectors.

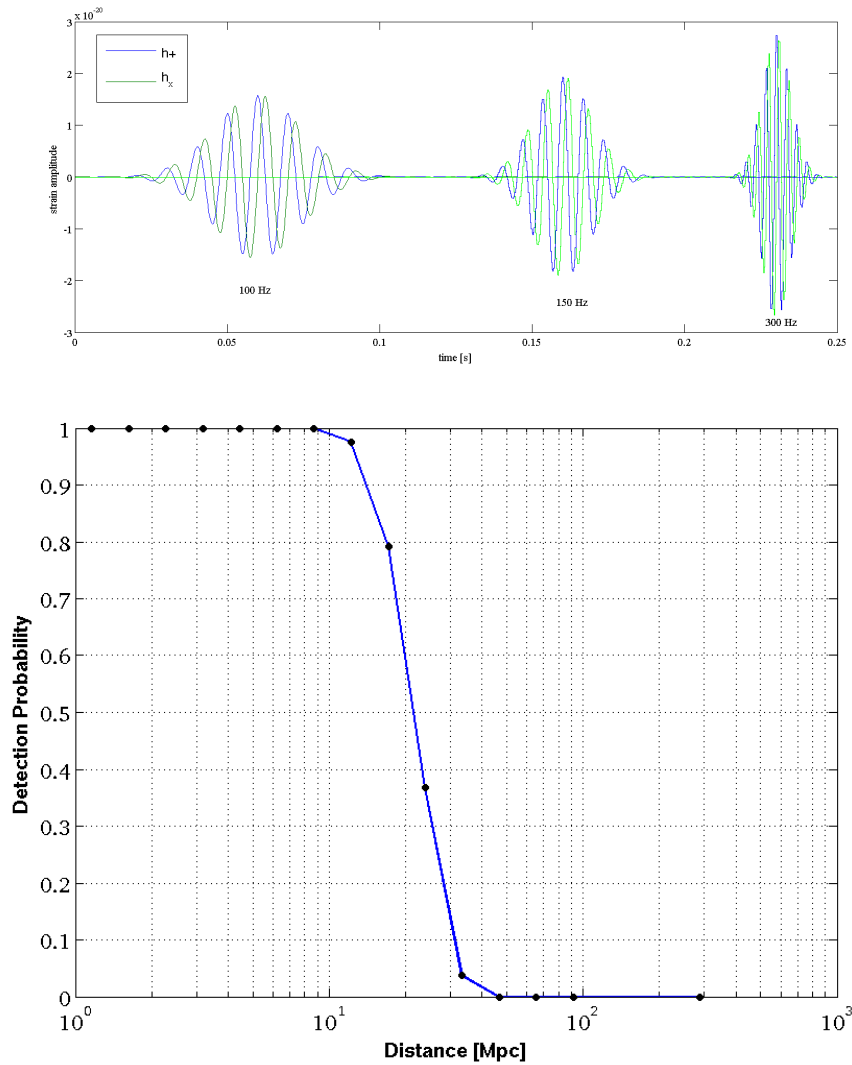


Figure 8.7: In the upper part there are 3 sin Gaussian waveforms at 100 Hz, 150 Hz, 300 Hz. The bottom plot shows the fraction of simulated Gravitational Waves signals detected at a false-alarm probability of 1%. To convert injected signal amplitude into distance we assume that an energy  $E_{GW} = 10^{-2} M_{\odot} c^2$  is emitted.

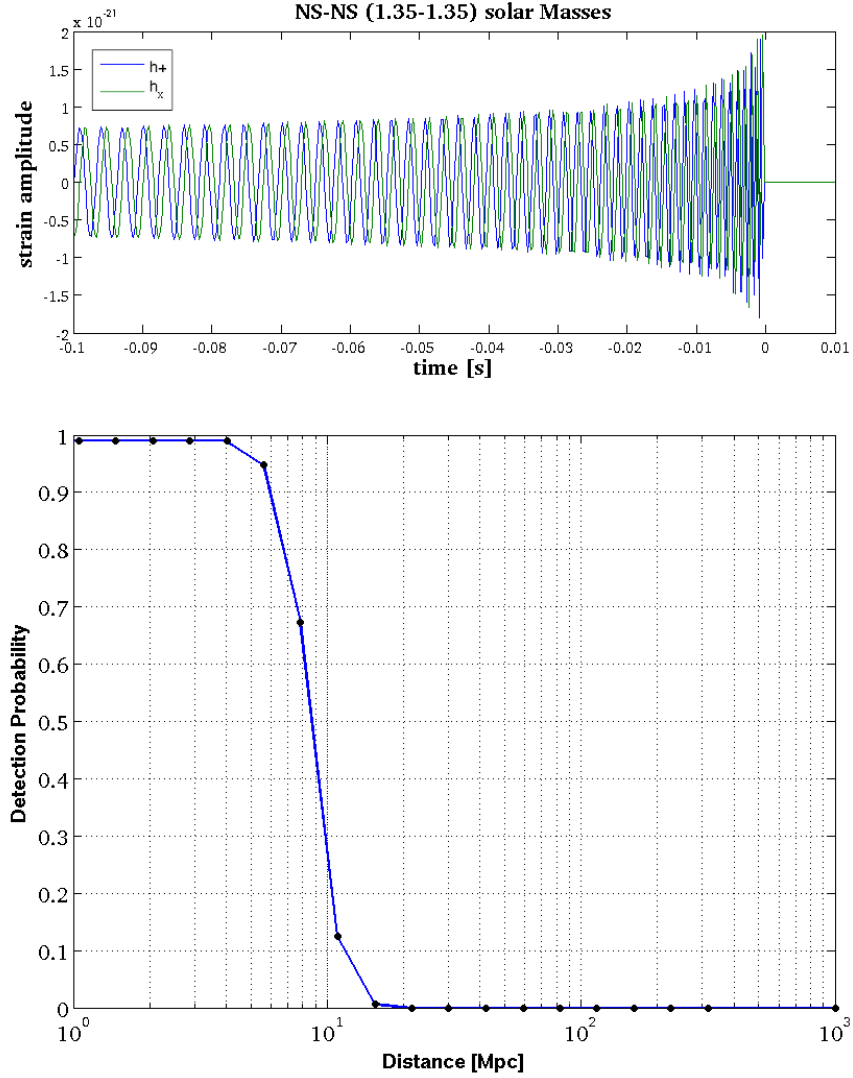


Figure 8.8: The first plot shows the inspiral waveform of two neutron stars of  $1.35 M_{\odot}$  in the last 100 ms before the merge. The second one is the detection efficiency plot: fraction of simulated Gravitational Waves signals detected at a false-alarm probability of 1%.

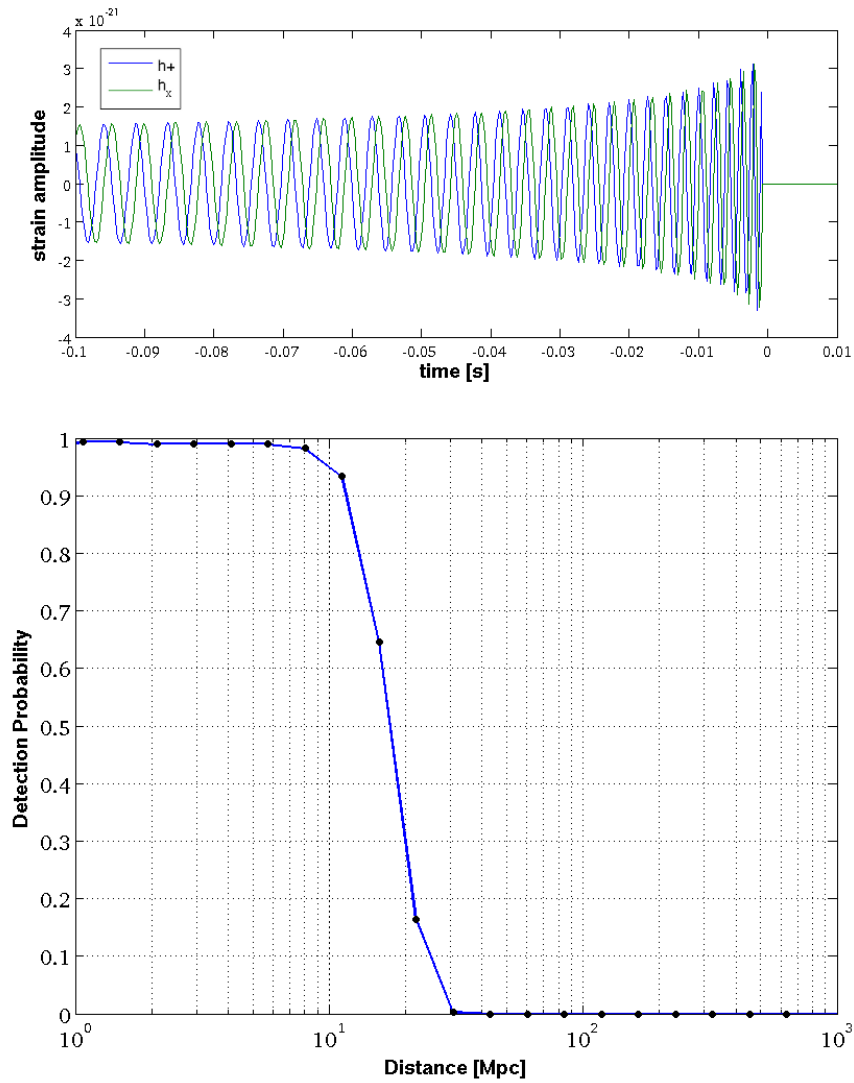


Figure 8.9: The first plot displays the inspiral waveform of a black hole of  $5M_{\odot}$  and a neutron stars of  $1.35 M_{\odot}$  in the last 100 ms before the merge. The second one is the detection efficiency plot: fraction of simulated Gravitational Waves signals detected at a false-alarm probability of 1%.

## 8.5 Search procedure: low and high frequency analysis

Given our knowledge of possible GW sources discussed in Chapter 3, the most likely detectable signals at extra-galactic distances are in the low-frequency band ( $f \lesssim 500$  Hz), where our detectors have maximum sensitivity, see Fig 4.4. At the same time, the computational cost of the search increases at high frequencies. This is in part due to the extra data to be analyzed because the frequency band is four times larger than the low frequency one, but also to the need for finer-resolution sky grids to keep time delay errors much smaller than one GW period. We therefore split the gravitational wave band into two regions: 60-500 Hz, and 500-2000 Hz.

The low-frequency band is analyzed for all HEN triggers – such a search is computationally feasible while covering the highest-sensitivity region of the GW detectors. However, compact objects such as neutron stars or collapsar cores have characteristic frequencies for GW emission above 500 Hz. Such emissions might be detectable from galactic sources such as soft gamma repeater giant flares, or possibly at nearby galaxies. Since the computational cost of a high-frequency search for all HEN triggers is prohibitive with the current analysis pipeline, we perform the 500-2000 Hz analysis on the 3-line HEN triggers only. The 3-line events are a small subset ( $\sim 10\%$ ) of the total trigger list and the most reliable, and have the smallest sky position uncertainties, and therefore the smallest computational cost for processing.

To reduce the computational cost further, we use the same sky grid for the high-frequency search as was used at low frequencies, after determining that the loss of sensitivity is acceptable, see plots 8.10 and 8.11. The high-frequency analysis is performed independently of the low-frequency analysis (independent tuning, background estimation, etc.) using the same automated procedure. In the following sections we will present the results of the low-frequency and high-frequency searches separately.

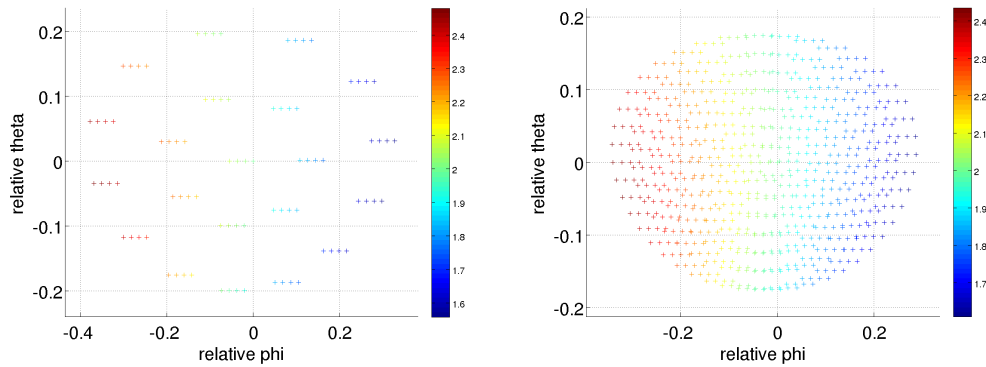


Figure 8.10: On the left there is the sky grid we use for the low-frequency and high-frequency analysis. On the right there is a finer sky grid we tested.

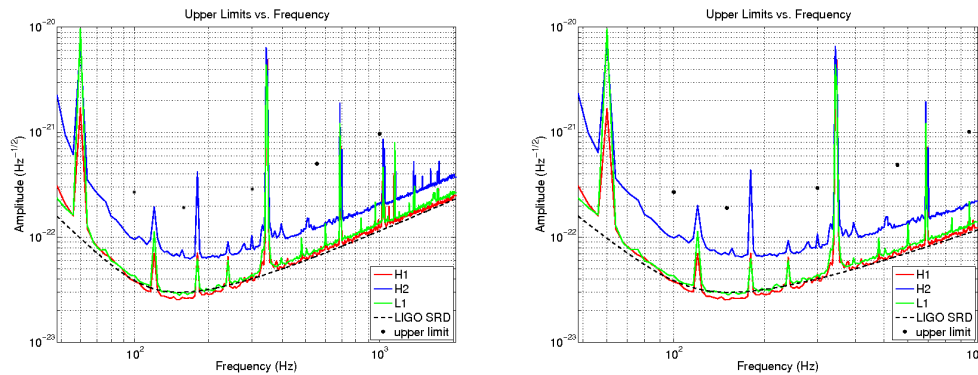


Figure 8.11: On the left, the upper limits are superimposed to the strain sensitivity curves, in a search done with the normal sky grid. On the right, the upper limits obtained using the finer grid. These upper limits differ only slightly less than 10% from the previous ones. For this reason we don't use the finer sky grid.

## 8.6 Coincident Search Results

From the full set of 216 independent neutrino candidates, 158 occurred at times when at least two gravitational-wave detectors were operating. Since

two or more detectors are required to discriminate GW signals from background noise (as described in Section 7.2.2), in the following we consider only these remaining 158 HEN candidates: 144 2-line events and 14 3-line events, for more details see sketch 8.12

<b>HENs (2 lines)</b>	<b>4 IFOs</b>	<b>3 IFOs</b>	<b>2 IFOs</b>
<b>144</b>	<b>60</b>	<b>59</b>	<b>25</b>
<b>HENs (3 lines)</b>	<b>4 IFOs</b>	<b>3 IFOs</b>	<b>2 IFOs</b>
<b>14</b>	<b>3</b>	<b>7</b>	<b>4</b>

Figure 8.12: This sketch displays the distribution of the 158 neutrino candidate considering the interferometers (IFOs) in network. (top) In the 144 2-line cases: 60 candidates are analysed with 4 detectors, 59 with 3 and 25 with 2 interferometers. (bottom) For the 14 3-line neutrinos: 3 have 4 detectors, 7 with 3 detectors and 4 with 2 interferometers.

As explained in chapter 7, the analysis is carried out in the search window (open-box) in the same way of the closed-box analysis. The same types of plots we have shown before for the off-source search, see figure 7.10, are generated for the on-source search, see figure 8.13. These plots display  $I_{\text{null}}$  vs.  $E_{\text{null}}$  for clusters produced by background noise and by simulated gravitational-wave signals in the on-source. Loud glitches are vetoed by discarding all clusters that fall below the dashed line.

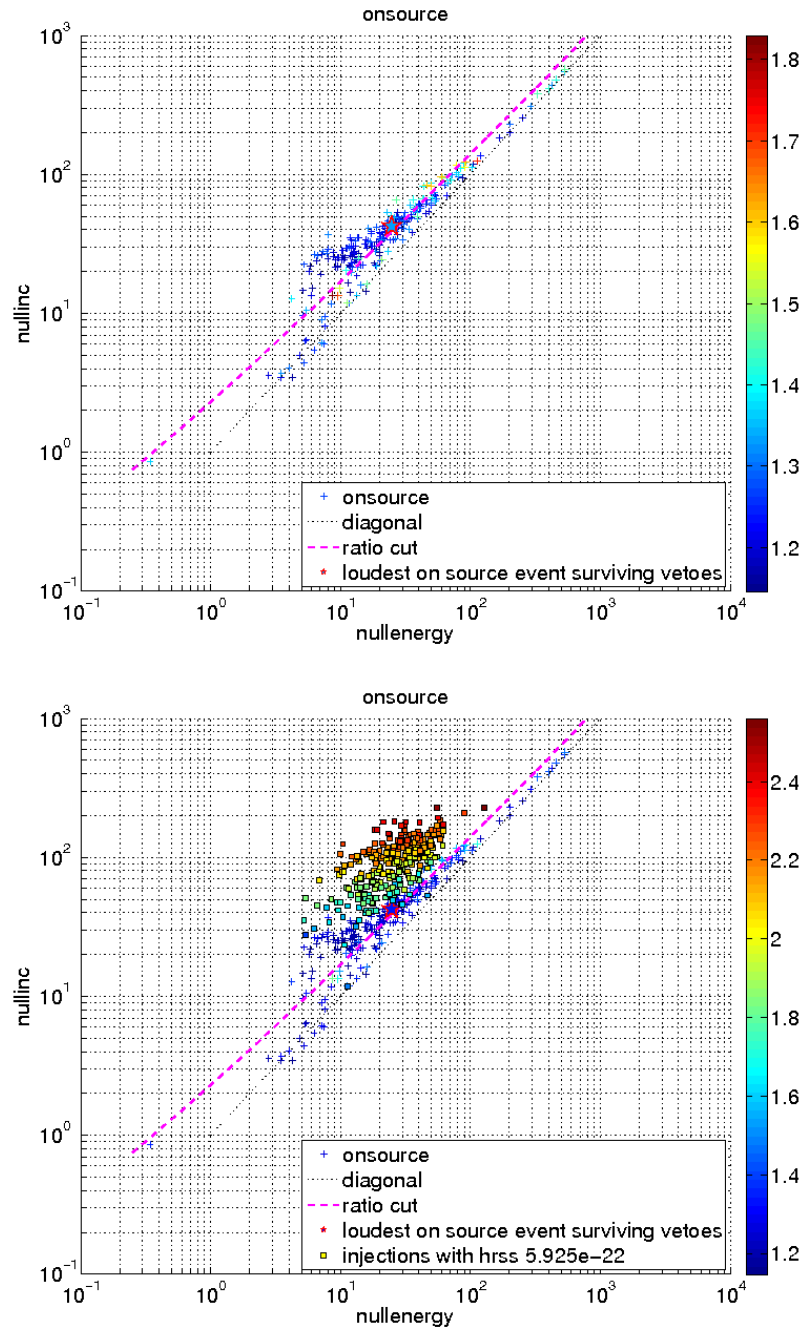


Figure 8.13:  $I_{\text{null}}$  vs.  $E_{\text{null}}$  for clusters produced by background noise (+) and by simulated gravitational-wave signals ( $\square$ ). The color axis is the base-10 logarithm of the cluster significance  $\mathcal{S}$ . Loud glitches are vetoed by discarding all clusters that fall below the dashed line.

### 8.6.1 Per-HEN GW Candidates

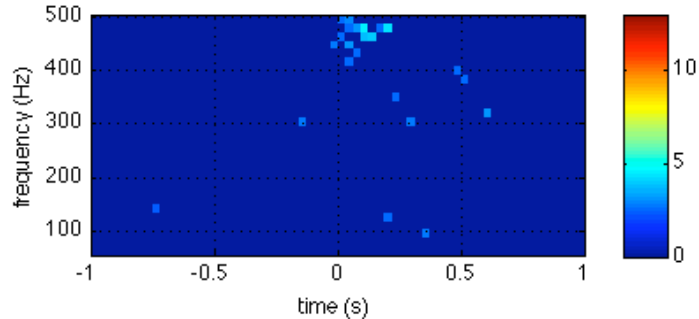


Figure 8.14: Time-frequency map of our outlier, ID = Nu385\_386, for the low-frequency analysis. The color-bar shows the signal to noise ratio (SNR) of this event.

We analyze gravitational data in coincidence with 158 neutrino triggers for the low frequency search, and 14 neutrino triggers for the high frequency search. In the low frequency analysis, only one neutrino trigger had a corresponding GW event with false alarm probability below the threshold of  $p = 0.01$  to warrant further investigations, see plot 8.14. We found no such candidates in the high frequency search.

For the low-frequency candidate with ID = 385\_386, additional time shifts totaling 18064 background trials yielded a refined false alarm probability of  $p = 0.004$ , which is not significant given a trials factor of 158 ( $158 \times 0.004$ ). This event came from analysis of the H1, H2, and V1 data, see tables 8.15. Follow-up checks were performed, including checks of detector performance recorded by monitoring programs and operator logs, and scans of data from detector and environmental monitoring equipment to look for anomalous behavior. In section 8.7 we will describe these follow-up checks. For this specific candidate while these checks did not uncover a physical cause for the event, they did reveal that it occurred during a period of glitches in V1, see plot 8.16.. We conclude that we have no clear gravitational wave burst signal associated with any of our sample of 158 neutrino triggers.

<b>name</b>	<b>Nu385_386</b>	<b>Frequency range</b>	<b>(480-504) Hz</b>
<b>Right ascension</b>	<b>204.404 deg</b>	<b>Duration</b>	<b>250 ms</b>
<b>Declination</b>	<b>-13.027 deg</b>	<b>SNR H1</b>	<b>6.7</b>
<b>GPS</b>	<b>873597124</b>	<b>SNR H2</b>	<b>6.3</b>
<b>network</b>	<b>H1H2V1</b>	<b>SNR V1</b>	<b>7.2</b>
<b>FAP (p-value)</b>	<b>0.004</b>		

Figure 8.15: These two table show the name, right ascension and declination, GPS time and network of our outlier. In addition there are the information coming from the search: false alarm probability, frequency range, duration and signal-to-noise-ratio (SNR) in each detector.

## 8.7 Follow up

Further investigations are needed when one has a GW candidate event to establish if it is a real signal or a background event. Through this process, known as *Follow-up*, we verify the status of all detectors available at that time and check the monitors in the control room to provide information regarding loss of lock, site disturbances, data corruptions and hardware injections. A complete web page with the whole set of checks, performed on the GW candidate associated with neutrino 385\_386, can be found at the following link [https://atlas1.atlas.aei.uni-hannover.de/~irene/FOLLOWUP/FollowUp385\\_386.html](https://atlas1.atlas.aei.uni-hannover.de/~irene/FOLLOWUP/FollowUp385_386.html)

- Gaussianity check,
- Data Quality near trigger,
- Hanford-Livingston ilog,
- Omega scan.

### 8.7.1 Gaussianity check

The top plot 8.16 shows the gaussianity measure versus frequency. In the plot one block of 256 s of data is displayed. The gaussianity measure is the ratio

between standard deviation and mean of a  $\chi^2$  variable obtained by summing in time the square modulo of FFT-ed blocks of data. The expected value for such variable is 2.

From the bottom plot 8.16 we see plenty of glitches in Virgo detector at the time of Nu385\_386 candidate, as already shown in the Gaussianity check. Such disturbances can mimic a real signal in the analysis as the one produced for our outlier.

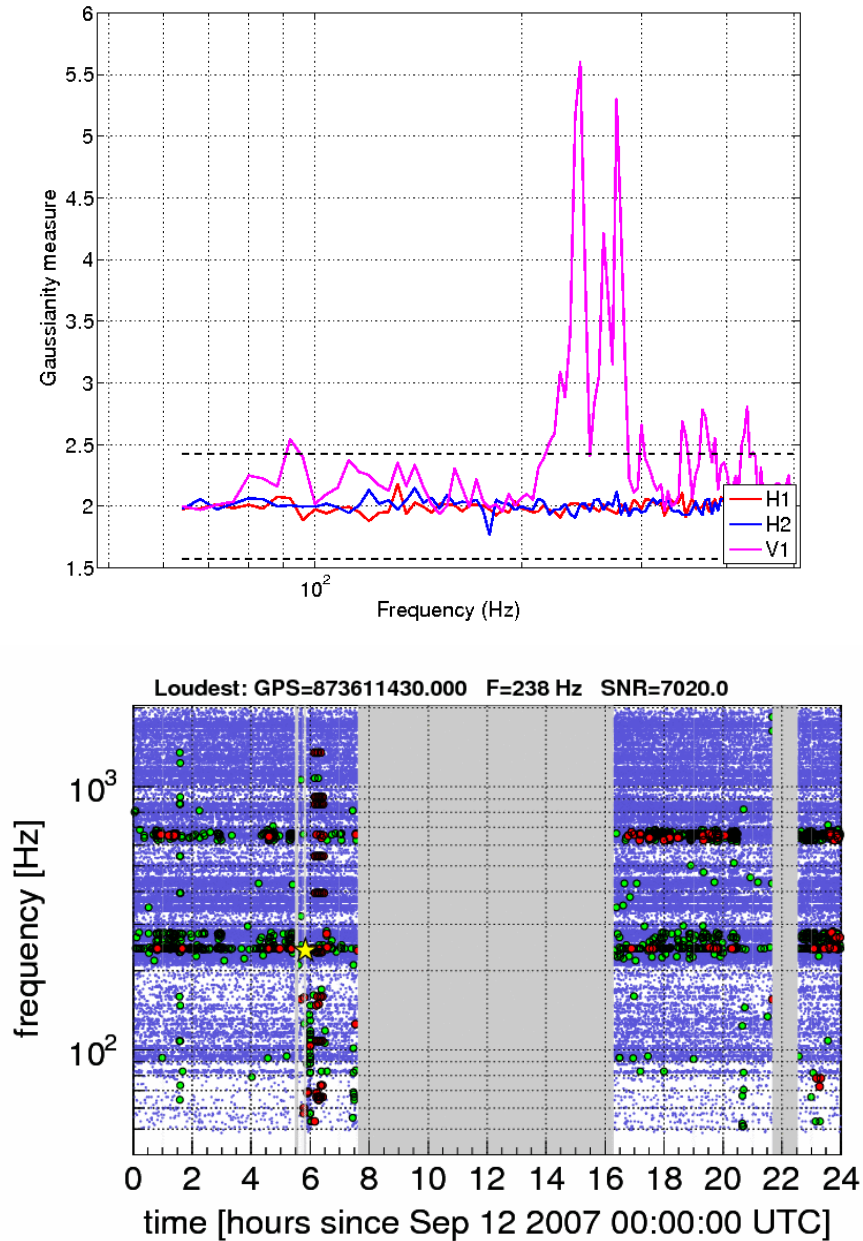


Figure 8.16: In the top plot is shown the Gaussianity check for the Nu385\_386 candidate corresponds to Sep 12 2007 01:50:26.5 UTC time, in which is evident the status of glitchiness in Virgo (V1). The dashed lines display the  $3\sigma$  deviation around the expected value. In the bottom plot is reported the status of the V1 detector glitchiness in the same day. To cross check the two plots is necessary to look at the UTC time and at the corresponding frequency, (480-504)Hz, of our outlier to see a cluster of glitches (green dots).

### 8.7.2 Figures of merit from Hanford and Livingston and data quality near trigger

Data quality flags indicate times when the detector isn't in its nominal operating range due to a saturation state in an actuator or sensor, or unusual environmental conditions. These series of data quality checks, to precisely identify the time periods to analyze, are shown in real time in the control room of each interferometer and then recorded in figures of merit (FoM).

We show few plots coming from FoMs of Sep 12 2007 with  $T_0 = 07:10:00$  UTC. The Nu385\_386 candidate appears at 01:50:26.5 UTC time. The x-axis of each plot goes from -12 to 0, that corresponds to  $T_0$ . To check what happened in coincidence with our outlier we need to look approximately in correspondence with -5 for the x-axis. We check the following plots:

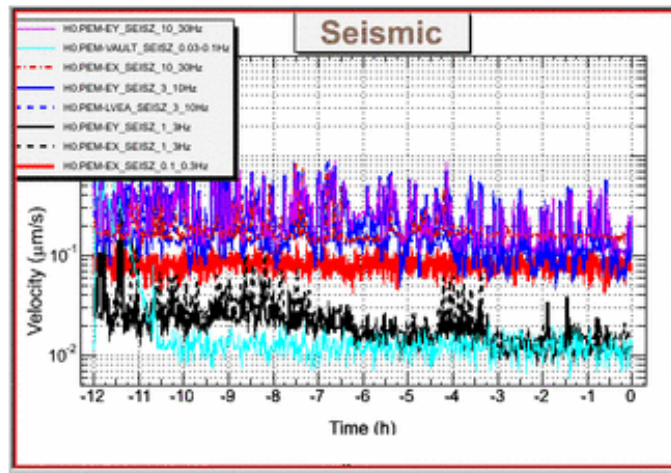


Figure 8.17: Seismic plot shows velocity in micrometers/second versus frequency in Hz. It is a fundamental tool to monitor the seismic noise produced in situ. The plot is related to Sep 12 2007 with  $T_0 = 07:10:00$  UTC. The Nu385\_386 candidate appears at 01:50:26.5 UTC time.

- 'Seismic plot' 8.17: the y axis shows the velocity in micrometers/second, to monitor the motion of the Earth. This plot displays the seismic noise (from earthquake, train, wind, storm to men at work near the interferometer) at different frequencies. In correspondence with -5 in time

there wasn't anything anomalous in the Earth's motion.

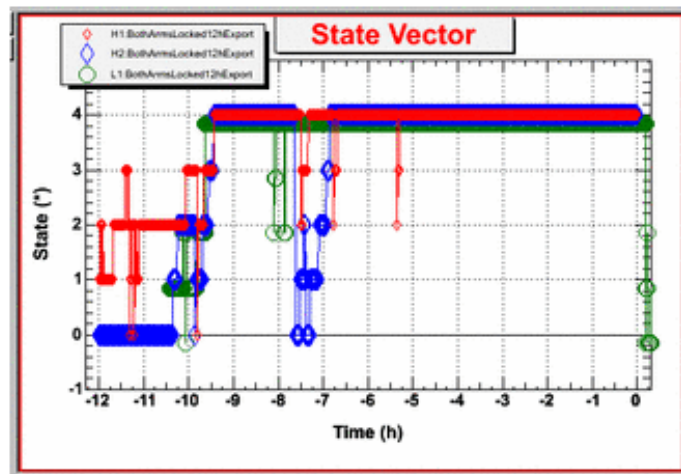


Figure 8.18: State vector plot displays if the detector is in science mode (4) or when is out of locking (0). The plot is related to Sep 12 2007 with  $T_0=07:10:00$  UTC. The Nu385\_386 candidate appears at 01:50:26.5 UTC time.

- 'State vector plot' 8.18: this is an integer between -1 and 4 indicating how close we are to science mode. 4 is science mode; 3 means ready to go to science mode if the operator and scimon judge it's appropriate. When the detector is not locked, the state vector falls well below -1, and no data is recorded for that time. The interferometers were in science mode at the time of our outlier.
- 'Calibration lines plot' 8.19 originate as the calibrator tracks the optical gain and the feedback loop of the servos, to verify the stability of the detector. It is important that the tracking is monitored continuously. In correspondence with the time of Nu385\_386 trigger there was a loss in the stability of H1.

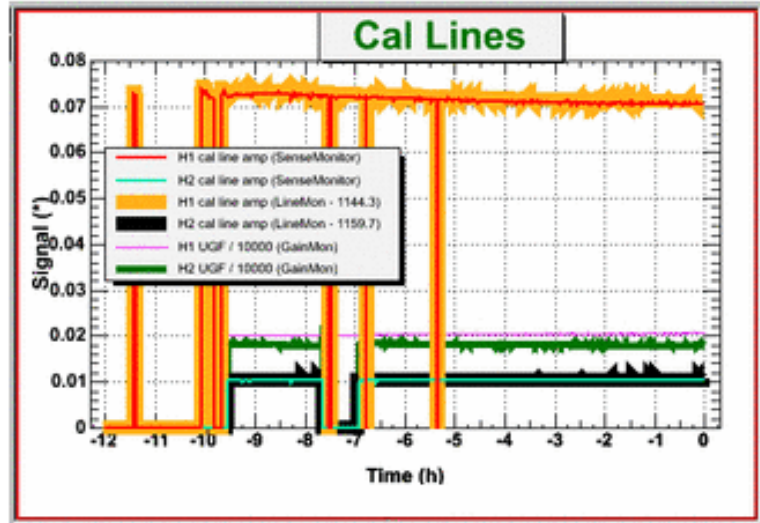


Figure 8.19: Calibration lines plot shows the stability of the detector. The plot is related to Sep 12 2007 with  $T_0 = 07:10:00$  UTC. The Nu385\_386 candidate appears at 01:50:26.5 UTC time.

Other important plot are:

- 'BurstMon plot' 8.20 indicates the present of glitches in the instrument. In coincidence with the time of Nu385\_386 candidate glitches are present both in H1 and H2.
- 'AS\_Q Band plot' 8.20 (bottom plot): this plot displays the raw output of the each interferometer, H1 and H2, divided in several frequency bands in function of the time. The black line is a pulsar injection line, that is continuous in time and it was there at the time of Nu385\_386 trigger. The injected pulsar signal was a few orders of magnitude lower than a detectable amplitude and could not have generated the Nu385\_386 candidate.

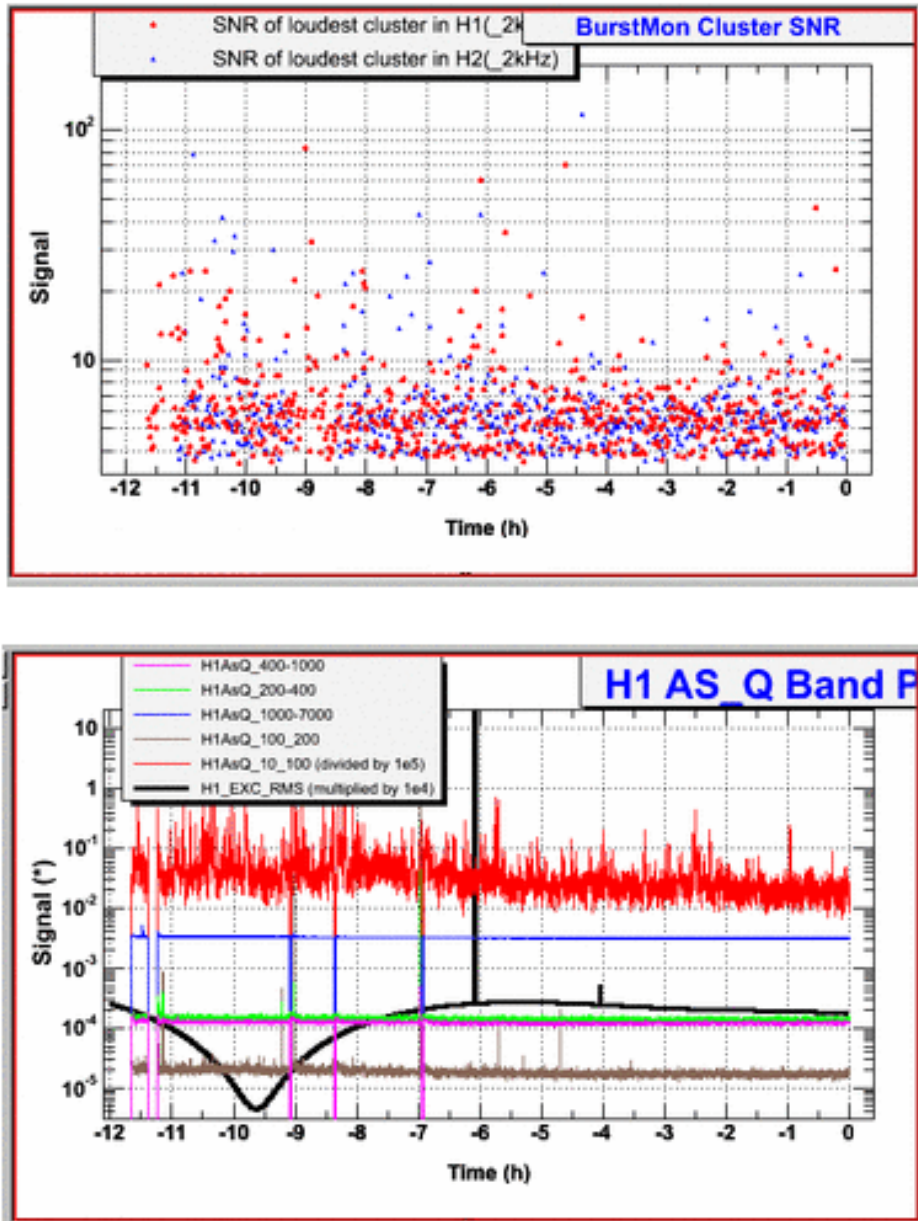


Figure 8.20: Top plot: BurstMon plot displays the status of glitchiness of each detector. The plot is related to Sep 12 2007 with  $T_0 = 07:10:00$  UTC. The Nu385\_386 candidate appears at 01:50:26.5 UTC time. Bottom plot: *AS\_Q* Band plot indicates the raw output of the each interferometer in several frequency bands in function of the time. The plot is related to Sep 12 2007 with  $T_0 = 07:10:00$  UTC. The Nu385\_386 candidate appears at 01:50:26.5 UTC time.

### 8.7.3 Omega scan

Omega scan is a tool for glitch investigation, to perform a detailed study of the LIGO-Virgo data stream around a specific time of interest (such as a candidate gravitational-wave event, a detector glitch, or a hardware injection). In addition to displaying the time series and time-frequency spectrograms of gravitational-wave channel data, Omega Scan can also efficiently search a large number of auxiliary and environmental channels for statistically significant signal content.

The program takes a specific time as an input, and produces a time-frequency plot of the gravitational wave channel, as well as any other channel that has a significant transient within half a second before or after the requested time. The program looks for matches to damped sinusoids, so each 'trigger' has a time, a frequency, a 'Q', an amplitude and a 'significance' (SNR).

The plots shown are whitened spectra (time-frequency plots), where large power ('glitches') are represented by red colors, which means high Signal-Noise-Ratio. Blue is low, ambient noise. At the top of every row of plots 8.21, there is information about the time when the most significant transient ('tile') is found in that channel within the 1 sec span in the leftmost plot; the frequency and the Q of the best template match to the glitch at that time, a 'significance Z ( $SNR = \sqrt{2Z}$ ).

The plots 8.21 don't show any cluster of pixel with high signal to noise ratio at the time and frequency of our outlier. This means that we don't have an excess in the data due to gravitational signal but to environmental disturbances. For a comparison the plot 8.22 shows a strong injected signal observed on September 16, 2010. This event is consistent with the expected signal from merger of two black holes and/or neutron stars. For more details see <http://www.ligo.org/news/blind-injection.php>.

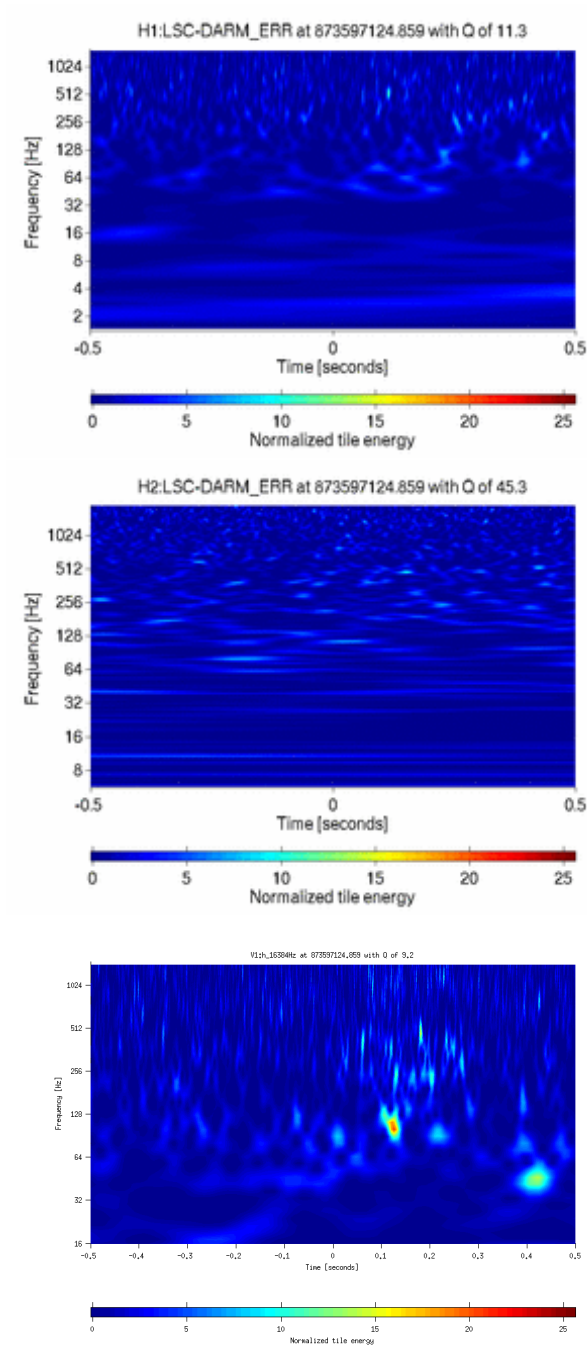


Figure 8.21: Glitch investigation plots for H1, H2 and V1 at the exact time of the trigger 873597124.859. The expected frequency of the outlier is between 480-504 Hz, with a duration of 250 ms, but there isn't any evidence of a gravitational wave signal due to the lack of cluster with high signal to noise ratio. See plot 8.22 as a reference for a fake signal.

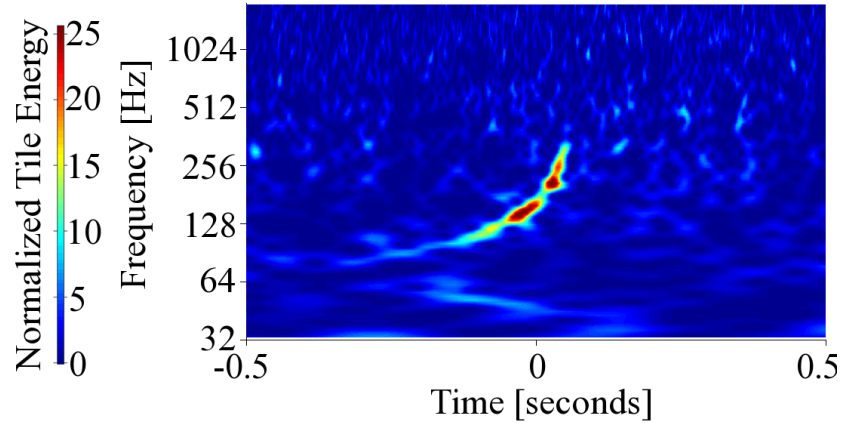


Figure 8.22: This plot is shown for a comparison with the figures 8.21. The LIGO Scientific Collaboration and the Virgo Collaboration conducted their latest joint observation run (using the LIGO Hanford, LIGO Livingston, Virgo and GEO 600 detectors) from July, 2009 through October 2010, and are jointly searching through the resulting data for gravitational wave signals standing above the detector noise levels. To make sure they get it right, they train and test their search procedures with many simulated signals that are injected into the detectors, or directly into the data streams. A rather strong signal was observed on September 16, 2010. The event was consistent with the expected signal from merger of two black holes and/or neutron stars. The figure above shows the strength of the signal (redder colors indicate more signal power) in time (horizontal axis) and frequency (vertical axis) in the LIGO Hanford detector. The signal sweeps upwards in frequency ('chirp') as the stars spiral into one another, approaching merger. Source: <http://www.ligo.org/news/blind-injection.php>

## 8.8 Search for a cumulative excess: Binomial Test

A quantitative analysis of the significance of any candidate gravitational-wave event must take into account the trials factor due to the number of neutrino triggers analyzed. To do this we use the binomial test. Under

the null hypothesis, the false alarm probabilities  $p$  associated with the most significant GW candidate from every HEN search is expected to be uniformly distributed between 0 and 1. The binomial test compares the measured  $p$  values to the uniform distribution to determine if there is a statistically significant excess of small  $p$  values (one or more) which may indicate the presence of gravitational wave signal.

Briefly, the binomial test sorts the set of  $N$  measured loudest event probabilities in ascending order:  $p_1 \leq p_2 \leq p_3, \dots, p_N$ . For each  $i \in [1, N_{\text{tail}}]$  we compute the binomial probability  $P_{\geq i}(p_i)$  of getting  $i$  or more events with  $p$  values  $\leq p_i$ :

$$P_{\geq i}(p_i) = \sum_{k=i}^N \frac{N!}{(N-k)!k!} p_i^k (1-p_i)^{N-k}. \quad (8.5)$$

Here  $N$  is the number of HEN analyzed (158 in the 60-500 Hz band and 14 in the 500-2000 Hz band). We only perform this test on  $N_{\text{tail}}$ , the top 5% of analyzed HENs. Hence,  $N_{\text{tail}} = 8$  for the low frequency band and  $N_{\text{tail}} = 1$  for the high frequency band.

The lowest  $P_{\geq i}(p_i)$  for  $i \in [1, N_{\text{tail}}]$  is taken as the most significant deviation from the null hypothesis. To assess the significance of the deviation, we repeat the test using  $p$  values drawn from a uniform distribution and count the fraction of such trials which give a lowest  $P_{\geq i}(p_i)$  smaller than that computed from the true measured  $p$  values.

Figures 8.23 show the cumulative distribution of  $p$  values measured in the low and high-frequency analyses. For the low-frequency search, bottom plot, the most significant deviation from the null hypothesis occurs for the third loudest event with  $p_3 \sim 0.013$ . In the high-frequency analysis the largest deviation from the uniform distribution is constrained to happen for  $p_1$  because we tested  $N_{\text{tail}} = 1$ . In both cases the measured  $p$  values are consistent with the null hypothesis.

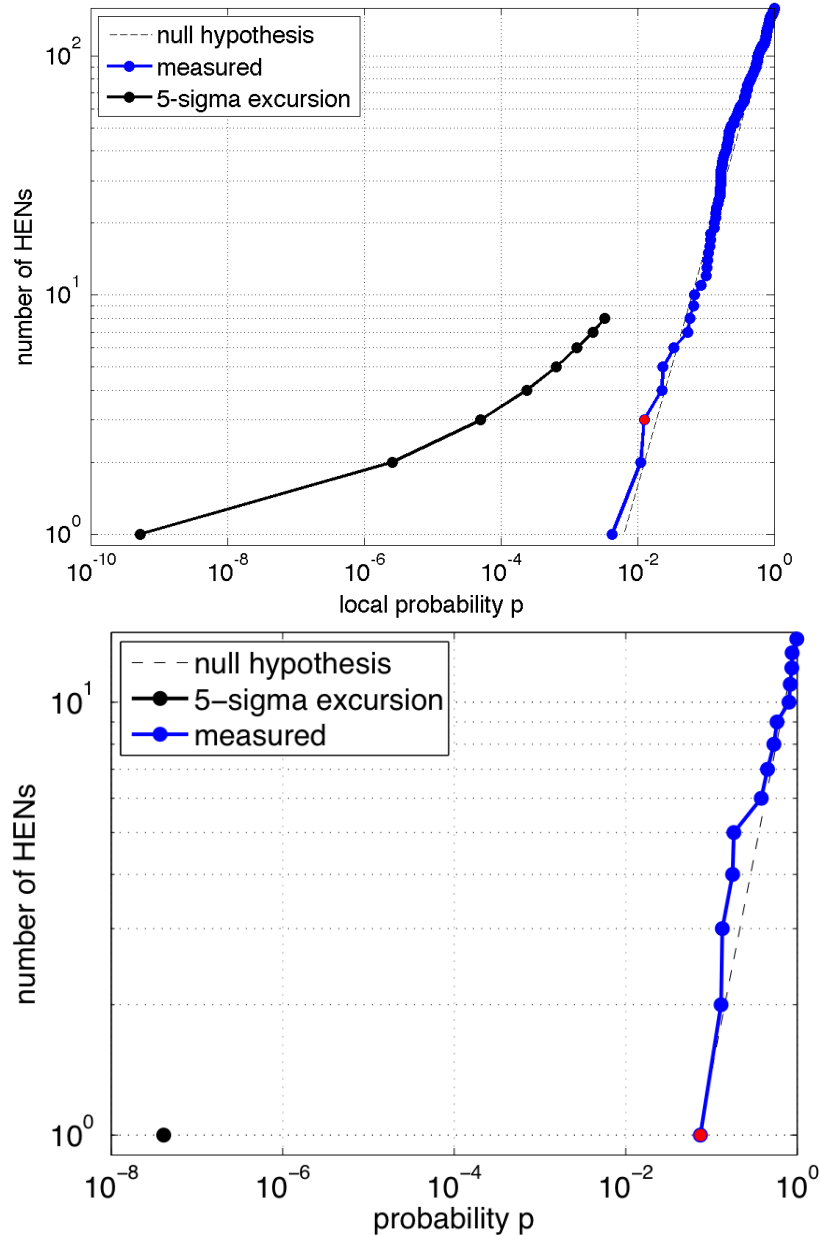


Figure 8.23: Cumulative distribution of observed  $p$  values for the loudest GW event associated with each neutrino analyzed in the low frequency analysis. The red dot indicates the largest deviation of the low  $p$  tail from the uniform distribution null hypothesis; (top plot) this occurs due to having the three loudest events below or equal  $p_3 \sim 0.013$ . Deviations this large or larger occur in approximately 64% of experiments under the null hypothesis. (bottom plot) Since  $N_{\text{tail}} = 1$ , This is is constrained to occur for  $p_1$ . Deviations this large or larger occur in approximately 66% of experiments under the null hypothesis. The black line shows the threshold for a 5-sigma deviation from the null hypothesis.

## 8.9 Upper limits and exclusion distances

The sensitivity of the search of gravitational waves is determined by a Monte Carlo analysis, as already explained in section 7.3.7. For each HEN, we add (or 'inject') simulated GWB signals into the detector data and repeat the analysis. We count an injected signal as 'detected' if it produces an event that is louder than the loudest on-source event within 100 ms of the injection time. For a given waveform morphology, we define the 90% confidence level upper limit on the signal amplitude as the minimum amplitude for which the detection probability is 0.9 or greater. The upper limits on the GWB amplitude and the corresponding lower limits on the distance for each of the HENs analyzed are given in Tables 9.2 and 9.3. These limits are computed for circularly polarized 100 Hz, 150 Hz and 300 Hz sine-Gaussian waveforms in the case of low-frequency analysis and 554Hz and 1000 Hz for the high frequency one. We compute the distance limits by assuming the source emitted  $E_{GW}^{iso} = 0.01M_{\odot}c^2 = 1.8 \times 10^{52}$  erg of energy isotropically in gravitational waves and use the following equation to infer a lower limit on  $D$ :

$$E_{GW}^{iso} \approx \frac{\pi^2 c^3}{G} D^2 f_0^2 h_{rss}^2 \quad (8.6)$$

where  $f_0$  is the central frequency,  $h_{rss}$  the root-sum-squared amplitude of the waveform and  $D$  the distance of the source.

We can associate a physical distance to each amplitude for the sine-Gaussian waveforms as well, by assuming a fixed energy in gravitational waves. For concreteness, we select  $E_{GW} = 10^{-2}M_{\odot}c^2$ . This value corresponds to the optimistic limit of possible gravitational-wave emission by various processes in the collapsing cores of rapidly rotating massive stars [274, 275, 278, 273], more conservative estimates based on 3D simulations have been made in [262, 272, 276, 271, 277]. Our 90% confidence level lower limit on the distance to a GW source associated with a given HEN trigger is then the maximum distance  $D_{90\%}$  such that for any distance  $D \leq D_{90\%}$  there is a probability of at least 0.9 that such a GW signal would have produced an event louder than the loudest on-source event actually measured.

For each type of gravitational wave simulated, the distributions of exclusion distances for our neutrino sample are shown in figures 8.24. For binary neutron star systems of  $(1.35 - 1.35)M_{\odot}$  and black hole - neutron star systems of  $(5 - 1.35)M_{\odot}$  typical distance limits are 5 Mpc and 10 Mpc respectively. For the sine-Gaussian waveforms in the low-frequency band the

typical distance limits are between 5 Mpc and 17 Mpc, while for those in the high-frequency band the typical limits are of order 1 Mpc, see plot 8.25.

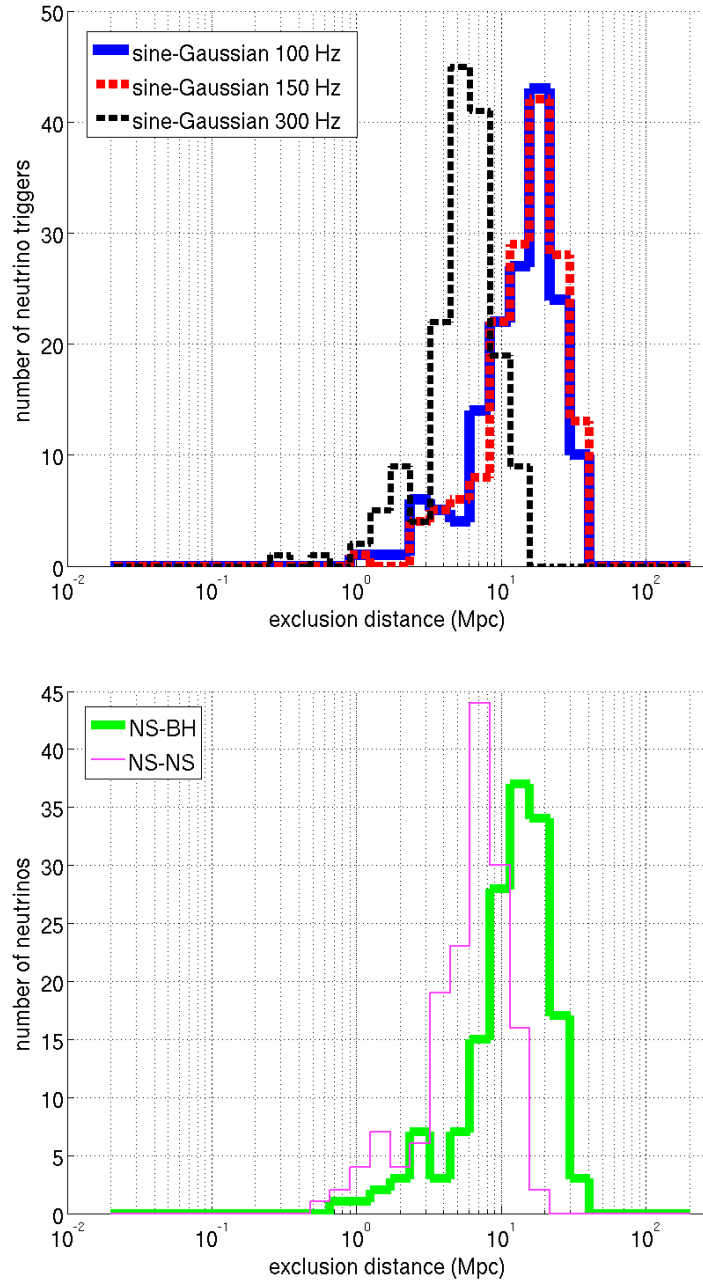


Figure 8.24: Low-frequency analysis: the top plot is the histogram for the sample of analyzed neutrinos of the distance exclusions at the 90% confidence level for the 3 types of circular sine-Gaussian models considered: 100 Hz, 150 Hz and 300 Hz. A standard siren gravitational wave emission of  $E_{GW} = 10^{-2} M_{\odot} c^2$  is assumed. The bottom plot shows histogram across the sample of analyzed neutrinos of the distance exclusions at the 90% confidence level for the 2 families of binary inspiral models considered: NS-NS and BH-NS.

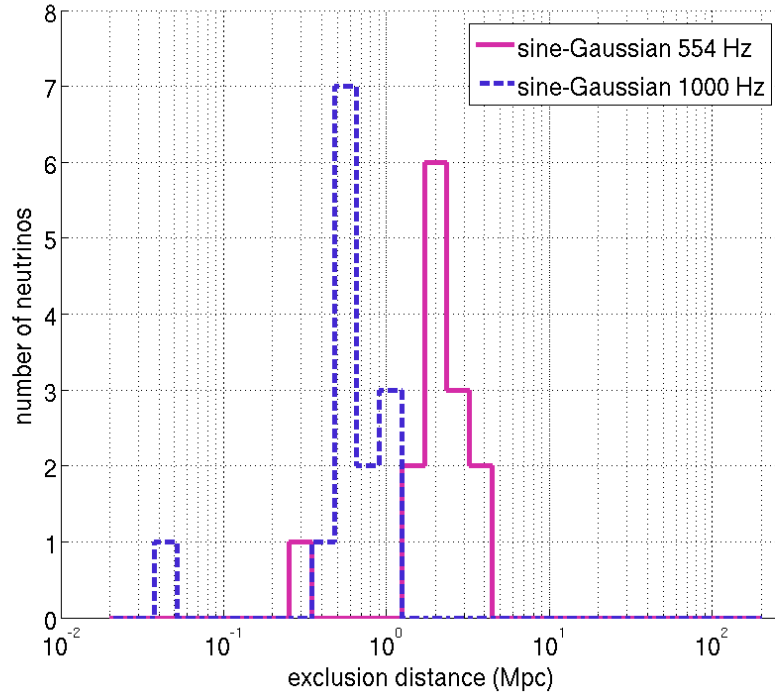


Figure 8.25: High-frequency analysis: the histogram for the sample of analyzed neutrinos of the distance exclusions at the 90% confidence level for the 2 frequencies of circular sine-Gaussian models considered: 554 Hz and 1000 Hz.

## 8.10 Astrophysical implications

Observational constraints on joint sources of GW and HEN signals have been derived in [265]. However, they are based on the interpretation and the combination of previously published and independent GW and HEN observational results. The results presented in this section are the first derived from a joint GW-HEN analysis, using concomitant data obtained with LIGO-Virgo and ANTARES.

### 8.10.1 Upper limits on GW-HEN populations

The present search for GW and HEN correlations in space and time revealed no evidence for coincident events. This implies a 90% confidence level upper limit on the rate of detectable coincidences of  $2.3/T_{\text{obs}}$ , where  $T_{\text{obs}} \approx 100$  days is the duration of coincident observations. This can be expressed as a limit on the rate density (number per unit time per unit volume)  $\rho_{\text{GW-HEN}}$  of objects which would yield coincident GW and HEN signals as follows:

$$\rho_{\text{GW-HEN}} V_{\text{GW-HEN}} \leq \frac{2.3}{T_{\text{obs}}}. \quad (8.7)$$

In this expression,  $V_{\text{GW-HEN}}$  is the volume of universe probed by the present analysis for typical GW-HEN sources. This volume is related to the GW and HEN detection efficiencies as a function of distance, and must be estimated for typical emission models.

We take as fiducial sources choked or failed GRBs, more generally two classes of objects: the final merger phase of the coalescence of two compact objects (short GRB-like), or the collapse of a massive object (long GRB-like), both followed by the emission of a relativistic hadronic jet. In the case of short GRBs (SGRB), the HEN horizon is estimated to be 4 Mpc using [264], while the typical GW horizon from the inspiral model is 5 - 10 Mpc depending on the binary masses. For long GRBs (LGRB) the HEN horizon increases to 12 Mpc using [264]. The GW emission associated with long GRBs is highly uncertain; our optimistic assumption of  $E_{\text{GW}} = 10^{-2} M_{\odot} c^2$  at low frequencies gives a typical horizon distance of 10-20 Mpc in GW. Using the lower of the GW and HEN distances in each case yields from equation (8.7) approximate limits on the population density of  $\rho_{\text{GW-HEN}}^{\text{SGRB}} \lesssim 10^{-2} \text{Mpc}^{-3} \text{yr}^{-1}$  for SGRB-like sources, related to the merger of two compact objects, and  $\rho_{\text{GW-HEN}}^{\text{LGRB}} \lesssim 10^{-3} \text{Mpc}^{-3} \text{yr}^{-1}$  for LGRB-like sources, related to the collapse of massive stars.

### 8.10.2 Comparison of limits with existing estimates

[270, 264] suggest a local rate density of SGRB of  $\rho_{\text{SGRB}} \lesssim 10^{-9} \text{Mpc}^{-3} \text{yr}^{-1}$ , and the abundance of binary neutron star mergers, their assumed progenitors, is estimated to be  $\rho_{\text{NS+NS}} \sim 10^{-6} \text{Mpc}^{-3} \text{yr}^{-1}$  [268, 269], well below the reach of the present search ( $\rho_{\text{GW-HEN}}^{\text{SGRB}} \lesssim 10^{-2} \text{Mpc}^{-3} \text{yr}^{-1}$ ). With  $T_{\text{obs}} = 1 \text{yr}$ , an improvement of a factor 10 on the detection distance is required in order to

be able to constrain the fraction of mergers producing coincident GW–HEN signals.

[264] estimate a total rate of long GRBs of  $\rho_{\text{LGRB}} \sim 3 \times 10^{-8} \text{Mpc}^{-3} \text{yr}^{-1}$ ; these sources are closely related to Type II and Type Ibc core-collapse supernovae. The local rate of SNIbc is  $\rho_{\text{SNIbc}} \sim 2 \times 10^{-5} \text{Mpc}^{-3} \text{yr}^{-1}$  [263], whereas  $\rho_{\text{SNI}} \sim 2 \times 10^{-4} \text{Mpc}^{-3} \text{yr}^{-1}$  [267], relatively close to the obtained limit  $\rho_{\text{GW-HEN}}^{\text{LGRB}} \lesssim 10^{-3} \text{Mpc}^{-3} \text{yr}^{-1}$  under our optimistic assumptions of GW emission in this scenario. A factor 10 only is required in order to constrain the fraction of star collapses producing coincident GW-HEN signals, which translates into a required improvement of 2 on the detection distance.

## 8.11 Conclusions

This first joint GW-HEN search using 2007 data, obtained with the ANTARES HEN Telescope and the Virgo/LIGO GW interferometers, opens the way to a novel and exciting multi-messenger astronomy. Limits on the rate density  $\rho_{\text{GW-HEN}}$  of joint GW-HEN emitting systems were extracted for the first time using the analysis of coincident GW-HEN data. We note that these limits are consistent with the ones obtained in [265] derived from independent GW-HEN observations. More stringent limits will be available by performing similar coincidence analyses using other data sets provided by the same instruments.

For instance, the sixth LIGO science run (S6) and second and third Virgo science runs (VSR2,3) covered the period from 7 July 2009 to 21 October 2010. Their enhanced sensitivities should permit a combined analysis to gain the factor required to obtain  $\rho_{\text{GW-HEN}}^{\text{LGRB}} \leq \rho_{\text{SNI/SNIbc}}$  and constrain for the first time the fraction of star collapses accompanied by the coincident emission of relativistic jets beamed towards Earth. The analysis of these data is underway.

Future schedules involving next-generation detectors with a sensitivity increased by at least one order of magnitude, such as KM3Net [261] and the advanced LIGO advanced Virgo projects [266], are likely to coincide as well. They will give other opportunities to look for potential coincident GW-HEN emissions.

# Chapter 9

## Tables

Time [JD]	RA [deg]	DEC [deg]	ASW(50%) [deg]	ASW(90%) [deg]	N lines- Nhits	weight	$\theta$	$m$	$\sigma$
2454141.1394	269.727	-5.896	2.2	12.1	2 - 13	0.5	2.43e-02	2.390	1.210
2454151.9187	269.100	-5.225	2.2	12.1	2 - 11	0.5	2.43e-02	2.390	1.210
2454151.9223	241.835	-44.333	2.7	14.3	2 - 11	0.5	4.86e-03	2.835	1.309
2454151.9223	268.385	-56.735	2.8	13.7	2 - 11	0.5	1.63e-09	2.866	1.182
2454154.8961	171.514	-2.570	2.5	11.5	2 - 8	0.5	1.25e-02	2.724	1.278
2454154.8961	182.212	-12.105	2.3	10.8	2 - 8	0.5	3.58e-02	3.998	1.666
2454155.3622	141.656	-3.301	2.4	11.5	2 - 12	0.5	1.54e-08	2.423	1.179
2454155.3622	137.665	-1.898	2.4	11.5	2 - 8	0.5	1.54e-08	2.423	1.179
2454157.1011	265.427	13.870	2.7	13.2	2 - 8	0.5	8.66e-08	2.810	1.209
2454157.1011	258.866	11.161	2.7	13.2	2 - 8	0.5	8.66e-08	2.810	1.209
2454157.4763	178.784	15.958	2.7	13.2	2 - 8	0.5	8.66e-08	2.810	1.209
2454157.4763	195.050	18.397	2.7	13.2	2 - 8	0.5	8.66e-08	2.810	1.209
2454160.5329	37.369	9.441	2.6	13.4	2 - 11	0.5	8.33e-12	2.729	1.195
2454160.5329	36.844	9.913	2.6	13.4	2 - 11	0.5	8.33e-12	2.729	1.195
2454161.0583	81.425	-66.051	2.9	12.7	2 - 7	0.5	3.40e-02	4.000	1.463
2454161.0583	82.243	-67.146	2.9	12.7	2 - 7	0.5	3.40e-02	4.000	1.463
2454161.3270	92.864	-81.097	2.8	12.0	2 - 9	0.5	3.36e-02	3.299	1.309
2454161.3270	129.851	-25.949	2.2	11.9	2 - 11	0.5	1.82e-08	2.322	1.241
2454163.1728	338.628	-3.347	2.4	11.9	2 - 11	0.5	3.52e-09	2.691	1.337
2454163.1728	335.093	-0.203	2.4	11.9	2 - 11	0.5	3.52e-09	2.691	1.337
2454169.0795	163.130	-53.750	2.7	12.6	2 - 14	0.5	7.46e-07	2.614	1.180
2454169.0795	163.227	-53.513	2.7	12.6	2 - 14	0.5	7.46e-07	2.614	1.180
2454169.1397	241.684	-12.750	2.4	11.1	2 - 10	0.5	1.25e-10	2.576	1.246
2454169.1397	245.557	-16.290	2.4	11.1	2 - 10	0.5	1.25e-10	2.576	1.246
2454169.1397	171.873	-48.288	2.4	13.5	2 - 12	0.5	1.21e-02	2.609	1.367
2454169.1397	172.030	-47.755	2.4	13.5	2 - 12	0.5	1.21e-02	2.609	1.367

Table 9.1: The table shows the time of the neutrino event in Julian Days, Right Ascension, Declination, the 50% and 90% angular search windows and the number of lines and hits involved in the reconstruction of the neutrino track. The weight is 0.5 for the 2-lines reconstruction and 1 for the 3-lines one.  $\theta$ ,  $m$  and  $\sigma$  are the fit parameters of eq. 6.9 for the position error box of each neutrino trigger (section 8.2.1).

Time [JD]	RA [deg]	DEC [deg]	ASW(50%) [deg]	ASW(90%) [deg]	N lines- Nhits	weight	$\theta$	$m$	$\sigma$
2454171.1618	222.093	-9.462	2.6	13.3	2 - 14	0.5	1.09e-02	2.942	1.271
	231.024	-8.124	2.6	13.3			1.09e-02	2.942	1.271
2454171.6172	95.248	9.228	2.7	13.6	2 - 8	0.5	1.09e-02	3.094	1.304
	81.565	18.948	2.7	13.2			8.66e-08	2.810	1.209
2454171.7935	68.347	-27.623	2.4	11.1	2 - 8	0.5	3.32e-09	2.499	1.228
	105.726	-12.393	2.3	10.8			3.58e-02	3.998	1.666
2454174.2813	253.257	-2.193	2.5	11.5	2 - 8	0.5	1.25e-02	2.724	1.278
	261.026	0.999	2.7	13.6			1.09e-02	3.094	1.304
2454175.5884	131.819	-20.081	2.4	11.6	2 - 10	0.5	1.15e-02	2.440	1.224
	122.059	-9.939	2.4	12.8			3.07e-08	2.510	1.228
2454181.8961	143.303	15.484	2.9	14.6	2 - 10	0.5	6.79e-03	2.878	1.195
	132.511	13.857	2.9	14.6			6.79e-03	2.878	1.195
2454182.0076	97.814	-46.952	2.8	14.1	2 - 8	0.5	4.07e-02	3.255	1.389
	97.943	-46.814	2.8	14.1			4.07e-02	3.255	1.389
2454193.5684	308.645	-27.445	2.2	11.9	2 - 9	0.5	1.82e-08	2.322	1.241
	305.123	-31.045	2.5	13.6			7.04e-03	2.697	1.275
2454193.7811	50.829	5.379	2.4	12.6	2 - 10	0.5	2.22e-02	2.597	1.218
	48.768	3.365	2.4	12.6			2.22e-02	2.597	1.218
2454194.7813	150.299	-77.968	2.6	12.9	2 - 15	0.5	1.98e-02	2.907	1.328
	156.866	-76.633	2.6	12.9			1.98e-02	2.907	1.328
2454194.9991	225.902	-75.442	2.6	13.2	2 - 10	0.5	1.39e-09	2.802	1.235
	225.423	-75.530	2.6	13.2			1.39e-09	2.802	1.235
2454195.3930	20.629	-35.163	1.8	9.9	2 - 17	0.5	2.02e-02	2.000	1.321
	347.615	-11.560	2.0	12.3			2.05e-02	2.210	1.390
2454195.7014	284.261	-63.530	2.6	13.9	2 - 9	0.5	1.22e-02	2.923	1.279
	218.911	-53.989	2.8	13.5			4.45e-03	2.946	1.205
2454203.0868	263.589	14.649	2.7	13.2	2 - 8	0.5	8.66e-08	2.810	1.209
	260.866	15.614	2.7	13.2			8.66e-08	2.810	1.209

Time [JD]	RA [deg]	DEC [deg]	ASW(50%) [deg]	ASW(90%) [deg]	N lines- Nhits	weight	$\theta$	$m$	$\sigma$
2454203.9701	163.191	13.525	2.9	14.6	2 - 10	0.5	6.79e-03	2.878	1.195
2454204.6903	209.132	20.246	3.0	13.9	2 - 10	0.5	2.36e-09	3.241	1.208
2454204.9204	190.930	-19.504	1.9	11.7	2 - 15	0.5	1.17e-02	2.000	1.246
2454210.2496	294.445	-56.125	2.3	11.6	2 - 10	0.5	1.08e-02	2.494	1.209
2454212.6772	155.305	29.493	3.0	13.9	2 - 10	0.5	2.36e-09	3.241	1.208
2454215.3102	136.620	21.682	3.0	13.9	2 - 10	0.5	2.36e-09	3.241	1.208
2454215.6690	269.679	-33.004	2.3	14.1	2 - 14	0.5	2.44e-02	2.247	1.234
2454215.7843	275.457	-26.270	2.3	11.5	2 - 7	0.5	1.01e-02	2.322	1.284
2454219.9375	219.066	-50.816	2.9	13.7	2 - 7	0.5	5.58e-11	3.152	1.223
2454221.4614	228.743	-55.593	2.9	13.7	2 - 10	0.5	5.58e-11	3.152	1.223
2454223.2816	203.485	4.419	2.4	12.6	2 - 10	0.5	2.22e-02	2.597	1.218
2454227.3729	201.561	6.136	2.4	12.6	2 - 10	0.5	2.22e-02	2.597	1.218
2454215.7959	87.019	-46.987	2.8	14.1	2 - 8	0.5	4.07e-02	3.255	1.389
2454215.7959	106.759	-56.383	3.0	14.0	2 - 9	0.5	4.40e-10	3.091	1.209
2454215.7959	70.732	23.316	3.1	12.4	2 - 9	0.5	2.95e-11	3.619	1.303
2454215.7959	104.638	28.376	3.1	12.4	2 - 11	0.5	2.95e-11	3.619	1.303
2454215.7959	100.890	16.445	3.0	16.0	2 - 11	0.5	1.78e-08	2.950	1.217
2454215.7959	119.579	24.205	2.7	14.5	2 - 7	0.5	3.86e-02	2.806	1.223
2454215.7959	287.770	-60.403	2.9	12.7	2 - 9	0.5	3.40e-02	4.000	1.463
2454215.7959	314.483	-64.565	2.9	12.7	2 - 9	0.5	3.40e-02	4.000	1.463
2454221.4614	201.285	9.447	2.5	14.2	2 - 11	0.5	1.65e-03	2.674	1.291
2454221.4614	181.498	6.488	2.5	14.2	2 - 11	0.5	1.65e-03	2.674	1.291
2454223.2816	7.264	-42.505	1.4	6.7	2 - 21	0.5	2.52e-02	2.000	1.420
2454223.2816	9.819	-52.971	1.5	7.5	2 - 21	0.5	2.98e-02	2.000	1.447
2454227.3729	280.223	-32.538	2.3	13.5	2 - 12	0.5	4.17e-03	2.390	1.244
2454227.3729	285.142	-77.100	3.0	13.0	2 - 12	0.5	5.43e-03	3.190	1.272
2454227.3729	282.423	-72.254	2.6	13.8	2 - 12	0.5	2.51e-10	2.697	1.204
2454227.3729	303.775	-34.271	2.5	12.7	2 - 12	0.5	5.16e-03	2.615	1.294

Time [JD]	RA [deg]	DEC [deg]	ASW(50%) [deg]	ASW(90%) [deg]	N lines- Nhits	weight	$\theta$	$m$	$\sigma$
2454229.3562	300.655	-54.450	3.0	14.0	2 - 8	0.5	4.40e-10	3.091	1.209
	307.533	-38.192	2.6	12.8			2.33e-02	2.682	1.300
2454238.9737	198.020	-86.779	3.1	14.2	2 - 10	0.5	3.36e-02	3.299	1.309
	305.321	-71.302	2.6	13.2			1.39e-09	2.802	1.235
2454239.4323	56.710	-66.576	2.6	13.0	2 - 8	0.5	1.22e-02	2.923	1.279
	72.496	-56.680	3.0	14.0			4.40e-10	3.091	1.209
2454240.3506	337.967	-14.623	2.4	11.1	2 - 10	0.5	1.25e-10	2.576	1.246
	3.574	-4.167	2.4	12.8			3.07e-08	2.510	1.228
2454240.5878	94.326	30.386	2.7	14.0	2 - 16	0.5	1.00e-02	2.647	1.162
	70.500	26.800	3.0	13.0			1.00e-02	3.207	1.289
2454240.7435	171.542	-8.538	2.5	11.5	2 - 8	0.5	1.25e-02	2.724	1.278
	190.430	-21.957	2.4	11.1			3.32e-09	2.499	1.228
2454240.8028	221.973	2.338	2.5	14.2	2 - 9	0.5	1.65e-03	2.674	1.291
	229.057	-3.810	2.6	12.5			1.23e-02	2.695	1.237
2454240.8601	278.238	-30.628	2.5	12.7	2 - 12	0.5	5.16e-03	2.615	1.294
	32.090	-70.124	2.6	13.8			2.51e-10	2.697	1.204
2454241.1051	353.364	-64.694	2.8	14.3	2 - 11	0.5	6.60e-03	2.869	1.253
	213.137	-80.939	2.8	14.3			3.95e-09	2.877	1.242
2454241.2372	183.490	-65.777	2.6	13.9	2 - 9	0.5	1.22e-02	2.923	1.279
	219.474	-50.999	2.8	13.5			4.45e-03	2.946	1.205
2454241.3704	68.000	-18.896	2.4	11.1	2 - 10	0.5	1.25e-10	2.576	1.246
	74.293	-26.323	2.4	11.6			1.15e-02	2.440	1.224
2454242.2654	291.863	-78.678	2.6	13.2	2 - 10	0.5	1.39e-09	2.802	1.235
	35.023	-39.429	2.3	14.1			7.34e-12	2.288	1.183
2454243.8112	196.672	23.463	2.7	14.5	2 - 11	0.5	3.86e-02	2.806	1.223
	139.296	15.187	3.0	16.0			1.78e-08	2.950	1.217
2454243.9673	137.376	-42.702	2.4	13.5	2 - 12	0.5	1.21e-02	2.609	1.367
	154.490	-24.212	2.3	11.8			3.60e-02	2.528	1.394

Time [JD]	RA [deg]	DEC [deg]	ASW(50%) [deg]	ASW(90%) [deg]	N lines- Nhits	weight	$\theta$	$m$	$\sigma$
2454245.1434	354.803	14.805	2.8	13.1	2 - 7	0.5	1.18e-02	2.979	1.251
	9.689	1.563	2.6	12.5			7.60e-03	2.828	1.287
2454245.5682	333.077	-58.212	3.0	14.0	2 - 8	0.5	4.40e-10	3.091	1.209
	325.250	-61.663	2.6	13.0			1.22e-02	2.923	1.279
2454245.7439	44.829	-39.450	2.5	13.6	2 - 9	0.5	7.04e-03	2.697	1.275
	51.871	-33.650	2.5	13.6			7.04e-03	2.697	1.275
2454245.7704	221.989	-9.384	2.5	11.5	2 - 8	0.5	1.25e-02	2.724	1.278
	211.845	-0.365	2.5	11.5			1.25e-02	2.724	1.278
2454246.9472	222.626	-3.783	2.4	12.1	2 - 16	0.5	3.04e-02	2.379	1.222
	223.882	-3.595	2.4	12.1			3.04e-02	2.379	1.222
2454247.1082	157.625	-57.749	2.7	12.6	2 - 14	0.5	7.46e-07	2.614	1.180
	162.832	-55.575	2.7	12.6			7.46e-07	2.614	1.180
2454248.1273	211.918	-37.909	2.3	13.5	2 - 11	0.5	4.17e-03	2.390	1.244
	195.713	-54.302	2.8	13.7			1.63e-09	2.866	1.182
2454249.2175	313.730	9.879	2.7	13.6	2 - 8	0.5	1.09e-02	3.094	1.304
	327.420	11.927	2.7	13.2			8.66e-08	2.810	1.209
2454250.4366	9.950	-40.778	2.7	14.3	2 - 11	0.5	4.86e-03	2.835	1.309
	7.979	-55.661	2.8	13.7			1.63e-09	2.866	1.182
2454250.7598	255.856	-80.091	2.8	14.3	2 - 11	0.5	3.95e-09	2.877	1.242
	258.188	-82.606	2.8	14.3			3.95e-09	2.877	1.242
2454251.0574	321.936	-68.670	2.0	12.0	2 - 18	0.5	2.11e-02	2.108	1.370
	325.168	-64.466	2.0	12.0			2.11e-02	2.108	1.370
2454251.1095	238.269	-7.189	2.4	12.2	2 - 7	0.5	2.95e-07	2.523	1.233
	232.079	-13.505	2.2	10.3			3.58e-02	3.998	1.666
2454254.4293	344.881	-5.502	2.4	12.8	2 - 10	0.5	3.07e-08	2.510	1.228
	348.470	-1.889	2.4	12.8			3.07e-08	2.510	1.228
2454254.8369	193.993	24.987	2.5	11.7	2 - 8	0.5	2.05e-08	2.605	1.183
	179.952	22.877	2.5	11.7			2.05e-08	2.605	1.183

Time [JD]	RA [deg]	DEC [deg]	ASW(50%) [deg]	ASW(90%) [deg]	N lines- Nhits	weight	$\theta$	$m$	$\sigma$
2454255.1030	345.153	-1.720	2.4	11.5	2 - 12	0.5	1.54e-08	2.423	1.179
	347.135	-3.442	2.4	11.5			1.54e-08	2.423	1.179
2454255.2705	40.160	-1.164	2.5	11.5	2 - 8	0.5	1.25e-02	2.724	1.278
	50.766	-10.585	2.3	10.8			3.58e-02	3.998	1.666
2454255.3098	244.494	-67.327	2.6	13.9	2 - 9	0.5	1.22e-02	2.923	1.279
	107.687	-51.331	2.8	13.5			4.45e-03	2.946	1.205
2454255.5141	118.830	-7.115	2.2	12.1	2 - 13	0.5	2.43e-02	2.390	1.210
	118.832	-7.116	2.2	12.1			2.43e-02	2.390	1.210
2454256.5425	69.510	-32.465	1.5	6.4	2 - 21	0.5	5.08e-03	2.000	1.352
	68.786	-33.374	1.5	6.4			5.08e-03	2.000	1.352
2454256.6070	74.790	-13.304	2.3	10.8	2 - 8	0.5	3.58e-02	3.998	1.666
	67.032	-21.222	2.4	11.1			3.32e-09	2.499	1.228
2454257.0885	243.852	-7.840	2.4	12.2	2 - 7	0.5	2.95e-07	2.523	1.233
	234.902	-16.721	2.2	10.3			3.58e-02	3.998	1.666
2454263.7037	225.524	-1.466	2.4	11.5	2 - 12	0.5	1.54e-08	2.423	1.179
	212.149	10.390	2.9	15.3			8.35e-03	2.924	1.209
2454263.7090	176.104	-4.906	2.6	13.3	2 - 14	0.5	1.09e-02	2.942	1.271
	180.786	-6.554	2.6	13.3			1.09e-02	2.942	1.271
2454263.8686	315.926	-52.252	2.9	13.7	2 - 7	0.5	5.58e-11	3.152	1.223
	345.948	-69.633	2.9	12.7			3.40e-02	4.000	1.463
2454264.0576	250.573	-56.700	1.5	7.5	2 - 21	0.5	2.98e-02	2.000	1.447
	249.147	-51.815	1.5	7.5			2.98e-02	2.000	1.447
2454264.5255	185.661	-18.497	2.4	11.1	2 - 10	0.5	1.25e-10	2.576	1.246
	191.976	-25.171	2.4	11.6			1.15e-02	2.440	1.224
2454265.7198	105.302	-48.715	2.2	12.0	2 - 14	0.5	1.14e-07	2.287	1.288
	108.571	-42.025	2.2	12.0			1.14e-07	2.287	1.288
2454266.3437	334.120	10.525	2.7	13.2	2 - 8	0.5	8.66e-08	2.810	1.209
	317.379	-5.615	2.5	11.5			1.25e-02	2.724	1.278

Time [JD]	RA [deg]	DEC [deg]	ASW(50%) [deg]	ASW(90%) [deg]	N lines- Nhits	weight	$\theta$	$m$	$\sigma$
2454266.7550	243.787	7.706	2.4	12.6	2 - 10	0.5	2.22e-02	2.597	1.218
2454267.8679	243.273	8.167	2.4	12.6	2 - 10	0.5	2.22e-02	2.597	1.218
2454269.0220	245.095	-41.674	2.5	14.1	2 - 13	0.5	2.94e-02	2.743	1.391
2454269.0220	244.581	-49.700	2.5	14.1	2 - 13	0.5	2.94e-02	2.743	1.391
2454269.0220	264.284	7.460	2.4	12.6	2 - 10	0.5	2.22e-02	2.597	1.218
2454269.0220	275.923	9.200	2.4	12.6	2 - 10	0.5	2.22e-02	2.597	1.218
2454269.2361	214.020	-45.460	2.7	13.0	2 - 7	0.5	4.03e-08	2.913	1.254
2454269.2361	218.092	-43.932	2.7	13.0	2 - 7	0.5	4.03e-08	2.913	1.254
2454269.4453	65.611	30.264	2.7	11.6	2 - 7	0.5	1.92e-02	2.827	1.326
2454269.4453	53.034	28.361	2.7	12.9	2 - 7	0.5	2.00e-02	2.960	1.326
2454270.5988	76.402	-5.303	2.6	12.5	2 - 9	0.5	1.23e-02	2.695	1.237
2454270.5988	69.266	-12.329	2.2	10.2	2 - 9	0.5	2.29e-03	2.398	1.234
2454270.6107	30.032	-44.490	2.8	14.1	2 - 8	0.5	4.07e-02	3.255	1.389
2454270.6107	51.381	-22.440	2.4	11.1	2 - 8	0.5	3.32e-09	2.499	1.228
2454271.3465	6.859	27.190	3.0	13.9	2 - 10	0.5	2.36e-09	3.241	1.208
2454271.3465	301.902	-27.997	2.4	11.6	2 - 10	0.5	1.15e-02	2.440	1.224
2454271.4466	10.513	9.391	2.6	13.4	2 - 11	0.5	8.33e-12	2.729	1.195
2454271.4466	0.779	-0.088	2.4	11.9	2 - 11	0.5	3.52e-09	2.691	1.337
2454271.5850	36.233	-15.941	2.2	10.2	2 - 9	0.5	2.29e-03	2.398	1.234
2454271.5850	41.249	-10.439	2.2	10.2	2 - 9	0.5	2.29e-03	2.398	1.234
2454272.0775	330.785	-51.720	2.8	13.7	2 - 11	0.5	1.63e-09	2.866	1.182
2454272.0775	308.261	-63.625	2.8	14.3	2 - 11	0.5	6.60e-03	2.869	1.253
2454272.3371	130.583	-22.860	2.3	11.8	2 - 12	0.5	3.60e-02	2.528	1.394
2454272.3371	127.841	-19.974	2.3	10.8	2 - 12	0.5	1.40e-02	2.336	1.232
2454272.7756	159.048	-56.631	2.6	12.9	2 - 13	0.5	6.26e-08	2.758	1.210
2454272.7756	157.412	-51.581	2.6	12.9	2 - 13	0.5	6.26e-08	2.758	1.210
2454273.6077	110.590	-62.003	2.2	11.4	2 - 16	0.5	7.77e-03	2.492	1.261
2454273.6077	106.030	-34.183	2.2	10.6	2 - 16	0.5	6.54e-03	2.285	1.231

Time [JD]	RA [deg]	DEC [deg]	ASW(50%) [deg]	ASW(90%) [deg]	N lines- Nhits	weight	$\theta$	$m$	$\sigma$
2454274.1225	341.193	-17.487	2.2	10.2	2 - 9	0.5	2.29e-03	2.398	1.234
	350.415	-24.207	2.2	11.9			1.82e-08	2.322	1.241
2454274.6804	218.474	-7.876	2.5	11.5	2 - 8	0.5	1.25e-02	2.724	1.278
	209.362	0.222	2.7	13.6			1.09e-02	3.094	1.304
2454274.8381	262.351	15.763	2.9	15.3	2 - 12	0.5	8.35e-03	2.924	1.209
	282.778	-0.445	2.4	11.5			1.54e-08	2.423	1.179
2454275.0929	296.443	0.405	2.6	13.4	2 - 12	0.5	5.02e-09	2.588	1.200
	282.465	-5.327	2.4	11.5			1.54e-08	2.423	1.179
2454275.6377	248.663	-18.524	2.4	11.1	2 - 10	0.5	1.25e-10	2.576	1.246
	240.028	-9.566	2.4	12.8			3.07e-08	2.510	1.228
2454276.3003	334.566	-37.820	2.3	14.1	2 - 10	0.5	7.34e-12	2.288	1.183
	327.476	-55.153	2.8	13.8			8.80e-09	2.970	1.175
2454276.8678	180.660	-9.331	2.4	12.8	2 - 10	0.5	3.07e-08	2.510	1.228
	176.465	-13.497	2.4	11.1			1.25e-10	2.576	1.246
2454276.8852	277.568	-18.608	2.0	10.8	2 - 13	0.5	1.75e-02	2.267	1.261
	274.240	-15.606	2.0	10.8			1.75e-02	2.267	1.261
2454276.8966	117.119	-58.422	3.0	14.0	2 - 8	0.5	4.40e-10	3.091	1.209
	115.838	-58.978	3.0	14.0			4.40e-10	3.091	1.209
2454284.6472	226.827	-37.946	2.5	13.6	2 - 9	0.5	7.04e-03	2.697	1.275
	226.432	-37.362	2.5	13.6			7.04e-03	2.697	1.275
2454285.3632	19.911	-19.930	2.4	11.1	2 - 10	0.5	1.25e-10	2.576	1.246
	15.209	-24.925	2.4	11.6			1.15e-02	2.440	1.224
2454285.3889	54.478	24.153	2.5	11.7	2 - 8	0.5	2.05e-08	2.605	1.183
	56.879	24.517	2.5	11.7			2.05e-08	2.605	1.183
2454289.4159	31.457	5.072	2.7	13.6	2 - 8	0.5	1.09e-02	3.094	1.304
	11.224	-14.410	2.3	10.8			3.58e-02	3.998	1.666
2454289.4231	63.809	-14.027	2.0	10.8	2 - 13	0.5	1.75e-02	2.267	1.261
	69.816	-11.537	2.0	10.8			1.75e-02	2.267	1.261

Time [JD]	RA [deg]	DEC [deg]	ASW(50%) [deg]	ASW(90%) [deg]	N lines- Nhits	weight	$\theta$	$m$	$\sigma$
2454289.6179	232.613	-31.071	2.3	14.1	2 - 10	0.5	7.34e-12	2.288	1.183
	229.716	-27.536	2.4	11.6			1.15e-02	2.440	1.224
2454290.1467	13.955	-18.175	1.9	11.7	2 - 15	0.5	1.17e-02	2.000	1.246
	22.329	-25.912	2.1	11.7			1.31e-09	2.137	1.229
2454291.4416	129.103	21.156	3.0	12.9	2 - 14	0.5	3.78e-02	3.258	1.179
	10.426	-17.959	2.2	11.7			2.45e-02	2.298	1.280
2454293.1712	132.546	-46.321	2.8	14.1	2 - 8	0.5	4.07e-02	3.255	1.389
	127.451	-44.018	2.8	14.1			4.07e-02	3.255	1.389
2454293.5238	310.901	-80.890	3.1	14.2	2 - 10	0.5	3.36e-02	3.299	1.309
	231.029	-68.654	2.8	13.0			1.20e-09	2.869	1.253
2454294.9015	156.498	-44.515	2.8	15.2	2 - 10	0.5	1.42e-07	3.043	1.376
	163.920	-37.889	2.3	14.1			7.34e-12	2.288	1.183
2454295.2877	323.255	-31.856	2.3	13.5	2 - 11	0.5	4.17e-03	2.390	1.244
	292.694	-61.914	2.8	14.3			6.60e-03	2.869	1.253
2454295.6503	225.563	15.197	2.7	13.2	2 - 8	0.5	8.66e-08	2.810	1.209
	222.912	17.104	2.7	13.2			8.66e-08	2.810	1.209
2454296.6418	91.013	-68.408	2.9	12.7	2 - 7	0.5	3.40e-02	4.000	1.463
	89.329	-72.391	2.7	12.3			3.03e-02	3.478	1.323
2454297.0217	281.709	7.398	2.6	12.5	2 - 7	0.5	7.60e-03	2.828	1.287
	281.149	7.167	2.6	12.5			7.60e-03	2.828	1.287
2454297.4646	159.050	-50.648	2.7	12.6	2 - 14	0.5	7.46e-07	2.614	1.180
	150.871	-32.595	2.3	14.1			2.44e-02	2.247	1.234
2454298.2156	316.715	-54.301	2.8	13.8	2 - 10	0.5	8.80e-09	2.970	1.175
	316.706	-54.331	2.8	13.8			8.80e-09	2.970	1.175
2454298.9448	316.932	-49.818	2.4	13.5	2 - 12	0.5	1.21e-02	2.609	1.367
	315.432	-40.966	2.4	13.5			1.21e-02	2.609	1.367
2454299.7766	145.556	-47.414	2.8	14.1	2 - 8	0.5	4.07e-02	3.255	1.389
	153.190	-36.257	2.6	12.8			2.33e-02	2.682	1.300

Time [JD]	RA [deg]	DEC [deg]	ASW(50%) [deg]	ASW(90%) [deg]	N lines- Nhits	weight	$\theta$	$m$	$\sigma$
2454299.8849	25.412	-48.599	2.8	14.1	2 - 8	0.5	4.07e-02	3.255	1.389
	31.744	-51.588	3.0	14.0			4.40e-10	3.091	1.209
2454300.0107	303.225	24.018	3.1	12.4	2 - 9	0.5	2.95e-11	3.619	1.303
	285.388	21.353	3.1	12.4			2.95e-11	3.619	1.303
2454300.8812	309.033	5.073	2.6	12.5	2 - 7	0.5	7.60e-03	2.828	1.287
	312.347	2.425	2.6	12.5			7.60e-03	2.828	1.287
2454301.7038	260.766	2.414	2.5	14.2	2 - 9	0.5	1.65e-03	2.674	1.291
	231.961	22.525	3.1	12.4			2.95e-11	3.619	1.303
2454301.9679	281.089	-18.601	2.0	11.3	2 - 21	0.5	1.51e-02	2.000	1.296
	275.695	-20.843	1.3	8.1			3.84e-02	2.000	1.638
2454302.4573	52.693	-62.817	2.6	13.9	2 - 9	0.5	1.22e-02	2.923	1.279
	66.669	-76.052	2.7	12.8			2.44e-02	2.768	1.308
2454302.7335	272.904	-41.637	2.8	14.1	2 - 8	0.5	4.07e-02	3.255	1.389
	267.355	-32.968	2.6	12.8			2.33e-02	2.682	1.300
2454303.3867	54.064	11.810	2.9	14.5	2 - 9	0.5	2.23e-02	3.207	1.320
	59.281	13.973	2.9	14.5			2.23e-02	3.207	1.320
2454308.5176	224.071	-26.055	2.4	11.6	2 - 10	0.5	1.15e-02	2.440	1.224
	219.776	-21.242	2.4	11.6			1.15e-02	2.440	1.224
2454308.7220	246.737	-62.145	2.7	13.6	2 - 13	0.5	2.42e-02	2.903	1.313
	193.715	-70.194	2.7	13.0			8.26e-03	2.738	1.210
2454310.8950	289.145	-66.105	2.7	13.6	2 - 13	0.5	2.42e-02	2.903	1.313
	284.831	-66.793	2.7	13.6			2.42e-02	2.903	1.313
2454312.6899	238.734	22.084	3.1	12.4	2 - 9	0.5	2.95e-11	3.619	1.303
	223.611	27.467	3.1	12.4			2.95e-11	3.619	1.303
2454313.4599	157.657	-7.508	2.4	11.9	2 - 11	0.5	3.52e-09	2.691	1.337
	170.529	-19.141	2.1	10.7			2.10e-02	2.349	1.316
2454314.8888	278.158	-23.780	2.1	11.9	2 - 13	0.5	2.11e-02	2.262	1.296
	255.549	-33.228	2.3	12.5			1.74e-02	2.345	1.230
2454315.1457	324.613	22.616	2.7	14.5	2 - 11	0.5	3.86e-02	2.806	1.223
	30.642	32.009	2.6	12.6			4.47e-11	2.708	1.089

Time [JD]	RA [deg]	DEC [deg]	ASW(50%) [deg]	ASW(90%) [deg]	N lines- Nhits	weight	$\theta$	$m$	$\sigma$
2454315.9173	312.685	-15.423	2.3	10.8	2 - 12	0.5	1.40e-02	2.336	1.232
	318.723	-19.782	2.3	10.8			1.40e-02	2.336	1.232
2454316.8106	196.944	-42.179	2.7	14.3	2 - 11	0.5	4.86e-03	2.835	1.309
	193.550	-50.772	2.8	13.7			1.63e-09	2.866	1.182
2454321.2856	5.062	8.864	2.7	13.6	2 - 8	0.5	1.09e-02	3.094	1.304
	352.372	-3.436	2.5	11.5			1.25e-02	2.724	1.278
2454322.4235	113.696	-9.511	2.6	12.5	2 - 9	0.5	1.23e-02	2.695	1.237
	86.891	-20.512	2.2	11.9			1.82e-08	2.322	1.241
2454323.0159	29.676	6.989	2.5	14.2	2 - 9	0.5	1.65e-03	2.674	1.291
	30.133	6.590	2.5	14.2			1.65e-03	2.674	1.291
2454323.0700	47.168	13.638	2.9	14.6	2 - 10	0.5	6.79e-03	2.878	1.195
	58.684	3.369	2.4	12.6			2.22e-02	2.597	1.218
2454323.7801	269.167	-29.192	2.1	11.9	2 - 13	0.5	2.11e-02	2.262	1.296
	262.969	-24.521	2.1	11.9			2.11e-02	2.262	1.296
2454324.5170	128.960	11.814	2.9	15.3	2 - 12	0.5	8.35e-03	2.924	1.209
	122.090	8.972	2.6	13.4			5.02e-09	2.588	1.200
2454327.9418	79.650	-49.468	2.7	14.3	2 - 11	0.5	4.86e-03	2.835	1.309
	76.665	-48.078	2.7	14.3			4.86e-03	2.835	1.309
2454328.6577	251.263	-70.004	2.7	12.3	2 - 7	0.5	3.03e-02	3.478	1.323
	203.788	-77.876	2.7	12.3			3.03e-02	3.478	1.323
2454328.6884	338.931	-38.534	2.3	14.1	2 - 10	0.5	7.34e-12	2.288	1.183
	5.985	-50.502	2.8	13.8			8.80e-09	2.970	1.175
2454329.1077	52.956	-7.846	2.4	11.9	2 - 11	0.5	3.52e-09	2.691	1.337
	58.320	-12.665	2.1	10.7			2.10e-02	2.349	1.316
2454329.7057	217.969	-1.198	2.4	11.9	2 - 11	0.5	3.52e-09	2.691	1.337
	192.916	-11.416	2.1	10.7			2.10e-02	2.349	1.316
2454329.9488	305.929	-57.179	2.4	10.5	2 - 17	0.5	3.75e-03	2.521	1.203
	333.756	-44.248	1.8	11.1			2.13e-02	2.000	1.376

Time [JD]	RA [deg]	DEC [deg]	ASW(50%) [deg]	ASW(90%) [deg]	N lines- Nhits	weight	$\theta$	$m$	$\sigma$
2454330.1217	288.717	-67.740	2.6	13.0	2 - 8	0.5	1.22e-02	2.923	1.279
	309.499	-36.607	2.6	12.8			2.33e-02	2.682	1.300
2454330.7119	108.346	-62.890	2.9	14.5	2 - 12	0.5	4.25e-08	3.059	1.268
	325.085	-46.658	2.4	13.5			1.21e-02	2.609	1.367
2454330.7831	204.260	-8.350	2.4	11.9	2 - 11	0.5	3.52e-09	2.691	1.337
	198.124	-14.434	2.1	10.7			2.10e-02	2.349	1.316
2454331.8917	285.323	-24.553	1.8	10.5	2 - 18	0.5	3.63e-09	2.000	1.218
	281.201	-26.281	1.8	10.5			3.63e-09	2.000	1.218
2454332.3270	128.079	-14.327	2.3	10.8	2 - 12	0.5	1.40e-02	2.336	1.232
	134.119	-19.894	2.3	10.8			1.40e-02	2.336	1.232
2454332.3284	45.668	-44.572	2.0	12.9	2 - 16	0.5	1.84e-02	2.000	1.321
	43.952	-52.533	2.6	11.2			1.31e-10	2.747	1.175
2454332.5284	207.394	-7.085	2.6	12.5	2 - 9	0.5	1.23e-02	2.695	1.237
	213.874	-12.913	2.2	10.2			2.29e-03	2.398	1.234
2454333.4661	146.739	-19.024	2.1	10.7	2 - 11	0.5	2.10e-02	2.349	1.316
	129.154	-21.672	2.4	12.0			1.44e-08	2.540	1.263
2454333.4703	32.756	-47.743	2.7	14.1	2 - 9	0.5	2.33e-03	3.041	1.344
	49.745	-33.037	2.5	13.6			7.04e-03	2.697	1.275
2454334.2672	151.686	5.626	2.6	12.5	2 - 7	0.5	7.60e-03	2.828	1.287
	157.289	-0.323	2.4	12.2			2.95e-07	2.523	1.233
2454334.2912	217.643	-64.229	2.6	13.0	2 - 8	0.5	1.22e-02	2.923	1.279
	248.117	-69.063	2.6	13.0			1.22e-02	2.923	1.279
2454334.9071	63.146	-50.480	3.0	14.0	2 - 8	0.5	4.40e-10	3.091	1.209
	72.562	-55.073	3.0	14.0			4.40e-10	3.091	1.209
2454336.3939	169.919	-41.444	2.4	13.5	2 - 12	0.5	1.21e-02	2.609	1.367
	87.048	-76.908	2.6	13.8			2.51e-10	2.697	1.204
2454336.5570	139.277	35.251	2.3	10.4	2 - 12	0.5	3.01e-02	2.708	1.089
	139.129	35.187	2.3	10.4			3.01e-02	2.708	1.089

Time [JD]	RA [deg]	DEC [deg]	ASW(50%) [deg]	ASW(90%) [deg]	N lines- Nhits	weight	$\theta$	$m$	$\sigma$
2454336.7181	342.495 331.390	-16.615 -5.283	2.3 2.5	10.8 11.5	2 - 8	0.5	3.58e-02 1.25e-02	3.998 2.724	1.666 1.278
2454337.1309	198.667 155.563	-71.659 -64.892	2.7 2.6	11.8 13.0	2 - 8	0.5	5.85e-09 1.22e-02	2.850 2.923	1.222 1.279
2454337.2807	148.536 146.588	-35.759 -33.056	2.5 2.5	13.6 13.6	2 - 9	0.5	7.04e-03 7.04e-03	2.697 2.697	1.275 1.275
2454338.1916	5.656 6.654	-21.570 -20.522	2.4 2.4	12.0 12.0	2 - 11	0.5	1.44e-08 1.44e-08	2.540 2.540	1.263 1.263
2454338.1955	97.792 94.131	-12.097 -8.805	2.2 2.4	10.3 12.2	2 - 7	0.5	3.58e-02 2.95e-07	3.998 2.523	1.666 1.233
2454340.0645	92.379 85.690	-28.143 -20.617	2.4 2.4	12.0 12.0	2 - 11	0.5	1.44e-08 1.44e-08	2.540 2.540	1.263 1.263
2454342.5581	227.603 227.576	-12.152 -12.128	2.4 2.4	11.1 11.1	2 - 10	0.5	1.25e-10 1.25e-10	2.576 2.576	1.246 1.246
2454342.7387	340.401 282.743	-15.541 31.144	2.1 2.6	10.7 12.6	2 - 11	0.5	2.10e-02 4.47e-11	2.349 2.708	1.316 1.089
2454343.2767	50.628 40.260	-18.442 -29.595	2.3 2.3	10.8 11.8	2 - 12	0.5	1.40e-02 3.60e-02	2.336 2.528	1.232 1.394
2454344.6710	293.005 279.752	-78.280 -83.314	3.0 2.8	13.0 14.3	2 - 11	0.5	5.43e-03 3.95e-09	3.190 2.877	1.272 1.242
2454344.8325	19.183 53.622	-51.645 -71.911	3.0 2.7	14.0 11.8	2 - 8	0.5	4.40e-10 5.85e-09	3.091 2.850	1.209 1.222
2454345.4903	106.003 164.626	3.695 26.647	2.4 3.0	12.6 13.9	2 - 10	0.5	2.22e-02 2.36e-09	2.597 3.241	1.218 1.208
2454345.8235	196.458 193.882	-32.132 -34.967	2.3 2.3	14.1 14.1	2 - 10	0.5	7.34e-12 7.34e-12	2.288 2.288	1.183 1.183
2454345.9526	311.524 301.324	5.403 1.212	2.4 2.4	12.6 12.6	2 - 10	0.5	2.22e-02 2.22e-02	2.597 2.597	1.218 1.218

Time [JD]	RA [deg]	DEC [deg]	ASW(50%) [deg]	ASW(90%) [deg]	N lines- Nhits	weight	$\theta$	$m$	$\sigma$
2454347.7304	292.962	-14.870	2.2	10.2	2 - 9	0.5	2.29e-03	2.398	1.234
	293.756	-15.599	2.2	10.2			2.29e-03	2.398	1.234
2454348.0597	71.000	17.105	2.9	14.6	2 - 10	0.5	6.79e-03	2.878	1.195
	80.587	8.648	2.4	12.6			2.22e-02	2.597	1.218
2454349.9693	43.966	-41.705	2.7	13.0	2 - 7	0.5	4.03e-08	2.913	1.254
	41.208	-37.233	2.5	11.8			2.09e-02	2.633	1.224
2454350.8475	209.570	-36.793	2.3	14.1	2 - 10	0.5	7.34e-12	2.288	1.183
	210.732	-35.487	2.3	14.1			7.34e-12	2.288	1.183
2454351.2312	110.102	-20.690	2.4	12.0	2 - 11	0.5	1.44e-08	2.540	1.263
	111.485	-21.999	2.4	12.0			1.44e-08	2.540	1.263
2454351.3717	119.374	9.659	2.5	14.2	2 - 9	0.5	1.65e-03	2.674	1.291
	114.682	8.950	2.5	14.2			1.65e-03	2.674	1.291
2454351.4529	54.103	-50.339	2.9	13.7	2 - 7	0.5	5.58e-11	3.152	1.223
	65.985	-38.835	2.5	11.8			2.09e-02	2.633	1.224
2454352.3639	139.148	15.752	3.0	16.0	2 - 11	0.5	1.78e-08	2.950	1.217
	205.192	-36.351	2.3	13.5			4.17e-03	2.390	1.244
2454353.4584	175.205	34.678	2.5	11.7	2 - 8	0.5	1.92e-02	2.827	1.326
	119.144	26.545	2.5	11.7			2.05e-08	2.605	1.183
2454354.4521	135.783	-7.072	2.2	12.1	2 - 13	0.5	2.43e-02	2.390	1.210
	141.124	-4.867	2.2	12.1			2.43e-02	2.390	1.210
2454355.5767	204.404	-13.027	2.2	11.7	2 - 14	0.5	2.45e-02	2.298	1.280
	192.597	-14.799	2.2	11.7			2.45e-02	2.298	1.280
2454355.6057	261.916	-5.552	2.4	12.8	2 - 10	0.5	3.07e-08	2.510	1.228
	263.749	-7.153	2.4	12.8			3.07e-08	2.510	1.228
2454356.2344	4.391	-43.740	2.8	14.1	2 - 8	0.5	4.07e-02	3.255	1.389
	7.376	-39.664	2.6	12.8			2.33e-02	2.682	1.300
2454373.7950	266.106	-19.385	1.9	11.7	2 - 15	0.5	1.17e-02	2.000	1.246
	255.400	-31.552	2.2	13.5			2.22e-02	2.141	1.326

Time [JD]	RA [deg]	DEC [deg]	ASW(50%) [deg]	ASW(90%) [deg]	N lines- Nhits	weight	$\theta$	$m$	$\sigma$
2454373.8405	119.701	-56.483	2.8	13.5	2 - 9	0.5	4.45e-03	2.946	1.205
	113.321	-55.503	2.8	13.5			4.45e-03	2.946	1.205
2454374.3825	144.614	1.995	2.6	13.4	2 - 11	0.5	8.33e-12	2.729	1.195
	144.786	2.021	2.6	13.4			8.33e-12	2.729	1.195
2454160.4265	153.898	-56.713	1.6	10.3	3 - 16	1.0	3.16e-02	2.000	1.422
2454161.1699	318.072	-28.220	1.6	10.0	3 - 10	1.0	1.00e-02	1.669	1.244
2454195.4027	11.915	-24.414	0.8	4.5	3 - 21	1.0	4.76e-02	2.000	1.848
2454209.9653	219.251	-6.209	1.4	9.3	3 - 15	1.0	3.59e-02	2.000	1.653
2454219.5168	356.106	-18.684	1.3	9.6	3 - 16	1.0	3.70e-02	2.000	1.563
2454240.3487	114.993	-49.673	1.4	9.6	3 - 13	1.0	2.91e-02	2.000	1.523
2454265.3665	319.886	-85.670	1.9	10.0	3 - 13	1.0	1.00e-02	2.109	1.194
2454268.9302	269.504	-12.775	1.5	10.6	3 - 17	1.0	4.09e-02	2.000	1.549
2454274.1077	265.994	-20.214	0.8	4.5	3 - 21	1.0	4.76e-02	2.000	1.848
2454292.0166	341.331	-1.554	1.8	11.3	3 - 11	1.0	4.33e-02	2.101	1.565
2454294.9270	215.370	-3.859	1.2	8.1	4 - 20	1.0	3.96e-02	2.000	1.592
2454301.9577	223.003	-52.132	1.9	10.4	3 - 12	1.0	1.00e-02	1.976	1.239
2454308.2615	349.538	5.588	1.7	12.0	3 - 10	1.0	4.08e-02	1.974	1.460
2454321.9169	205.088	-52.846	1.9	10.4	3 - 13	1.0	1.00e-02	1.976	1.239
2454323.5135	60.742	-10.266	1.1	6.3	3 - 19	1.0	2.37e-02	2.000	1.446
2454327.6088	141.478	-51.063	1.1	5.9	3 - 21	1.0	4.17e-02	2.000	1.567
2454331.0192	31.224	3.464	1.4	12.3	3 - 14	1.0	4.09e-02	2.074	1.636
2454374.3285	53.560	-47.757	1.5	11.7	3 - 14	1.0	3.09e-02	2.000	1.575

Name	Network	p-value	$h_{100\text{ Hz}}$ [ $H z^{-\frac{1}{2}}$ ] [Mpc]	$h_{150\text{ Hz}}$ [ $H z^{-\frac{1}{2}}$ ] [Mpc]	$D_{150\text{ Hz}}$ [Mpc]	$h_{300\text{ Hz}}$ [ $H z^{-\frac{1}{2}}$ ] [Mpc]	$D_{300\text{ Hz}}$ [Mpc]	$h_{NS-NS}$ [ $H z^{-\frac{1}{2}}$ ] [Mpc]	$D_{NS-NS}$ [Mpc]	$h_{NS-BH}$ [ $H z^{-\frac{1}{2}}$ ] [Mpc]	$D_{NS-BH}$ [Mpc]
1_2	H1H2	0.595	6.8e-22	4.1e-22	12.3	5.5e-22	5.1	3.9e-22	4.9	4.9e-22	8.7
7_8	H1H2L1	0.209	5.8e-22	4.0e-22	12.6	5.0e-22	5.2	3.8e-22	5.8	4.4e-22	10.5
9_10	H1H2L1	0.132	1.8e-21	1.3e-21	20.0	1.5e-21	6.4	1.2e-21	8.8	1.4e-21	17.3
11_12	H1L1	0.868	1.6e-21	1.0e-21	9.4	1.8e-21	5.1	1.1e-21	4.6	1.4e-21	8.7
13_14	H1H2L1	0.635	5.6e-22	3.0e-22	4.8	4.2e-22	2.4	3.1e-22	1.3	3.9e-22	2.4
17_18	H1H2L1	0.307	4.5e-22	3.3e-22	3.4	5.1e-22	1.7	3.1e-22	0.8	3.7e-22	1.5
19_20	H1H2	0.688	9.8e-22	6.0e-22	17.8	7.6e-22	6.4	6.6e-22	7.5	7.5e-22	14.5
21_22	H1H2	0.572	6.5e-22	4.3e-22	14.2	5.6e-22	3.6	4.3e-22	6.4	5.0e-22	12.3
23_24	H1H2	0.435	1.2e-21	7.6e-22	26.3	8.2e-22	8.8	7.3e-22	11.8	8.0e-22	23.2
27_28	H1H2L1	0.460	6.5e-22	4.1e-22	4.0	6.9e-22	1.6	4.4e-22	1.6	5.1e-22	3.1
35_36	H1H2L1	0.164	5.1e-22	3.2e-22	32.0	4.2e-22	9.4	3.5e-22	12.1	3.7e-22	24.4
39_40	H1H2L1	0.591	4.0e-22	2.7e-22	23.8	3.8e-22	6.6	2.6e-22	8.9	3.0e-22	17.0
41_42	H1H2	0.976	8.0e-22	3.9e-22	24.1	4.9e-22	8.9	3.8e-22	9.2	4.6e-22	17.8
43_44	H1H2L1	0.332	7.5e-22	4.4e-22	33.3	7.6e-22	12.4	3.9e-22	12.2	4.9e-22	22.8
49_50	H1H2L1	0.085	1.9e-21	1.1e-21	17.4	1.6e-21	6.6	1.1e-21	7.9	1.4e-21	13.2
53_54	H1H2	0.138	8.1e-22	4.2e-22	18.2	5.5e-22	7.2	4.3e-22	8.0	5.2e-22	14.7
59_60	H1H2L1	0.794	1.5e-21	7.7e-22	5.6	9.2e-22	2.4	7.1e-22	2.6	7.8e-22	4.8
63_64	H1H2L1	0.407	5.3e-22	3.1e-22	7.1	4.9e-22	2.1	3.6e-22	2.6	3.9e-22	4.7
65_66	H1H2	0.109	7.6e-22	3.5e-22	23.8	4.7e-22	8.7	3.7e-22	9.8	3.9e-22	16.7
69_70	H1H2L1	0.540	1.1e-21	7.5e-22	22.0	7.9e-22	7.1	6.7e-22	9.7	7.7e-22	17.6
71_72	H1H2L1	0.187	2.0e-21	1.5e-21	12.1	1.9e-21	4.8	1.7e-21	4.7	1.9e-21	8.7
73_74	H1H2L1	0.055	5.4e-22	3.4e-22	16.9	4.2e-22	6.5	3.5e-22	7.1	3.8e-22	13.1
75_76	H1H2L1	0.013	7.9e-22	5.6e-22	9.5	7.7e-22	4.4	5.9e-22	4.2	6.3e-22	8.1

Table 9.2: This table shows the results of the analysis, in the first columns there are: the label used for each neutrino trigger; the network specifies all detectors involved and the False Alarm Probability of the loudest GW trigger in coincidence with each neutrino. In the last five columns are shown the ULs, so the  $h_{r_{ss}}^{90\%}$  and the exclusion distances  $D$  in Mpc for the three sin-Gaussian at 100 Hz, 150 Hz and 300 Hz, and for two inspiral waveforms NS-NS and BH-NS.

Name	Network	p-value	$h_{100\text{Hz}}$ [ $H z^{-\frac{1}{2}}$ ]	$D_{100\text{Hz}}$ [Mpc]	$h_{150\text{Hz}}$ [ $H z^{-\frac{1}{2}}$ ]	$D_{150\text{Hz}}$ [Mpc]	$h_{300\text{Hz}}$ [ $H z^{-\frac{1}{2}}$ ]	$D_{300\text{Hz}}$ [Mpc]	$h_{\text{NS-NS}}$ [ $H z^{-\frac{1}{2}}$ ]	$D_{\text{NS-NS}}$ [Mpc]	$h_{\text{NS-BH}}$ [ $H z^{-\frac{1}{2}}$ ]	$D_{\text{NS-BH}}$ [Mpc]
79_80	H1L1	0.899	4.6e-22	16.7	3.2e-22	17.8	4.8e-22	5.2	3.3e-22	7.0	3.8e-22	12.8
81_82	H1H2	0.568	5.1e-22	21.2	3.5e-22	22.8	4.1e-22	8.7	3.6e-22	8.9	3.9e-22	17.4
85_86	H1H2L1	0.780	5.2e-22	27.3	3.3e-22	26.7	5.0e-22	9.5	3.7e-22	11.7	3.9e-22	21.8
89_90	H1H2V1	0.150	1.3e-21	13.6	8.0e-22	18.4	1.0e-21	7.5	8.3e-22	8.0	8.1e-22	14.3
91_92	H1H2L1V1	0.059	1.8e-21	14.4	1.1e-21	16.4	8.2e-22	4.8	8.8e-22	7.9	1.0e-21	13.2
93_94	H1H2L1V1	0.170	7.0e-22	5.6	4.6e-22	6.3	7.0e-22	2.3	5.0e-22	2.8	5.4e-22	4.7
95_96	H1H2	0.167	7.4e-22	13.3	5.1e-22	17.2	5.7e-22	6.6	4.8e-22	7.1	5.4e-22	12.4
97_98	H1L1V1	0.227	5.6e-22	7.2	3.6e-22	9.4	5.7e-22	3.9	3.8e-22	4.3	4.0e-22	8.4
99_100	H1H2V1	0.853	9.3e-22	20.6	6.6e-22	23.5	8.6e-22	7.3	6.5e-22	8.6	7.2e-22	16.8
101_102	L1V1	0.746	5.9e-22	14.4	4.0e-22	20.5	6.3e-22	7.7	3.6e-22	8.4	3.8e-22	16.6
103_104	H1H2V1	1.000	1.4e-21	9.8	9.3e-22	9.7	1.2e-21	4.6	8.7e-22	4.6	9.9e-22	8.5
109_110	H1H2L1V1	0.831	3.0e-22	5.5	2.0e-22	4.7	2.9e-22	1.9	2.0e-22	1.8	2.3e-22	3.5
111_112	H1H2V1	0.954	5.5e-22	19.9	3.6e-22	21.2	4.2e-22	8.6	3.7e-22	8.8	4.0e-22	17.1
113_114	H1H2V1	0.163	3.8e-22	13.7	2.6e-22	13.0	3.6e-22	4.7	2.6e-22	5.2	2.8e-22	10.3
117_118	H1V1	0.808	1.2e-21	23.7	5.9e-22	22.4	7.8e-22	7.5	7.0e-22	9.4	7.4e-22	17.2
119_120	H1H2L1V1	0.341	5.7e-22	21.2	4.1e-22	20.8	6.5e-22	8.7	4.0e-22	8.6	5.1e-22	16.7
121_122	H1H2L1V1	0.119	2.9e-22	20.7	2.0e-22	21.6	3.1e-22	7.1	2.0e-22	8.3	2.1e-22	16.3
123_124	H1H2L1V1	0.201	2.8e-22	8.3	2.0e-22	9.1	3.9e-22	3.5	2.0e-22	3.7	2.1e-22	8.1
125_126	H1H2L1V1	0.520	8.1e-22	6.2	5.7e-22	6.6	9.1e-22	4.4	5.9e-22	3.5	7.3e-22	6.5
129_130	H1H2L1V1	0.989	4.2e-22	15.4	2.7e-22	15.6	4.5e-22	5.2	2.8e-22	6.2	3.1e-22	12.0
131_132	H1H2V1	0.216	1.0e-21	14.7	7.2e-22	14.3	8.5e-22	6.4	7.0e-22	6.4	7.7e-22	12.1
133_134	H1H2L1V1	0.177	6.7e-22	19.3	4.7e-22	20.1	5.8e-22	6.3	3.9e-22	8.2	4.6e-22	16.2
135_136	H1H2L1	0.167	6.7e-22	11.4	4.1e-22	10.9	7.0e-22	4.2	3.9e-22	4.7	4.9e-22	8.9

Name	Network	p-value	$h_{100 H_z}$ [ $H z^{-\frac{1}{2}}$ ]	$D_{100 H_z}$ [Mpc]	$h_{150 H_z}$ [ $H z^{-\frac{1}{2}}$ ]	$D_{150 H_z}$ [Mpc]	$h_{300 H_z}$ [ $H z^{-\frac{1}{2}}$ ]	$D_{300 H_z}$ [Mpc]	$h_{NS-NS}$ [ $H z^{-\frac{1}{2}}$ ]	$D_{NS-NS}$ [Mpc]	$h_{NS-BH}$ [ $H z^{-\frac{1}{2}}$ ]	$D_{NS-BH}$ [Mpc]
137_138	H1H2L1V1	0.754	1.1e-21	13.6	6.7e-22	12.6	7.3e-22	4.4	7.0e-22	6.0	8.1e-22	11.8
139_140	H1H2L1V1	0.115	4.5e-22	7.7	3.0e-22	7.7	5.0e-22	3.0	3.3e-22	3.5	3.6e-22	6.5
141_142	H1H2L1V1	0.273	5.5e-22	36.7	3.8e-22	35.0	7.0e-22	12.5	3.8e-22	14.8	4.4e-22	27.7
143_144	H1H2L1V1	0.104	5.6e-22	19.6	3.8e-22	20.0	6.6e-22	8.0	3.9e-22	8.2	4.1e-22	15.9
145_146	H1H2L1V1	0.461	5.4e-22	28.6	3.9e-22	28.2	5.8e-22	10.1	3.7e-22	11.7	4.1e-22	23.0
147_148	H1H2L1V1	0.503	5.2e-22	8.9	3.2e-22	12.2	5.8e-22	4.6	3.7e-22	4.4	4.0e-22	8.7
149_150	H2L1V1	0.625	1.4e-21	18.9	8.0e-22	17.4	1.0e-21	5.5	1.1e-21	7.4	1.2e-21	12.7
153_154	H1H2L1V1	0.384	3.7e-22	38.1	2.4e-22	35.5	3.8e-22	11.6	2.6e-22	15.5	2.8e-22	30.9
155_156	H1H2L1V1	0.281	5.2e-22	38.2	3.3e-22	36.3	4.8e-22	9.4	3.6e-22	15.8	3.9e-22	31.3
157_158	H1H2L1	0.623	5.5e-22	13.5	3.6e-22	12.7	4.9e-22	4.0	3.6e-22	5.2	3.9e-22	8.9
159_160	H1H2V1	0.669	6.9e-22	26.1	4.1e-22	26.5	5.1e-22	8.0	3.8e-22	11.2	4.8e-22	21.1
161_162	H1H2L1	0.406	4.4e-22	10.5	3.5e-22	10.0	5.6e-22	4.3	3.6e-22	4.4	3.9e-22	8.5
163_164	H1H2L1V1	0.712	3.9e-22	16.2	2.1e-22	15.3	3.7e-22	6.3	2.6e-22	8.0	2.8e-22	13.9
165_166	H1H2L1V1	0.831	9.8e-22	16.2	5.0e-22	17.6	7.9e-22	5.2	5.0e-22	7.8	5.9e-22	13.3
167_168	H1H2L1V1	0.948	2.9e-22	9.8	2.0e-22	10.9	2.9e-22	4.9	2.1e-22	4.4	2.4e-22	8.0
169_170	H1H2V1	0.730	2.2e-21	24.2	1.1e-21	24.5	1.6e-21	7.3	1.7e-21	9.3	2.2e-21	17.9
171_172	L1V1	0.011	2.7e-21	19.7	1.4e-21	19.3	1.6e-21	5.2	1.9e-21	8.0	2.0e-21	14.7
173_174	L1V1	0.569	1.2e-20	19.5	7.5e-21	18.8	5.7e-21	5.5	5.7e-21	7.9	8.2e-21	15.9
175_176	H1H2L1V1	0.716	1.1e-21	20.1	5.7e-22	18.4	6.1e-22	6.3	5.9e-22	8.3	7.3e-22	16.1
177_178	H1L1V1	0.034	2.2e-21	20.9	1.1e-21	22.6	1.1e-21	6.3	1.5e-21	8.3	1.9e-21	16.2
179_180	H1H2L1V1	0.228	3.7e-22	7.7	2.1e-22	9.1	3.0e-22	3.5	2.6e-22	2.9	2.7e-22	5.4
181_182	L1V1	0.102	4.3e-21	29.4	2.2e-21	30.4	2.5e-21	9.5	2.9e-21	11.8	5.2e-21	23.3
183_184	H1H2V1	0.782	1.1e-21	20.8	6.7e-22	21.8	8.6e-22	7.6	7.1e-22	8.5	7.8e-22	16.9

Name	Network	p-value	$h_{100} H_z$ [ $H z^{-\frac{1}{2}}$ ]	$D_{100} H_z$ [Mpc]	$h_{150} H_z$ [ $H z^{-\frac{1}{2}}$ ]	$D_{150} H_z$ [Mpc]	$h_{300} H_z$ [ $H z^{-\frac{1}{2}}$ ]	$D_{300} H_z$ [Mpc]	$h_{NS-NS}$ [ $H z^{-\frac{1}{2}}$ ]	$D_{NS-NS}$ [Mpc]	$h_{NS-BH}$ [ $H z^{-\frac{1}{2}}$ ]	$D_{NS-BH}$ [Mpc]
185_186	H1H2V1	0.940	8.2e-22	19.6	5.2e-22	20.0	5.7e-22	7.4	4.9e-22	8.5	5.5e-22	16.5
187_188	H2L1	0.195	6.9e-21	15.8	2.5e-21	17.8	2.7e-21	7.1	2.8e-21	8.1	3.3e-21	13.6
189_190	H1V1	0.974	3.5e-21	24.6	1.6e-21	20.6	1.6e-21	6.5	3.5e-21	8.6	5.4e-21	16.9
191_192	H1H2L1V1	0.583	4.1e-22	28.0	2.9e-22	34.1	4.6e-22	9.6	3.3e-22	11.9	3.4e-22	23.5
193_194	H1H2L1V1	0.778	5.9e-22	11.1	4.1e-22	14.3	7.8e-22	4.6	4.5e-22	6.2	5.4e-22	11.0
199_200	H1H2L1	0.830	3.5e-22	37.2	2.4e-22	35.5	4.1e-22	12.3	2.7e-22	13.4	2.8e-22	26.3
201_202	H1H2L1V1	0.217	7.8e-22	4.8	5.4e-22	6.3	9.1e-22	2.3	5.5e-22	1.8	6.3e-22	2.9
205_206	H1H2L1V1	0.795	3.9e-22	4.1	2.7e-22	5.1	3.8e-22	2.3	2.7e-22	1.6	2.9e-22	3.2
207_208	H1H2L1V1	0.539	1.0e-21	0.9	5.4e-22	1.0	8.0e-22	0.6	5.0e-22	0.5	5.7e-22	0.8
209_210	H1H2L1V1	0.212	6.3e-22	9.5	4.4e-22	12.7	7.3e-22	5.9	4.7e-22	5.2	5.2e-22	8.9
211_212	H1H2L1V1	0.426	3.5e-22	4.8	2.5e-22	6.6	2.9e-22	3.4	2.6e-22	2.0	2.7e-22	3.5
213_214	H1H2L1V1	0.858	9.0e-22	29.1	6.5e-22	33.7	7.9e-22	12.2	6.8e-22	12.1	7.0e-22	23.7
217_218	L1V1	0.132	4.1e-21	2.5	2.3e-21	3.3	3.0e-21	1.5	3.0e-21	1.1	3.7e-21	1.3
219_220	H1H2V1	0.262	5.0e-21	9.6	2.5e-21	10.8	2.2e-21	4.2	2.5e-21	4.3	2.7e-21	8.4
221_222	H1H2V1	0.296	1.5e-21	13.2	7.9e-22	14.0	7.8e-22	6.3	7.7e-22	6.2	8.7e-22	11.8
223_224	H1H2L1V1	0.216	6.6e-22	1.6	4.0e-22	2.9	7.9e-22	1.4	4.5e-22	1.1	5.0e-22	2.0
225_226	H1H2L1V1	0.498	7.6e-22	3.1	5.1e-22	4.6	7.7e-22	2.3	5.4e-22	0.9	5.8e-22	1.2
229_230	H1H2V1	0.411	1.3e-21	26.5	7.6e-22	25.3	7.9e-22	7.9	8.5e-22	9.3	9.7e-22	19.3
231_232	L1V1	0.382	3.9e-21	18.4	2.0e-21	17.8	1.8e-21	4.6	2.0e-21	6.9	2.2e-21	12.1
233_234	H1H2L1	0.357	2.7e-22	31.3	1.9e-22	30.1	2.8e-22	8.9	1.9e-22	11.5	2.1e-22	22.9
235_236	H2L1V1	0.385	8.0e-22	13.9	5.6e-22	13.4	6.8e-22	4.0	5.5e-22	5.6	6.6e-22	10.4
237_238	H1H2L1V1	0.176	3.0e-22	27.6	2.1e-22	26.8	3.0e-22	9.4	2.3e-22	11.3	2.6e-22	22.7
241_242	H1H2L1V1	0.570	1.2e-21	10.8	7.9e-22	13.4	1.1e-21	4.5	9.0e-22	6.2	1.0e-21	11.4
243_244	H1H2L1V1	0.185	1.6e-21	17.1	9.6e-22	16.4	1.8e-21	4.9	1.0e-21	6.5	1.1e-21	12.5

Name	Network	p-value	$h_{100 H_z}$ [ $H z^{-\frac{1}{2}}$ ]	$D_{100 H_z}$ [Mpc]	$h_{150 H_z}$ [ $H z^{-\frac{1}{2}}$ ]	$D_{150 H_z}$ [Mpc]	$h_{300 H_z}$ [ $H z^{-\frac{1}{2}}$ ]	$D_{300 H_z}$ [Mpc]	$h_{NS-NS}$ [ $H z^{-\frac{1}{2}}$ ]	$D_{NS-NS}$ [Mpc]	$h_{NS-BH}$ [ $H z^{-\frac{1}{2}}$ ]	$D_{NS-BH}$ [Mpc]
245_246	H1H2V1	0.162	6.7e-22	31.4	4.1e-22	29.0	5.3e-22	12.6	3.9e-22	11.9	4.7e-22	23.7
247_248	H1H2V1	1.000	2.8e-21	12.1	2.1e-21	11.2	1.0e-20	4.6	2.7e-21	4.5	3.1e-21	9.2
251_252	H1H2L1	0.410	4.8e-22	2.7	3.2e-22	3.1	5.0e-22	1.2	3.7e-22	1.0	3.9e-22	1.7
255_256	H1H2L1	0.168	3.7e-22	2.1	2.4e-22	2.9	3.9e-22	1.7	2.7e-22	1.2	2.9e-22	2.4
257_258	L1V1	0.822	3.4e-21	7.2	1.6e-21	9.2	1.6e-21	4.7	1.9e-21	4.0	2.3e-21	7.5
259_260	H1H2L1	0.066	5.9e-22	16.6	4.2e-22	17.8	5.7e-22	4.6	4.7e-22	6.7	5.1e-22	12.9
261_262	L1V1	0.776	1.5e-21	14.2	7.5e-22	14.3	7.9e-22	4.7	1.2e-21	5.7	1.5e-21	11.2
263_264	H1H2L1V1	0.260	9.9e-22	8.5	6.5e-22	9.6	9.8e-22	4.6	7.3e-22	3.6	7.8e-22	6.7
267_268	H1H2L1V1	0.747	4.7e-22	2.8	3.0e-22	3.6	5.8e-22	2.1	3.7e-22	1.5	3.9e-22	2.9
269_270	H1L1V1	0.534	1.3e-21	39.7	7.3e-22	38.0	1.1e-21	13.0	7.3e-22	15.8	8.8e-22	31.7
271_272	H1H2L1	0.138	7.7e-22	13.6	5.6e-22	12.9	7.5e-22	5.3	5.3e-22	5.7	5.8e-22	9.8
275_276	H1H2L1V1	0.118	6.1e-22	36.6	4.3e-22	34.6	7.2e-22	12.2	4.8e-22	13.2	5.4e-22	25.3
273_274	H1H2L1	0.957	4.3e-22	9.3	3.0e-22	9.1	4.5e-22	3.2	3.1e-22	3.4	3.8e-22	6.4
277_278	H1H2L1	0.144	5.7e-22	6.8	4.1e-22	7.5	7.1e-22	2.0	4.4e-22	3.0	5.1e-22	5.8
281_282	H1H2L1	0.154	5.8e-22	16.3	4.1e-22	17.7	6.1e-22	6.8	4.9e-22	8.0	5.0e-22	14.0
289_290	H1H2L1V1	0.869	3.8e-22	3.8	3.2e-22	3.5	3.9e-22	0.3	2.8e-22	1.2	3.1e-22	2.1
293_294	H1H2L1V1	0.869	9.9e-22	22.6	5.9e-22	22.5	8.3e-22	7.2	6.8e-22	8.4	7.7e-22	16.7
295_296	H1H2L1V1	0.068	1.6e-21	29.3	1.1e-21	29.7	1.5e-21	9.2	1.4e-21	11.5	1.5e-21	22.7
297_298	H1H2L1V1	0.165	5.9e-22	3.2	4.5e-22	4.5	7.4e-22	2.3	4.5e-22	1.6	5.1e-22	2.9
303_304	H1H2	0.625	8.8e-22	18.3	5.5e-22	17.3	6.5e-22	6.3	5.4e-22	6.5	6.0e-22	12.7
305_306	H1H2V1	0.314	1.2e-21	7.2	7.8e-22	9.6	9.2e-22	4.6	7.6e-22	2.5	8.8e-22	4.4
311_312	H1H2L1V1	0.387	7.0e-22	10.9	4.1e-22	11.2	5.6e-22	3.7	4.6e-22	4.2	5.0e-22	8.3
313_314	H1H2L1V1	0.883	7.9e-22	23.1	5.2e-22	24.0	8.1e-22	6.2	5.3e-22	8.4	5.7e-22	16.7

Name	Network	p-value	$h_{100\text{Hz}}$ [ $H z^{-\frac{1}{2}}$ ]	$D_{100\text{Hz}}$ [Mpc]	$h_{150\text{Hz}}$ [ $H z^{-\frac{1}{2}}$ ]	$D_{150\text{Hz}}$ [Mpc]	$h_{300\text{Hz}}$ [ $H z^{-\frac{1}{2}}$ ]	$D_{300\text{Hz}}$ [Mpc]	$h_{NS-NS}$ [ $H z^{-\frac{1}{2}}$ ]	$D_{NS-NS}$ [Mpc]	$h_{NS-BH}$ [ $H z^{-\frac{1}{2}}$ ]	$D_{NS-BH}$ [Mpc]
315_316	H1H2L1V1	0.166	6.1e-22	8.2	4.4e-22	9.9	6.4e-22	3.2	4.6e-22	4.2	5.5e-22	7.2
317_318	H1H2L1V1	0.842	7.0e-22	14.1	4.9e-22	12.9	7.4e-22	4.8	5.0e-22	5.8	5.6e-22	11.3
319_320	H1H2L1V1	0.499	4.8e-22	25.1	2.9e-22	24.0	5.4e-22	8.1	3.3e-22	9.9	3.9e-22	17.0
321_322	H1H2L1V1	0.024	5.7e-22	17.8	4.0e-22	16.8	6.1e-22	5.0	4.1e-22	6.4	4.2e-22	12.0
331_332	H1H2L1	0.023	5.6e-22	19.0	4.0e-22	17.6	5.9e-22	5.1	3.9e-22	7.0	4.5e-22	12.9
333_334	H1H2L1	0.586	4.0e-21	18.6	2.8e-21	17.6	3.8e-21	5.9	2.2e-21	6.4	2.6e-21	13.1
335_336	H1H2L1V1	0.846	7.4e-22	28.4	4.8e-22	22.7	6.9e-22	9.2	4.8e-22	11.1	5.4e-22	21.0
337_338	H1H2L1V1	0.523	4.8e-22	11.0	3.0e-22	12.4	4.2e-22	4.3	3.3e-22	4.5	3.7e-22	8.5
339_340	H1H2	0.769	7.0e-22	6.7	4.6e-22	6.3	5.5e-22	2.4	4.8e-22	2.3	5.3e-22	4.4
343_344	H1H2L1V1	0.961	5.7e-22	18.4	3.8e-22	16.0	7.1e-22	4.9	3.8e-22	6.9	5.0e-22	12.6
345_346	H1H2L1V1	0.553	5.3e-22	12.3	3.5e-22	13.1	5.0e-22	5.6	3.6e-22	5.8	3.9e-22	10.8
347_348	H1H2V1	0.405	8.0e-22	9.1	5.6e-22	9.3	7.4e-22	3.9	5.4e-22	4.0	5.7e-22	7.4
349_350	H1H2L1V1	0.484	5.3e-22	15.6	3.0e-22	17.8	4.8e-22	6.5	3.6e-22	6.7	3.8e-22	13.1
351_352	H1H2L1V1	0.366	3.7e-22	13.8	2.6e-22	13.8	4.9e-22	4.5	2.7e-22	5.7	2.9e-22	11.3
355_356	H1H2L1	0.776	5.2e-22	17.7	3.3e-22	16.4	4.5e-22	5.6	3.6e-22	6.6	3.8e-22	11.8
359_360	H1H2L1V1	0.904	1.3e-21	15.5	7.5e-22	14.8	9.5e-22	4.9	7.5e-22	6.2	8.4e-22	11.6
361_362	H1H2L1V1	0.553	2.8e-22	22.8	2.0e-22	24.6	2.7e-22	6.7	2.0e-22	9.3	2.2e-22	16.6
363_364	H1H2L1V1	0.735	8.3e-22	19.1	5.7e-22	17.9	8.0e-22	5.9	6.1e-22	7.4	6.9e-22	15.3
367_368	H1H2	0.661	5.0e-22	19.5	3.3e-22	17.9	3.9e-22	6.2	2.8e-22	7.9	3.2e-22	14.4
369_370	H1H2L1V1	0.736	1.0e-21	2.7	6.4e-22	2.6	1.0e-21	1.0	7.3e-22	1.4	7.8e-22	2.5

Name	Network	p-value	$h_{100\text{Hz}}$ [ $H z^{-\frac{1}{2}}$ ] [Mpc]	$D_{100\text{Hz}}$ [Mpc]	$h_{150\text{Hz}}$ [ $H z^{-\frac{1}{2}}$ ] [Mpc]	$D_{150\text{Hz}}$ [Mpc]	$h_{300\text{Hz}}$ [ $H z^{-\frac{1}{2}}$ ] [Mpc]	$D_{300\text{Hz}}$ [Mpc]	$h_{NS-NS}$ [ $H z^{-\frac{1}{2}}$ ] [Mpc]	$D_{NS-NS}$ [Mpc]	$h_{NS-BH}$ [ $H z^{-\frac{1}{2}}$ ] [Mpc]	$D_{NS-BH}$ [Mpc]
371_372	H1H2	0.291	5.1e-22	14.6	3.4e-22	14.9	3.9e-22	5.2	3.3e-22	6.4	3.8e-22	12.0
373_374	H1H2V1	0.214	1.5e-21	17.3	8.1e-22	17.3	1.0e-21	5.6	7.6e-22	7.9	9.1e-22	14.1
375_376	H1H2L1V1	0.859	8.0e-22	15.4	5.7e-22	15.8	7.0e-22	6.5	5.4e-22	6.4	6.1e-22	12.3
377_378	H2L1V1	0.746	6.9e-22	19.0	4.0e-22	19.1	5.3e-22	5.1	4.3e-22	8.2	5.0e-22	13.0
383_384	H1L1V1	0.179	7.8e-22	20.5	5.5e-22	20.5	7.9e-22	7.2	5.3e-22	8.5	5.8e-22	16.7
385_386	H1H2V1	0.004	9.9e-22	13.6	6.6e-22	13.0	8.2e-22	4.9	7.3e-22	5.7	8.5e-22	11.4
387_388	H1H2L1V1	0.435	4.1e-22	20.4	2.9e-22	24.0	4.1e-22	7.4	3.1e-22	8.5	3.2e-22	17.1
395_396	H1H2V1	0.801	1.1e-21	29.2	5.8e-22	28.0	7.5e-22	7.3	6.1e-22	11.6	7.0e-22	22.8
398	H1H2	0.542	1.1e-21	21.0	5.9e-22	21.8	7.1e-22	8.0	6.3e-22	8.6	7.5e-22	16.9
400	H1H2	0.469	1.0e-21	8.6	5.8e-22	9.6	7.0e-22	3.8	5.3e-22	3.9	6.2e-22	7.8
401	H1H2L1	0.233	5.5e-22	38.4	3.6e-22	36.7	5.6e-22	13.3	3.5e-22	15.5	3.7e-22	29.2
402	H1H2V1	0.777	9.7e-22	13.0	5.8e-22	12.7	7.6e-22	4.5	5.9e-22	5.0	6.9e-22	9.4
404	L1V1	0.202	1.6e-21	21.7	8.9e-22	21.8	8.9e-22	9.2	9.5e-22	11.0	1.1e-21	20.1
405	H1V1	0.794	2.5e-21	10.6	1.3e-21	11.2	1.1e-21	3.6	1.3e-21	4.2	1.6e-21	8.3
406	H1H2V1	0.570	7.1e-22	21.4	4.0e-22	21.4	5.6e-22	9.3	3.9e-22	9.3	4.1e-22	17.4
407	H1H2L1	0.671	7.2e-22	7.5	5.1e-22	8.9	1.0e-21	3.5	4.8e-22	4.1	5.3e-22	7.2
408	H1H2L1	0.304	3.8e-22	13.5	2.8e-22	12.8	4.1e-22	5.1	2.6e-22	5.7	2.8e-22	10.6
409	H1H2V1	0.260	3.1e-21	15.8	1.8e-21	18.2	2.3e-21	6.8	1.9e-21	7.1	2.1e-21	13.1
410	H1H2L1V1	0.364	2.9e-22	13.8	2.3e-22	13.1	3.9e-22	4.6	2.5e-22	5.9	2.7e-22	11.3
411	H1H2L1V1	0.107	5.3e-22	10.9	3.0e-22	11.0	5.5e-22	4.4	3.5e-22	4.2	3.8e-22	7.7
413	H1H2V1	0.984	4.3e-22	26.6	3.0e-22	24.7	4.1e-22	8.7	3.3e-22	9.8	3.6e-22	20.1
414	H1H2L1V1	0.366	3.7e-22	10.3	2.2e-22	12.5	2.9e-22	4.8	2.5e-22	5.1	2.9e-22	9.3

Name	Network	p-value	$h_{554\text{ Hz}}$ [ $\text{Hz}^{-\frac{1}{2}}$ ]	$D_{554\text{ Hz}}$ [Mpc]	$h_{1000\text{ Hz}}$ [ $\text{Hz}^{-\frac{1}{2}}$ ]	$D_{1000\text{ Hz}}$ [Mpc]
398	H1H2	0.183	1.1e-21	1.8	2.1e-21	0.5
400	H1H2	0.873	1.1e-21	1.9	1.8e-21	0.6
401	H1H2L1	0.829	7.5e-22	2.5	1.4e-21	0.7
402	H1H2V1	0.450	1.1e-21	1.8	2.2e-21	0.5
404	L1V1	0.803	1.0e-21	1.9	2.0e-21	0.5
405	H1V1	0.074	1.2e-21	1.7	2.2e-21	0.5
406	H1H2V1	0.134	1.1e-21	1.8	1.9e-21	0.6
407	H1H2L1	0.536	1.2e-21	1.6	2.7e-21	0.4
408	H1H2L1	0.129	5.8e-22	3.4	1.1e-21	1.0
409	H1H2V1	0.867	5.9e-21	0.3	2.3e-20	0.0
410	H1H2L1V1	0.583	6.8e-22	2.9	1.2e-21	0.9
411	H1H2L1V1	0.991	6.6e-22	2.7	1.4e-21	0.7
413	H1H2V1	0.176	9.0e-22	2.2	1.7e-21	0.6
414	H1H2L1V1	0.381	5.2e-22	3.7	9.6e-22	1.1

Table 9.3: This table shows the results of the *high frequency* analysis, in the first columns there are: the label used for each neutrino trigger; the network specifies all detectors involved and the False Alarm Probability of the loudest GW trigger in coincidence with each neutrino. In the last columns are shown the ULs, so the  $h_{rss}^{90\%}$  and the exclusion distances  $D$  in Mpc for the sin-Gaussian at 554 Hz and 1000 Hz.

# Chapter 10

## Appendix A

### 10.1 Dominant Polarization Frame

The definition of the detector response  $d$  to a gravitational signal  $h_+, h_\times$  is

$$d = F_+ h_+ + F_\times h_\times \quad (10.1)$$

We can even define complex waveforms  $u$  and antenna patterns  $A$  as

$$u = h_+ + i h_\times, \quad (10.2)$$

$$A = \frac{1}{2}(F_+ + i F_\times) \quad (10.3)$$

where  $i$  is the imaginary unity. With such notation, the detector response becomes

$$d = A^* u + A u^*, \quad (10.4)$$

where  $*$  is the conjugate. In fact

$$A^* u = \frac{1}{2}(F_+ - i F_\times)(h_+ + i h_\times) = \frac{1}{2}F_+ h_+ + \frac{i}{2}F_+ h_\times - \frac{i}{2}F_\times h_+ + \frac{1}{2}F_\times h_\times \quad (10.5)$$

$$A u^* = \frac{1}{2}(F_+ + i F_\times)(h_+ - i h_\times) = \frac{1}{2}F_+ h_+ - \frac{i}{2}F_+ h_\times + \frac{i}{2}F_\times h_+ + \frac{1}{2}F_\times h_\times \quad (10.6)$$

If we sum the equation 10.5 and 10.6, we'll have the number 10.4, and a coordinate transformation in the wave coordinate frame is performed by a rotation of the type:

$$u' = e^{-i2\psi} u \quad (10.7)$$

$$A' = e^{-i2\psi} A. \quad (10.8)$$

Hence, a coordinate transformation does not change the detector response.

$$\begin{aligned} A' &= (\cos 2\psi - i \sin 2\psi) \frac{1}{2} (F_+ + iF_\times) = \\ &= \frac{1}{2} F_+ \cos 2\psi + \frac{i}{2} F_\times \cos 2\psi - \frac{i}{2} F_+ \sin 2\psi + \frac{1}{2} F_\times \sin 2\psi = \\ &= \frac{1}{2} (F_+ \cos 2\psi + F_\times \sin 2\psi) + \frac{i}{2} (-F_+ \sin 2\psi + F_\times \cos 2\psi) \end{aligned} \quad (10.9)$$

so from the last line, we can find in the new coordinate frame

$$F'_+ = F_+ \cos 2\psi + F_\times \sin 2\psi \quad (10.10)$$

$$F'_\times = -F_+ \sin 2\psi + F_\times \cos 2\psi \quad (10.11)$$

If we multiply the equation number 10.8 for  $e^{i2\psi}$ , we have

$$A = e^{i2\psi} A' \quad (10.12)$$

and take the square

$$(A)^2 = e^{4i\psi} (A')^2 \quad (10.13)$$

$$(A')^2 = \left[ \frac{1}{2} (F'_+ + iF'_\times) \right]^2 = \frac{1}{4} (F'_+)^2 - \frac{1}{4} (F'_\times)^2 + \frac{i}{2} F'_+ \cdot F'_\times \quad (10.14)$$

If we have a network of detectors  $k = 1, \dots, N$  then equation 10.14 holds individually for each detector. Summing over all detectors gives

$$|\vec{A}'|^2 = \frac{1}{4} |\vec{F}'_+|^2 - \frac{1}{4} |\vec{F}'_\times|^2 + \frac{i}{2} \vec{F}'_+ \cdot \vec{F}'_\times \quad (10.15)$$

where  $\vec{F}'_+ \equiv (F'_{+,1}, F'_{+,2}, \dots, F'_{+,N})$ , and similarly for  $\vec{F}'_\times, \vec{A}$ . Similarly, in the original frame

$$|\vec{A}|^2 = \frac{1}{4} |\vec{F}_+|^2 - \frac{1}{4} |\vec{F}_\times|^2 + \frac{i}{2} \vec{F}_+ \cdot \vec{F}_\times. \quad (10.16)$$

The Dominant Polarization Frame may be defined as the frame in which  $\vec{F}'_+ \cdot \vec{F}'_\times = 0$  and  $|\vec{F}'_+| > |\vec{F}'_\times|$ . Hence from 10.15  $|\vec{A}'|^2$  is real in the DPF. From

the previous equations, 10.15 and 10.16, we can define the transformation from a general frame  $F_+, F_\times$  to the DPF,  $F'_+, F'_\times$ , by expressing the angle  $\psi$  as a function of  $F_+, F_\times$ . Due to the fact that  $|\vec{A}'|^2$  is real, even its square is real so we can write

$$\frac{1}{4}(F_+)^2 - \frac{1}{4}(F_\times)^2 + \frac{i}{2}F_+F_\times = |\vec{A}|^2 = (|\vec{A}'|e^{i2\psi})^2 = |\vec{A}'|^2e^{4i\psi} \quad (10.17)$$

and by using the identity  $e^{4i\psi} = \cos(4\psi) + i \sin(4\psi)$ , we have

$$\frac{1}{4}(F_+)^2 - \frac{1}{4}(F_\times)^2 + \frac{i}{2}F_+F_\times = |\vec{A}|^2 = |\vec{A}'|^2e^{4i\psi} = |\vec{A}'|^2[\cos(4\psi) + i \sin(4\psi)] \quad (10.18)$$

From this we have

$$\cos(4\psi)|\vec{A}'|^2 = \frac{1}{4}[|\vec{F}_+|^2 - |\vec{F}_\times|^2] \quad (10.19)$$

$$\sin(4\psi)|\vec{A}'|^2 = \frac{1}{2}\vec{F}_+ \cdot \vec{F}_\times \quad (10.20)$$

$$\tan(4\psi) = 2\frac{\vec{F}_+ \cdot \vec{F}_\times}{[|\vec{F}_+|^2 - |\vec{F}_\times|^2]} \quad (10.21)$$

We can easily see that these transformations assure the orthogonality of  $\vec{F}'_+$  and  $\vec{F}'_\times$  is impose  $\Im(A')^2 = 0$ ,

$$\begin{aligned} \vec{F}'_+ \cdot \vec{F}'_\times &= (\vec{F}_+ \cos 2\psi + \vec{F}_\times \sin 2\psi)(-\vec{F}_+ \sin 2\psi + \vec{F}_\times \cos 2\psi) = \quad (10.22) \\ &= -|\vec{F}_+|^2 \cos 2\psi \sin 2\psi + \vec{F}_+ \cdot \vec{F}_\times \cos^2 2\psi - \vec{F}_+ \cdot \vec{F}_\times \sin^2 2\psi + |\vec{F}_\times|^2 \cos 2\psi \sin 2\psi = \\ &= -(|\vec{F}_+|^2 - |\vec{F}_\times|^2)(\cos 2\psi \sin 2\psi) + (\vec{F}_+ \cdot \vec{F}_\times)(\cos^2 2\psi - \sin^2 2\psi) = \\ &= -\frac{1}{2}(|\vec{F}_+|^2 - |\vec{F}_\times|^2) \sin(4\psi) + (\vec{F}_+ \cdot \vec{F}_\times) \cos(4\psi) = 0. \end{aligned}$$

## 10.2 Standard likelihood

Having expressed detector strain in a convenient basis we can use it to detect GWs. When analyzing those strains we want to separate between two possible hypotheses: strains are a sum of GW signal with noise, or strains

contain only detector noise. From the frequentist point of view the optimal choice for differentiating two hypotheses is to look at their likelihood ratio

$$L = \frac{P(d|signal)}{P(d|noise)}. \quad (10.23)$$

It is the ratio of the probability of the obtaining the detector strains that we see given each hypothesis. The optimality is given by Neyman-Pearson lemma. This lemma states that for deciding between two hypotheses, comparing the likelihood to a threshold gives the minimal rate of false negatives (missed signals) for a fixed rate of false positives (noise tagged as signal), where the false positive rate is fixed by the choice of threshold. We can use the assumption of Gaussian noise to compute this likelihood ratio:

$$P(d|noise) = \frac{1}{(\sqrt{2\pi})^N} \exp\left(-\frac{1}{2}|\vec{d}_i|^2\right) = \frac{1}{(2\pi)^{N/2}} \exp\left(-\frac{1}{2}d^T d\right) \quad (10.24)$$

because we have already whitened the data. Getting the numerator of 10.23 is a little harder because we need to marginalize over all the possible waveforms ( $h_+$ ,  $h_\times$ ). If we knew the exact waveform then

$$\begin{aligned} P(d|h_+, h_\times, signal) &= \\ &= \frac{1}{(2\pi)^{N/2}} \exp\left[-\frac{1}{2}\left[|\vec{d} - \vec{F}_+ h_+|^2 + |\vec{d} - \vec{F}_\times h_\times|^2 - |\vec{d}|^2\right]\right] \end{aligned} \quad (10.25)$$

Without this knowledge we marginalize this expression assuming that all values of  $h_+$ ,  $h_\times$  are equally probable, by using an integral of a Gaussian function

$$\int e^{-fx^2+gx+l} dx = \sqrt{\frac{\pi}{f}} \exp\left(\frac{g^2}{4f} + l\right) \quad (10.26)$$

where in our case the integral is

$$\int dh_+ \exp\left(-\frac{1}{2}|\vec{d} - \vec{F}_+ h_+|^2\right) = \sqrt{\frac{2\pi}{|\vec{F}_+|^2}} \exp\left(-\frac{1}{2}|\vec{d}|^2 + \frac{1}{2} \frac{(\vec{d} \cdot \vec{F}_+)^2}{|\vec{F}_+|^2}\right) \quad (10.27)$$

and  $f = \frac{1}{2}(\vec{F}_+ \cdot \vec{F}_+) = \frac{1}{2}|\vec{F}_+|^2$  (scalar),  $g = \vec{d} \cdot \vec{F}_+$  (scalar) and  $l = -\frac{1}{2}|\vec{d}|^2$  (scalar). It is the same in the other polarization

$$\int dh_\times \exp\left(-\frac{1}{2}|\vec{d} - \vec{F}_\times h_\times|^2\right) = \sqrt{\frac{2\pi}{|\vec{F}_\times|^2}} \exp\left(-\frac{1}{2}|\vec{d}|^2 + \frac{1}{2} \frac{(\vec{d} \cdot \vec{F}_\times)^2}{|\vec{F}_\times|^2}\right) \quad (10.28)$$

where  $f = \frac{1}{2}(\vec{F}_+ \cdot \vec{F}_+) = \frac{1}{2}|\vec{F}_+|^2$  (scalar),  $g = \vec{d} \cdot \vec{F}_+$  (scalar) and  $l = -\frac{1}{2}|\vec{d}|^2$  (scalar). So,

$$P(d|signal) = \iint dh_+ dh_\times P(d|h_+, h_\times, signal) = \quad (10.29)$$

$$\sqrt{\frac{2\pi}{|\vec{F}_+|^2}} \sqrt{\frac{2\pi}{|\vec{F}_\times|^2}} \exp\left(-\frac{1}{2}|\vec{d}|^2 + \frac{1}{2}\frac{(\vec{d} \cdot \vec{F}_+)^2}{|\vec{F}_+|^2} - \frac{1}{2}|\vec{d}|^2 + \frac{1}{2}\frac{(\vec{d} \cdot \vec{F}_\times)^2}{|\vec{F}_\times|^2} + \frac{1}{2}|\vec{d}|^2\right)$$

where  $\widehat{e}_+ \equiv \vec{F}_+ / |\vec{F}_+|$  and  $\widehat{e}_\times \equiv \vec{F}_\times / |\vec{F}_\times|$  are the unit vectors in the DPF, and the energies in the plus and cross polarizations are

$$E_+ \equiv \frac{(\vec{d} \cdot \vec{F}_+)^2}{|\vec{F}_+|^2} = (\vec{d} \cdot \widehat{e}_+)^2 \quad (10.30)$$

$$E_\times \equiv \frac{(\vec{d} \cdot \vec{F}_\times)^2}{|\vec{F}_\times|^2} = (\vec{d} \cdot \widehat{e}_\times)^2 \quad (10.31)$$

$$E_{SL} \equiv E_+ + E_\times = (\vec{d} \cdot \widehat{e}_+)^2 + (\vec{d} \cdot \widehat{e}_\times)^2 \quad (10.32)$$

The likelihood ratio becomes

$$L = \frac{P(d|signal)}{P(d|noise)} = \frac{\sqrt{\frac{2\pi}{|\vec{F}_+|^2}} \sqrt{\frac{2\pi}{|\vec{F}_\times|^2}} \exp\left[\frac{1}{2}[(\vec{d} \cdot \widehat{e}_+)^2 + (\vec{d} \cdot \widehat{e}_\times)^2 - \frac{1}{2}|\vec{d}|^2]\right]}{(2\pi)^{N/2} \exp(-\frac{1}{2}|\vec{d}|^2)} \quad (10.33)$$

$$L = \frac{(2\pi)^{-\frac{N-2}{2}}}{\sqrt{|\vec{F}_+|^2 |\vec{F}_\times|^2}} \exp\left[\frac{1}{2}[(\vec{d} \cdot \widehat{e}_+)^2 + (\vec{d} \cdot \widehat{e}_\times)^2]\right] \quad (10.34)$$

### 10.3 Meaning of DPF

The definition of the detector response  $d$  to a gravitational signal  $h_+, h_\times$  is

$$\vec{d} = \vec{f}_+ h_+ + \vec{f}_\times h_\times \quad (10.35)$$

where  $\vec{f}_+ = \frac{\vec{F}_+}{\sigma}$  and  $\vec{f}_\times = \frac{\vec{F}_\times}{\sigma}$  are divided by the noise rms.

$$\vec{d} * (\vec{f}_+, \vec{f}_\times) \quad (10.36)$$

from this multiplication we have the matrix below for deriving the eigenvalues, where  $\vec{f}_+$  and  $\vec{f}_\times$  are vectors:

$$MATRIX = \begin{pmatrix} |\vec{f}_+|^2 & (\vec{f}_+ \cdot \vec{f}_\times) \\ (\vec{f}_\times \cdot \vec{f}_+) & |\vec{f}_\times|^2 \end{pmatrix} \quad (10.37)$$

To justify why the matrix 10.37 is important. This matrix appears naturally when you try to invert 10.35 to solve for  $(h_+, h_\times)$ . Specifically, defining the matrix  $F = [\vec{f}_+ \vec{f}_\times]$ , we can solve to get

$$[h_+; h_\times] = (F^T F)^{-1} F^T d \quad (10.38)$$

where the notation is the following: row [a b] and column [c ; d] vectors. This is easily verified by substituting (1) and getting consistency:

$$[h_+; h_\times] = (F^T F)^{-1} F^T d = (F^T F)^{-1} (F^T F) [h_+; h_\times] = [h_+; h_\times] \quad (10.39)$$

So, we need to compute the inverse of the 2x2 matrix  $(F^T F)$  to solve for the GW waveform.  $(F^T F)$  is just the matrix 10.37; this is why we want to solve for the eigenvalues of this matrix. A value near zero means we have very poor sensitivity to that polarization. We need to calculate the det of  $(MATRIX - \lambda I)$ , that has to be equal to 0

$$MATRIX - \lambda I = \begin{pmatrix} |\vec{f}_+|^2 - \lambda & (\vec{f}_+ \cdot \vec{f}_\times) \\ (\vec{f}_\times \cdot \vec{f}_+) & |\vec{f}_\times|^2 - \lambda \end{pmatrix} \quad (10.40)$$

and the det is:

$$\begin{aligned} det &= (|\vec{f}_+|^2 - \lambda)(|\vec{f}_\times|^2 - \lambda) - (\vec{f}_+ \cdot \vec{f}_\times)^2 \\ &= |\vec{f}_+|^2 |\vec{f}_\times|^2 - |\vec{f}_+|^2 \lambda - |\vec{f}_\times|^2 \lambda + \lambda^2 - (\vec{f}_+ \cdot \vec{f}_\times)^2 \\ &= \lambda^2 - (|\vec{f}_+|^2 + |\vec{f}_\times|^2) \lambda + |\vec{f}_+|^2 |\vec{f}_\times|^2 - (\vec{f}_+ \cdot \vec{f}_\times)^2 \end{aligned} \quad (10.41)$$

To solve the second order equation, we calculate the quantity under the square root

$$\begin{aligned} \Delta &= (|\vec{f}_+|^2 + |\vec{f}_\times|^2)^2 - 4[|\vec{f}_+|^2 |\vec{f}_\times|^2 - (\vec{f}_+ \cdot \vec{f}_\times)^2] = \\ &= |\vec{f}_+|^4 + |\vec{f}_\times|^4 + 2|\vec{f}_+|^2 |\vec{f}_\times|^2 - 4|\vec{f}_+|^2 |\vec{f}_\times|^2 + 4(\vec{f}_+ \cdot \vec{f}_\times)^2 = \\ &= |\vec{f}_+|^4 + |\vec{f}_\times|^4 - 2|\vec{f}_+|^2 |\vec{f}_\times|^2 + 4(\vec{f}_+ \cdot \vec{f}_\times)^2 = \\ &= (|\vec{f}_+|^2 - |\vec{f}_\times|^2)^2 + 4(\vec{f}_+ \cdot \vec{f}_\times)^2 \end{aligned} \quad (10.42)$$

The eigenvalues are:

$$\lambda_{1,2} = \frac{|\vec{f}_+|^2 + |\vec{f}_\times|^2 \pm \sqrt{(|\vec{f}_+|^2 - |\vec{f}_\times|^2)^2 + 4(\vec{f}_+ \cdot \vec{f}_\times)^2}}{2} \quad (10.43)$$

How we saw with the derivation of the Dominat Polarization Frame, by introducing an arbitrary rotation of  $\vec{f}_+$  and  $\vec{f}_\times$  the equation above is invariant and we can kill the cross term.

$$\lambda_{1,2} = \frac{|\vec{f}'_+|^2 + |\vec{f}'_\times|^2 \pm \sqrt{(|\vec{f}'_+|^2 - |\vec{f}'_\times|^2)^2}}{2} = \frac{(|\vec{f}'_+|^2 + |\vec{f}'_\times|^2 \pm (|\vec{f}'_+|^2 - |\vec{f}'_\times|^2))}{2} \quad (10.44)$$

$|\vec{f}'_+|^2$  and  $|\vec{f}'_\times|^2$  Hence,  $|\vec{f}'_+|^2$  and  $|\vec{f}'_\times|^2$  are eigenvalues of the network response matrix. This is the network sensitivity to the  $h_+$  and  $h_\times$  polarization components defined in DPF. They tell us how well each component is detected by a given network. For example, for aligned detectors (like H1H2)  $|\vec{f}'_\times| = 0$ . For closely aligned detectors like L1H1H2,  $|\vec{f}'_\times| \ll |\vec{f}'_+|$  This is used as a powerful constraint in the analysis.



# Chapter 11

## Appendix B

### 11.1 Introduction

The aim of the GWHEN project is to study the connection between the concurrent emission of high energy neutrino (HEN) fluxes and gravitational waves (GWs). Unlike photons or protons, both these probes travel vast cosmological distances without hindrance, unabsorbed by intervening matter and undeflected by intergalactic magnetic fields. Cataclysmic cosmic events can be plausible sources of both Gravitational Waves (GWs) and High Energy Neutrinos (HENs). Both GWs and HENs are cosmic messengers complementary to photons that can escape very dense media and travel unaffected over cosmological distances, carrying information from the innermost regions of the astrophysical engines. For the same reasons, such messengers could also reveal new, hidden sources that are not observed by conventional photon astronomy. Requiring consistency between GW and HEN detection channels shall enable new searches and a detection will yield significant additional information about the common source. A neutrino telescope such as ANTARES can determine accurately the time and direction of high energy neutrino events. A network of gravitational wave detectors such as LIGO and Virgo can also provide timing/directional information for gravitational wave bursts. By combining the information from these totally independent detectors, one can search for cosmic events that may arrive from common astrophysical sources. For the joint analysis we consider the data from the LIGO and VIRGO GW detectors and from the ANTARES neutrino telescope. Before the starting of this search we need to understand how the

exchanged neutrino triggers are reconstructed. Various strategies have been devised to reconstruct the muon track from the times at which the photon hits occur in the optical module, and all these approaches are very well known in the ANTARES collaboration. In the following we will outline a general method to understand the case of a detection by using only two ANTARES strings. The reconstruction with 2 detector lines, due to the symmetry of the detector, drives in a particular case in which it is not possible to distinguish between the real track and the mirror one, how we will explain, using as starting point the recent ANTARES article [209] .

## 11.2 Generalities

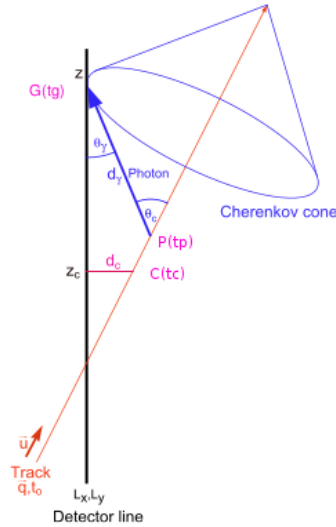


Figure 11.1: Picture number 2 from the article [209]

In reference to the picture 2 of the article [209], we indicate  $d(P)\hat{\gamma}(P)$  as the photon travel path,  $d(P)$  is its length and  $\hat{\gamma}(P)$  is a unit vector. The starting point for the photon is the point  $P$ , and the arrival one is  $G$ . The vector  $\hat{\gamma}$  and the length  $d$  depend on  $P$ .

The muon is described through  $Q, t_0$  as the reference point and with the unit vector  $\hat{u}$ .  $C, t_c$  is the point of closest approach of a particle track to a detector line.

To summarize what we said before we can write

- $G = \{0, 0, z\}$  ,  $t_\gamma$
- $C = \{x_c, y_c, z_c\}$  ,  $t_c$
- $P = \{x_p, y_p, z_p\}$  ,  $t_p$

Let's express  $t_\gamma$  as function of  $z$ , remembering that:

- the angles in the picture can be calculated through dot products
- the time difference  $t_G - t_P$  is necessary for the photon to cover the distance  $d$
- the time difference  $t_P - t_C$  is necessary for the muon to go from point  $C$  to  $P$

The particle is assumed to move with the speed of light in vacuum. All space-time points,  $\vec{p}(t)$ , that are part of the track can be parameterized as

$$\vec{p}(t) = \vec{q} + c(t - t_0)\hat{u} \quad (11.1)$$

The particle passes through the point  $\vec{q}$  at time  $t_0$  and moves in the direction  $\vec{u}$ . We can get the relation between  $\overrightarrow{QP}$  and  $\overrightarrow{QC}$

$$\overrightarrow{QP} = \overrightarrow{QC} + c(t_p - t_c)\hat{u} \quad (11.2)$$

For the photon we can write down a similar relation,

$$\overrightarrow{QG} = \overrightarrow{QP} + \frac{c}{n}(t_\gamma - t_p)\hat{\gamma} \quad (11.3)$$

using  $\frac{c}{n}(t_\gamma - t_p) = d$ , it becomes

$$\overrightarrow{QG} = \overrightarrow{QP} + d\hat{\gamma} \quad (11.4)$$

We need to find the expression between  $\gamma$ ,  $d$  as function of  $(z, t_\gamma)$ . Composing the previous equations:

$$\overrightarrow{QG} = \overrightarrow{QP} + d\hat{\gamma} = \overrightarrow{QC} + c(t_p - t_c)\hat{u} + d\hat{\gamma} = \overrightarrow{QC} + ct\hat{u} + d\hat{\gamma} \quad (11.5)$$

where  $\overrightarrow{QP} = \overrightarrow{QC} + c(t_p - t_c)\hat{u}$  and  $t = t_p - t_c$ .

Moreover, we remember that:

- $\hat{u}$  and  $\hat{\gamma}$  are unitary vectors ( $\hat{u} \cdot \hat{u} = 1$ ,  $\hat{\gamma} \cdot \hat{\gamma} = 1$ )
- The angle between them is the Cherenkov one  $\theta_c$  ( $\hat{u} \cdot \hat{\gamma} = \cos(\theta_c) = 1/n$ )
- The cosine of  $\hat{\gamma}$  as regards  $z$  ( $\theta_\gamma$ ) is the coordinate  $\gamma_z$

We can now rewrite the equation Eq: 11.5  $\overrightarrow{QG} = \overrightarrow{QC} + ct\hat{u} + d\hat{\gamma}$  in its components:

$$\begin{cases} 0 = x_c + ctu_x + d\gamma_x \\ 0 = y_c + ctu_y + d\gamma_y \\ z = z_c + ctu_z + d\gamma_z \end{cases} \quad (11.6)$$

From the last one we have  $ct$  as function of other variables:

$$ct = \frac{(z - z_c) - d\gamma_z}{u_z} \quad (11.7)$$

### 11.3 The z-component of the point of closest approach $z_c$ and its distance $d_c$

Looking at the picture  $C$  is the point of closest approach of a particle track to a detector line. We want to obtain time and position for the point of closest approach.

The detector lines are approximated as vertical lines along the  $z$ -axis at fixed horizontal positions  $L_x, L_y$ . Taking a generic point on the muon track:  $\overrightarrow{p}(t) = \{x, y, z\} = \overrightarrow{q} + c(t - t_0)\hat{u}$ . The distance between track and detector line is  $d = \sqrt{(x - L_x)^2 + (y - L_y)^2}$ .

To minimize this distance:

$$\begin{aligned} \frac{\delta d^2}{\delta t} &= \frac{\delta[(x - L_x)^2 + (y - L_y)^2]}{\delta t} = \\ &= 2(x - L_x) \frac{\delta x}{\delta t} + 2(y - L_y) \frac{\delta y}{\delta t} = \\ &= 2[q_x + c(t - t_0)u_x - L_x]cu_x + 2[q_y + c(t - t_0)u_y - L_y]cu_y = \\ &= 2c[q_x u_x + c(t - t_0)u_x^2 + q_y u_y + c(t - t_0)u_y^2 - u_x L_x - u_y L_y] = 0 \end{aligned} \quad (11.8)$$

So, we have:

$$\begin{aligned} c(t_c - t_0) &= \frac{u_x L_x + u_y L_y - q_x u_x - q_y u_y}{u_x^2 + u_y^2} = \\ &= \frac{u_x L_x + u_y L_y + q_z u_z - (\vec{q} \cdot \hat{u})}{1 - u_z^2} \end{aligned} \quad (11.9)$$

where  $q \cdot \hat{u} = q_x u_x + q_y u_y + q_z u_z$  and  $u_x^2 + u_y^2 + u_z^2 = 1$ .

Substituting  $t_c$  in the third component of  $p(t)$  we get  $z_c$ , the z-component of the point of closest approach of a particle track to a detector line:

$$\begin{aligned} z_c &= q_z + c(t_c - t_0)u_z = \\ &= q_z + u_z \frac{u_x L_x + u_y L_y + q_z u_z - (\vec{q} \cdot \hat{u})}{1 - u_z^2} = \\ &= \frac{q_z(1 - u_z^2) + u_z(u_x L_x + u_y L_y) + q_z u_z^2 - u_z(\vec{q} \cdot \hat{u})}{1 - u_z^2} = \\ &= \frac{q_z + u_z(u_x L_x + u_y L_y) - u_z(\vec{q} \cdot \hat{u})}{1 - u_z^2} \end{aligned} \quad (11.10)$$

at a distance

$$d_c = \sqrt{(p_x(t_c) - L_x)^2 + (p_y(t_c) - L_y)^2} \quad (11.11)$$

From the eq 11.10 we can obtain  $q_z$

$$q_z = (1 - u_z^2)z_c - u_z(u_x L_x + u_y L_y) + u_z(\vec{q} \cdot \hat{u}) \quad (11.12)$$

and we substitute it in the eq. 11.9 to have

$$c(t_c - t_0) = \frac{(1 - u_z^2)(u_x L_x + u_y L_y) - (1 - u_z^2)(\vec{q} \cdot \hat{u}) + u_z(1 - u_z^2)z_c}{1 - u_z^2} \quad (11.13)$$

$$t_c = t_0 + \frac{1}{c}(L_x u_x + L_y u_y + z_c u_z - \vec{q} \cdot \vec{u}) \quad (11.14)$$

For a single line fit the detector string can be placed at the origin of the coordinate system  $(L_x, L_y) = (0, 0)$ , so the eq 11.9 will be simplified as follows. In fact, when we now consider a generic point of the muon track:

$\vec{p}(t) = \{x, y, z\} = \vec{q} + c(t - t_0)\hat{u}$ , its distance from the z-axis is  $d = \sqrt{x^2 + y^2}$ . To minimize this distance we derive it

$$\begin{aligned} \frac{\delta d^2}{\delta t} &= \frac{\delta(x^2 + y^2)}{\delta t} = \\ &= 2x \frac{\delta x}{\delta t} + 2y \frac{\delta y}{\delta t} = \\ &= 2[q_x + c(t - t_0)u_x]cu_x + 2[q_y + c(t - t_0)u_y]cu_y = \\ &= 2c[q_x u_x + c(t - t_0)u_x^2 + q_y u_y + c(t - t_0)u_y^2] = 0 \end{aligned} \quad (11.15)$$

Therefore,

$$c(t - t_0) = -\frac{q_x u_x + q_y u_y}{u_x^2 + u_y^2} = \frac{q_z u_z - (\vec{q} \cdot \hat{u})}{1 - u_z^2} \quad (11.16)$$

where  $\hat{u} \cdot \hat{u} = q_x u_x + q_y u_y + q_z u_z$  and  $u_x^2 + u_y^2 + u_z^2 = 1$ .

## 11.4 Photon inclination with respect to the detector line, $\cos \theta_\gamma$

Rewriting the system of Eq. 11.6 in the following way:

$$\begin{cases} -x_c = ctu_x + d\gamma_x \\ -y_c = ctu_y + d\gamma_y \\ z - z_c = ctu_z + d\gamma_z \end{cases} \quad (11.17)$$

Multiplying the first equation by  $u_x$ , and the second by  $u_y$  and the third by  $u_z$ :

$$\begin{cases} -u_x x_c = ctu_x^2 + du_x \gamma_x \\ -u_y y_c = ctu_y^2 + du_y \gamma_y \\ u_z(z - z_c) = ctu_z^2 + du_z \gamma_z \end{cases} \quad (11.18)$$

Now, we sum them together:

$$\begin{aligned} -u_x x_c - u_y y_c + u_z(z - z_c) &= ct(u_x^2 + u_y^2 + u_z^2) + d(u_x \gamma_x + u_y \gamma_y + u_z \gamma_z) \\ -u_x x_c - u_y y_c + u_z(z - z_c) &= ct + \frac{d}{n} \end{aligned} \quad (11.19)$$

where  $\hat{u} \cdot \hat{\gamma} = \cos \vartheta_c = \frac{1}{n}$

The term  $-u_x x_c - u_y y_c$  is zero, as we can see in the following.  
 The starting point is the equation 11.1  $\vec{p}(t) = \vec{q} + c(t - t_0)\hat{u}$

$$\begin{cases} x_c = q_x + c(t_c - t_0)u_x \\ y_c = q_y + c(t_c - t_0)u_y \end{cases} \quad (11.20)$$

where from the eq. 11.16 we can obtain  $c(t_c - t_0)$ :

$$c(t_c - t_0) = \frac{q_z u_z - (\vec{q} \cdot \mathbf{u})}{1 - u_z^2} = \frac{-q_x u_x - q_y u_y}{1 - u_z^2} \quad (11.21)$$

so,

$$\begin{aligned} x_c u_x + y_c u_y &= q_x u_x + c(t_c - t_0)u_x^2 + q_y u_y + c(t_c - t_0)u_y^2 = \\ &= q_x u_x + q_y u_y + (u_x^2 + u_y^2) \frac{-q_x u_x - q_y u_y}{1 - u_z^2} = \\ &= q_x u_x + q_y u_y + (1 - u_z^2) \frac{-q_x u_x - q_y u_y}{1 - u_z^2} = 0 \end{aligned} \quad (11.22)$$

Using this knowledge and with the eq. 11.19 e 11.7

$$\begin{aligned} u_x x_c - u_y y_c + u_z(z - z_c) &= ct + \frac{d}{n} \\ u_z(z - z_c) &= \frac{(z - z_c) - d\gamma_z}{u_z} + \frac{d}{n} \\ u_z^2(z - z_c) &= (z - z_c) - d\gamma_z + u_z \frac{d}{n} \\ \cos \theta_\gamma(z) = \gamma_z &= \frac{(1 - u_z^2)(z - z_c)}{d} + \frac{u_z}{n} \end{aligned} \quad (11.23)$$

## 11.5 Travel path of the photon $d_\gamma$

Considering again the system in 11.17

$$\begin{cases} -x_c = ctu_x + d\gamma_x \\ -y_c = ctu_y + d\gamma_y \\ z - z_c = ctu_z + d\gamma_z \end{cases} \quad (11.24)$$

we calculate the square of these and then the sum:

$$\begin{aligned}
 x_c^2 + y_c^2 + (z - z_c)^2 &= (ct)^2 + d^2 + 2(ct)\frac{d}{n} \\
 d_c^2 + (z - z_c)^2 &= (ct)^2 + 2(ct)\frac{d}{n} + \frac{d^2}{n^2} - \frac{d^2}{n^2} + d^2 \\
 d_c^2 + (z - z_c)^2 &= \left(ct + \frac{d}{n}\right)^2 + d^2 \left(1 - \frac{1}{n^2}\right)
 \end{aligned} \tag{11.25}$$

Through the Eq. 11.19 we know that  $ct + \frac{d}{n} = u_z(z - z_c)$ , so:

$$\begin{aligned}
 d_c^2 + (z - z_c)^2 &= \left(ct + \frac{d}{n}\right)^2 + d^2 \left(1 - \frac{1}{n^2}\right) \\
 d_c^2 + (z - z_c)^2 &= u_z^2(z - z_c)^2 + d^2 \left(1 - \frac{1}{n^2}\right) \\
 d_c^2 + (1 - u_z^2)(z - z_c)^2 &= d^2 \frac{n^2 - 1}{n^2} \\
 d^2 &= \frac{n^2}{n^2 - 1} [d_c^2 + (1 - u_z^2)(z - z_c)^2]
 \end{aligned} \tag{11.26}$$

The travel path of the photon  $d_\gamma$  is

$$d_\gamma = \frac{n}{\sqrt{n^2 - 1}} \sqrt{d_c^2 + (1 - u_z^2)(z - z_c)^2} \tag{11.27}$$

## 11.6 The arrival time $t_\gamma$ of a Cherenkov photon at the detector line

Let write  $t_\gamma = (t_\gamma - t_p) + t_p = (t_\gamma - t_p) + (t_p - t_c) + t_c - t_0$  and from the Eq. 11.2 e 11.3 we have  $t_\gamma - t_p = \frac{n}{c\gamma_z}(z - z_p)$  and  $t_p - t_c = \frac{1}{cu_z}(z_p - z_c)$ .

Then,  $z_p - z_c = (z_p - z) + (z - z_c) = -(z - z_p) + (z - z_c)$  and  $(z - z_p) = d_\gamma \gamma_z$  where the last equation derives from 11.4.

$$\begin{aligned}
 t_\gamma &= (t_c - t_0) + \frac{n}{c}d + \frac{1}{cu_z}[-d\gamma_z + (z - z_c)] \\
 t_\gamma &= (t_c - t_0) + \frac{1}{cu_z} [(z - z_c) + d_\gamma u_z n - d\gamma_z]
 \end{aligned} \tag{11.28}$$

and substituting  $d\gamma_z = (1 - u_z^2)(z - z_c) + u_z d/n$  we obtain the arrival time

$t_\gamma$  of a Cherenkov photon:

$$\begin{aligned}
t_\gamma &= (t_c - t_0) + \frac{1}{cu_z} [(z - z_c) + d_\gamma u_z n - d_\gamma] \\
t_\gamma &= (t_c - t_0) + \frac{1}{cu_z} \left[ (z - z_c) + d_\gamma u_z n - (1 - u_z^2)(z - z_c) - \frac{u_z d_\gamma}{n} \right] \\
t_\gamma &= (t_c - t_0) + \frac{1}{cu_z} \left[ u_z^2(z - z_c) + u_z d_\gamma \left( n - \frac{1}{n} \right) \right] \\
t_\gamma &= (t_c - t_0) + \frac{1}{c} \left[ u_z(z - z_c) + d_\gamma \frac{n^2 - 1}{n} \right]
\end{aligned} \tag{11.29}$$

## 11.7 Reconstruction of the muon track with only two detector lines

For the following we consider 3 hits for each line to procedure for a two-lines fit. Each system is compose of three equations with time differences of photons and three equations of their corresponding travel paths. The first system is for the first detector line involved and the other one for the second detector line.

$$\left\{ \begin{aligned}
t_\gamma^i - t_\gamma^j &= \frac{1}{c} [(z_i - z_c^I)u_z + \frac{n^2-1}{n} d_\gamma^i(z_i)] - \frac{1}{c} [(z_j - z_c^I)u_z + \frac{n^2-1}{n} d_\gamma^j(z_j)] \\
t_\gamma^i - t_\gamma^k &= \frac{1}{c} [(z_i - z_c^I)u_z + \frac{n^2-1}{n} d_\gamma^i(z_i)] - \frac{1}{c} [(z_k - z_c^I)u_z + \frac{n^2-1}{n} d_\gamma^k(z_k)] \\
t_\gamma^j - t_\gamma^k &= \frac{1}{c} [(z_j - z_c^I)u_z + \frac{n^2-1}{n} d_\gamma^j(z_j)] - \frac{1}{c} [(z_k - z_c^I)u_z + \frac{n^2-1}{n} d_\gamma^k(z_k)] \\
d_\gamma^i(z_i) &= \frac{n}{\sqrt{n^2-1}} \sqrt{d_c^{I2} + (z_i - z_c^I)^2(1 - u_z^2)} \\
d_\gamma^j(z_j) &= \frac{n}{\sqrt{n^2-1}} \sqrt{d_c^{I2} + (z_j - z_c^I)^2(1 - u_z^2)} \\
d_\gamma^k(z_k) &= \frac{n}{\sqrt{n^2-1}} \sqrt{d_c^{I2} + (z_k - z_c^I)^2(1 - u_z^2)}
\end{aligned} \right. \tag{11.30}$$

In the first system we have 6 equations and 6 unknowns:  $z_c^I, u_z, d_c^I, d_\gamma^i, d_\gamma^j, d_\gamma^k$ , so we can calculate all.

For the second system we have the same type of equations with several dif-

ferences of arrival times and their travel paths.

$$\left\{ \begin{array}{l} t_{\gamma}^m - t_{\gamma}^n = \frac{1}{c}[(z_m - z_c^{II})u_z + \frac{n^2-1}{n}d_{\gamma}^m(z_m)] - \frac{1}{c}[(z_n - z_c^{II})u_z + \frac{n^2-1}{n}d_{\gamma}^n(z_n)] \\ t_{\gamma}^m - t_{\gamma}^l = \frac{1}{c}[(z_m - z_c^{II})u_z + \frac{n^2-1}{n}d_{\gamma}^m(z_m)] - \frac{1}{c}[(z_l - z_c^{II})u_z + \frac{n^2-1}{n}d_{\gamma}^l(z_l)] \\ t_{\gamma}^n - t_{\gamma}^l = \frac{1}{c}[(z_n - z_c^{II})u_z + \frac{n^2-1}{n}d_{\gamma}^n(z_n)] - \frac{1}{c}[(z_l - z_c^{II})u_z + \frac{n^2-1}{n}d_{\gamma}^l(z_l)] \\ d_{\gamma}^m(z_m) = \frac{n}{\sqrt{n^2-1}}\sqrt{d_c^{II2} + (z_m - z_c^{II})^2(1 - u_z^2)} \\ d_{\gamma}^n(z_n) = \frac{n}{\sqrt{n^2-1}}\sqrt{d_c^{II2} + (z_n - z_c^{II})^2(1 - u_z^2)} \\ d_{\gamma}^l(z_l) = \frac{n}{\sqrt{n^2-1}}\sqrt{d_c^{II2} + (z_l - z_c^{II})^2(1 - u_z^2)} \end{array} \right. \quad (11.31)$$

As in the previous system we have 6 equations and 6 unknowns:

$z_c^{II}, u_z, d_c^{II}, d_{\gamma}^m, d_{\gamma}^n, d_{\gamma}^l$ , so we can obtain all. The common unknown is  $u_z$ :

$$u_z = \frac{(z_c^I - z_c^{II})}{c[(t_c^I - t_0) - (t_c^{II} - t_0)]} \quad (11.32)$$

At this point by using the equations obtained before we can calculate the time differences:

$$(t_c^I - t_0) = t_{\gamma}^i - \frac{1}{c} \left[ u_z(z_i - z_c^I) + d_{\gamma}^i \frac{n^2 - 1}{n} \right] \quad (11.33)$$

and

$$(t_c^{II} - t_0) = t_{\gamma}^m - \frac{1}{c} \left[ u_z(z_m - z_c^{II}) + d_{\gamma}^m \frac{n^2 - 1}{n} \right] \quad (11.34)$$

The muon track is defined by a total of 5 parameters: three values to fix  $\vec{q}$  for a given time and two angles to define  $\vec{u}$ :

$$\vec{u} = [\cos \theta \cos \phi, \cos \theta \sin \phi, \sin \theta] \quad (11.35)$$

To reach our aim, we need a system of 11 equations in which there are terms from the first and the second line

$$z_c^I = \frac{q_z - u_z(\vec{q} \cdot \vec{u}) + u_z(L_x^I u_x + L_y^I u_y)}{1 - u_z^2} \quad (11.36)$$

$$z_c^{II} = \frac{q_z - u_z(\vec{q} \cdot \vec{u}) + u_z(L_x^{II} u_x + L_y^{II} u_y)}{1 - u_z^2} \quad (11.37)$$

$$t_c^I = t_0 + \frac{1}{c}(L_x^I u_x + L_y^I u_y + z_c^I u_z - \vec{q} \cdot \vec{u}) \quad (11.38)$$

$$t_c^{II} = t_0 + \frac{1}{c}(L_x^{II}u_x + L_y^{II}u_y + z_c^{II}u_z - \vec{q} \bullet \vec{u}) \quad (11.39)$$

$$d_c^I = \sqrt{(p_x^I(t_c^I) - L_x^I)^2 + (p_y^I(t_c^I) - L_y^I)^2} \quad (11.40)$$

$$d_c^{II} = \sqrt{(p_x^{II}(t_c^{II}) - L_x^{II})^2 + (p_y^{II}(t_c^{II}) - L_y^{II})^2} \quad (11.41)$$

$$p_x^I(t_c^I) = q_x + c(t_c^I - t_0)u_x \quad (11.42)$$

$$p_y^I(t_c^I) = q_y + c(t_c^I - t_0)u_y \quad (11.43)$$

$$p_x^{II}(t_c^{II}) = q_x + c(t_c^{II} - t_0)u_x \quad (11.44)$$

$$p_y^{II}(t_c^{II}) = q_y + c(t_c^{II} - t_0)u_y \quad (11.45)$$

$$u_x^2 = 1 - u_y^2 - u_z^2 \quad (11.46)$$

The 12 unknowns are  $q_x, q_y, q_z, u_x, u_y, t_c^I, t_c^{II}, t_0, p_x^I, p_x^{II}, p_y^I, p_y^{II}$ . Performing  $z_c^I - z_c^{II}$  and substituting  $u_x^2 = 1 - u_y^2 - u_z^2$  we have

$$(z_c^I - z_c^{II})(1 - u_z^2) = u_z(L_x^I \sqrt{1 - u_y^2 - u_z^2} + L_y^I u_y - L_x^{II} \sqrt{1 - u_y^2 - u_z^2} - L_y^{II} u_y) \quad (11.47)$$

$$\begin{aligned} & [(z_c^I - z_c^{II})(1 - u_z^2) - u_z L_y^I u_y + L_y^{II} u_y u_z]^2 = \\ & u_z^2 L_x^I 2(1 - u_y^2 - u_z^2) + L_x^{II} 2u_z^2(1 - u_y^2 - u_z^2) - 2u_z^2 L_x^I L_x^{II} (1 - u_y^2 - u_z^2) \end{aligned} \quad (11.48)$$

squared each term

$$\begin{aligned} & (z_c^I - z_c^{II})^2(1 - u_z^2)^2 + u_z^2 L_y^I 2u_y^2 + L_y^{II} 2u_y^2 u_z^2 - 2(z_c^I - z_c^{II})(1 - u_z^2)u_z L_y^I u_y \\ & + 2(z_c^I - z_c^{II})(1 - u_z^2)L_y^{II} u_y u_z - 2u_z^2 u_y^2 L_y^I L_y^{II} = u_z^2 L_x^I 2 - u_z^2 L_x^I 2u_y^2 - u_z^4 L_x^I 2 + \\ & + L_x^{II} 2u_z^2 - u_z^2 L_x^I 2u_y^2 - u_z^4 L_x^{II} 2 - 2u_z^2 L_x^I L_x^{II} + 2u_z^4 L_x^I L_x^{II} + 2u_z^2 L_x^I L_x^{II} u_y^2 \end{aligned} \quad (11.49)$$

$$\begin{aligned} & (z_c^I - z_c^{II})^2(1 - u_z^2)^2 + u_y^2 [L_y^I 2u_z^2 + L_y^{II} 2u_z^2 - 2u_z^2 L_y^I L_y^{II}] + \\ & + 2u_y [ (z_c^I - z_c^{II})(1 - u_z^2) ] [-u_z L_y^I + L_y^{II} u_z] = \\ u_y^2 [-u_z^2 L_x^I 2 - u_z^2 L_x^{II} 2 + 2u_z^2 L_x^I L_x^{II}] + u_z^2 [L_x^I 2 - u_z^2 L_x^I 2 + L_x^{II} 2 - u_z^2 L_x^{II} 2 - 2L_x^I L_x^{II} + 2u_z^2 L_x^I L_x^{II}] \end{aligned} \quad (11.50)$$

$$\begin{aligned} & (z_c^I - z_c^{II})^2(1 - u_z^2)^2 + u_y^2 u_z^2 (L_y^{II} - L_y^I)^2 + 2u_y u_z (z_c^I - z_c^{II})(1 - u_z^2)(L_y^{II} - L_y^I) = \\ & - u_y^2 u_z^2 (L_x^{II} - L_x^I)^2 + u_z^2 (1 - u_z^2)(L_x^{II} - L_x^I)^2 \end{aligned} \quad (11.51)$$

$$\begin{aligned} & u_y^2 u_z^2 [(L_y^{II} - L_y^I)^2 + (L_x^{II} - L_x^I)^2] + 2u_y u_z (z_c^I - z_c^{II})(1 - u_z^2)(L_y^{II} - L_y^I) + \\ & + [(z_c^I - z_c^{II})^2(1 - u_z^2)^2 - u_z^2(1 - u_z^2)(L_x^{II} - L_x^I)^2] = 0 \end{aligned} \quad (11.52)$$

$$u_y^2 u_z^2 [(L_y^{II} - L_y^I)^2 + (L_x^{II} - L_x^I)^2] + u_y [2u_z (z_c^I - z_c^{II})(1 - u_z^2)(L_y^{II} - L_y^I)] + [(z_c^I - z_c^{II})^2 (1 - u_z^2)^2 - u_z^2 (1 - u_z^2)(L_x^{II} - L_x^I)^2] = 0 \quad (11.53)$$

$$u_y = \frac{-[2u_z (z_c^I - z_c^{II})(1 - u_z^2)(L_y^{II} - L_y^I)]}{2u_z^2 [(L_y^{II} - L_y^I)^2 + (L_x^{II} - L_x^I)^2]} + \frac{\sqrt{[2u_z (z_c^I - z_c^{II})(1 - u_z^2)(L_y^{II} - L_y^I)]^2 + 4u_z^2 [(L_y^{II} - L_y^I)^2 + (L_x^{II} - L_x^I)^2] [(z_c^I - z_c^{II})^2 (1 - u_z^2)^2 - u_z^2 (1 - u_z^2)(L_x^{II} - L_x^I)^2]}}{2u_z^2 [(L_y^{II} - L_y^I)^2 + (L_x^{II} - L_x^I)^2]} \quad (11.54)$$

Having  $u_y$  we can obtain  $(\vec{q} \bullet \vec{u})$  by using the following equation:

$$c(t_c^I - t_0) = L_x^I u_x + L_y^I u_y + z_c^I u_z - (\vec{q} \bullet \vec{u}) \quad (11.55)$$

then

$$-(\vec{q} \bullet \vec{u}) = c(t_c^I - t_0) - L_x^I u_x - L_y^I u_y - z_c^I u_z \quad (11.56)$$

Now, we substitute this value in one of the equation for  $z_c$  to have  $q_z$

$$z_c^I = \frac{q_z - u_z (\vec{q} \bullet \vec{u}) + u_z (L_x^I u_x + L_y^I u_y)}{(1 - u_z^2)} \quad (11.57)$$

$$z_c^I (1 - u_z^2) = q_z + u_z [c(t_c^I - t_0) - L_x^I u_x - L_y^I u_y - z_c^I u_z] + u_z (L_x^I u_x + L_y^I u_y) \quad (11.58)$$

$$q_z = z_c^I (1 - u_z^2) - u_z c(t_c^I - t_0) + u_z L_x^I u_x + u_z L_y^I u_y + z_c^I u_z^2 - u_z L_x^I u_x - u_z L_y^I u_y \quad (11.59)$$

$$q_z = z_c^I - u_z c(t_c^I - t_0) \quad (11.60)$$

The same you can do from the equation:

$$z_c^{II} = \frac{q_z - u_z (\vec{q} \bullet \vec{u}) + u_z (L_x^{II} u_x + L_y^{II} u_y)}{1 - u_z^2} \quad (11.61)$$

and get

$$q_z = z_c^{II} - u_z c(t_c^{II} - t_0) \quad (11.62)$$

where Eq. 11.60 and 11.62 have to be the same.

To obtain  $q_y$  the starting point is the equation of  $d_c^I$

$$d_c^{I2} = [q_x + c(t_c^I - t_0)u_x - L_x^I]^2 + [q_y + c(t_c^I - t_0)u_y - L_y^I]^2 \quad (11.63)$$

$$d_c^{I2} = \left[ \frac{(\vec{q} \bullet \vec{u})}{u_x} - \frac{q_y u_y}{u_x} - \frac{q_z u_z}{u_x} + c(t_c^I - t_0)u_x - L_x^I \right]^2 + [q_y + c(t_c^I - t_0)u_y - L_y^I]^2 \quad (11.64)$$

$$\begin{aligned} d_c^{I2} = & \frac{(\vec{q} \bullet \vec{u})^2}{u_x^2} + \frac{q_y^2 u_y^2}{u_x^2} + \frac{q_z^2 u_z^2}{u_x^2} + c^2(t_c^I - t_0)^2 u_x^2 + L_x^{I2} + \\ & - 2 \frac{(\vec{q} \bullet \vec{u}) q_y u_y}{u_x^2} - 2 \frac{(\vec{q} \bullet \vec{u}) q_z u_z}{u_x^2} + \\ & + 2 \frac{(\vec{q} \bullet \vec{u}) c(t_c^I - t_0) u_x}{u_x} - 2 \frac{(\vec{q} \bullet \vec{u}) L_x^I}{u_x} + 2 \frac{q_y u_y q_z u_z}{u_x^2} - 2 \frac{q_y u_y}{u_x} c(t_c^I - t_0) u_x + \\ & + 2 \frac{q_y u_y}{u_x} L_x^I - 2 \frac{q_z u_z}{u_x} c(t_c^I - t_0) u_x + 2 \frac{q_z u_z}{u_x} L_x^I - 2 c(t_c^I - t_0) u_x L_x^I + \\ & + q_y^2 + c^2(t_c^I - t_0)^2 u_y^2 + L_y^{I2} + 2 q_y c(t_c^I - t_0) u_y - 2 q_y L_y^I - 2 c(t_c^I - t_0) u_y L_y^I \end{aligned} \quad (11.65)$$

$$\begin{aligned} d_c^{I2} = & q_y^2 \left( 1 - \frac{u_y^2}{u_x^2} \right) + q_y \left[ -2(\vec{q} \bullet \vec{u}) \frac{u_y}{u_x^2} + 2 q_z u_z \frac{u_y}{u_x^2} - 2 u_y c(t_c^I - t_0) + \right. \\ & \left. + 2 \frac{u_y}{u_x} L_x^I + 2 c(t_c^I - t_0) u_y - 2 L_y^I \right] + \\ & + \frac{(\vec{q} \bullet \vec{u})^2}{u_x^2} + \frac{q_z^2 u_z^2}{u_x^2} + c^2(t_c^I - t_0)^2 u_x^2 + L_x^{I2} - 2(\vec{q} \bullet \vec{u}) \frac{q_z u_z}{u_x^2} + \\ & + 2(\vec{q} \bullet \vec{u}) c(t_c^I - t_0) - 2 \frac{(\vec{q} \bullet \vec{u}) L_x^I}{u_x} - 2 q_z u_z c(t_c^I - t_0) + 2 \frac{q_z u_z}{u_x} L_x^I - 2 c(t_c^I - t_0) u_x L_x^I + \\ & + c^2(t_c^I - t_0)^2 u_y^2 + L_y^{I2} - 2 c(t_c^I - t_0) u_y L_y^I \end{aligned} \quad (11.66)$$

$$\begin{aligned} 0 = & q_y^2 \left( 1 - \frac{u_y^2}{u_x^2} \right) + q_y \left[ -2(\vec{q} \bullet \vec{u}) \frac{u_y}{u_x^2} + 2 q_z u_z \frac{u_y}{u_x^2} + 2 \frac{u_y}{u_x} L_x^I - 2 L_y^I \right] + \\ & + \frac{(\vec{q} \bullet \vec{u})^2}{u_x^2} + \frac{q_z^2 u_z^2}{u_x^2} + c^2(t_c^I - t_0)^2 u_x^2 + L_x^{I2} - 2(\vec{q} \bullet \vec{u}) \frac{q_z u_z}{u_x^2} + \\ & + 2(\vec{q} \bullet \vec{u}) c(t_c^I - t_0) - 2 \frac{(\vec{q} \bullet \vec{u}) L_x^I}{u_x} - 2 q_z u_z c(t_c^I - t_0) + \\ & + 2 \frac{q_z u_z}{u_x} L_x^I - 2 c(t_c^I - t_0) u_x L_x^I + c^2(t_c^I - t_0)^2 u_y^2 + L_y^{I2} - 2 c(t_c^I - t_0) u_y L_y^I - d_c^{I2} \end{aligned} \quad (11.67)$$

Due to the fact that the expression of  $q_y$  has to be the same if it is derived from the equation of the first detector line 11.67 and the second one 11.69.

We impose their equality to gain  $q_y$ .

First of all by using the following equation we have the equation of  $q_y$  from the second detector line

$$d_c^{II2} = [q_x + c(t_c^{II} - t_0)u_x - L_x^{II}]^2 + [q_y + c(t_c^{II} - t_0)u_y - L_y^{II}]^2 \quad (11.68)$$

$$\begin{aligned}
0 = & q_y^2 \left(1 - \frac{u_y^2}{u_x^2}\right) + q_y \left[-2(\vec{q} \bullet \vec{u}) \frac{u_y}{u_x^2} + 2q_z u_z \frac{u_y}{u_x^2} + 2\frac{u_y}{u_x} L_x^{II} - 2L_y^{II}\right] + \\
& + \frac{(\vec{q} \bullet \vec{u})^2}{u_x^2} + \frac{q_z^2 u_z^2}{u_x^2} + c^2 (t_c^{II} - t_0)^2 u_x^2 + L_x^{II2} - 2(\vec{q} \bullet \vec{u}) \frac{q_z u_z}{u_x^2} + \\
& + 2(\vec{q} \bullet \vec{u}) c (t_c^{II} - t_0) - 2\frac{(\vec{q} \bullet \vec{u})}{u_x} L_x^{II} - 2q_z u_z c (t_c^{II} - t_0) + \\
& + 2\frac{q_z u_z}{u_x} L_x^{II} - 2c(t_c^{II} - t_0) u_x L_x^{II} + c^2 (t_c^{II} - t_0)^2 u_y^2 + L_y^{II2} - 2c(t_c^{II} - t_0) u_y L_y^{II} - d_c^{II2}
\end{aligned} \tag{11.69}$$

Now we put the eq 11.67 equal to eq 11.69:

$$\begin{aligned}
& q_y^2 \left(1 - \frac{u_y^2}{u_x^2}\right) + q_y \left[-2(\vec{q} \bullet \vec{u}) \frac{u_y}{u_x^2} + 2q_z u_z \frac{u_y}{u_x^2} + 2\frac{u_y}{u_x} L_x^I - 2L_y^I\right] + \\
& + \frac{(\vec{q} \bullet \vec{u})^2}{u_x^2} + \frac{q_z^2 u_z^2}{u_x^2} + c^2 (t_c^I - t_0)^2 u_x^2 + L_x^{I2} - 2(\vec{q} \bullet \vec{u}) \frac{q_z u_z}{u_x^2} + \\
& + 2(\vec{q} \bullet \vec{u}) c (t_c^I - t_0) - 2\frac{(\vec{q} \bullet \vec{u})}{u_x} L_x^I - 2q_z u_z c (t_c^I - t_0) + \\
& + 2\frac{q_z u_z}{u_x} L_x^I - 2c(t_c^I - t_0) u_x L_x^I + c^2 (t_c^I - t_0)^2 u_y^2 + L_y^{I2} - 2c(t_c^I - t_0) u_y L_y^I - d_c^{I2} = \\
& = q_y^2 \left(1 - \frac{u_y^2}{u_x^2}\right) + q_y \left[-2(\vec{q} \bullet \vec{u}) \frac{u_y}{u_x^2} + 2q_z u_z \frac{u_y}{u_x^2} + 2\frac{u_y}{u_x} L_x^{II} - 2L_y^{II}\right] + \\
& + \frac{(\vec{q} \bullet \vec{u})^2}{u_x^2} + \frac{q_z^2 u_z^2}{u_x^2} + c^2 (t_c^{II} - t_0)^2 u_x^2 + L_x^{II2} - 2(\vec{q} \bullet \vec{u}) \frac{q_z u_z}{u_x^2} + \\
& + 2(\vec{q} \bullet \vec{u}) c (t_c^{II} - t_0) - 2\frac{(\vec{q} \bullet \vec{u})}{u_x} L_x^{II} - 2q_z u_z c (t_c^{II} - t_0) + \\
& + 2\frac{q_z u_z}{u_x} L_x^{II} - 2c(t_c^{II} - t_0) u_x L_x^{II} + c^2 (t_c^{II} - t_0)^2 u_y^2 + L_y^{II2} - 2c(t_c^{II} - t_0) u_y L_y^{II} - d_c^{II2}
\end{aligned} \tag{11.70}$$

In this way we get an equation of first order in  $q_y$ ,

$$\begin{aligned}
& q_y \left[-2(\vec{q} \bullet \vec{u}) \frac{u_y}{u_x^2} + 2q_z u_z \frac{u_y}{u_x^2} + 2\frac{u_y}{u_x} L_x^I - 2L_y^I\right] + \\
& - q_y \left[-2(\vec{q} \bullet \vec{u}) \frac{u_y}{u_x^2} + 2q_z u_z \frac{u_y}{u_x^2} + 2\frac{u_y}{u_x} L_x^{II} - 2L_y^{II}\right] = \\
& \frac{(\vec{q} \bullet \vec{u})^2}{u_x^2} + \frac{q_z^2 u_z^2}{u_x^2} + c^2 (t_c^{II} - t_0)^2 u_x^2 + L_x^{II2} - 2(\vec{q} \bullet \vec{u}) \frac{q_z u_z}{u_x^2} + \\
& + 2(\vec{q} \bullet \vec{u}) c (t_c^{II} - t_0) - 2\frac{(\vec{q} \bullet \vec{u})}{u_x} L_x^{II} - 2q_z u_z c (t_c^{II} - t_0) + \\
& + 2\frac{q_z u_z}{u_x} L_x^{II} - 2c(t_c^{II} - t_0) u_x L_x^{II} + c^2 (t_c^{II} - t_0)^2 u_y^2 + L_y^{II2} - 2c(t_c^{II} - t_0) u_y L_y^{II} - d_c^{II2} + \\
& - \frac{(\vec{q} \bullet \vec{u})^2}{u_x^2} + \frac{q_z^2 u_z^2}{u_x^2} + c^2 (t_c^I - t_0)^2 u_x^2 + L_x^{I2} - 2(\vec{q} \bullet \vec{u}) \frac{q_z u_z}{u_x^2} + \\
& + 2(\vec{q} \bullet \vec{u}) c (t_c^I - t_0) - 2\frac{(\vec{q} \bullet \vec{u})}{u_x} L_x^I - 2q_z u_z c (t_c^I - t_0) + \\
& + 2\frac{q_z u_z}{u_x} L_x^I - 2c(t_c^I - t_0) u_x L_x^I + c^2 (t_c^I - t_0)^2 u_y^2 + L_y^{I2} - 2c(t_c^I - t_0) u_y L_y^I - d_c^{I2}
\end{aligned} \tag{11.71}$$

$$\begin{aligned}
& q_y \left[2\frac{u_y}{u_x} (L_x^I - L_x^{II}) - 2(L_y^I - L_y^{II})\right] = c^2 [(t_c^{II} - t_0) - (t_c^I - t_0)] u_x^2 + L_x^{II2} - L_x^{I2} + \\
& + 2(\vec{q} \bullet \vec{u}) c [(t_c^{II} - t_0) - (t_c^I - t_0)] - 2\frac{(\vec{q} \bullet \vec{u})}{u_x} (L_x^{II} - L_x^I) + \\
& - 2q_z u_z c [(t_c^{II} - t_0) - (t_c^I - t_0)] + 2\frac{q_z u_z}{u_x} (L_x^{II} - L_x^I) - 2cu_x [L_x^{II} (t_c^{II} - t_0) - L_x^I (t_c^I - t_0)] + \\
& + c^2 [(t_c^{II} - t_0)^2 - (t_c^I - t_0)^2] u_y^2 + L_y^{II2} - L_y^{I2} + \\
& - 2cu_y [L_y^{II} (t_c^{II} - t_0) - L_y^I (t_c^I - t_0)] - d_c^{II2} + d_c^{I2}
\end{aligned} \tag{11.72}$$

$$A = \left[ 2 \frac{u_y}{u_x} (L_x^I - L_x^{II}) - 2(L_y^I - L_y^{II}) \right] \quad (11.73)$$

$$\begin{aligned} B = & c^2 [(t_c^{II} - t_0) - (t_c^I - t_0)] u_x^2 + L_x^{II2} - L_x^{I2} + \\ & + 2(\vec{q} \bullet \vec{u}) c [(t_c^{II} - t_0) - (t_c^I - t_0)] - 2 \frac{(\vec{q} \bullet \vec{u})}{u_x} (L_x^{II} - L_x^I) + \\ & - 2q_z u_z c [(t_c^{II} - t_0) - (t_c^I - t_0)] + 2 \frac{q_z u_z}{u_x} (L_x^{II} - L_x^I) - 2c u_x [L_x^{II} (t_c^{II} - t_0) - L_x^I (t_c^I - t_0)] + \\ & + c^2 [(t_c^{II} - t_0)^2 - (t_c^I - t_0)^2] u_y^2 + L_y^{II2} - L_y^{I2} - 2c u_y [L_y^{II} (t_c^{II} - t_0) - L_y^I (t_c^I - t_0)] - d_c^{II2} + d_c^{I2} \end{aligned} \quad (11.74)$$

$$q_y = \frac{B}{A} \quad (11.75)$$

To calculate  $q_x$

$$(\vec{q} \bullet \vec{u}) = q_x u_x + q_y u_y + q_z u_z \quad (11.76)$$

$$q_x = \frac{(\vec{q} \bullet \vec{u}) - q_y u_y - q_z u_z}{u_x} \quad (11.77)$$

The muon track is finally defined by a total number of 5 parameters  $q_x, q_y, q_z, u_x$  or  $(u_y), u_z$ .

In the following by using the ANTARES neutrino triggers detected with only two lines we could see the physical behaviour produced from the muon track in this case. We'll give a brief introduction on Astronomical Coordinate Systems and a description of Horizontal System that will be the fundamental step to understand the duplicity of the neutrino reconstruction.

In astronomy, a celestial coordinate system is a coordinate system for mapping positions on the celestial sphere. There are different celestial coordinate systems each using a system of spherical coordinates projected on the celestial sphere, in analogy to the geographic coordinate system used on the surface of the Earth. The coordinate systems differ only in their choice of the fundamental plane, which divides the sky into two equal hemispheres along a great circle. For example, the fundamental plane of the geographic system is the Earth's equator. Each coordinate system is named Zenith. The pole of the lower hemisphere is called the Nadir.

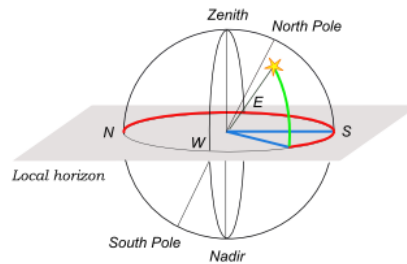


Figure 11.2: Horizontal Coordinates. Azimuth is the angle from the North point till the projection of the star on the local horizon (red). Altitude one is in green angle.

The horizontal coordinates are:

- altitude (Alt), sometimes referred to as elevation, that is the angle between the object and the observer's local horizon.
- azimuth (Az), that is the angle of the object around the horizon, usually measured from the north point towards the east.

The horizontal coordinate system is fixed to the Earth, not the stars. Therefore, the altitude and azimuth of an object changes with time, as the object appears to drift across the sky. In addition, because the horizontal system is defined by the observer's local horizon, the same object viewed from different locations on Earth at the same time will have different values of altitude and

azimuth.

Horizontal coordinates are very useful for determining the rise and set times of an object in the sky. When an object's altitude is  $0^\circ$ , it is on the horizon. If at that moment its altitude is increasing, it is rising, but if its altitude is decreasing it is setting. However, all objects on the celestial sphere are subject to diurnal motion, which is always from east to west. One can determine whether altitude is increasing or decreasing by instead considering the azimuth of the celestial object:

- if the azimuth is between  $0^\circ$  and  $180^\circ$  (north-east-south), it is rising.
- if the azimuth is between  $180^\circ$  and  $360^\circ$  (south-west-north), it is setting.

There are the following special cases:

- At the north pole all directions are south, and at the south pole all directions are north, so the azimuth is undefined in both locations. A star (or any object with fixed equatorial coordinates) has constant altitude, and therefore never rises or sets when viewed from either pole. The Sun, Moon, and planets can rise or set over the span of a year when viewed from the poles because their right ascensions and declinations are constantly changing.
- At the equator objects on the celestial poles stay at fixed points on the horizon.

Note that the above considerations are strictly speaking true for the geometric horizon only: the horizon as it would appear for an observer at sea level on a perfectly smooth Earth without an atmosphere. In practice the apparent horizon has a negative altitude, whose absolute value gets larger as the observer ascends higher above sea level, due to the curvature of the Earth. In addition, atmospheric refraction causes celestial objects very close to the horizon to appear about half a degree higher than they would if there were no atmosphere.

We would have the positions of our neutrino triggers in Horizontal Coordinates System that implies a change in the fundamental plane from the celestial equator to the local horizon. It is possible to convert from the equatorial coordinate system to the horizontal coordinate system. Define variables as follows:

1.  $\alpha$  is the neutrino right ascension,
2.  $\delta$  is the neutrino declination,
3.  $H$  is the hour angle,
4.  $\phi$  is the geographic latitude of the observer (ANTARES site) ( $42^\circ 48' N = 42.8^\circ$ ),
5.  $a$  is the elevation angle,
6.  $A$  is the azimuth angle,
7.  $\theta$  is the zenith distance ( $0^\circ = \textit{zenith}$ ,  $90^\circ = \textit{horizon}$ ,  $180^\circ = \textit{nadir}$ ),

$$\sin a = \cos \theta = \sin \phi \sin \delta + \cos \phi \cos \delta \cos H \quad (11.78)$$

$$\cos A = \frac{\cos \phi \sin \delta - \sin \phi \cos \delta \cos H}{\cos a} \quad (11.79)$$

$$H = LST - \alpha \quad (11.80)$$

where  $LTS = \text{Local Sidereal Time}$

Sidereal time is a system of timekeeping based on the rotation of the Earth with respect to the fixed stars in the sky. More specifically, it is the measure of the hour angle of the vernal equinox. If the hour angle is measured with respect to the true equinox, apparent sidereal time is being measured. If the hour angle is measured with respect to the mean equinox, mean sidereal time

is being measured. When the measurements are made with respect to the meridian at Greenwich, the times are referred to as Greenwich mean sidereal time (GMST) and Greenwich apparent sidereal time (GAST).

Let  $JD$  be the Julian date of the time of interest. Let  $JD_0$  be the Julian date of the previous midnight ( $0h$ ) UT, and let  $H$  be the hours of UT elapsed since that time. Thus we have  $JD = JD_0 + \frac{H}{24}$ , so  $H = 24(JD - JD_0)$ . For both of these Julian dates, compute the number of days and fraction from 2000 January 1,  $12^h$  UT, Julian date 2451545.0:

$$D = JD - 2451545.0 \quad (11.81)$$

$$D_0 = JD_0 - 2451545.0 \quad (11.82)$$

Then the Greenwich mean sidereal time in hours is

$$GMST = 6.697374558 + 0.06570982441908D_0 + 1.00273790935H + 0.000026T^2 \quad (11.83)$$

where  $T = \frac{D}{36525}$  is the number of centuries since the year 2000. It is necessary to convert the Greenwich mean sidereal time in degrees and sum the Longitude of ANTARES site ( $6^\circ 10' E = 6.16667^\circ$ ) to have the Local Sidereal Time.

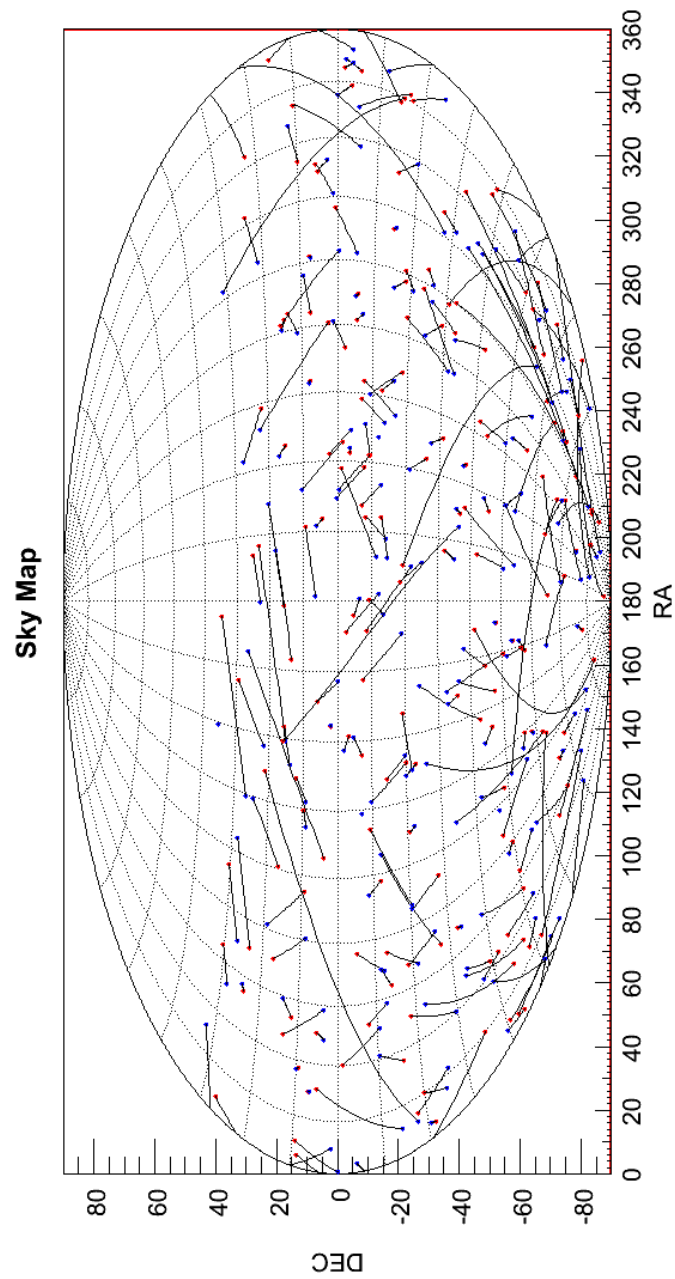


Figure 11.3: Sky map of 198 couples of neutrino triggers detected with only two lines. Each couple (red and blue dots) is connected through a black line.

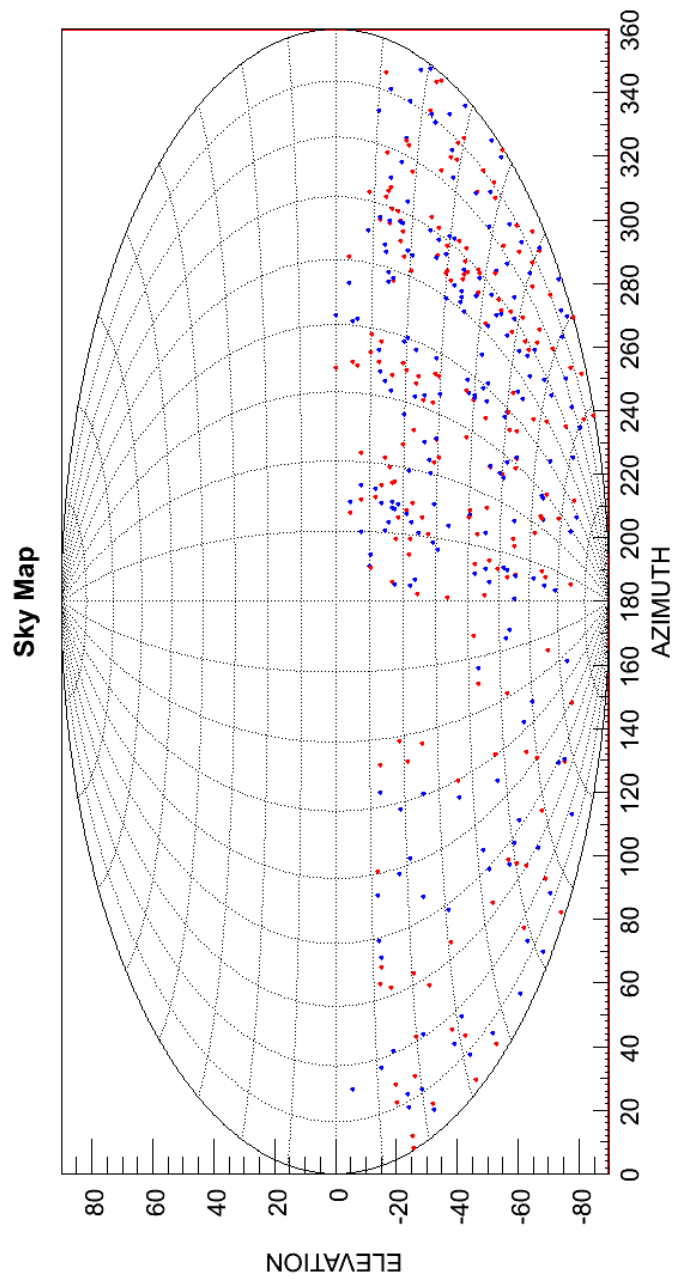


Figure 11.4: This picture shows the same data set of 198 neutrino couples, from February to September 2007, in the Horizontal System of ANTARES.

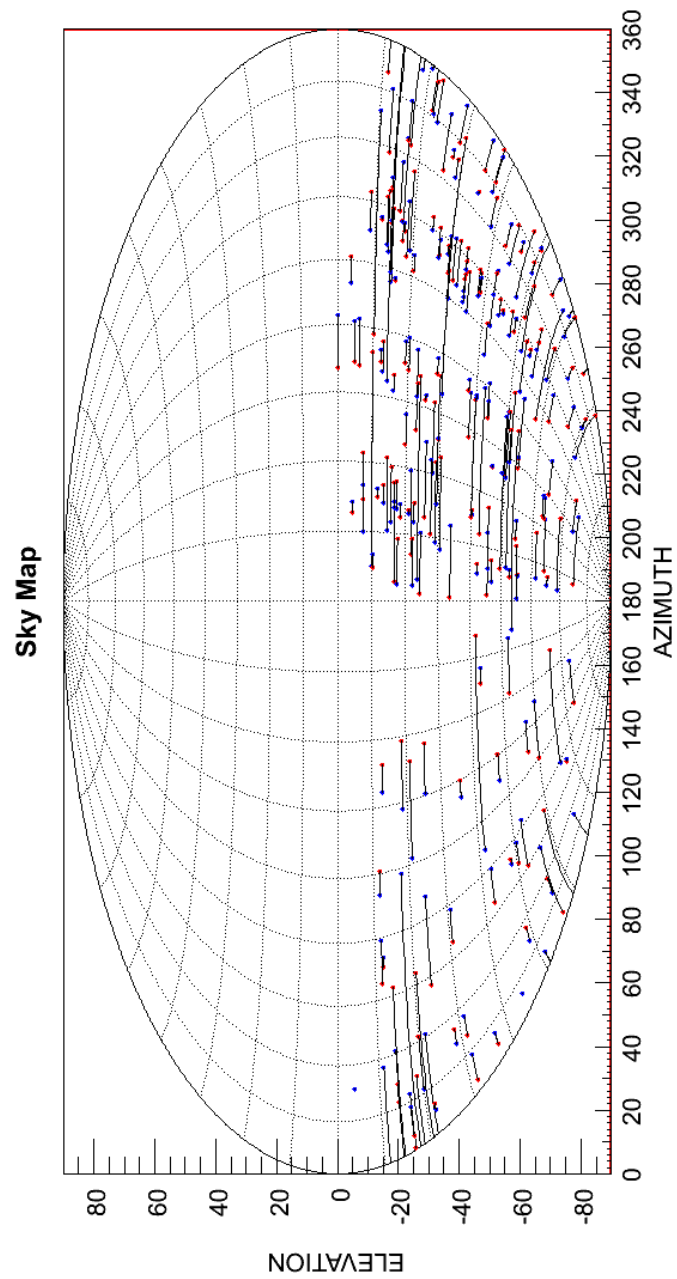


Figure 11.5: Sky map of the same data set with the black segments to connect red and blue dots belonged to the same couple.

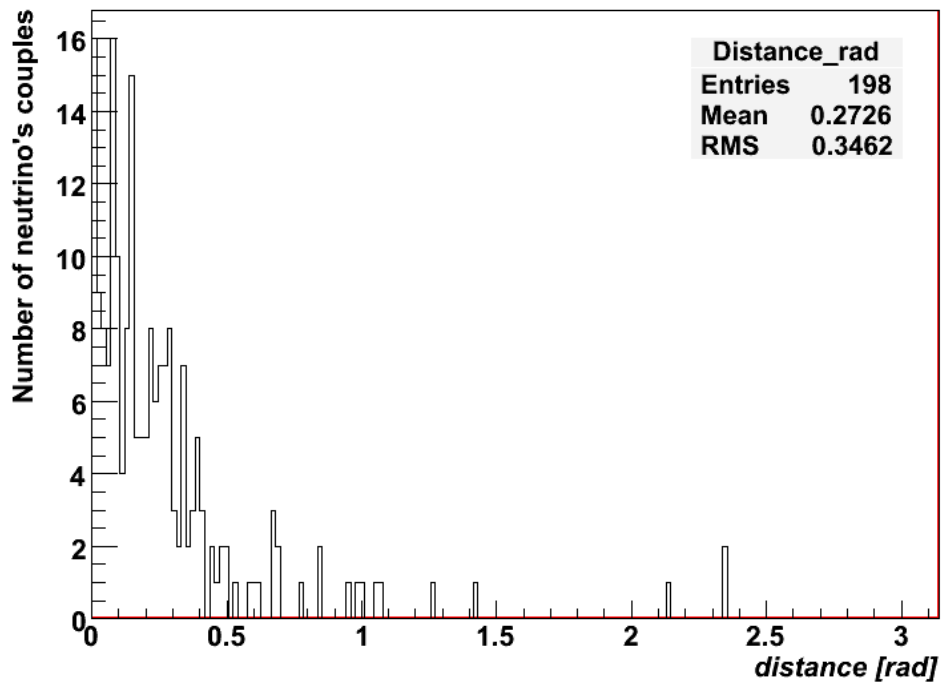
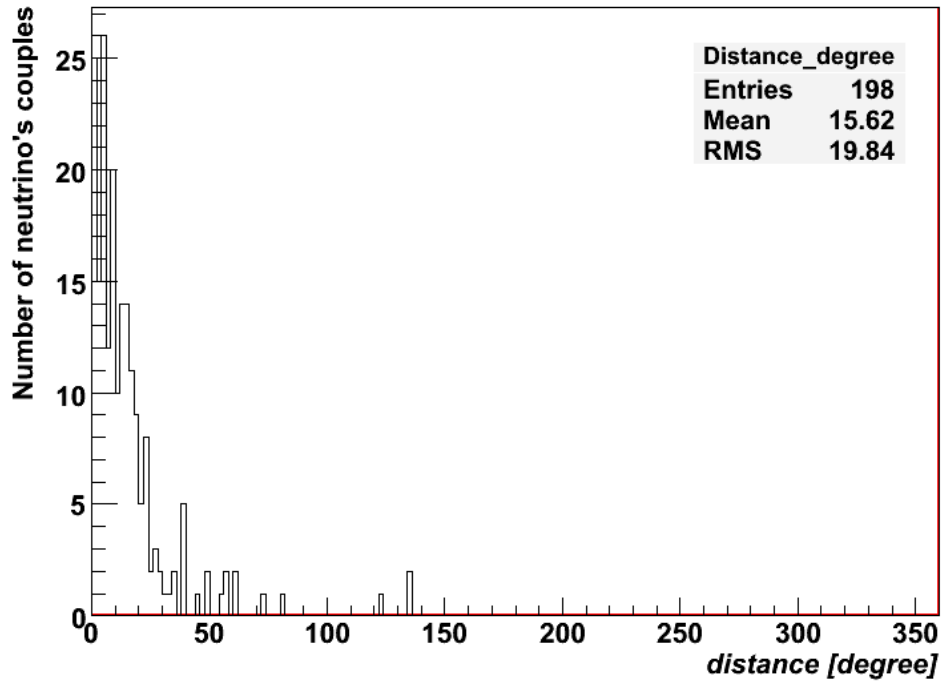


Figure 11.6: Histograms of the angular distance between the two possible sky positions associated with the same 2-line triggers.

As you can notice from Figure 11.5, each neutrino couple has the same elevation angle and different azimuth. This feature is due to the fact that the muon track is reconstructed with only two detector lines. In this case in fact a muon that impinges the geometrical plane passing through the two lines with an angle of incidence ( $\alpha$ , angle between the normal to the plane and the muon track) is undistinguishable from a muon that impinges with the mirror angle  $\pi - \alpha$  because the two cases generate the same hits at the same time. In other words, the indetermination results from the symmetry of the detector.

In addition to that, this mirror problem is really connected to the reconstruction algorithm used for this data set, which basically merges the hits received by the three Optical Modules (OMs) of each storey into one *fake* OM located at the center of the storey.

This degeneracy can be cancelled when considering the hits of each individual optical module, and taking into account further information, for instance the angular acceptance of the optical modules.

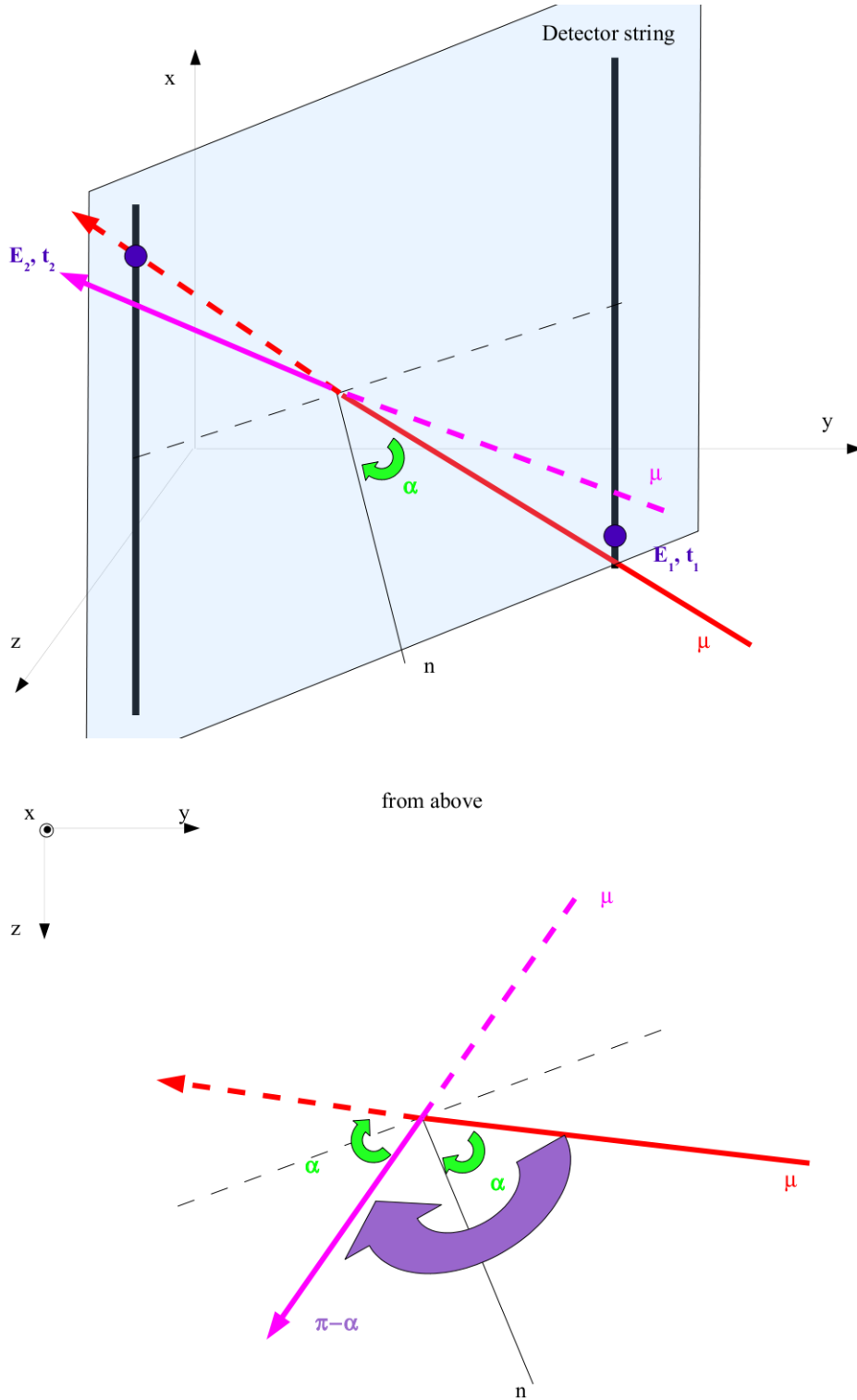


Figure 11.7:



# Bibliography

- [1] A first course in General Relativity, Bernard Schutz, Cambridge University Press
  
- [2] Gravitational waves, Volume 1: Theory and Experiments, Michele Maggiore, Oxford University Press
  
- [3] General Relativity and Gravitation, volume 1, Held A., Plenum London
  
- [4] General Relativity and Gravitation, volume 2, Held A., Plenum London
  
- [5] Course of Theoretical Physics, volume I, Landau and Lifshitz, Pergamon Oxford
  
- [6] Course of Theoretical Physics, volume II, Landau and Lifshitz, Pergamon Oxford
  
- [7] Course of Theoretical Physics, volume IV, Landau and Lifshitz, Pergamon Oxford
  
- [8] Course of Gravitational Waves, lectures, V. Ferrari, <http://www.roma1.infn.it/teongrav/teaching2011-12.html>

- 
- [9] A modern introduction to quantum field theory, Michele Maggiore, Oxford University Press
- [10] The detection of Gravitational Waves, Pallottino and Pizzella, Cambridge University Press
- [11] Gravitational Waves I, B. Schutz and F. Ricci, Inst. of Phys. Publishing Bristol
- [12] Tensor Analysis on Manifolds, R. Bishops and S. Goldberg, Dover New York
- [13] M. Kamionkowski and A. Jaffe. *Int. J. Mod. Phys. A*, 16:116, 2001.
- [14] A. Lommen and D.C. Backer. *Astrophys. J.*, 2002. in press; [astro-ph/0107470](http://arxiv.org/abs/astro-ph/0107470).
- [15] Schutz B F Data processing analysis and storage for interferometric antennas 1991 *The Detection of Gravitational Waves* ed D G Blair (Cambridge: Cambridge University Press) pp 406–52
- [16] Schutz B F The detection of gravitational waves 1996 *Astrophysical Sources of Gravitational Radiation* ed J-P Marck and J-A Lasota
- [17] Blanchet L, Damour T, Iyer B R, Will C M and Wiseman A G 1995 *Phys. Rev. Lett.* 74 3515
- [18] Cutler C, Apostolatos T A, Bildsten L, Finn L S, Flanagan E E, Kennefick D I, Markovic D M, Ori A, Poisson E, Sussman G J and Thorne K S 1993 The last three minutes: issues in gravitational wave measurements of coalescing binaries *Phys. Rev. Lett.* 70 1984

- 
- [19] Tutukov A V and Yungelson L R 1993 *Mon. Not. R. Astron. Soc.* 260 675
- [20] Yamaoka H, Shigeyama T and Nomoto K 1993 *Astron. Astrophys.* 267 433
- [21] Narayan R, Piran T and Shemi A 1991 Neutron star and black hole binaries in the Galaxy *Astrophys. J.* 379 L17
- [22] Phinney E S 1991 The rate of neutron star binary mergers in the Universe: minimal predictions for gravity wave detectors *Astrophys. J.* 380 117
- [23] Brustein R, Gasperini M, Giovannini M and Veneziano G 1995 Relic gravitational waves *Phys. Lett.* 361B 45
- [24] Aharonian F., et al. (2006), *J. Phys. Conf. Ser.*, 39, 408.
- [25] Aiello S., et al. (2007), *Astroparticle Physics*, 28, 1.
- [26] Waxman, E., and J. Bahcall, 1997, *Physical Review Letters* 78, 2292.
- [27] Meszaros, P., 2001, *Science*, Volume 291, Issue 5501, pp. 79-84 (2001). 291, 79.
- [28] Belczynski, K., T. Bulik, and V. Kalogera, 2002, *Ap. J. Lett.*, 571, L147.
- [29] Corsi A., and B. J. Owen (2011), *Phys. Rev. D*, D83, 104014, 1102.3421.
- [30] Guetta, D., T. Piran, and E. Waxman, 2003, *ArXiv Astrophysics e-prints astro-ph/0311488*.
- [31] Duncan R. C., and C. Thompson (1992), *ApJ*, 392, L9.
- [32] Thompson C., and R. C. Duncan (1996), *ApJ*, 473, 322.

- 
- [33] Meszaros, P., and E. Waxman, 2001, *Physical Review Letters* 87, 171102.
- [34] Vilenkin and E.P.S. Shellard, *Cosmic Strings and Other Topological Defects*, Cambridge University Press (1994)
- [35] E. J. Copeland and T. W. B. Kibble, *Proc. Roy. Soc. Lond. A* 466, 623 (2010) arXiv : hep-th/0911.1345
- [36] V. Bereinsky, K. D. Olum, E. Sabancilar, A. Vilenkin, *Phys. Rev. D* 80, 023014 (2009) arXiv : astro-ph.HE/0901.0527
- [37] A. Babul, B. Paczynski and D.N. Spergel, *Ap. J. Lett.* 316, L49 (1987)
- [38] V. Bereinsky, B. Hnatyk and A. Vilenkin, *Phys. Rev. D* 64, 043004 (2001)
- [39] Damour and Vilenkin, A. 2000, *Phys. Rev. Lett.*, 85, 3761
- [40] Siemens et al. 2006, *Phys. Rev. D*, 73, 105001
- [41] Bereinsky, et al. 2011, *Phys.Rev.D*84:085006
- [42] Cuesta, Gonzalez 2001, *Phys.Lett.B*500:215-221
- [43] Sari, R., and T. Piran, 1997, *Ap. J.*, 485, 270
- [44] Eichler D. (2003), *MNRAS*, 335, 883, astro-ph/0204512.
- [45] Halzen F., et al. (2005), TeV photons and neutrinos from giant soft-gamma repeaters flares, arXiv:astro-ph/0503348v1.
- [46] Rees, M. J., and P. Meszaros, 1992, *Mon. Not. RAS* 258, 41P.
- [47] Greisen, K., 1966, *Physical Review Letters* 16, 748.
- [48] Eichler, D., M. Livio, T. Piran, and D. N. Schramm, 1989, *Nature (London)* 340, 126.

- [49] Van Putten, M. H. P. M., 2001, *Physics Reports* 345, 1.
- [50] Freedman, D. L., and E. Waxman, 2001, *Ap. J.*, 547, 922.
- [51] Waxman E., and J. N. Bahcall (2000), *ApJ*, 541, 707.
- [52] Meszaros, P., and M. J. Rees, 1997, *Ap. J.*, 476, 232.
- [53] Piran T. astro-ph/0405503v1
- [54] Kochanek, C. S., and T. Piran, 1993, *Ap. J. Lett.*, 417, L17.
- [55] Cuesta H. J. M. and Gonzalez D. M, *Physics Letters B* 500 (2001) 215-221
- [56] Vietri, M., 2002, astro-ph , 0212352.
- [57] Nakar, E., and T. Piran, 2002, *Mon. Not. RAS* 331, 40.
- [58] G. Raffelt, *Stars as Laboratories for Fundamental Physics*, Univ. of Chicago Press, 1996.
- [59] V. Berezhinsky, B. Hnatyk, A. Vilenkin, astro-ph/0001213
- [60] Gaisser, T. K., 1991, *Cosmic Rays and Particle Physics (Cosmic Rays and Particle Physics, Cambridge University Press, 1991)*.
- [61] Razzaque, S., P. Meszaros, and E. Waxman, 2003, *Phys. Rev. D* 68, 083001.
- [62] Piran T. astro-ph/9810256v1
- [63] Meszaros P., Kobayashi S., Razzaque S and Zhang B. astro-ph/0305066v1
- [64] McBreen, S., F. Quilligan, B. McBreen, L. Hanlon, and D. Watson, 2001, *Astron. Astrophys.*, 380, L31.
- [65] Waxman E., *Physical Review Letters*, 75, 3.
- [66] Piran T., astro-ph/9801001v1
- [67] Weinberg, S., 1973, *Gravitation and Cosmology (Wiley)*.

- 
- [68] Finn, L. S., S. D. Mohanty, and J. D. Romano, 1999, *Phys. Rev. D* 60, 121101.
- [69] Waxman E., astro-ph/0502159v1.
- [70] Rees, M. J., and P. Meszaros, 1994, *Ap. J. Lett.*, 430, L93.
- [71] Nakar, E., and T. Piran, 2002, *Mon. Not. RAS* 331, 40.
- [72] Mirabel I. F., V. Dhawan, S. Chaty, L. F. Rodriguez, J. Marti, C. R. Robinson, J. Swank, and T. Geballe (1998), *A&A*, 330, L9, arXiv:astro-ph/9711097.
- [73] Meszaros P., and M. J. Rees (1993), *ApJ*, 405, 278.
- [74] Rosswog S. *Science* 2 January 2004, 303.
- [75] Piran T. (2004), *Rev. Mod. Phys.*, 76, 1143, astro-ph/0405503.
- [76] Piran T., astro-ph/0405503v1.
- [77] Romero G. E., D. F. Torres, M. M. K. Bernado, and I. F. Mirabel (2003), *Astron. Astrophys.*, 410, L1, arXiv:astro-ph/0309123.
- [78] Allen B., Ottewill A. C., gr-qc/0009091
- [79] Rachen J., Meszaron P., *Phys. Rev. D*, 58, 123005 (1998).
- [80] Braun J., Baker M., Dumm J., Finley C., Karle A. and Montaruli T arXiv:0912.1572v1.
- [81] Ramirez-Ruiz, E., and A. Merloni, 2001, *Mon. Not. RAS* 320, L25.
- [82] Distefano C., D. Guetta, E. Waxman, and A. Levinson (2002), *Astrophys. J.*, 575, 378, arXiv:astro-ph/0202200.
- [83] Vietri M. 1995, *Astrophys. J.* 453, 883.
- [84] Waxman E. 1995a, *Phys. Rev. Lett.* 75, 386
- [85] Waxman E. 1995b, *Astrophys. J.* 452, L1.
- [86] Guetta D. and Granot J. 2003, *Phys. Rev. Lett.* 90, 201103

- 
- [87] Waxman E. 2004b, *Astrophys. J.* 606, 988.
- [88] Waxman E. and Bahcall J. 1999, *Phys. Rev. D* 59, 023002
- [89] Alvarez-Muniz J., Halzen F. and Hooper D. 2000, *Phys. Rev. D* 62, 093015.
- [90] Bahcall J. and Waxman E. 2001, *Phys. Rev. D* 64, 023002.
- [91] Ruffert M. and Janka H.-Th. astro-ph/9804132v1.
- [92] D. Burlon, et al., Time resolved spectral behavior of bright BATSE precursors, *Astronomy and Astrophysics* 505 (2009) 569-575.
- [93] W. S. Paciesas, et al., The Fourth BATSE Gamma-Ray Burst Catalog (Revised), *The Astrophysical Journal Supplement Series* 122 (1999) 465-495.
- [94] Kotake K. and Yamada S.
- [95] Abbott B et al. *Classical Quantum Gravity* 25, 114051, 2008.
- [96] Guetta D., and Piran T. 2007, *JCAP*, 07, 3.
- [97] Hopman C., Guetta D., Waxman E. and Portegies Zwart, S. F. 2006, *ApJ*, 643, L91 (H06).
- [98] Cutler C., and Thorne K. S. 2002, *Proc. of GR16*, [arXiv:gr-qc/0204090].
- [99] Hurley K. (2010), *Mem. Soc. Astr. It.*, 81, 432.
- [100] Goodman J. 1986, *ApJ*, 308, L47.
- [101] Paczynski B. 1986, *ApJ*, 308, L43.
- [102] Vila G. S., and G. E. Romero (2010), *MNRAS*, 403, 1457, 1001.0959.
- [103] S. Horiuchi, S. Ando, High-energy neutrinos from reverse shocks in choked and successful relativistic jets, *Physical Review D* 77 (2008) 063007.

- 
- [104] S. Razzaque, P. Meszaros, E. Waxman, Neutrino tomography of gamma ray bursts and massive stellar collapses, *Physical Review D* 68 (2003) 083001.
- [105] Narayan R., Paczynski B., and Piran T. 1992, *ApJ*, 395, L83.
- [106] Guetta D., Hooper D. W., Alvarez-Muniz J., Halzen F. and Reuveni E. 2004 *Astropar. Phys.* 20, 429.
- [107] Fryer C., Woosley E. and Hartmann D. H. 1999 *Astrophys. J.* 526.
- [108] Eberl T., Janka H.-T., Ruert M., and Fryer, C. L. 1999.
- [109] Woosley S. E. and Weaver T. A. 1995, *ApJS*, 101, 181.
- [110] Brown, G. E. 1995, *ApJ*, 440, 270 First.
- [111] Bethe, H. A., Brown, G. E. 1998, *ApJ*, 506, 780.
- [112] Aptekar R. L., et al. (2009), *ApJ Lett.*, 698, L82, arXiv:0902.3391 [astro-ph.HE].
- [113] Mereghetti S. (2008), *A&A Rev.*, 15, 225, arXiv:0804.0250.
- [114] Homepage of the LIGO Scientific Collaboration, <http://www.ligo.org>.
- [115] Abramovici A et al 1992 LIGO: the Laser Interferometer Gravitational-Wave Observatory *Science* 256 325–333.
- [116] Cutler C and Thorne K S 2002 An overview of gravitational-wave sources arXiv:gr-qc/0204090v1.
- [117] Weisberg J M and Taylor J H 2005 The relativistic binary pulsar B1913 + 16: thirty years of observations and analysis *Binary Radio Pulsars* ed F A Rasio and I H Stairs.
- [118] Meers B J 1988 Recycling in laser interferometric gravitational wave detectors *Phys. Rev. D* 38 2317–26
- [119] Takahashi R 2004 Status of TAMA300 *Class. Quantum Grav.* 21 S403–8

- 
- [120] Luck H et al 2006 Status of the GEO600 detector *Class. Quantum Grav.* 23 S71â€”S8
- [121] Acernese F et al 2006 The Virgo status *Class. Quantum Grav.* 23 S635â€”S42
- [122] Kuroda K and the LCGT Collaboration 2006 The status of LCGT *Class. Quantum Grav.* 23 S215â€”S21
- [123] KAGRA website <http://gwcenter.icrr.u-tokyo.ac.jp/en/>
- [124] Wei D T 1989 Ion beam interference coating for ultralow optical loss *Appl. Opt.* 28 2813â€”S6
- [125] Rempe G, Thompson R J, Kimble H J and Lalezari R 1992 Measurement of ultralow losses in an optical interferometer *Opt. Lett.* 17 363â€”S5
- [126] Ottaway D, Betzwieser J, Ballmer S, Waldman S and Kells W 2006 In situ measurement of absorption in high-power interferometers by using beam diameter measurements *Opt. Lett.* 31 450â€”S2
- [127] Vinet J-Y, Brisson V and Braccini S 1996 Scattered light noise in gravitational wave interferometric detectors: coherent effects *Phys. Rev. D* 54 1276â€”S86
- [128] Vinet J-Y et al 1997 Scattered light noise in gravitational wave interferometric detectors: a statistical approach *Phys. Rev. D* 56 6085â€”S95
- [129] Drever R W P, Hall J L, Kowalski F V, Hough J, Ford G M, Munley A J and Ward H 1983 Laser phase and frequency stabilization using an optical resonator *Appl. Phys. B: Lasers Opt.* 31 97â€”S105
- [130] Penn S D et al. 2006 Frequency and surface dependence of the mechanical loss in fused silica *Phys. Lett. A* 352 3â€”S6
- [131] Willke B, Uehara N, Gustafson E K, Byer R L, King P J, Seel S U and Savage R L Jr 1998 Spatial and temporal filtering of a 10 W Nd : YAG laser with a Fabryâ€”Perot ring-cavity pre-mode cleaner *Opt. Lett.* 23 1704â€”S6

- [132] Levin Y 1998 Internal thermal noise in the LIGO test masses: a direct approach *Phys. Rev. D* 57 659–663
- [133] Zucker M E and Whitcomb S E 1996 Measurement of optical path fluctuations due to residual gas in the LIGO 40 meter interferometer *Proc. 7th Marcel Grossman Meeting on Recent Developments in Theoretical and Experimental General Relativity, Gravitation, and Relativistic Field Theories* ed R T Jantzen et al (Stanford, CA, USA, 24–29 July 1994) (Singapore: World Scientific) pp 1434–1436
- [134] K. C. Cannon, *Classical and Quantum Gravity* 25, 105024, 2008
- [135] C. D. Ott, *Classical and Quantum Gravity* 26, 063001, 2009, 0809.0695.
- [136] Ott C. D., et al. (2011), *Phys. Rev. Lett.*, 106, 161103, arXiv:1012.1853.
- [137] Romero G. E., M. M. Reynoso, and H. R. Christiansen (2010), *A&A*, 524, A4+, arXiv:1009.3679.
- [138] C. Cutler et al., *Phys. Rev. Lett.* 70, 2984 (1993).
- [139] J. Abadie et al., 'Predictions for rates of compact binary coalescences observable by ground-based gravitational wave detectors', arXiv:1003.2480v2
- [140] S. Mohanty, M. Rakhmanov, S. Klimenko, and G. Mitselmakher, *Class. Quant. Grav.* 23, 4799 (2006), gr-qc/0601076.
- [141] P. A Cherenkov. Visible Radiation Produced by Electrons Moving in a Medium with Velocities Exceeding that of Light. *Physical Review*, 52:378, 1937.
- [142] W. G. Anderson, P. R. Brady, J. D. E. Creighton, and E. E. Flanagan, *Phys. Rev. D* 63, 042003 (2001).
- [143] M. Rakhmanov, *Class. Quant. Grav.* 23, S673 (2006), gr-qc/0604005.
- [144] T. Z. Summerscales, A. Burrows, L. S. Finn, and C. D. Ott, *The Astrophysical Journal* 678, 1142 (2008), 0704.2157.
- [145] K. Hayama, S. D. Mohanty, M. Rakhmanov, and S. Desai, *Class. Quant. Grav.* 24, S681 (2007), 0709.0940.

- 
- [146] A. C. Searle, P. J. Sutton, M. Tinto, and G. Woan, *Class. Quant. Grav.* 25, 114038 (2008), 0712.0196.
- [147] A. C. Searle, P. J. Sutton, and M. Tinto, *Class. Quant. Grav.* 26, 155017 (2009), 0809.2809.
- [148] S. Klimenko, I. Yakushin, A. Mercer, and G. Mitselmakher, *Class. Quant. Grav.* 25, 114029 (2008), 0802.3232.
- [149] S. Fairhurst, *New Journal of Physics* 11, 123006 (2009).
- [150] V. Van Elewyck et al., *Int. J. Mod. Phys. D* 18, 1655 (2009), 0906.4957.
- [151] Pradier T. 2008, Antares/Virgo Coincidences: a feasibility study, (arXiv:0807.2567v1)
- [152] Aso Y. et al. 2008, *Class. Quant. Grav.* 25, 114039.
- [153] Ioka K. et al. 2005, *Astrophys. J.* 633, 1013.
- [154] Ando S. and Beacom J. 2005, *Phys. Rev. Lett.* 95(6), 061103
- [155] B. P. Abbott et al., *Phys. Rev. D* 80, 102001 (2009), 0905.0020.
- [156] B. P. Abbott et al., *Phys. Rev. D* 79, 122001 (2009), 0901.0302.
- [157] J. Sylvestre, *Phys. Rev. D* 66, 102004 (2002).
- [158] Y. Gursel and M. Tinto, *Phys. Rev. D* 40, 3884 (1989).
- [159] Nagar A., O. Zanotti, J. A. Font, and L. Rezzolla (2007), *Phys. Rev. D*, 75, 044016, arXiv:gr-qc/0610131.
- [160] M. Tinto, in *Proceedings of the International Conference on Gravitational Waves: Source and Detectors.* (World Scientific (Singapore), 1996).
- [161] E. E. Flanagan and S. A. Hughes, *Phys. Rev. D* 57, 4566 (1998).
- [162] J. Sylvestre, *Phys. Rev. D* 68, 102005 (2003).
- [163] L. Cadonati, *Class. Quantum Grav.* 21, S1695 (2004).
- [164] L. Wen and B. Schutz, *Class. Quantum Grav.* 22, S1321 (2005).

- 
- [165] S. Klimenko, S. Mohanty, M. Rakhmanov, and G. Mitselmakher, *Phys. Rev. D* 72, 122002 (2005).
- [166] S. Klimenko, S. Mohanty, M. Rakhmanov, and G. Mitselmakher, *J. Phys. Conf. Ser.* 32, 12 (2006).
- [167] B. Abbott et al., *Astrophys. J.* 681, 1419 (2008), 0711.1163.
- [168] L. Blackburn et al., *Class. Quant. Grav.* 25, 184004 (2008), 0804.0800.
- [169] N. Leroy, *Class. Quant. Grav.* 26, 204007 (2009).
- [170] <https://geco.phys.columbia.edu/xpipeline/wiki>.
- [171] S. Chatterji, A. Lazzarini, L. Stein, P. Sutton, A. Searle, and M. Tinto, *Phys. Rev. D* 74, 082005 (2006).
- [172] B. P. Abbott et al., *The Astrophysical Journal*, (2010), 0908.3824.
- [173] K. C. Cannon, *Classical and Quantum Gravity* 25, 105024 (13pp) (2008).
- [174] W. G. Anderson, P. R. Brady, J. D. E. Creighton, and E. E. Flanagan, *Phys. Rev. D* 63, 042003 (2001).
- [175] P. Meszaros, *Rept. Prog. Phys.* 69, 2259 (2006), astro-ph/0605208.
- [176] C. Cutler and K. S. Thorne (2002), gr-qc/0204090.
- [177] J. S. Bloom et al. (2009), 0902.1527.
- [178] J. Kanner et al., *Class. Quant. Grav.* 25, 184034 (2008), 0803.0312.
- [179] E. E. Flanagan and S. A. Hughes, *New Journal of Physics* 7, 204 (2005), gr-qc/0501041.
- [180] B. Abbott et al., *Nucl. Inst. & Meth. in Phys. Res.* 517, 154 (2004).
- [181] B. Abbott et al., *Rep. Prog. Phys.* 72, 076901 (2009), arXiv:0711.3041
- [182] F. Acernese et al., *Classical and Quantum Gravity* 25, 114045 (2008).
- [183] H. Grote et al., *Classical and Quantum Gravity* 25, 114043 (2008).

- 
- [184] S. Chatterji, L. Blackburn, G. Martin, and E. Kasavounidis, *Class. Quant. Grav.* 21, S1809 (2004).
- [185] B. Abbott et al., *Phys. Rev. D* 72, 042002 (2005), gr-qc/0501068.
- [186] B. Abbott et al., *Phys. Rev. D* 77, 062004 (2008), gr-qc/0709.0766.
- [187] P. R. Brady, J. D. E. Creighton, and A. G. Wiseman, *Class. Quant. Grav.* 21, S1775 (2004), gr-qc/0405044.
- [188] R. Biswas, P. R. Brady, J. D. E. Creighton, and S. Fairhurst, *Classical and Quantum Gravity* 26, 175009, 0710.0465.
- [189] B. Abbott et al., *Phys. Rev. Lett.* 101, 211102 (2008).
- [190] K. Riles, LIGO Document: LIGO-T040055-00-Z (2004).
- [191] N. Gehrels et al., *Astrophys. J.* 611, 1005 (2004).
- [192] B. Abbott et al. 2005, *Phys. Rev. D* 72, 062001
- [193] Skeldon K D, Strain K A, Grant A I and Hough J 1996 Test of an 18-m-long suspended modecleaner cavity *Rev. Sci. Instrum.* 67 2443–2448
- [194] Giaime J, Saha P, Shoemaker D and Sievers L 1996 A passive vibration isolation stack for LIGO: design, modeling, and testing *Rev. Sci. Instrum.* 67 208–214
- [195] Abbott R et al 2004 Seismic isolation enhancements for initial and advanced LIGO *Class. Quantum Grav.* 21 S915–S921
- [196] Fritschel P, Bork R, Gonzalez G, Mavalvala N, Ouimette D, a Rong H, Sigg D and Zucker M 2001 Readout and control of a power-recycled interferometric gravitational-wave antenna *Appl. Opt.* 40 4988–4998
- [197] Landry M and the LIGO Scientific Collaboration 2005 Improvements in strain calibration for the third LIGO science run *Class. Quantum Grav.* 22 985
- [198] Abadie, J. et al. 2012
- [199] Abbott, et al. 2008, *Astrophys. J.*, 683, L45

- [Abbott et al.(2009)] Abbott, et al. 2009, Rep. Prog. Phys., 72, 076901
- [200] Abbott, et al., 2010, Astrophysical Journal, 715, 1438
- [201] Was, M., Sutton, P., & Jones, G. 2012
- [202] Brady, P. et al., 2004, Classical and Quantum Gravity 21, gr-qc/0405044
- [203] Sutton P. J. et al., X-Pipeline: An analysis package for autonomous gravitational-wave burst searches, New J.Phys. 12:053034, 2010
- [204] Sutton P. J. et al., Coherent network analysis technique for discriminating gravitational-wave bursts from instrumental noise, Phys.Rev.D74:082005, 2006
- [205] Meers B J 1989 The frequency response of interferometric gravitational wave detectors Phys. Lett. A 142 465–470
- [206] I. Bartos, C. Ott, and S. Marka. High-energy neutrinosphere of stellar envelopes in core-collapse supernovae.
- [207] Shunsaku Horiuchi and Shin'ichiro Ando. High-energy neutrinos from reverse shocks in choked and successful relativistic jets. Phys. Rev. D, 77(6):063007, Mar 2008.
- [208] Cote P J and Meisel L V 1991 Self-organized criticality and the Barkhausen effect Phys. Rev. Lett. 67 1334
- [209] J.A. Aguilar et al. 2011 *Astropart. Phys.*, Volume 34, Issue 9, April 2011, Pages 652-662
- [210] Belczynski K, Kalogera V and Bulik T 2001 A comprehensive study of binary compact objects as gravitational wave sources: evolutionary channels, rates, and physical properties Astrophys. J. 572 407–431
- [211] Dimmelmeier H, Font J A and Muller E 2001 Gravitational waves from relativistic rotational core collapse Astrophys. J. 560 L163–166
- [212] Jaranowski P, Krolak A and Schutz B F 1998 Data analysis of gravitational-wave signals from spinning neutron stars: I. The signal and its detection Phys. Rev. D 58 063001

- 
- [213] Maggiore M 2000 Gravitational wave experiments and early universe cosmology *Phys. Rep.* 331 283–367
- [214] Blanchet L 2006 Gravitational radiation from post-Newtonian sources and inspiralling compact binaries *Living Rev. Rel.* 9 4
- [215] Tagoshi H and Sasaki M 2003 Analytic black hole perturbation approach to gravitational radiation *Living Rev. Rel.* 6 6
- [216] Buonanno A. et al. 'Detection template families for gravitational waves from the final stages of binary-black-hole inspirals: Nonspinning case', arXiv:gr-gc/0205122v3
- [217] Hannam M 2009 Status of black-hole-binary simulations for gravitational-wave detection arXiv:0901.2931 [gr-qc]
- [218] Ott C D 2009 The gravitational wave signature of core-collapse supernovae *Class. Quantum Grav.* 26 063001
- [219] Abadie J et al. 2011 Beating the spin-down limit on gravitational wave emission from the Vela pulsar, arXiv:1104.2712v2
- [220] Abbott B et al 2008 Beating the spin-down limit on gravitational wave emission from the Crab pulsar *Astrophys. J.* 683 L45–50
- [221] Allen B 1996 The stochastic gravity-wave background: sources and detection arXiv:gr-qc/9604033v3
- [222] R. G. Herb, D. B. Parkinson, D. W. Kerst, *Phys. Rev.* 51, 75, 1937.
- [223] John David Jackson, *Classical Electrodynamics*, John Wiley and sons, Inc. 1998.
- [224] J.G. Learned and S. Pakvasa *Astropart. Phys.*, vol. 3, p. 267, 1995.
- [225] L. D. Landau and E. M. Lifshitz, *Electrodynamics of continuous media*, volume 8, 1984.
- [226] J. V. Jelley, *Cherenkov radiation and its applications*, 1958.
- [227] R. Ghandi et al, 'Ultra-high-energy Neutrino Interactions', *Astropart. Phys.*, vol. 5, p. 81, 1996.

- [228] P. Cherenkov, 'Visible radiation produced by electrons moving in a medium with velocities exceeding that of light', *Phys. Rev.*, vol. 52, p. 378, 1937.
- [229] The Antares Collaboration, Conceptual design report.
- [230] The Antares Collaboration, Technical design report.
- [231] The KM3NeT Consortium, Conceptual design report.
- [232] A.M. Markov. In *Proceeding of the Rochester Conference*, New York, 1960
- [233] P. Amram et al., 'The ANTARES optical module', *Nucl. Instrum. Meth.*, vol. A484, pp. 369–383, 2002.
- [234] W. M. Yao et al. Review of particle physics. *J. Phys.*, G33:1–1232, 2006.
- [235] S. Vecchio, 'Analysis of the optical background sources in the antares experiment and preliminary studies related to a larger scale detector', Dissertation, Universita di Pisa, 2004.
- [236] J. Brunner, 'Upgrade on K40 simulation', ANTARES Internal Note, ANTARES-PHYS-2006-005, 2006.
- [237] S. Escoffier, 'Bioluminescence studies with the ANTARES Prototype Sector Line', ANTARES Internal Note, ANTARES-SITE-2005-001, 2005.
- [238] Particle Data Group, 'Passage of Particle through Matter', *European Physics Journal C*, vol. 3, p. 144, 1998.
- [239] S. Klimushin et al., 'Precise parameterizations of muon energy losses in water', *Proceedings of ICRC*, 2001.
- [240] J. A. Aguilar, 'The data acquisition system for the antares neutrino telescope', *Nucl. Instrum. Meth.*, vol. A570, pp. 107–116, 2007.

- 
- [241] P. Lucas, 'An object-oriented language system for implementing concurrent, hierarchical, finite state machines', Technical Report UIUCDCS-R-94-1868, University of Illinois at Urbana-Champaign, 1994.
- [242] R. Gurin and A. Maslennikov, 'ControlHost: Package for Distributed Data Handling', CASPUR Inter-Universitij Computing Consortium Rome, 1995.
- [243] M. Bouwhuis, 'Detection of neutrinos from gamma-ray bursts.', PhD thesis, Universiteit van Amsterdam, 2005.
- [244] D. White, E. Daw and V Dhillonl, 'A List of Galaxies for Gravitational Wave Searches', astro-ph:1103.0695v1
- [245] Sutton P. et al. 2010, 'X-Pipeline: an analysis package for autonomous gravitational-wave burst searches', New J. Phys. 12 053034
- [246] arXiv:0908.3665
- [247] arXiv:0908.3665
- [248] arXiv:0908.3824
- [249] Baret et al., Bounding the Time Delay between High-energy Neutrinos and Gravitational-wave Transients from Gamma-ray Bursts, arXiv:1101.4669v1
- [250] J.A. Aguilar et al. 2011 Astropart. Phys., Volume 34, Issue 9, April 2011, Pages 652-662
- [251] I. Di Palma, Derivation of the ANTARES 2-line muon trajectory reconstruction cases in the context of GW-HEN analysis, LIGO-T1100197-v2
- [252] I. Di Palma, Description of the X Pipeline output web page, LIGO-T1100287

- 
- [253] A. Margiotta, Monte Carlo simulation of atmospheric muons, ANTARES-SOFT-2008-005
- [254] G. Carminati, A. Margiotta and M. Spurio, Atmospheric MUons from PArametric formulas: a fast GEnerator for neutrino telescope (MUPAGE), *comput. Phys. Common*, 179:915-923, 2008
- [255] G. Battistoni, A. Ferrarib, T. Montarulic and P.R. Sala, The atmospheric neutrino fluxes below 100 MeV: the FLUKA results, *Nuclear Physics B (Proc. Suppl.)* 145 (2005) 128131, August 2005
- [256] A. Heijboer, 'Track reconstruction and point source searches with antares', PhD thesis, NIKHEF, Amsterdam, 2004.
- [257] F. Fehr, 'Systematic studies, calibration, and software development for event reconstruction and data analysis using the ANTARES deep sea neutrino telescope', Erlangen, 2010.
- [258] D. J. L. Bailey, *Genhen v5r1:Software/2002-2004 Software Documentation*, ANTARES-Software/2002-2004
- [259] G. Battistoni et al, The FLUKA atmospheric neutrino flux calculation, [arXiv:hep-ph/0207035v2](https://arxiv.org/abs/hep-ph/0207035v2), 20 Jan 2003
- [260] John Carr, Stphanie Escoffier and Dmitry Zaborov, Proposition for an alternative trigger based on the T3 cluster trigger, ANTARES-SOFT-2007-016
- [261] Hernandez-Rey, J. J. 2009, *J. Phys. Conf. Ser.*, 171, 012047
- [262] Dimmelmeier, H., et al. 2008, *Phys. Rev. D*, 78
- [263] Guetta, D., and Valle, M. D. 2007, *Astroparticle Physics*, 657, L73
- [264] Guetta, D., et al. 2004, *Astroparticle Physics*, 20, 429
- [265] Bartos, I., et al. 2011, *Phys. Rev. Lett.*, 107, 251101
- [266] Harry, G. M., et al. 2010, *Classical and Quantum Gravity*, 27, 084006
- [267] Bazin, G., et al. 2009, *Astronomy and Astrophysics*, 499, 653
- [268] Kalogera, V., et al. 2004, *ApJ*, 601, L179

- [269] Belczynski, K., et al. 2011, Proceedings of The Rencontres de Moriond and GPhyS colloquium, La Thuile, Italy, eprint 1106.0397
- [270] Nakar, E. 2007, Phys. Rept., 442, 166
- [271] Ott, C., et al. 2011, Phys. Rev. Lett, 106
- [272] Ott, C. D. 2009, Classical and Quantum Gravity, 26, 063001
- [273] Fryer, C., and New, K. 2011, Living Rev. Relativity, 14
- [274] Fryer, C., et al. 2002, The Astrophysical Journal, 565, 430
- [275] Kobayashi, S., and Meszaros, P. 2003, The Astrophysical Journal, 589, 861
- [276] Scheidegger, S., et al. 2010, Astronomy and Astrophysics, 514
- [277] Takiwaki, T., and Kotake, K. 2011, The Astrophysical Journal, 743
- [278] Piro, A. L., and Pfahl, E. 2007, The Astrophysical Journal, 658, 1173



# Acknowledgements

The completion of this work would not have been possible without the immeasurable support of a large number of people.

I have had the great privilege of pursuing this research under the guidance of my thesis advisers, Bruce Allen and Maria Alessandra Papa. I appreciate the possibilities of traveling to broaden my horizon by meeting other scientists and sharing their knowledge. I cannot thank them enough for the opportunity, support, and guidance they have provided. I am very grateful for the freedom of research I experienced while working at the AEI.

I am also indebted to the members of the LIGO Scientific Collaboration, in particular its Burst Analysis Group, for providing an excellent forum for the exchange of ideas, many of which have had a profound impact on this work. In particular, the Data Analysis Group, I have had the privilege to work with many extraordinarily talented people who have helped make this work possible. While I have appreciated the countless hours of discussion and assistance they have provided while this research was carried out, above all I have appreciated working in such an enjoyable group. In particular, I would like to thank Patrick Sutton, Gareth Jones and Michal Was for their assistance. I look forward to continuing to work with them within the LIGO Scientific Collaboration.

On my thesis committee, I would also like to thank Szabi Marka, who introduced me to the challenge of multimessenger astronomy and astrophysics, and who was also instrumental in bringing me into the AEI graduate physics program. I extend my gratitude to Patrick Sutton for co-refereeing this dissertation.

Many thanks are due to the great support and care of the ATLAS cluster administrators, Carsten Aulbert and Henning Fehrmann.

For support, inspiration and friendship, I also thank Paola Leaci, Francesco Salemi, Giulio Mazzolo, Miroslav Shaltev, Marco Drago and Lisa Langella.

For that, I am extremely thankful.

Finally, I would not have been able to accomplish this monumental task without the support of my family. All of them have been a constant source of support, understanding, and encouragement throughout this process. I am proud to share this with you all.

# List of Publications

*A First Search for coincident Gravitational Waves and High Energy Neutrinos using LIGO, Virgo and ANTARES data from 2007*, Adrián-Martínez, ..., I. Di Palma, ..., J. Zweizig, arXiv:1205.3018, 2012.

*Multi-messenger astronomy with gravitational waves and high-energy neutrinos*, V. Van Elewyck, ..., I. Di Palma, arXiv:1203.5192, 2012.

*Multi-messenger Science Reach and Analysis Method for Common Sources of Gravitational Waves and High-energy Neutrinos* B. Baret, ..., I. Di Palma, ..., G. Vedovato, 2012 PRD 85, 103004, arXiv:1112.1140v1.

*Bounding the Time Delay between High-energy Neutrinos and Gravitational-wave Transients from Gamma-ray Bursts*, B. Baret, ..., I. Di Palma, ..., P. Sutton, arXiv:1101.4669, 2011.

*Search for gravitational waves associated with gamma-ray bursts during LIGO science run 6 and Virgo science runs 2 and 3*, M. Briggs, ..., I. Di Palma, ..., J. Zweizig, arXiv:1205.2216v1, 2012

*Swift follow-up observations of candidate gravitational-wave transient events*, P. Evans, ..., I. Di Palma, ..., J. Zweizig, arXiv:1205.1124, 2012

*Sensitivity Achieved by the LIGO and Virgo Gravitational Wave Detectors during LIGO's Sixth and Virgo's Second and Third Science Runs*, J. Abadie, ..., I. Di Palma, ..., J. Zweizig, arXiv:1203.2674, 2012.

*Search for Electromagnetic Counterparts to LIGO-Virgo Candidates: Expanded Very Large Array*, J. Lazio, ..., I. Di Palma, ..., J. Zweizig, arXiv:1203.0093,

2012.

*All-sky search for gravitational-wave bursts in the second joint LIGO-Virgo run*, J. Abadie,....., I. Di Palma, ..., J. Zweizig, arXiv:1202.2788, 2012.

*Search for Gravitational Waves from Intermediate Mass Binary Black Holes*, J. Abadie,....., I. Di Palma, ..., J. Zweizig, arXiv:1201.5999, 2012.

*Implications For The Origin Of GRB 051103 From LIGO Observations*, J. Abadie,....., I. Di Palma, ..., J. Zweizig, arXiv:1201.4413, 2012.

*First Low-Latency LIGO+Virgo Search for Binary Inspirals and their Electromagnetic Counterparts*, J. Abadie,....., I. Di Palma, ..., J. Zweizig, arXiv:1112.6005, 2011.

*Search for Gravitational Waves from Low Mass Compact Binary Coalescence in LIGO's Sixth Science Run and Virgo's Science Runs 2 and 3*, J. Abadie,....., I. Di Palma, ..., J. Zweizig, arXiv:1111.7314, 2011.

*All-sky Search for Periodic Gravitational Waves in the Full S5 LIGO Data*, J. Abadie,....., I. Di Palma, ..., J. Zweizig, arXiv:1110.0208, 2011.

*Implementation and testing of the first prompt search for gravitational wave transients with electromagnetic counterparts*, J. Abadie,....., I. Di Palma, ..., J. Zweizig, arXiv:1109.3498, 2011.

*A gravitational wave observatory operating beyond the quantum shot-noise limit: Squeezed light in application*, J. Abadie,....., I. Di Palma, ..., J. Zweizig, arXiv:1109.2295, 2011.

*Beating the spin-down limit on gravitational wave emission from the Vela pulsar*, J. Abadie,....., I. Di Palma, ..., J. Zweizig, arXiv:1104.2712, 2011.

*Search for gravitational waves from binary black hole inspiral, merger and ringdown*, J. Abadie,....., I. Di Palma, ..., J. Zweizig, arXiv:1102.3781, 2011.

*Search for Gravitational Wave Bursts from Six Magnetars*, J. Abadie,....., I. Di Palma, ..., J. Zweizig, arXiv:1011.4079, 2011.

*A search for gravitational waves associated with the August 2006 timing glitch of the Vela pulsar*, J. Abadie,....., I. Di Palma, ..., J. Zweizig, arXiv:1011.1357, 2011.

*Calibration of the LIGO Gravitational Wave Detectors in the Fifth Science Run*, J. Abadie,....., I. Di Palma, ..., J. Zweizig, arXiv:1007.3973, 2010.

*First search for gravitational waves from the youngest known neutron star*, J. Abadie,....., I. Di Palma, ..., J. Zweizig, arXiv:1006.2535, 2010.

*Search for Gravitational Waves from Compact Binary Coalescence in LIGO and Virgo Data from S5 and VSR1*, J. Abadie,....., I. Di Palma, ..., J. Zweizig, arXiv:1005.4655, 2010.

*Sensitivity to Gravitational Waves from Compact Binary Coalescences Achieved during LIGO's Fifth and Virgo's First Science Run*, J. Abadie,....., I. Di Palma, ..., J. Zweizig, arXiv:1003.2481, 2010.

*Predictions for the Rates of Compact Binary Coalescences Observable by Ground-based Gravitational-wave Detectors*, J. Abadie,....., I. Di Palma, ..., J. Zweizig, arXiv:1003.2480, 2010.

*All-sky search for gravitational-wave bursts in the first joint LIGO-GEO-Virgo run*, J. Abadie,....., I. Di Palma, ..., J. Zweizig, arXiv:1002.1036, 2010.

## Curriculum Vitae et Studiorum

### Irene Di Palma

	Name
February 2009-present	Doctoral Studies, International Max Planck Research School on Gravitational Wave Astronomy, Max-Planck-Institut für Gravitationsphysik (Albert-Einstein-Institut) and Leibniz Universität Hannover, Germany Advisers: Prof. Bruce Allen and Dr. M.Alessandra Papa
26 June 2008	Master Degree in Astronomy and Astrophysics (110/110) cum laude at University 'La Sapienza' in Rome Thesis: <i>Neutrino fluxes detection from galactic sources with the underwater detector ANTARES</i> Advisers: Prof. Antonio Capone and Dr. Fabrizio Lucarelli
30 October 2006	Bachelor Degree in Physics and Astrophysics (110/110) cum laude at University 'La Sapienza' in Rome Thesis: <i>Reduction of thermal noise in the gravitational experiments: study of the last suspension stadium of VIRGO mirrors for cryogenic environments</i> Adviser: Prof. Fulvio Ricci
<b>Fellowships</b>	
2009 ARAP	Prize for the best Master Degree Thesis in Astroparticle Physics
30 June - 7 September 2008	Summer Fellowship INFN-NSF/LIGO at 'Columbia University' of New York about <i>Search method for coincident events from LIGO-VIRGO-IceCube-ANTARES detectors</i> Adviser: Prof. Szabolcs Marka